AIX-MARSEILLE UNIVERSITÉ
ED 184 Mathématiques et Informatique de Marseille
Institut de Mathématiques de Marseille / Analyse Appliquée

Thèse présentée pour obtenir le grade universitaire de docteur

Discipline: Mathématiques Appliquées

Clément COLAS

Formulation Intégrale Implicite pour la Modélisation des Écoulements Fluides en Milieu Encombré

Time-Implicit Integral Formulation for Fluid Flow Modelling in Congested Media

Soutenue le 14/11/2019 devant le jury composé de:

Michel Belliard	CEA Cadarache	Rapporteur
Hervé Guillard	INRIA Sophia Antipolis	Rapporteur
Christophe Chalons	Université de Versailles St-Quentin-en-Yvelines	Examinateur
Cédric Galusinski	Université de Toulon	Examinateur
Raphaèle Herbin	Université d'Aix-Marseille	Examinateur
Jean-Marc Hérard	EDF R&D	Directeur de thèse
Jean-Claude Latché	IRSN Cadarache	Co-directeur de thèse
Invités		
Martin Ferrand	EDF R&D	Encadrant industriel
Erwan Le Coupanec	EDF R&D	Co-encadrant industriel

Contents

Introduction

Les travaux de recherche de la thèse ont été menés dans le cadre du contrat EDF-CIFRE 2016/0728. Ils se sont déroulés dans le groupe EDF, au sein d'EDF R&D, dans le département Mécanique des Fluides, Énergies, Environnement (MFEE) sur le site EDF Lab Chatou. Ils ont été réalisés en partenariat avec l'Institut de Mathématiques de Marseille (I2M, UMR CNRS 7373), plus précisément avec le groupe Analyse Appliquée. Les ressources informatiques de calcul ont été fournies par EDF R&D.

1 Contexte industriel

1.1 Principe de fonctionnement d'un *Réacteur à Eau Pressurisée*

Une part importante de la production d'électricité d'EDF est d'origine nucléaire et produite par des *Réacteurs à Eau Pressurisée*. Dans ces réacteurs, de l'eau sous pression est utilisée pour extraire la chaleur produite dans le cœur du réacteur par des réactions nucléaires de fission. C'est la source chaude dans le cycle thermodynamique du fonctionnement des turbines entraînant l'alternateur qui produit l'électricité. Pour garantir la sûreté de fonctionnement et son efficacité, il est nécessaire de comprendre et de décrire le plus exactement possible les écoulements et les échanges de chaleur qui interviennent dans les différents éléments des circuits de refroidissement du réacteur. Dans ce but, EDF R&D développe des outils de simulation numérique pour la mécanique des fluides et la thermohydraulique. Les travaux réalisés dans cette thèse s'inscrivent dans ce cadre.

Trois circuits d'eau, assurant les échanges de chaleur, interviennent dans le fonctionnement du réacteur (cf. FIGURE 1). Pour des raisons de sûreté, ces trois circuits sont, par conception, parfaitement distincts, sans aucun échange de masse entre eux.

Le circuit primaire permet l'extraction de la chaleur produite dans le cœur du réacteur, constitué d'assemblages de crayons de combustible de petit diamètre (moins d'un centimètre). Pour assurer une meilleure efficacité, le circuit contient de l'eau liquide à haute pression (environ 155 *bar*) et à température élevée en sortie de cœur (environ 320 °C), la pression de saturation de l'eau à cette température étant de 76 *bar*. En cas de détérioration de la gaine des crayons de combustible, l'eau du circuit primaire peut être contaminée. Il est donc indispensable qu'elle ne soit en contact avec aucun autre fluide et qu'elle reste à l'intérieur du bâtiment réacteur. Une fois chauffée dans le cœur du réacteur, l'eau du circuit primaire est envoyée dans les générateurs de vapeur où elle circule dans un grand nombre de tubes de faible section en contact avec l'eau du circuit secondaire, permettant un échange optimum de chaleur. Refroidie par cet échange, l'eau est renvoyée vers le cuve du réacteur : on ferme ainsi la boucle du circuit.

Dans le circuit secondaire, de l'eau, à plus basse pression (60 à 80 *bar*), est vaporisée et la vapeur chauffée jusqu'à une température de 280 °C dans les générateurs de vapeur. Les turbines sont mises en mouvement par la détente de cette vapeur et entraînent ainsi l'alternateur. En sortie de turbines, la vapeur d'eau est liquéfiée dans le condenseur, puis renvoyée vers le générateur de vapeur.

Le circuit tertiaire est la source froide du cycle thermodynamique. Dans le condenseur, l'eau de ce circuit permet de condenser la vapeur d'eau et de refroidir l'eau du circuit secondaire qui circule dans des faisceaux de tubes de faible diamètre pour maximiser les échanges thermiques (comme dans le générateur de vapeur). Seul ce circuit est ouvert sur l'extérieur (océan, fleuve ou tours aéroréfrigérantes).

Un point commun entre ces divers circuits est la présence de nombreux et petits (par rapport à la taille des composants du circuit) obstacles rigides de géométrie complexe autour desquels l'eau doit s'écouler : assemblages de crayons de combustible dans le cœur du réacteur, faisceaux de tubes de faible section dans le générateur de vapeur ou le condenseur. Cette large gamme d'échelles dans les circuits et les éléments internes induit des régimes d'écoulements monophasiques ou diphasiques complexes.

Cette problématique motive, depuis de nombreuses années, des travaux de recherche sur la modélisation et la simulation numérique des écoulements en milieu encombré.

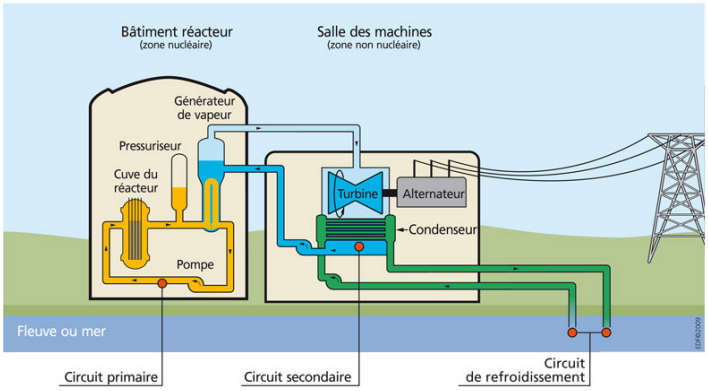

FIGURE 1 – *Principe de fonctionnement d'un Réacteur à Eau Pressurisée [1]* © IRSN.

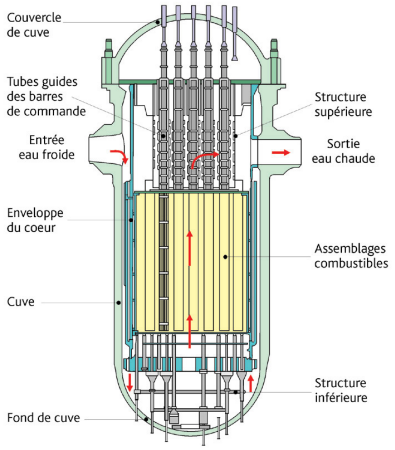

FIGURE 2 – *Schéma d'une coupe de cuve (réacteur 900 MWe) [2]* © *Georges Goué/IRSN.*

1.2 Les composants d'un réacteur : des milieux encombrés

Dans un réacteur, les deux principaux composants présentant un intérêt pour la modélisation et la simulation numérique des écoulements en milieu encombré sont : la cuve contenant le cœur du réacteur et les générateurs de vapeur contenant l'échangeur de chaleur.

1.2.1 La cuve contenant le cœur

La cuve, en acier, est l'organe principal du circuit primaire, où la chaleur est extraite du combustible par l'eau liquide sous pression. Elle contient le cœur du réacteur, constitué d'environ deux cents assemblages, regroupant chacun plus de deux cents crayons de combustible. Ces crayons sont constitués d'une gaîne, encapsulant les pastilles de matières fissiles. La cuve mesure environ dix mètres de haut et quatre mètres de diamètre, alors que la plus petite échelle entre les crayons de combustible est de moins d'un centimètre. On y trouve d'autres structures tels que les tubes guides, les barres de commande pour piloter la puissance du réacteur et les instruments de mesure (cf. FIGURE 2), mais également des structures de type plaque comme les grilles de mélange.

1.2.2 Les générateurs de vapeur

Un générateur de vapeur est également un organe très encombré. Selon la puissance du réacteur, il y a trois ou quatre boucles, chacune équipée d'un générateur de vapeur. Il permet d'extraire la chaleur du circuit primaire circulant à l'intérieur d'un faisceau de tubes de petit diamètre (de l'ordre de deux centimètres) pour vaporiser l'eau du circuit secondaire. Le générateur, de forme cylindrique, mesure une vingtaine de mètres de hauteur pour quartes mètres de diamètre au maximum. Il renferme de trois à six mille tubes en forme de "U" inversé. Ces tubes sont fixés à la base par une plaque tubulaire, et maintenus à intervalle régulier par des plaques entretoises.

Pour ces deux composants, la puissance des machines de calcul disponibles ne permet pas actuellement de prendre en compte simultanément dans une même simulation numérique instationnaire des échelles aussi différentes dues aux éléments constitutifs allant de quelques centimètres à plusieurs mètres. En effet, un maillage fin millimétrique nécessiterait des milliards de mailles pour discrétiser la géométrie de ces composants.

1.3 Les différentes échelles de simulation numérique en thermohydraulique

Pour simuler les écoulements dans les circuits d'un *Réacteur à Eau Pressurisée*, trois échelles différentes de description ont été développées par le passé : l'échelle système, l'échelle composant et l'échelle locale, décrites succinctement ci-dessous. Chaque échelle de représentation fait appel à des codes de calcul dédiés.

1.3.1 L'échelle système

L'échelle système est l'échelle la plus large. Elle a pour but la simulation en temps réel d'un circuit complet en régime de fonctionnement nominal ou accidentel. A cette échelle, de nombreux éléments technologiques sont inclus, comme le cœur, le générateur de vapeur, les condenseurs et les pompes. Elle repose sur des descriptions zéro-dimensionnelles ou uni-dimensionnelles des circuits thermohydrauliques et permet d'avoir une vision d'ensemble du comportement des différents circuits de manière séparée ou couplée.

Le code industriel de référence en France est CATHARE (Code Avancé de ThermoHydraulique pour les Accidents de Réacteurs à Eau) [3], historiquement issu du code RELAP (Reactor Excursion and Leak Analysis Program) développé aux États-Unis. Il est développé, depuis 1979, dans le cadre d'un accord réunissant le CEA (Commissariat à l'Énergie Atomique et aux Énergies Alternatives), EDF, IRSN (Institut de Radioprotection et Sûreté Nucléaire) et Framatome. La discrétisation en espace des équations résolues utilise une méthode mixte Volumes Finis et Différences Finies sur grille décalée grossière, tandis que l'intégration en temps s'effectue avec une méthode implicite de type Newton-Raphston, permettant d'accroître la stabilité à grand pas de temps de calcul.

1.3.2 L'échelle composant

L'échelle composant, ou échelle intermédiaire, est apparue pour simuler de manière plus précise la thermohydraulique dans les différents composants de réacteur : par exemple le cœur et les générateurs de vapeur. Ils se caractérisent par une structure de grande taille (plusieurs mètres) encombrée d'internes nombreux et de petites dimensions (de l'ordre du centimètre). Deux ordres de grandeur les séparent. Ainsi, la complexité des géométries et cette différence de dimension dans le domaine de calcul sont prises en compte au travers d'une représentation équivalente homogénéisée des internes dans le composant. Les internes, comme par exemple les barreaux de

combustible dans le cœur, ne sont pas explicitement représentés dans la maille de calcul. Cela permet d'utiliser des maillages grossiers cartésiens, mais empêche un raffinement en maillage pour des géométries complexes.

Les codes utilisés industriellement depuis les années quatre-vingt sont : THYC (ThermoHYdraulique des Composants) [4, 5], développé à EDF, FLICA-4 [6] et Génépi [7], développés au CEA. Ces codes combinent des modèles d'équations avec des lois de fermeture sous forme de corrélations. Ces corrélations sont *ad hoc*, c'est-à-dire spécifiques à une gamme de fonctionnement et à une géométrie. Par exemple, les corrélations utilisées pour la simulation du cœur sont différentes de celles utilisées pour le générateur de vapeur.

1.3.3 L'échelle locale

L'échelle locale est la plus petite échelle. Elle a pour objectif de décrire finement et directement, sans modélisation simplificatrice des composants et en évitant de faire appel à des corrélations, l'écoulement entre les internes. La géométrie réelle complexe est alors représentée par un maillage fin tri-dimensionnel. L'avantage est de pouvoir s'affranchir des contraintes dues aux plages restreintes de conditions thermohydrauliques d'utilisation, des codes à l'échelle système et composant. Par contre, elle est plus coûteuse en temps de calcul (CPU) et en mémoire. Elle ne peut être conduite actuellement sur l'intégralité des circuits, du fait de la complexité des échelles spatiales et temporelles mises en jeu dans ces installations industrielles.

A l'heure actuelle, les simulations à l'échelle locale sont, en grande partie, réservées à des études avancées sur des domaines de calcul restreints. Cependant l'augmentation constante de la puissance de calcul des ordinateurs disponibles amène à intensifier l'utilisation industrielle des calculs à l'échelle locale et à envisager un fort développement de leur usage dans les vingt ans à venir.

Des codes industriels, appelés codes de simulation CFD (Computational Fluid Dynamics), ont été développés depuis la fin des années quatre-vingt-dix, comme, par exemple, les logiciels libres : *Code_Saturne* à EDF [8, 9], TrioCFD [10] au CEA ou OpenFOAM [11], et les logiciels propriétaires sous licence : NEPTUNE_CFD [12] (collaboration CEA, EDF, Framatome et IRSN) ou les logiciels américains du commerce, ANSYS Fluent [13], Star-CCM+ [14] et COMSOL Multiphysics [15]. La plupart de ces codes cherche à résoudre les équations de la mécanique des fluides tri-dimensionnelles, plus précisément les équations de Navier-Stokes, en utilisant une méthode numérique de Volumes Finis sur maillage non-structuré (cf. [16] pour plus de détails).

2 Contexte scientifique

Tout d'abord, les modèles fluides basés sur les équations de Navier-Stokes ou d'Euler (lorsqu'on néglige les effets de la viscosité du fluide) sont rapidement rappelés : ils permettent la description locale des écoulements.

Puis, les modèles moyennés, usuels dans le domaine de la thermohydraulique, qui permettent de décrire un écoulement en milieu encombré à l'échelle composant, sont brièvement décrits. Ces modèles utilisent comme point de départ pour leur élaboration les équations de Navier-Stokes moyennées. L'établissement de ces systèmes d'équations aux dérivées partielles n'est volontairement pas détaillé ici.

Tous les modèles présentés ici utilisent une approche eulérienne de la description des écoulements.

2.1 Modélisation des écoulements

2.1.1 Équations de Navier-Stokes

Les équations locales pour modéliser l'écoulement de fluides compressibles monophasiques sont les équations de Navier-Stokes, définies dans un domaine Ω, ouvert borné connexe de $\mathbb{R}^3$, à tout instant $t \geq 0$. Elles traduisent la conservation de la masse, $\int_\Omega \rho(\boldsymbol{x},t)\mathrm{d}\boldsymbol{x}$, de quantité de mouvement $\int_\Omega \boldsymbol{Q}(\boldsymbol{x},t)\mathrm{d}\boldsymbol{x}$, avec $\boldsymbol{Q} = \rho\boldsymbol{u}$, et de l'énergie totale $\int_\Omega \rho(\boldsymbol{x},t)e(\boldsymbol{x},t)\mathrm{d}\boldsymbol{x}$ (cf. [17, 18] pour l'établissement des équations).

Résoudre le problème de Navier-Stokes dans $\Omega \times (0,T)$, $T > 0$, consiste à déterminer les trois variables indépendantes qui sont la masse volumique $\rho : \Omega \times (0,T) \to \mathbb{R}$, le vecteur vitesse $\boldsymbol{u} : \Omega \times (0,T) \to \mathbb{R}^3$ et la pression $P : \Omega \times (0,T) \to \mathbb{R}$ (ou l'énergie totale spécifique e), vérifiant :

$$\left\{ \begin{array}{l} \partial_t \rho + \mathrm{div}\,(\rho\boldsymbol{u}) = 0, \\ \partial_t(\rho\boldsymbol{u}) + \mathbf{div}\,(\boldsymbol{u}\otimes\rho\boldsymbol{u}) + \boldsymbol{\nabla} P = \rho\boldsymbol{f} + \mathbf{div}\,(\boldsymbol{\tau}), \\ \partial_t \rho e + \mathrm{div}\,(\boldsymbol{u}(\rho e + P)) = \rho\boldsymbol{f}\cdot\boldsymbol{u} + \mathrm{div}\,(\boldsymbol{\tau}\,\boldsymbol{u}) - \mathrm{div}\,(\boldsymbol{\varphi}_{th}), \end{array} \right. \tag{1}$$

ainsi que des conditions initiales, à $t = 0$, et des conditions aux limites prescrites sur $\partial\Omega$.

Ici, nous notons $\boldsymbol{f}$ une force extérieure spécifique comme la gravité, $\boldsymbol{\tau}$ le tenseur des contraintes visqueuses, $\boldsymbol{\varphi}_{th}$ le flux thermique. Dans le cadre des équations de Navier-Stokes, le fluide est supposé newtonien et suit donc le modèle de Stokes :

$$\boldsymbol{\tau} = \mu\left(\boldsymbol{\nabla}\boldsymbol{u} + \boldsymbol{\nabla}\boldsymbol{u}^{\mathsf{T}} - \frac{2}{3}\mathrm{div}\,(\boldsymbol{u})\,\mathbf{Id}\right),$$

où μ est la viscosité dynamique du fluide, reliée à la viscosité cinématique, ν, par $\mu = \rho\nu$.

Au système d'équations aux dérivées partielles (1) est associée une équation d'état, qui caractérise la compressibilité du fluide, fonction des variables d'état thermodynamiques. Elle permet de relier la masse volumique, la pression et l'énergie interne, $\epsilon = e - \frac{1}{2}|\boldsymbol{u}|^2$, par une relation de la forme :

$$P = \mathcal{P}(\rho, \epsilon). \tag{2}$$

2.1.2 Équations d'Euler

Le système d'équations aux dérivées partielles homogène (3) associé à (1) est le système des équations d'Euler. Il décrit le mouvement d'un fluide parfait, c'est-à-dire en négligeant les frottements visqueux, et s'écrit, en l'absence de forces extérieures :

$$\left\{ \begin{array}{l} \partial_t \rho + \mathrm{div}\,(\rho\boldsymbol{u}) = 0, \\ \partial_t(\rho\boldsymbol{u}) + \mathbf{div}\,(\boldsymbol{u}\otimes\rho\boldsymbol{u}) + \boldsymbol{\nabla} P = 0, \\ \partial_t \rho e + \mathrm{div}\,(\boldsymbol{u}(\rho e + P)) = 0. \end{array} \right. \tag{3}$$

On rappelle (cf. [19, 20]) que ce système non-linéaire est hyperbolique pour une équation d'état appropriée. En posant $\boldsymbol{W} = (\rho, \rho\boldsymbol{u}, \rho e)^{\mathsf{T}}$ le vecteur d'état, rassemblant les grandeurs conservées, et la fonction flux $\boldsymbol{F}(\boldsymbol{W}) = (\rho\boldsymbol{u}, \rho\boldsymbol{u}\otimes\boldsymbol{u} + P\,\mathbf{Id}, (\rho e + P)\boldsymbol{u})^{\mathsf{T}}$, l'équation (3) s'écrit sous la forme d'une loi de conservation :

$$\partial_t \boldsymbol{W} + \mathbf{div}\,(\boldsymbol{F}(\boldsymbol{W})) = 0 \quad \text{dans } \Omega \times (0,T)\,.$$

En se plaçant dans un cadre uni-dimensionnel, les valeurs propres réelles de sa matrice jacobienne $\frac{\partial \boldsymbol{F}(\boldsymbol{W})}{\partial \boldsymbol{W}}$ sont $\{u - c, u, u + c\}$, où c est la vitesse du son définie par :

$$c^2 = \left.\frac{\partial P}{\partial \rho}\right|_s,$$

avec s, l'entropie spécifique du fluide, et $\mathcal{T}$, sa température telle que $\mathcal{T} = \frac{\partial \epsilon}{\partial s}\big|_\rho$. L'identité thermodynamique fondamentale suivante est vérifiée :

$$\mathrm{d}\epsilon = \mathcal{T}\mathrm{d}s + \frac{P}{\rho^2}\mathrm{d}\rho.$$

Les deux champs caractéristiques, associés aux valeurs propres $\{u - c, u + c\}$, sont vraiment non linéaires et correspondent à des ondes simples de détente ou de choc. Ils modélisent les phénomènes rapides de propagation d'ondes de pression.

Le champ caractéristique associé à la valeur propre $\{u\}$ est, quant à lui, linéairement dégénéré, et correspond à une onde simple de discontinuité de contact. Il modélise les phénomènes de propagation d'ondes matérielles.

Rappelons également que :

- les 1-invariants de Riemann (du 1-champ caractéristique), constants le long de la 1-onde de détente, sont :
$$s \text{ et } u + \int_0^\rho \frac{c(\varrho, s)}{\varrho}\mathrm{d}\varrho,$$
- les 2-invariants de Riemann (du 2-champ caractéristique), constants le long de la 2-onde de discontinuité de contact, sont :
$$u \text{ et } P,$$
- les 3-invariants de Riemann (du 3-champ caractéristique), constants le long de la 3-onde de détente, sont :
$$s \text{ et } u - \int_0^\rho \frac{c(\varrho, s)}{\varrho}\mathrm{d}\varrho.$$

Les relations de saut de Rankine-Hugoniot pour une 1 ou 3-onde de choc, qui caractérisent une solution discontinue, sont données par le système :

$$-\sigma\,[\boldsymbol{W}] + [\boldsymbol{F}(\boldsymbol{W})] = 0,$$

où σ est la vitesse de la discontinuité, séparant les deux états gauche et droit de part et d'autre de cette discontinuité.

L'analyse mathématique des équations d'Euler (détaillée dans [19, 20]) permet de résoudre analytiquement certains problèmes, comme le problème de Riemann uni-dimensionnel plan, correspondant à un problème de Cauchy avec un vecteur d'état initial constant par morceaux, et également de concevoir des schémas numériques permettant d'approximer les équations d'Euler en préservant les propriétés du modèle hyperbolique au niveau discret (par exemple le respect du caractère conservatif, de la positivité des variables et de l'inégalité d'entropie).

2.1.3 Présence d'obstacles : conditions aux limites de paroi

Lorsque le fluide s'écoule, dans le domaine Ω, autour d'obstacles rigides, les modèles fluides de type (1) ou (3) prennent en compte les obstacles au moyen de conditions aux limites de paroi. Cette condition aux limites est imposée à la frontière $\partial\Omega_p$ des obstacles : la condition de paroi est soit de type adhérence (appelée également condition de non glissement) lorsque le fluide est considéré visqueux ($\mu \neq 0$) :

$$\boldsymbol{u}|_{\partial\Omega_p} = 0,$$

soit de type glissement lorsque le fluide est considéré parfait ($\mu = 0$) :

$$\boldsymbol{u} \cdot \boldsymbol{n}|_{\partial\Omega_p} = 0,$$

où $\boldsymbol{n}$ est un vecteur normal à la paroi.

En présence de nombreux obstacles, il est important de noter que la résolution du problème, ainsi posé, peut être très lourde et compliquée, du fait, entre autres, de l'effet de couche limite autour des obstacles et des différentes structures complexes se développant dans l'écoulement.

Une autre approche revient à modéliser le milieu fluide encombré en homogénéisant les obstacles dans le domaine Ω. Le domaine fluide est alors remplacé par un milieu équivalent rempli d'une pseudo-matière plus ou moins poreuse.

2.2 Modélisation des écoulements en milieu encombré

La modélisation des écoulements en milieu encombré est un sujet de recherche depuis plus de quarante ans dans la communauté de la thermohydraulique nucléaire. Le modèle le plus utilisé dans la littérature et dans les codes industriels de simulation à l'échelle composant est le modèle moyenné en espace des équations locales de la mécanique des fluides dit "approche poreuse" [5, 6, 7, 21, 22] : les différents obstacles encombrant le milieu fluide sont pris en compte dans le domaine de calcul au moyen d'une porosité volumique indépendante du temps. Le milieu encombré physique est alors modélisé par un milieu poreux équivalent.

2.2.1 Définition d'un milieu poreux

Un milieu poreux est un milieu physique constitué de matière et de pores, au travers desquels un fluide peut s'écouler plus ou moins facilement [23]. Définissant d comme l'échelle caractéristique du pore, la porosité sur un volume macroscopique $\mathcal{V}_{total} \gg d^3$ est définie par :

$$\varepsilon = \frac{\mathcal{V}_{fluide}}{\mathcal{V}_{total}}, \tag{4}$$

avec $\mathcal{V}_{fluide} = \mathcal{V}_{total} - \mathcal{V}_{solide}$, où $\mathcal{V}_{solide}$ est le volume de matière solide dans le volume total. En passant à la limite dans le cadre des hypothèses de la mécanique des milieux continus [18], la porosité locale $\varepsilon(\boldsymbol{x})$ est définie pour tout $\boldsymbol{x} \in \Omega$.

Dans le contexte de l'échelle composant, un milieu poreux sert à modéliser un écoulement à une échelle bien supérieure à celle du sous-canal (équivalent du pore) dans lequel le fluide s'écoule entre les solides. L'échelle mésoscopique (ou de filtrage) de définition de la porosité locale doit être plus petite que l'échelle du maillage de discrétisation spatiale du domaine de calcul. Ainsi, le domaine de calcul maillé peut être assimilé à un milieu poreux à l'échelle du composant, malgré la connaissance des petits éléments le constituant et de leur disposition, dans le but de simuler globalement l'écoulement à cette échelle de raffinement en maillage.

2.2.2 Équations du modèle moyenné dit poreux

Le système d'équations aux dérivées partielles (5) est constitué des trois équations de conservation de la mécanique des fluides, moyennées en espace par l'introduction de la notion de porosité volumique : conservation de la masse, de la quantité de mouvement et de l'énergie totale. Par souci de simplicité, il est écrit pour un fluide monophasique. Les modèles diphasiques utilisés ne sont pas discutés dans ces travaux de thèse :

$$\begin{cases} \partial_t(\varepsilon\rho) + \operatorname{div}(\rho\varepsilon\boldsymbol{u}) = 0, \\ \partial_t(\varepsilon\rho\boldsymbol{u}) + \mathbf{div}(\boldsymbol{u}\otimes\varepsilon\rho\boldsymbol{u}) + \varepsilon\boldsymbol{\nabla}P = \varepsilon\rho\boldsymbol{f} + \mathbf{div}(\varepsilon\boldsymbol{\tau}) - \varepsilon\rho\boldsymbol{K}\,\boldsymbol{u}, \\ \partial_t(\varepsilon\rho e) + \operatorname{div}(\varepsilon\boldsymbol{u}(\rho e + P)) = \varepsilon\rho\boldsymbol{f}\cdot\boldsymbol{u} + \operatorname{div}(\varepsilon\boldsymbol{\tau}\,\boldsymbol{u}) - \operatorname{div}(\varepsilon\boldsymbol{\varphi}_{th}). \end{cases} \tag{5}$$

A ce système d'équations (5), l'équation d'état thermodynamique précédente (2) doit être ajoutée pour prendre en compte la compressibilité du fluide.

$\boldsymbol{K}$ est un tenseur de corrélation prenant en compte une part de l'interaction fluide-solide, appelé tenseur des pertes de charges. Ce terme ainsi que le flux thermique du aux solides chauffants donnent lieu à des lois de fermeture dues à la présence de solides pris en compte par homogénéisation.

On suppose que la porosité est une donnée du problème indépendante du temps. Les variables fluides, $\varphi = (\rho, \rho\boldsymbol{u}, \rho e)$ ou P, sont moyennées sur un volume de contrôle quelconque $\mathcal{V}_{total}(\boldsymbol{x})$ de Ω. Elles sont définies classiquement, à tout instant $t \geqslant 0$, par :

$$\varphi(\boldsymbol{x}, t) = \frac{1}{\mathcal{V}_{vide}(\boldsymbol{x})} \int_{\mathcal{V}_{vide}(\boldsymbol{x})} \varphi(\boldsymbol{v}, t) \mathrm{d}\boldsymbol{v} = \frac{1}{\varepsilon(\boldsymbol{x})} \frac{1}{\mathcal{V}_{total}(\boldsymbol{x})} \int_{\mathcal{V}_{total}(\boldsymbol{x})} \varphi(\boldsymbol{v}, t) \mathrm{d}\boldsymbol{v}. \tag{6}$$

La vitesse moyenne est, quant à elle, définie par :

$$\boldsymbol{u} = \frac{\rho\boldsymbol{u}}{\rho}. \tag{7}$$

En se focalisant uniquement sur le système homogène associé à (5) avec $\partial_t \varepsilon = 0$,

$$\begin{cases} \partial_t(\varepsilon\rho) + \operatorname{div}(\rho\varepsilon\boldsymbol{u}) = 0, & \text{(8a)} \\ \partial_t(\varepsilon\rho\boldsymbol{u}) + \mathbf{div}(\boldsymbol{u} \otimes \varepsilon\rho\boldsymbol{u}) + \varepsilon\boldsymbol{\nabla} P = 0, & \text{(8b)} \\ \partial_t(\varepsilon\rho e) + \operatorname{div}(\varepsilon\boldsymbol{u}(\rho e + P)) = 0, & \text{(8c)} \end{cases}$$

on peut montrer que ce système (8) est hyperbolique, pour le vecteur d'état $\boldsymbol{W} = (\varepsilon\rho, \varepsilon\rho\boldsymbol{u}, \varepsilon\rho e)^{\mathsf{T}}$ avec les trois valeurs propres $\{u - c, u, u + c\}$. Il comporte également un produit non-conservatif, proportionnel au gradient de la pression moyenne. On note l'analogie avec le système d'Euler à section variable [24].

2.3 Simulation numérique des écoulements en milieu encombré

L'approche poreuse, décrite dans la partie précédente, est utilisée dans les différents codes de simulation tri-dimensionnels des écoulements thermohydrauliques à l'échelle composant, déjà cités : THYC, FLICA-4 ou Génépi.

Par contre, différentes méthodes de discrétisation sont adoptées pour la simulation numérique du modèle dit poreux, équation (5), qui est un système d'équations aux dérivées partielles de type convection-diffusion avec terme source. Les différents codes ont en commun l'utilisation de schémas en temps implicites ou semi-implicites, permettant d'effectuer des simulations stables à grands pas de temps par rapport au temps caractéristique des ondes acoustiques, et d'atteindre rapidement un régime stationnaire. Cela est pertinent pour la simulation des écoulements considérés, qui sont souvent quasi-stationnaires.

On note que la convergence des méthodes numériques utilisées n'est pas toujours démontrée théoriquement. Il est alors primordial d'apporter un soin tout particulier au processus de vérification et de validation des codes. Ce dernier est important pour toute simulation numérique, mais devient fondamental pour la sûreté nucléaire. Toute nouvelle modélisation ou méthode numérique implémentée doit suivre ce processus.

2.3.1 THYC

Le code THYC est principalement utilisé pour les calculs dans le cœur du réacteur ou dans le générateur de vapeur pour des études en régime stationnaire [5, 4]. La méthode numérique utilisée dans ce code est basée sur une discrétisation Volumes Finis en espace sur quatre grilles cartésiennes (maillage structuré orthogonal) décalées en trois dimensions et sur une méthode à pas fractionnaires pour la discrétisation en temps du système d'équations.

La méthode à pas fractionnaires consiste à diviser en trois étapes l'intégration temporelle du système (8), chacune consacrée à un phénomène physique différent : partant de la condition initiale à $t = t^n$, et notant $\delta\varphi = \varphi^{n+1} - \varphi^n$ l'incrément temporel de la variable φ, la première étape est dédiée à la résolution de l'équation de bilan d'énergie réécrite avec l'inconnue entropie s :

$$\varepsilon\rho^n T^n \left(\frac{\delta s}{\Delta t} + \frac{\boldsymbol{Q}^n}{\rho^n} \boldsymbol{\nabla} s^{n+1} \right) = -\mathrm{div}\left(\varepsilon\varphi_{th}^n\right). \tag{9}$$

La deuxième étape correspond à l'approximation de la solution du bilan de quantité mouvement, en estimant, à l'instant intermédiaire $t^\star$, la variable de quantité de mouvement $\boldsymbol{Q}^\star$ en partant de l'instant t^n :

$$\varepsilon \frac{\boldsymbol{Q}^\star - \boldsymbol{Q}^n}{\Delta t} + \mathbf{div}\left(\varepsilon \boldsymbol{u}^n \otimes \boldsymbol{Q}^\star\right) + \varepsilon \boldsymbol{\nabla} P^n = \mathbf{div}\left(\varepsilon\nu \boldsymbol{\nabla} \boldsymbol{Q}^\star\right) - \varepsilon \boldsymbol{K}\, \boldsymbol{Q}^\star. \tag{10}$$

La troisième et dernière étape est dédiée à la résolution de l'équation de bilan de masse écrite en pression et couplée à une partie du bilan de quantité de mouvement, en considérant la condition initiale $(P^n, \boldsymbol{Q}^\star)$:

$$\begin{cases} \varepsilon \dfrac{1}{c^2} \dfrac{\delta P}{\Delta t} + \mathrm{div}\left(\varepsilon \boldsymbol{Q}^{n+1}\right) = -\varepsilon\beta \dfrac{\delta s}{\Delta t}, \\ \varepsilon \dfrac{\boldsymbol{Q}^{n+1} - \boldsymbol{Q}^\star}{\Delta t} + \varepsilon \boldsymbol{\nabla} \delta P = -\varepsilon \boldsymbol{K}\left(\boldsymbol{Q}^{n+1} - \boldsymbol{Q}^\star\right). \end{cases} \tag{11}$$

La masse volumique est mise à jour :

$$\rho^{n+1} = \rho^n + \frac{\delta P}{c^2} + \beta \delta s, \quad \text{avec } \beta = \left.\frac{\partial \rho}{\partial s}\right|_P .$$

Cette dernière étape (11) est appelée étape de propagation-conservation de la masse. Elle permet de propager les ondes acoustiques avec un schéma implicite en temps, et ainsi de relâcher la contrainte CFL basée sur les ondes rapides. Cette discrétisation en temps est une méthode de correction de pression incrémentale. En effet, à l'instar des méthodes de projection (dans l'espace des vitesses à divergence nulle) pour discrétiser les équations de Navier-Stokes incompressibles [25, 26, 27, 28], la conservation de la masse est assurée au moyen du calcul d'une pression.

2.3.2 FLICA-4

FLICA-4 est principalement dédié à l'analyse de régimes transitoires et stationnaires dans le cœur [6]. Ce code du CEA est basé sur une méthode numérique de Volumes Finis en espace sur grille co-localisée, c'est-à-dire que toutes les variables principales sont calculées sur la même maille de discrétisation en espace. La discrétisation temporelle est implicite et utilise un solveur de Riemann approché linéarisé, qui est une extension du schéma de Roe [29].

2.3.3 Génépi

Génépi est un outil numérique pour la simulation dans le cœur et le générateur de vapeur pour des états stationnaires [7, 30, 31, 32, 33, 34]. Une méthode à pas fractionnaires à correction de pression est également adoptée pour la discrétisation en temps : les bilans successifs d'énergie (écrit en enthalpie) puis de quantité de mouvement (prédiction de la vitesse) et de masse (correction de la vitesse) sont résolus. Une méthode de projection incrémentale de type incompressible est utilisée pour corriger la vitesse en assurant l'équation de continuité $\mathrm{div}\left(\varepsilon\rho\boldsymbol{u}\right) = 0$ (la variation temporelle de la masse volumique $\partial_t(\varepsilon\rho)$ est ici négligée). L'intégration temporelle des équations est faite avec un schéma implicite de Crank-Nicolson.

A la différence des deux autres codes, la discrétisation en espace s'effectue via une méthode d'Éléments Finis de type $\mathbb{Q}_1$ (pour la vitesse et l'enthalpie) et $\mathbb{Q}_0$ (pour la pression).

L'ensemble de ces codes permet de simuler correctement des écoulements en milieu encombré régis par le système d'équations (5) pour des distributions spatiales régulières de porosité (équivalente) dans le domaine de calcul. Néanmoins, pour la simulation en entrée de cœur et de générateur de vapeur, on sait que cette régularité n'est pas acquise.

De sérieuses difficultés de simulation peuvent apparaître quand les caractéristiques du milieu réel varient brusquement en espace, comme le passage discontinu d'une zone libre à une zone encombrée : c'est par exemple le cas dans le fond de cuve, lorsque l'eau du circuit primaire rentre dans le cœur du réacteur.

Une première approche possible est d'améliorer le schéma numérique de résolution du modèle poreux (8).

2.3.4 Schémas "well-balanced"

Des schémas numériques dits "équilibrés" ou "well-balanced", introduits dans [35] et [36], et revisités dans [24], permettent d'obtenir des solutions approximées convergées du système (8) pour des porosités discontinues, en considérant une onde supplémentaire stationnaire. Pour cela, l'approche "well-balanced" introduit une équation triviale dans le système (8) qui correspond à la stationnarité de la porosité :

$$\partial_t \varepsilon = 0. \tag{12}$$

Cette équation (12) ajoute une valeur propre nulle au système initial (8), c'est-à-dire une onde stationnaire linéairement dégénérée. Ainsi, le problème de Riemann résolu à chaque interface du maillage et à chaque pas de temps par le schéma "well-balanced" impose la préservation des trois invariants de Riemann de cette onde stationnaire, soit pour le système (8)-(12) le flux de masse εQ , le flux d'enthalpie εQH (avec $H = e + \frac{P}{\rho}$, l'enthalpie totale spécifique) et l'entropie s. De plus amples détails sur cette approche sont donnés dans [21, 22, 24, 35, 36, 37].

Malheureusement, le modèle poreux, utilisant un milieu poreux équivalent, est en fait physiquement inapproprié pour simuler cette transition discontinue entre un domaine libre et encombré. Une illustration en est donnée dans [38] par la comparaison numérique entre des calculs bidimensionnels CFD à l'échelle locale, où la géométrie réelle des obstacles est représentée (cf. Figure 3), et le calcul à l'échelle composant avec une approche utilisant un milieu poreux équivalent uni-dimensionnelle (cf. Figure 4). Cette comparaison [38] montre une inadéquation des résultats à l'interface associée à la discontinuité du champ de porosité équivalent, positionnée en : $x = x_0$, pour $u_{inlet} \neq 0$.

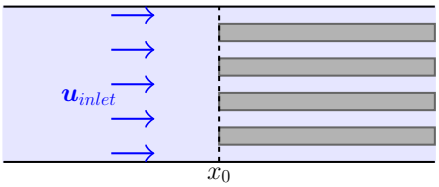

Figure 3 – *Modèle fluide 2D.*

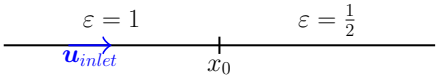

Figure 4 – *Modèle poreux 1D.*

La solution du calcul CFD, considérée comme la référence, n'est pas retrouvée. Cet écart peut être attribué au fait que la perte de charge singulière (en $x = x_0$) dans l'équation de bilan de quantité de mouvement n'est pas prise en compte dans l'approche poreuse (8) : l'entropie ne doit en effet pas nécessairement être préservée à l'interface stationnaire. En effet, l'équation de quantité de mouvement (8b) n'intègre aucune masse de Dirac portée en $x = x_0$, de type

$M(x_0, t)\delta(x - x_0)$. Une estimation de cette masse de Dirac est proposée dans [39], modifiant ainsi l'équation de quantité de mouvement dans le système (8), et donc les conditions de raccord à l'interface stationnaire.

Dans ce cas, le nouveau schéma "well-balanced" [39] permet de retrouver une approximation plus satisfaisante des résultats de référence bidimensionnels obtenus avec le modèle fluide. Elle n'est néanmoins pas optimale d'une part, au sens où les nouvelles conditions d'interface peuvent sans doute être améliorées, et d'autre part, une extension de cette condition d'équilibre appropriée au cadre bidimensionnel ou tridimensionnel semble difficile. Cette condition nécessite en outre, tout comme la condition classique, un traitement adapté lorsque le système non linéaire scalaire à résoudre de chaque côté de l'interface n'admet pas de solution. A court terme, la voie proposée dans [39] reste donc à approfondir et n'est pas non plus la plus naturelle.

Cette synthèse de travaux existants étant faite, nous en venons aux objectifs de la thèse.

2.4 Objectifs des travaux

Le but de la thèse est de proposer une alternative aux approches en milieu poreux équivalent (8), présentées dans la partie précédente, avec deux objectifs principaux :

- premièrement de dépasser la difficulté, relevée dans [38] et rappelée précédemment, qui survient lorsque la porosité du milieu modélisé est discontinue (passage brusque d'un milieu libre à encombré) ;
- deuxièmement, de naturellement redonner le modèle fluide de type équations d'Euler (3) ou de Navier-Stokes (1) de l'échelle locale, lorsque le maillage du domaine de calcul est raffiné et devient exactement adapté à la géométrie des obstacles encombrant ce domaine.

Cette approche, appelée ici approche ou formulation intégrale, a été introduite dans les travaux [40, 41]. Dans lesquels, elle est discrétisée au moyen d'une méthode numérique explicite en temps avec un solveur approché de Godunov (schéma VFRoe-ncv).

Pour ce faire, la dérivation d'un modèle continu équivalent est abandonnée. De manière alternative, les équations de bilans du modèle fluide (3) ou (1) sont directement écrites sous forme intégrale sur les volumes de contrôle pouvant contenir des obstacles, à la manière d'une approche Volumes Finis standard. Des intégrales de bord solide apparaissent et doivent alors être estimées. En particulier, un traitement adéquat des forces de pression sur les solides permet d'injecter au niveau discret des pertes de charges singulières. Il en est de même pour des pertes de charge régulières associées aux forces de frottement visqueux à la paroi.

On notera que cette procédure diffère d'une discrétisation Volumes Finis standard d'un système d'équations aux dérivées partielles, au sens où, les enjeux de consistance et de convergence du schéma n'ont plus de sens, puisque le système discret obtenu ne peut être considéré comme associé à un problème continu, jusqu'au moment où le raffinement du maillage permet de retouver le modèle CFD classique. En pratique, un gain significatif de précision sur les grandeurs d'intérêt simulées (chute de pression par exemple) est attendu pour certaines géométries d'obstacles ; des test numériques seront réalisés pour quantifier cette effet.

La stratégie globale est, d'un point de vue industriel, de rassembler dans un même outil numérique les capacités des approches à l'échelle composant et locale, et pouvoir ainsi passer naturellement d'une échelle à l'autre. Cette stratégie apparaît particulièrement intéressante dans le contexte actuel de croissance de la puissance de calcul qui permet la réalisation de simulation numérique sur des maillages de plus en plus fins.

Dans cette thèse, l'approche intégrale est discrétisée au moyen de schémas implicites en temps, particulièrement bien adaptés à des écoulements de fluides faiblement compressibles comme l'eau ou pour des dynamiques lentes.

L'ensemble des développements informatiques a été intégré dans le code libre *Code_Saturne* développé à EDF R&D.

2.5 Vérification et validation

Cette thèse s'inscrit dans un projet de conception et de développement d'outils numériques qualifiés. A ce titre, une attention particulière est portée au processus de vérification et de validation (V&V) pour un logiciel de calcul scientifique défini dans [42], qui intervient à toutes les étapes de son cycle de vie. Dans le domaine de la sûreté nucléaire, le guide de l'ASN (Autorité de Sûreté Nucléaire) n°28 [43] : "Qualification des outils de calcul scientifique utilisés dans la démonstration de sûreté nucléaire – 1^{re} barrière" est la référence. Il s'appuie sur l'arrêté du 7 février 2012 modifié fixant les règles générales relatives aux INB (Installations Nucléaires de Base) [44].

La vérification répond à la question : "Avons-nous bien discrétisé les équations du modèle ?" en vérifiant que le code permet d'obtenir des solutions approximées des équations conformes à une spécification. La vérification est une étape essentiellement numérique, dans laquelle l'approximation numérique des équations est analysée. La validation répond, quant à elle, à la question : "Avons-nous discrétisé les bonnes équations ?" et examine la capacité du code à simuler le phénomène dont l'utilisateur a besoin. La validation est une étape physique, dans laquelle le choix des équations du modèle et donc des phénomènes physiques représentés sont questionnés.

Pour les modèles d'équations aux dérivées partielles de la mécanique des fluides (présentés dans la partie précédente), la vérification consiste à s'assurer que la solution des équations est bien approximée, au sens où cette solution est la limite à convergence en espace et en temps des approximations numériques. Pratiquement, des cas tests unitaires disposant de solutions analytiques sont réalisés avec étude de convergence, c'est-à-dire en vérifiant que l'approximation numérique obtenue converge vers la solution analytique, avec l'ordre de convergence théorique escompté. Cela permet de détecter d'éventuelles erreurs dans l'implémentation des schémas numériques, mais aussi les limites des schémas. D'autres cas tests consistent à comparer l'approximation numérique à des solutions particulières construites au préalable, utilisant la méthode des solutions manufacturées, généralement utilisée pour des systèmes complexes multidimensionnels.

La validation consiste à s'assurer, pour des applications dans un domaine de fonctionnement cible, que l'approximation numérique, convergée en maillage, est conforme aux résultats expérimentaux reflétant la réalité (en analysant l'écart aux résultats). Pour ce faire, des cas tests expérimentaux doivent être disponibles ou réalisés avec des mesures physiques suffisamment nombreuses et fiables.

Ici, les travaux mettent l'accent sur la vérification des équations d'Euler (3). Les cas tests de vérification consistent à résoudre des problèmes de Riemann uni-dimensionnels plans bien posés, c'est-à-dire à résoudre les équations d'Euler (3) sur $\mathbb{R}$, associées à une condition initiale, formée de deux états constants :

$$\boldsymbol{W}_0(x) = \begin{cases} \boldsymbol{W}_L, & x < 0, \\ \boldsymbol{W}_R, & x > 0, \end{cases}$$

et en se donnant une équation d'état. La convergence de la solution approximée, en fonction du pas d'espace à ratio $\frac{\Delta t}{\Delta x}$ fixé (classiquement avec une condition CFL), est alors étudiée.

La validation est peu abordée. Elle devra intervenir dans des travaux ultérieurs. Un cas test de pseudo-validation est présenté dans le chapitre 1 de la thèse. Les données expérimentales sont remplacées par des données numériques issues d'une simulation très fine CFD de référence. Il correspond à l'impact d'une onde de choc sur un assemblage d'obstacles dans de l'eau liquide, représentative d'un scénario d'accident de réactivité dans le cœur du réacteur.

3 Synthèse des travaux

3.1 Chapitre 1 : Formulation intégrale pour la modélisation des écoulements en milieu encombré : application aux équations d'Euler compressibles

Ce chapitre est consacré à la construction de l'approche intégrale multidimensionnelle pour les équations d'Euler pour les écoulements de fluide parfait compressible, obéissant à une équation d'état générale. Nous faisons ici le choix de négliger les effets visqueux. Cette construction s'effectue en deux parties : une première dédiée à la formulation intégrale des équations d'Euler sur des volumes de contrôle pouvant contenir des solides, puis une seconde consiste à discrétiser en temps et en espace la formulation obtenue.

Dans la première partie, la formulation intégrale fait appel à la définition de grandeurs géométriques supplémentaires en présence d'obstacles dans le volume de contrôle Ω : les volumes fluides Ω^ϕ et les surfaces fluides Γ^ϕ qui interviennent respectivement dans le terme instationnaire (ainsi que les termes sources éventuels) et la fonction flux.

$$\frac{d}{dt}\int_{\Omega^\phi} \boldsymbol{W}\,\mathrm{d}\boldsymbol{x} + \int_{\Gamma^\phi} \boldsymbol{F}\left(\boldsymbol{W}\right)\cdot\boldsymbol{n}\mathrm{d}\gamma + \int_{\Gamma^p} \boldsymbol{F}\left(\boldsymbol{W}\right)\cdot\boldsymbol{n}\mathrm{d}\gamma = \int_{\Omega^\phi} \boldsymbol{D}\left(\boldsymbol{W}\right)\mathrm{d}\boldsymbol{x}. \tag{13}$$

Dans la deuxième partie, la méthode numérique est basée sur un schéma Volumes Finis standard d'ordre 1 en espace sur maillage co-localisé. Une attention particulière est apportée à l'estimation proposée de la pression exercée sur les solides, apparaissant dans le flux sur bords solides ; celle-ci est basée sur un développement limité en nombre de Mach de la solution analytique d'un problème de Riemann à l'interface solide : $P|_{\Gamma^p} = P + \rho c \boldsymbol{u}\cdot\boldsymbol{n}|_{\Gamma^p}$, où les grandeurs sont celles de la maille contenant le solide. Cette estimation, injectée dans le terme de forces de pression discrète, permet de retrouver la bonne chute de pression, en se comparant aux calculs à l'échelle locale CFD, au passage d'une restriction brusque de section fluide.

La discrétisation temporelle utilise un schéma à correction de pression original, permettant de traiter des régimes à tout nombre de Mach. Cette technique discrétise de manière semi-implicite les trois équations de conservation : en allant de l'itération temporelle t^n à t^{n+1} avec $\Delta t = t^{n+1} - t^n$, une première étape résout la conservation de la masse couplée à une partie du bilan de quantité de mouvement (s'apparentant à un système acoustique) avec un schéma implicite, impliquant un opérateur parabolique discret du second ordre en espace sur la pression :

$$\frac{1}{(c^2)^n}\frac{P^\star - P^n}{\Delta t} + \mathrm{div}\,\left(\rho^n\mathbf{u}^n - \Delta t\boldsymbol{\nabla}P^\star\right) = 0, \tag{14}$$

et

$$\rho^{n+1} = \rho^n + \frac{P^\star - P^n}{(c^2)^n} \quad \text{and} \quad \boldsymbol{Q}^\star = \rho^n\mathbf{u}^n - \Delta t\boldsymbol{\nabla}P^\star. \tag{15}$$

Une deuxième et troisième étape résolvent respectivement la conservation de la quantité de mouvement et de l'énergie totale avec un schéma semi-implicite.

$$\frac{\delta(\rho\mathbf{u})}{\Delta t} + \mathbf{div}\,\left(\mathbf{u}^{n+1}\otimes\boldsymbol{Q}^\star\right) = -\boldsymbol{\nabla}P^\star + \rho^{n+1}\boldsymbol{f}^n, \tag{16}$$

$$\frac{\delta(\rho e)}{\Delta t} + \mathrm{div}\,\left(e^{n+1}\boldsymbol{Q}^\star\right) = -\mathrm{div}\,\left(\frac{P^\star}{\rho^{n+1}}\boldsymbol{Q}^\star\right) + \rho^{n+1}\boldsymbol{f}^n\cdot\mathbf{u}^{n+1}. \tag{17}$$

A l'issue de ces trois étapes, la pression est corrigée avec l'équation d'état.

$$P^{n+1} = \mathcal{P}(\rho^{n+1}, \epsilon^{n+1}) \quad \text{avec} \quad \epsilon^{n+1} = e^{n+1} - \frac{1}{2}(\mathbf{u}^{n+1}\cdot\mathbf{u}^{n+1}), \tag{18}$$

en notant pour une variable φ, l'incrément temporel :

$$\delta\varphi = \varphi^{n+1} - \varphi^n.$$

Le schéma numérique proposé est conservatif en temps et espace [45], et préserve la positivité au niveau discret de la densité et de l'énergie interne sous des conditions CFL matérielles. La démonstration de la positivité est faite [46].

Dans une dernière partie consacrée aux tests numériques, plusieurs cas de vérification sur problèmes de Riemann (fortement non-linéaires), en configuration uni-dimensionnelle, illustrent numériquement la convergence du schéma en mesurant l'ordre de convergence en norme L^1 discrète ainsi que sa stabilité à (grand) pas de temps, vérifiant la contrainte CFL matérielle. Dans ce cas, la diffusion numérique est importante. L'accent est particulièrement porté sur des cas à bas nombre de Mach, en allant jusqu'à 10^{-3}, avec une équation d'état analytique de gaz raide (dite "stiffened gas" [47]) modélisant le comportement thermodynamique de l'eau liquide. Les premiers cas tests sont de type tube à choc en milieu libre, alors que les derniers sont en milieu fermé et moins standards. Ils simulent la réflexion d'une 3-onde de choc plane sur un mur plan (condition aux limites de paroi), puis l'interaction de la 2-onde de discontinuité de contact initiale avec l'onde de choc réfléchie.

Finalement, afin de valider l'approche intégrale en milieu encombré en se comparant à des résultats à l'échelle locale CFD, une expérience numérique est réalisée. Une 3-onde de choc impactant un ensemble d'obstacles rigides immobiles immergés dans l'eau liquide est simulée. Les résultats portant sur des grandeurs d'intérêt, comme les forces de pression s'exerçant sur les obstacles ou les champs fluides intégrés, sont obtenus avec l'approche intégrale sur maillages grossiers encombrés. La comparaison avec les données CFD de référence (80 millions de mailles) montre un bon accord malgré le faible nombre de mailles utilisées avec l'approche intégrale (un facteur 10^5 entre le nombre de mailles des deux approches est effectif). D'un point de vue industriel, ce dernier cas test imite l'impact d'une onde de pression sur un faisceau de crayons combustible dans le cœur du réacteur, pouvant se produire durant un scenario d'accident de réactivité (de type RIA "Reactivity Initiated Accident") [48].

3.2 Chapitre 2 : Schéma numérique volumes finis co-localisé pour la simulation des écoulements à saut de section fluide : application aux équations d'Euler incompressibles

De nombreuses configurations d'écoulements industriels en thermohydraulique donnent lieu à des écoulements, en charge, dans des conduites où la section des tuyaux peut varier brusquement (élargissement ou rétrécissement). C'est par exemple le cas, dans la cuve du réacteur, où l'entrée dans le cœur se fait avec une variation brusque de la section de passage du fluide.

Le but de ce chapitre est de proposer, en s'appuyant sur la formulation intégrale présentée dans le chapitre 1, une nouvelle méthode numérique pour simuler ce type de configuration pour un fluide incompressible. Le maillage du domaine de calcul n'est toujours pas suffisamment fin dans la direction tangentielle à la section de passage discontinue pour prendre en compte la paroi par une condition limite de paroi et adopter ainsi le formalisme CFD de l'échelle locale.

La formulation intégrale est appliquée aux équations d'Euler en régime incompressible et est discrétisée en temps de manière implicite en utilisant une méthode de projection incrémentale. La discrétisation en espace utilise une méthode Volumes Finis co-localisée, où les variables scalaires et vectorielle sont calculées sur un même maillage primal.

Pour ce faire, la discontinuité géométrique, due au saut de section, est prise en compte par le calcul des surfaces fluides du maillage encombré. La nature discontinue du problème conduit à proposer une estimation adaptée de la pression à l'interface discontinue, pour retrouver la bonne variation de pression au niveau de cette interface.

La stratégie présentée dans ce chapitre consiste à adapter le schéma numérique co-localisé en espace pour pouvoir traiter numériquement le saut de section de passage fluide. Pour ce faire, notre démarche s'appuie sur une correction de l'interpolation des grandeurs discrètes de maille (vitesse, pression) aux faces du maillage permettant ainsi de préserver l'équilibre stationnaire exact à travers cette discontinuité de section. Un cas test de vérification permet de s'assurer que le schéma numérique permet de retrouver la solution analytique formée d'un état stationnaire constant de part et d'autre de la discontinuité de section de passage.

3.3 Chapitre 3 : Étude de convergence numérique de conditions limites discrètes pour la sortie d'ondes dans les équations d'Euler compressibles

Dans ce chapitre, des conditions limites numériques pour faire sortir les ondes du domaine de calcul Ω sont étudiées : la consistance et la convergence de la solution approchée sont vérifiées numériquement. Ce type de conditions limites a pour but d'approcher l'écoulement associé à un domaine infini, le domaine de calcul étant borné. Le système d'équations considéré est toujours le système d'Euler :

$$\begin{cases} \partial_t \rho + \operatorname{div}(\rho \boldsymbol{u}) = 0, \\ \partial_t(\rho \boldsymbol{u}) + \mathbf{div}(\boldsymbol{u} \otimes \rho \boldsymbol{u}) + \boldsymbol{\nabla} P = 0, \\ \partial_t \rho e + \operatorname{div}(\boldsymbol{u}(\rho e + P)) = 0, \end{cases} \tag{19}$$

avec une équation d'état de gaz parfait ou de gaz raide pour modéliser respectivement un composant gazeux ou liquide.

On s'intéresse plus particulièrement à la sortie d'ondes rapides associées aux deux champs vraiment non-linéaires ($\lambda = u \pm c$), lorsque l'état extérieur au domaine de calcul est **totalement inconnu**. Pour ce faire, plusieurs formulations de conditions limites reposant sur les propriétés des ondes sont proposées. La technique consiste à résoudre un problème de Riemann à la frontière du domaine de calcul avec un état gauche calculé par le schéma interne, l'état intérieur, et un état droite inconnu, qui est l'état extérieur à évaluer en fonction des données de l'intérieur du domaine. Les trois formulations envisagées, dont la première est classique, et les deux dernières sont à notre connaissance nouvelles, sont :

1. imposer l'état extérieur égal à l'état intérieur (condition classiquement utilisée dans les simulations industrielles),
2. imposer l'état extérieur en le reliant à l'état intérieur soit à partir des invariants de Riemann pour une onde de détente, soit à partir des relations de saut pour une onde de choc,
3. imposer un autre état extérieur, en considérant un domaine physique intermédiaire fictif.

Ces conditions sont ensuite testées sur deux cas tests de vérification correspondant à deux problèmes de Riemann uni-dimensionnels subsoniques :

- une 1-onde de détente pure sortant par la gauche du domaine de calcul ;
- une 3-onde de choc pure sortant par la droite du domaine.

Les cas tests sont simulés avec un solveur de Godunov approché explicite : le schéma VFRoencv.

Les études de convergence numériques (en norme L^1 discrète) montrent que les formulations de conditions limites "1." et "2." sont consistantes et convergent en maillage pour le premier cas (sortie d'une onde de détente).

Par contre, ce n'est pas le cas pour l'onde de choc sortante, la consistance de la solution approchée n'étant plus assurée. La formulation "3.", quant à elle, permet d'être consistant sur le cas de la sortie d'une onde de choc.

Notons que, contrairement à la stabilité numérique, la consistance du schéma en incluant les conditions limites numériques est rarement étudiée dans ces conditions (sans information extérieure).

3.4 Annexes

Trois annexes complètent le document :

- L'**annexe A** présente un cas test de vérification bidimensionnel de l'algorithme de correction de pression présenté dans le chapitre 1 : il s'agit de la simulation d'un écoulement stationnaire bidimensionnel subsonique dans une tuyère (cas test de la tuyère de Laval).

- L'**annexe B** décrit un nouveau schéma pour la résolution numérique des équations d'Euler compressibles, adapté au régime stationnaire. Ce schéma est basé sur une méthode de Volumes Finis co-localisée en espace et utilise pour la discrétisation en temps une technique de correction de pression sous forme incrémentale. Il correspond à une extension du schéma de résolution des équations d'Euler incompressibles, présenté dans le chapitre 2, au régime compressible. Cela permet ainsi d'utiliser les développements du chapitre 2 pour traiter les discontinuités de section fluide en régime compressible. L'algorithme est vérifié sur différents problèmes de Riemann (tube à choc de Sod, problème de Riemann avec une équation d'état de type gaz raide, discontinuité de contact instationnaire).

- L'**annexe C** propose une extension de la formulation intégrale, décrite dans les chapitres 1 et 2, aux équations de Navier-Stokes incompressibles en prenant en compte les effets visqueux. Le terme de frottement visqueux en paroi est modélisé grâce à une loi de paroi, qui disparaît lorsque le maillage est raffiné. Cette méthode est vérifiée sur le cas de l'écoulement laminaire en canal plan de Poiseuille. Elle permet de retrouver la perte de charge régulière analytique sur des maillages grossiers encombrés.

3.5 Valorisation des travaux

Les travaux présentés dans cette thèse ont fait l'objet des publications suivantes :

- Un article portant sur les travaux du chapitre 1 a été publié dans la revue internationale Computers & Fluids [46] : C. Colas, M. Ferrand, J.-M. Hérard, J.-C. Latché, and E. Le Coupanec, *An Implicit Integral Formulation to Model Inviscid Fluid Flows in Obstructed Media*, Computers & Fluids, vol. 188, pages 136 –163, 2019.

  Ces travaux ont été également présentés lors du congrès international ICIAM 2019 (9^{th} International Congress on Industrial and Applied Mathematics), Valence (Espagne), 15-19 juillet 2019.

  Une version préliminaire a été présentée en 2017 au congrès FVCA8 (Finite Volumes for Complex Applications 8). La référence de l'article des proceedings est [49] : C. Colas, M. Ferrand, J.-M. Hérard, E. Le Coupanec, and X. Martin, *An Implicit Integral Formulation for the Modeling of Inviscid Fluid Flows in Domains Containing Obstacles*, Finite Volumes for Complex Applications 8, Springer Proceedings in Mathematics and Statistics, vol. 200, pages 53 – 61, 2017.

- Une note courte reprenant une synthèse des travaux du chapitre 3 est en cours de rédaction.

Références

[1] *Institut de Radioprotection et de Sûreté Nucléaire (IRSN), Fonctionnement d'un réacteur nucléaire*. 2019. URL : https://www.irsn.fr/FR/connaissances/Installations_nucleaires/Les-centrales-nucleaires/reacteurs-nucleaires-France/Pages/1-reacteurs-nucleaires-France-Fonctionnement.aspx#.XXUg5_c685k (cf. p. 8).

[2] *Institut de Radioprotection et de Sûreté Nucléaire (IRSN), Les composants d'un réacteur en détail*. 2019. URL : https://www.irsn.fr/FR/connaissances/Installations_nucleaires/Les-centrales-nucleaires/reacteurs-nucleaires-France/Pages/3-reacteurs-nucleaires-France-Description-detaillee.aspx?dId=82471a77-677a-40cf-8010-5c30f29507df&dwId=231c8e52-c3bd-4187-990e-01a6e97b5418#.XXUlXfc685k (cf. p. 8).

[3] F. Barre et M. Bernard. "The CATHARE code strategy and assessment". In : *Nuclear Engineering and Design* 124(3) :257-284 (1990) (cf. p. 9, 28).

[4] S. Aubry, C. Caremoli, J. Olive et P. Rascle. "The THYC three-dimensional thermal-hydraulic code for rod bundles : recent developments and validation tests". In : *Nuclear technology* 112.3 (1995), p. 331–345 (cf. p. 10, 14, 28, 110, 215).

[5] G. Le Coq, S. Aubry, J. Cahouet, P. Lequesne, G. Nicolas et S. Pastorini. "The THYC computer code. A finite volume approach for 3 dimensional two-phase flows in tube bundles". In : *Bulletin de la Direction des Etudes et Recherches - Electricité de France. Série A, nucléaire, hydraulique, thermique. In french* 1 (1989), p. 61–76 (cf. p. 10, 13, 14).

[6] I. Toumi, A. Bergeron, D. Gallo, E. Royer et D. Caruge. "FLICA-4 : A three-dimensional two-phase flow computer code with advanced numerical methods for nuclear applications". In : *Nuclear Engineering and Design* 200 (2000), p. 139–155 (cf. p. 10, 13, 15, 28).

[7] M. Grandotto, M. Bernard, J.P. Gaillard et P. Miranda. *Méthodes numériques utilisées dans le logiciel* TRIO-GENEPI *(Version 1)*. Rapp. tech. DER/SCC/LTDE 91-004, CEA, Saclay, 1991 (cf. p. 10, 13, 15).

[8] *Logiciel libre Code_Saturne (EDF)*. 2019. URL : https://www.code-saturne.org (cf. p. 10).

[9] *Code_Saturne 5.2.0 Theory Guide*. EDF R&D. 2018. URL : https://code-saturne.org/cms/sites/default/files/docs/5.2/theory.pdf (cf. p. 10, 28, 92, 93, 176).

[10] *Logiciel libre TrioCFD (CEA)*. 2019. URL : http://triocfd.cea.fr (cf. p. 10).

[11] *Logiciel libre OpenFOAM*. 2019. URL : https://openfoam.org (cf. p. 10).

[12] *Logiciel propriétaire NEPTUNE_CFD (CEA, EDF, Framatome et IRSN*. 2019. URL : https://www.code-saturne.org/cms/neptune-cfd (cf. p. 10).

[13] *Logiciel propriétaire ANSYS Fluent*. 2019. URL : https://www.ansys.com/fr-fr/products/fluids/ansys-fluent (cf. p. 10).

[14] *Logiciel propriétaire STAR-CCM+*. 2019. URL : https://www.plm.automation.siemens.com/global/fr/products/simcenter/STAR-CCM.html (cf. p. 10).

[15] *Logiciel propriétaire COMSOL Multiphysics*. 2019. URL : https://www.comsol.fr (cf. p. 10).

[16] R. Eymard, T. Gallouët et R. Herbin. "Finite Volume Methods". In : *Handbook for Numerical Analysis, P.G. Ciarlet, J.L. Lions eds, North Holland* 7 (2006), p. 713–1020 (cf. p. 10, 29, 33, 92, 94, 120, 177).

[17] E. Guyon, J.-P. Hulin et L. Petit. *Hydrodynamique Physique*. Sous la dir. de CNRS éditions. 3e. CNRS éditions - EDP sciences, 2012 (cf. p. 11).

[18] P. Chassaing. *Mécanique des fluides, éléments d'un premier parcours*. 3e édition. Cépaduès, 2010 (cf. p. 11, 13, 193).

[19] E. Godlewski et P.-A. Raviart. *Numerical approximation of hyperbolic systems of conservation laws*. T. 118. Applied Mathematical Sciences. New York : Springer-Verlag, 1996 (cf. p. 11, 12, 119, 120, 127, 181).

[20] J. Smoller. *Shock Waves and Reaction-Diffusion Equations*. T. 258. A Series of Comprehensive Studies in Mathematics. New York : Springer-Verlag, 1994 (cf. p. 11, 12, 47, 82, 119, 127, 181).

[21] D. Rochette, S. Clain et T. Buffard. "Numerical scheme to complete a compressible gas flow in variable porosity media". In : *International Journal of Computational Fluid Dynamics* 19.9 (2005), p. 299–309 (cf. p. 13, 16).

[22] L. Girault et J.-M. Hérard. "A two-fluid hyperbolic model in a porous medium." In : *ESAIM : Mathematical Modelling and Numerical Analysis* 44.6 (2010), p. 1319–1348 (cf. p. 13, 16).

[23] Y. Davit, C.G. Bell, H.M. Byrne, L.A.C. Chapman, L.S. Kimpton, K.H.L. Lang G.E. Leonard, J.M. Oliver, N.C. Pearson, R.J. Shipley, S.L. Waters, J.P. Whiteley, B.D. Wood et M. Quintard. "Homogenization via formal multiscale asymptotics and volume averaging : how do the two techniques compare ?" In : *Advances in Water Resources* 62 (2013), p. 178–206 (cf. p. 13, 29).

[24] D. Kröner et M.-D. Thanh. "Numerical solution to compressible flows in a nozzle with variable cross-section". In : *SIAM - J. Numer. Anal.* 43 (2006), p. 796–824 (cf. p. 14, 16).

[25] A.-J. Chorin. "Numerical solution of the Navier-Stokes equations". In : *Mathematics of Computation* 22(104) :745–762 (1968) (cf. p. 15, 29, 90, 92, 176).

[26] R. Temam. "Sur l'approximation de la solution des équations de Navier-Stokes par la méthode des pas fractionnaires (I)". In : *Archive for Rational Mechanics and Analysis* 32.5 (1969), p. 135–153 (cf. p. 15, 90, 92, 176).

[27] R. Temam. "Sur l'approximation de la solution des équations de Navier-Stokes par la méthode des pas fractionnaires (II)". In : *Archive for Rational Mechanics and Analysis* 33.5 (1969), p. 377–385 (cf. p. 15, 29, 90, 92, 176).

[28] J.-L. Guermond, P. Minev et J. Shen. "An overview of projection methods for incompressible flows". In : *Computer Methods in Applied Mechanics and Engineering* 195 (sept. 2006), p. 6011–6045 (cf. p. 15, 92).

[29] I. Toumi. "A weak formulation of Roe's approximate Riemann solver". In : *Journal of Computational Physics* 102.2 (1992), p. 360 –373 (cf. p. 15).

[30] M. Grandotto et P. Obry. "Steam generators two phase flows numerical simulation with liquid and gas momentum equations". In : *Nuclear Science and Engineering* 151 (2005), p. 313–318. URL : https://hal-cea.archives-ouvertes.fr/cea-00275766 (cf. p. 15, 28).

[31] M. Grandotto et P. Obry. "Calculs des écoulements diphasiques dans les échangeurs par une méthode aux éléments finis". In : *Revue Européenne des Eléments Finis* 5.1 (1996), p. 53–74 (cf. p. 15, 28).

[32] M. Belliard et M. Grandotto. “Computation of two-phase flow in steam generator using domain decomposition and local zoom methods”. In : *Nuclear Engineering and Design* 213.2-3 (2002), p. 223–239 (cf. p. 15).

[33] M. Belliard. “Méthodes de décomposition de domaine et de frontière immergée pour la simulation des composants nucléaires”. Habilitation à Diriger des Recherches. Aix-Marseille Université, 2014. URL : https://tel.archives-ouvertes.fr/tel-01085328 (cf. p. 15, 28).

[34] M. Grandotto. “Simulation numérique des écoulements diphasiques dans les échangeurs”. Habilitation à Diriger des Recherches. Université de la Méditerranée - Aix-Marseille II, 2006. URL : https://tel.archives-ouvertes.fr/tel-00275746 (cf. p. 15).

[35] J. Greenberg et A.-Y. Leroux. “A Well-Balanced Scheme for the Numerical Processing of Source Terms in Hyperbolic Equations”. In : *SIAM - J. Numer. Anal.* 33 (1996), p. 1–16 (cf. p. 16).

[36] L. Gosse. “A well-balanced scheme using non-conservative products designed for hyperbolic systems of conservation laws with source terms”. In : *Mathematical Models and Methods in Applied Sciences* 11.2 (2001), p. 339–365 (cf. p. 16).

[37] S. Clain et D. Rochette. “First and second-order Finite Volume methods for the one-dimensional non-conservative Euler system”. In : *Journal of Computational Physics* 228 (2009), p. 8214–8248 (cf. p. 16).

[38] L. Girault et J.-M. Hérard. “Multidimensional computations of a two-fluid hyperbolic model in a porous medium”. In : *International Journal on Finite Volumes* 7.1 (2010), p. 1–33. URL : https://hal.archives-ouvertes.fr/hal-01114209 (cf. p. 16, 17, 29).

[39] J.-M. Hérard et J. Jung. “An interface condition to compute compressible flows in variable cross-section ducts”. In : *Comptes Rendus Mathématique* 354 (2016), p. 323–327 (cf. p. 17).

[40] X. Martin. “Modélisation d’écoulements fluides en milieu encombré d’obstacles”. Thèse de doct. Aix-Marseille Université, 2015. URL : https://tel.archives-ouvertes.fr/tel-01235089 (cf. p. 17, 90, 91, 176).

[41] J.-M. Hérard et X. Martin. “An integral approach to compute compressible fluid flows in domains containing obstacles.” In : *International Journal on Finite Volumes* 12.1 (2015), p. 1–39. URL : https://hal.archives-ouvertes.fr/hal-01166478/ (cf. p. 17, 29, 60).

[42] W. L. Oberkampf et C. J. Roy. *Verification and Validation in Scientific Computing*. Cambridge Univeristy Press, 2010 (cf. p. 18).

[43] *Guide de l’ASN numéro 28 : Qualification des outils de calcul scientifique utilisés dans la démonstration de sûreté nucléaire - première barrière*. 2017. URL : https://www.asn.fr/Professionnels/Installations-nucleaires/Centrales-nucleaires/Guides-de-l-ASN-dans-le-domaine-des-installations-nucleaires/Guide-de-l-ASN-n-28-Qualification-des-outils-de-calcul-scientifique-utilises-dans-la-demonstration-de-surete-nucleaire (cf. p. 18).

[44] *Arrêté du 7 février 2012 fixant les règles générales relatives aux installations nucléaires de base*. 2012. URL : https://www.legifrance.gouv.fr/affichTexte.do?cidTexte=JORFTEXT000025338573&dateTexte=20160205 (cf. p. 18).

[45] F. Archambeau, J.-M. Hérard et J. Laviéville. “Comparative study of pressure-correction and Godunov-type schemes on unsteady compressible cases”. In : *Computers & Fluids* 38 (2009), p. 1495–1509 (cf. p. 20, 29, 33, 43).

[46] C. Colas, M. Ferrand, J.-M. Hérard, J.-C. Latché et E. Le Coupanec. "An Implicit Integral Formulation to Model Inviscid Fluid Flows in Obstructed Media". In : *Computers & Fluids* 188 (2019), p. 136–163. URL : https://hal.archives-ouvertes.fr/hal-01969129 (cf. p. 20, 22, 90, 91, 113, 121, 176, 179).

[47] R. Menikoff et B.J. Plohr. "The Riemann problem for fluid flow of real materials". In : *Rev. Mod. Phy.* 61.1 (1989), p. 75–130 (cf. p. 20, 31).

[48] *Institut de Radioprotection et de Sûreté Nucléaire (IRSN), Reactivity-Initiated Accident (RIA)*. 2019. URL : https://www.irsn.fr/FR/connaissances/Installations_nucleaires/Les-centrales-nucleaires/criteres_surete_ria_aprp/Pages/1-accident-reactivite-RIA.aspx (cf. p. 20, 28, 30, 59).

[49] C. Colas, M. Ferrand, J.-M. Hérard, E. Le Coupanec et X. Martin. "An Implicit Integral Formulation for the Modeling of Inviscid Fluid Flows in Domains Containing Obstacles". In : *Finite Volumes for Complex Applications 8*. T. 200. Springer Proceedings in Mathematics and Statistics. Juin 2017, p. 53–61. URL : https://hal.archives-ouvertes.fr/hal-01579372 (cf. p. 22).

Chapter 1

An Implicit Integral Formulation to Model Inviscid Fluid Flows in Obstructed Media

Contents

1 Introduction

The issue of dealing with congested media is pervasive in industrial Computational Fluid Dynamics applications. In the easiest cases, the computational domain (*i.e.*, in practice, the mesh) may be fitted to the boundary of each of the present solids, but in many applications, these latter are too numerous or too small with respect to the computational domain characteristic dimensions to be dealt with in such a way: this would imply using so refined meshes that the computational cost would become prohibitive. In nuclear industry, occurrences of such problems are numerous. One may think for instance of safety issues as possible cables train fires, hydrogen deflagration in the reactor building rooms where numerous pipes are present... For the computation of the flow in the primary circuit of Pressurized Water Reactors, both in operating and accident conditions [50, 48], the problem has been tackled now for more than forty years, and has motivated the development of, schematically speaking, three categories of simulation softwares, each acting at its own scale:

- At the largest scale, referred to as the *system* scale, a 0D/1D description is used, with the aim to provide a real time simulation of full circuits (system transient analysis). A reference industrial code in France is CATHARE [3], developed from the end of the 70s thanks to a joint effort by several partners, among which, in particular, CEA (Commissariat à l'Énergie Atomique et aux Énergies Alternatives), EDF and IRSN (Institut de Radioprotection et de Sûreté Nucléaire).

- The finest one is the CFD (Computational Fluid Dynamics) scale, referred to as the *local* scale, that allows a fine 3D description on restricted physical domains. In that case, the Navier-Stokes equations, with suitable turbulence modelling, are solved on fine computational meshes, and all solid boundaries of obstacles in the computational domain are meshed through standard wall boundary conditions. *Code_Saturne* [9] (developed by EDF R&D since 1997) is one of the CFD codes used in this context.

- Since computations at the largest scale may be too crude and application at the local scale are often too time-consuming, an intermediate approach, aiming at the description of one component of the primary circuit such as the reactor core or the steam generator, has been developed; softwares dedicated to this purpose are said to operate at the *component* scale. In this case, an homogenized representation is chosen: the congested medium is considered as a porous medium, in which three-dimensional balance equations (mass, momentum and energy) are solved; the influence of the solid obstacles is taken into account, besides of course a reduction of the porosity, through exchange terms (a friction term for the momentum balance and a heat exchange term for the energy balance) obtained by upscaling techniques. The component approach is implemented, for instance, in codes developed in the 80s such as THYC [4], FLICA-4 [6] or GENEPI [30, 31, 33].

Enlarging the scope to another already mentioned safety problem, namely turbulent deflagrations, a strategy similar to what is done in thermal-hydraulics at the component scale is employed in the commercial code FLACS [51].

The "equivalent porous media approach", as used in component codes, has now proven to yield accurate results for incompressible or quasi-incompressible flows in porous media where a micro-scale and a representative elementary volume associated to this scale may be identified [23] (so, in particular, for periodic media). Its extension to compressible flows is however less standard and, in addition, serious difficulties may appear when the characteristics of the equivalent porous medium sharply vary with space. In particular, the numerical study [38] shows that the porous model is not physically suitable to manage sudden free/porous transitions: the comparison between the multi-dimensional CFD computation, including the true geometry of obstacles (as shown on FIGURE 1.1), and the equivalent porous computation (see FIGURE 1.2) shows discrepancies at the interface associated with the discontinuity in the equivalent porosity profile. These discrepancies may be attributed to the fact that the singular head loss in the momentum balance is not accounted for in the porous approach in an appropriate way.

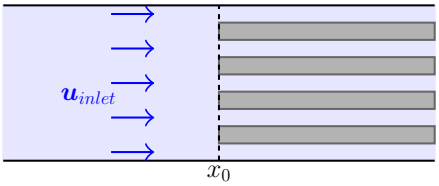

FIGURE 1.1 – *2D fluid model.*

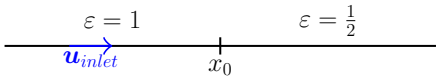

FIGURE 1.2 – *1D porous model (ε the porosity).*

The aim of this paper is to propose an alternative to the porous media approach, with two essential objectives: first, to circumvent the above mentioned difficulty, *i.e.* to allow to cope with discontinuous porosity media; second, to naturally boil down to the CFD model, when the mesh exactly fits the obstacles. To this purpose, we give up the derivation of an equivalent model at the continuous level. Instead, we directly integrate the balance equations over the control volumes, mimicking to some extent the usual finite-volume procedure, to the "real" fluid medium; doing so, integrals over the solid surfaces appear, for which expressions are given. In particular, a suitable treatment of the pressure forces naturally re-injects in the discrete system the above mentioned singular losses. Note that, conceptually, this procedure differs for a standard finite volume discretization of a set of PDEs: for instance, consistency and convergence issues make no more sense, since the discrete system cannot be seen associated to a continuous problem, up to the point at which the CFD model is recovered. In practice, we expect a significant gain in accuracy, at least for some solid obstacles geometry of interest; the numerical tests presented in this paper support this expectation. We also stress that, from an industrial point of view, gathering in the same numerical tool the capabilities of both the component and local approach is appealing, especially in a context of increasing computational power and thus, accordingly, a progressive drift toward more and more refined computations.

The proposed technique, which we refer to as the "integral approach", is applied here to compressible inviscid flows obeying the Euler equations, with general equation of states. We work here in the context of the open-source *Code_Saturne* software, using the same control volumes for both the scalar and velocity unknowns in a way consistent with a collocated finite volume scheme (see [16] for more details on finite volumes), and a fractional-step time discretization involving an elliptic step for a pressure correction (in other words, falling in the class of pressure correction algorithms [25, 27, 52, 53, 54, 55]), able to cope with all the Mach numbers regimes [45]. A first attempt to implement the integral approach with an explicit in time scheme (the so-called VFRoe-ncv approximate Godunov solver) may also be found in [41].

The paper outline is as follows. First, the multi-dimensional integral formulation of the compressible Euler equations is described. The time and spatial discretization of the formulation is proposed through a pressure-correction collocated finite volume scheme preserving the positivity of the density and the internal energy under a CFL condition based on the velocity of the fluid. Then, several fluid verification test cases are presented to illustrate the stability and the accuracy of this method with a numerical convergence analysis. The case of low Mach number flows is particularly investigated. Two one-dimensional Riemann problems with an analytical thermodynamic law (Equation Of State (EOS)) are considered:

- a Riemann problem in a free domain using a stiffened gas EOS, modelling a gas or liquid fluid,
- a shock wave reflection on a wall using a stiffened gas EOS, the exact solution of which is detailed in 1.D. This test corresponds to a water flow impacting an obstacle.

Finally, a two-dimensional **validation** test case with the integral approach in an obstructed medium is performed, where a pressure shock wave hits transversal rod bundles surrounded by a liquid; the formulation of the pressure forces on the solid boundaries takes here the same form as for the reflection boundary conditions used in the previous test, to deal within the integral approach framework with the macroscopic pressure jumps due to the sudden restriction of the flow passage section. Results are compared with a "reference" CFD computation, *i.e.* the 2D detailed solution, in particular through the evaluation of resultant forces acting on rods, to check that the integral approach indeed converges as expected towards the fine CFD computation when refining the mesh. From an industrial point of view, this latter test is reminiscent of a pressure wave impacting a rod bundle, as may occur in a reactor core during a Reactivity Initiated Accident [48].

2 An Integral Formulation

2.1 Set of governing equations

The compressible Euler equations (1.1) governing inviscid fluid flows are considered in an open subset of $\mathbb{R}^d$ ($d = 1, 2$ or 3) and in a bounded time interval $(0, T)$, $T \in \mathbb{R}_+^*$. The unknowns ρ, $\boldsymbol{u}$, P respectively denote the density, the velocity and the pressure of the fluid, while the momentum is $\boldsymbol{Q} = \rho\boldsymbol{u}$. The volumetric total energy E is such that:

$$E = \rho\left(\frac{\boldsymbol{u}^2}{2} + \epsilon(P,\rho)\right),$$

where the internal energy $\epsilon(P,\rho)$ is prescribed by the Equation Of State (EOS). Besides, in the right hand side of system (1.1), $\boldsymbol{f}$ is a mass external force and Φ_v a mass heat transfer source term. Thus the set of governing equations is:

$$\left\{\begin{array}{lcl} \partial_t\rho & + & \operatorname{div}\boldsymbol{Q} = 0, \\ \partial_t\boldsymbol{Q} & + & \mathbf{div}\,(\boldsymbol{u}\otimes\boldsymbol{Q}) + \boldsymbol{\nabla}P = \rho\boldsymbol{f}, \\ \partial_t E & + & \operatorname{div}\,(\boldsymbol{u}(E+P)) = \rho\boldsymbol{f}\cdot\boldsymbol{u} + \rho\Phi_v. \end{array}\right. \tag{1.1}$$

The speed of sound, noted c, is such that:

$$c^2 = \left(\frac{P}{\rho^2} - \frac{\partial\epsilon(P,\rho)}{\partial\rho}\right) \Big/ \left(\frac{\partial\epsilon(P,\rho)}{\partial P}\right).$$

The EOS for a stiffened gas, which generalizes the usual ideal gas EOS and is used for a weakly compressible liquid (see [47]), is defined by

$$\rho\epsilon = \frac{P + \gamma\Pi_\infty}{\gamma - 1}, \tag{1.2}$$

with $\gamma > 1$ the heat capacity ratio and $\Pi_\infty \geq 0$ the stiffened gas pressure parameter. The admissible thermodynamic state is $P \in [-\Pi_\infty, +\infty)$. The speed of sound c is given by

$$c^2 = \frac{\gamma(P + \Pi_\infty)}{\rho}.$$

The specific enthalpy is $h = \epsilon(P, \rho) + \frac{P}{\rho}$, and the total enthalpy reads:

$$H = \frac{E + P}{\rho}.$$

Thereafter, $\boldsymbol{W}$ is the conservative variable:

$$\boldsymbol{W} = (\rho, \boldsymbol{Q}, E)^\mathsf{T}.$$

The conservation laws (1.1) can be written as follows:

$$\partial_t \boldsymbol{W} + \mathbf{div}\left(\boldsymbol{F}\left(\boldsymbol{W}\right)\right) = \boldsymbol{D}\left(\boldsymbol{W}\right), \tag{1.3}$$

where

$\boldsymbol{F}\left(\boldsymbol{W}\right) = \left(\boldsymbol{Q}, \boldsymbol{u} \otimes \boldsymbol{Q} + P\,\mathbf{Id}, \boldsymbol{u}\left(E + P\right)\right)^\mathsf{T}$ is the convective flux,

$\boldsymbol{D}\left(\boldsymbol{W}\right) = \left(0, \rho\boldsymbol{f}, \rho\left(\boldsymbol{f} \cdot \boldsymbol{u} + \Phi_v\right)\right)^\mathsf{T}$ is the source term.

2.2 Integral form

The integral formulation of conservation laws described in [56] is considered. Set of equations (1.1) is integrated on control volumes Ω_i, $i \in \mathbb{N}$, which may contain many disjoint solid obstacles. All Ω_i cells form a mesh of the computational domain Ω, an open bounded connected polygonal subset of $\mathbb{R}^d$, such that $\overline{\Omega} = \cup_i \overline{\Omega}_i$ and $\cap_i \Omega_i = \emptyset$. Obstacles may be completely or partially included in Ω_i. Part of a control volume boundary may coincide with the surface of an obstacle. FIGURE 1.3 is a sketch of the admissible situations.

The whole volume occupied by solid obstacles within the control volume Ω_i is denoted by Ω_i^S. Thus, the volume occupied by fluid within Ω_i is $\Omega_i^\phi = \Omega_i \setminus \overline{\Omega_i^S}$. The mean value of the fluid state variable $\boldsymbol{W}(\mathbf{x}, t)$, with $\mathbf{x} \in \Omega$ and $t \in (0, T)$, over each fluid cell Ω_i^ϕ reads:

$$\boldsymbol{W}_i(t) = \frac{1}{\left|\Omega_i^\phi\right|} \int_{\Omega_i^\phi} \boldsymbol{W}(\mathbf{x}, t) \mathrm{d}\boldsymbol{x}.$$

Equation (1.3) is integrated over the bounded time interval $[t_0, t_1] \subset (0, T)$ and over the fluid cell Ω_i^ϕ. The flux-divergence theorem allows to get:

$$\left|\Omega_i^\phi\right|\left(\boldsymbol{W}_i\left(t_1\right) - \boldsymbol{W}_i\left(t_0\right)\right) + \int_{t_0}^{t_1}\int_{\Gamma_i} \boldsymbol{F}\left(\boldsymbol{W}\left(\mathbf{x}, t\right)\right) \cdot \boldsymbol{n}(\mathbf{x}) \mathrm{d}\gamma dt = \int_{t_0}^{t_1}\int_{\Omega_i^\phi} \boldsymbol{D}\left(\boldsymbol{W}\left(\mathbf{x}, t\right)\right) \mathrm{d}\boldsymbol{x}\, dt, \tag{1.4}$$

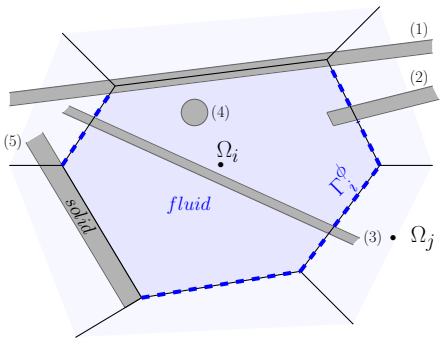

FIGURE 1.3 – *A (blue) control volume Ω_i includes (gray) obstacles numbered from 1 to 5. Obstacles may: overlap part of the boundary of Ω_i (1); partially occupy fluid cell (2); fully cross Ω_i and halve it (3); be totally included in Ω_i (4); or be aligned with part of the boundary of Ω_i (5). The dashed blue surface corresponds to the fluid part Γ_i^ϕ of the boundary of Ω_i.*

where, $\Gamma_i = \partial\Omega_i^\phi$ denotes the whole boundary of the fluid cell Ω_i^ϕ with $\boldsymbol{n}(\mathbf{x})$ its unit outward normal vector. Fluid $\Gamma_i^\phi = \Gamma_i \setminus \partial\Omega_i^S$ and wall $\Gamma_i^w = \Gamma_i \cap \partial\Omega_i^S$ boundaries of each fluid cell Ω_i^ϕ are distinguished, such that:

$$\Gamma_i = \Gamma_i^\phi \cup \Gamma_i^w \quad \text{and} \quad \Gamma_i^\phi \cap \Gamma_i^w = \emptyset.$$

The integral formulation for all Ω_i holds:

$$\begin{aligned} \left|\Omega_i^\phi\right|\left(\boldsymbol{W}_i\left(t_1\right) - \boldsymbol{W}_i\left(t_0\right)\right) + \int_{t_0}^{t_1}\int_{\Gamma_i^\phi} \boldsymbol{F}\left(\boldsymbol{W}\right)\cdot\boldsymbol{n}\mathrm{d}\gamma dt \; + \int_{t_0}^{t_1}\int_{\Gamma_i^w} \boldsymbol{F}\left(\boldsymbol{W}\right)\cdot\boldsymbol{n}\mathrm{d}\gamma dt \\ = \int_{t_0}^{t_1}\int_{\Omega_i^\phi} \boldsymbol{D}\left(\boldsymbol{W}\right)\mathrm{d}\boldsymbol{x}\, dt. \end{aligned} \tag{1.5}$$

The inner product between the normal $\boldsymbol{n}$ and the flux function $\boldsymbol{F}$ reads:

$$\boldsymbol{F}\left(\boldsymbol{W}\right)\cdot\boldsymbol{n} = \left(\rho\boldsymbol{u}\cdot\boldsymbol{n}, \left(\rho\boldsymbol{u}\cdot\boldsymbol{n}\right)\boldsymbol{u} + P\boldsymbol{n}, \left(E+P\right)\boldsymbol{u}\cdot\boldsymbol{n}\right)^{\mathsf{T}}.$$

Note that the flux is null through Γ_i^w wall boundaries inside Ω_i, since $\boldsymbol{u}\cdot\boldsymbol{n}|_w = 0$, except the pressure flux $P\boldsymbol{n}|_w$.

In the sequel, the subscript ij refers to the interfaces between the neighbouring control volumes Ω_i and Ω_j, where $j \in N(i)$, and $N(i)$ defines the set of neighbouring cells of Ω_i. Besides, the superscript ϕ refers to the fluid volumes and the fluid interfaces ij where the fluid may cross the interface, noted Γ_{ij}^ϕ of measure $S_{ij}^\phi = \left|\Gamma_{ij}^\phi\right|$. The superscript w refers to solid interfaces where a wall boundary Γ_i^w of measure S_i^w is located inside the control volume Ω_i or on its boundary.

Remark 2.1. *In practice, the geometrical quantities, as defined in the integral formulation, have to be pre-processed. This step uses the mesh of the computational domain and the known geometry of the obstacles, for instance the multidimensional computer-aiding drafting (CAD). This pre-processing may turn to be tedious but it is performed once and can be parallelized in space.*

3 Time scheme

The time discretization of Equation (1.5) is based on an implicit first order Euler scheme. It is assumed that all numerical fluxes may be evaluated by means of a standard finite volume

method, considering one mean value $\mathbf{W}_i^n$ per cell Ω_i at each time t^n, see [16] for more details. $\mathbf{W}_i^n$ is an approximation of $\boldsymbol{W}_i(t^n)$, and the time step at the n^{th} iteration is $\Delta t^n = t^{n+1} - t^n$. The numerical algorithm uses a pressure-correction scheme, with prediction and correction of the pressure [55, 45, 56].

Each time stepping is thus divided in three steps: first, the mass balance, which is used to update the density from ρ^n to ρ^{n+1}, and to predict a temporary pressure P^* and a convective mass flux $\boldsymbol{Q}^* \cdot \boldsymbol{n}$, second, the momentum balance, where the velocity is updated from $\mathbf{u}^n$ to $\mathbf{u}^{n+1}$, and third, the last step, the energy balance that allows to update the total energy from E^n to E^{n+1} and thus to correct the pressure with the EOS. The superscript $(\cdot)^*$ states that the variable is predicted for the current step. The time semi-discrete algorithm is summarized below, starting with the initial condition $\mathbf{W}_i^n$ for all $n \in \mathbb{N}$:

1. Compute P^* solution of the mass balance, with $\delta\rho = \frac{\delta P}{(c^2)^n} = \frac{P^* - P^n}{(c^2)^n}$:

$$\frac{\delta P}{(c^2)^n} + \Delta t^n \mathrm{div}\ (\rho^n \mathbf{u}^n - \Delta t^n \boldsymbol{\nabla} P^*) = 0, \tag{1.6}$$

   and update:

$$\rho^{n+1} = \rho^n + \frac{\delta P}{(c^2)^n} \quad \text{and} \quad \boldsymbol{Q}^* = \rho^n \mathbf{u}^n - \Delta t^n \boldsymbol{\nabla} P^*. \tag{1.7}$$

2. Compute $\mathbf{u}^{n+1}$ solution of the momentum balance, with $\delta(\rho\mathbf{u}) = \rho^{n+1}\mathbf{u}^{n+1} - \rho^n\mathbf{u}^n$:

$$\delta(\rho\mathbf{u}) + \Delta t^n \mathbf{div}\ \left(\mathbf{u}^{n+1} \otimes \boldsymbol{Q}^*\right) = -\Delta t^n \boldsymbol{\nabla} P^* + \Delta t^n \rho^{n+1} \boldsymbol{f}^n. \tag{1.8}$$

3. Compute E^{n+1} solution of the total energy balance, with $\delta E = E^{n+1} - E^n$:

$$\delta E + \Delta t^n \mathrm{div}\ \left(\frac{E^{n+1}}{\rho^{n+1}} \boldsymbol{Q}^*\right) = -\Delta t^n \mathrm{div}\ \left(\frac{P^*}{\rho^{n+1}} \boldsymbol{Q}^*\right) + \Delta t^n \rho^{n+1} \left(\boldsymbol{f}^n \cdot \mathbf{u}^{n+1} + \Phi_v^n\right), \tag{1.9}$$

   and update, using the EOS:

$$P^{n+1} = \mathcal{P}(\rho^{n+1}, \epsilon^{n+1}) \quad \text{with} \quad \epsilon^{n+1} = \frac{E^{n+1}}{\rho^{n+1}} - \frac{1}{2}(\mathbf{u}^{n+1} \cdot \mathbf{u}^{n+1}). \tag{1.10}$$

3.1 Mass balance

The pressure and the density are implicit, while the velocity and the entropy are considered frozen at time t^n. An acoustic mass flux $\boldsymbol{Q}^* \cdot \boldsymbol{n}$ is computed from the simplified momentum equation (1.14) given below. Integration of the mass balance equation, between t^n and t^{n+1} and over Ω_i^ϕ, gives the following implicit time scheme:

$$\left|\Omega_i^\phi\right| \left(\rho_i^{n+1} - \rho_i^n\right) + \Delta t^n \int_{\Gamma_i} \boldsymbol{Q}^* \cdot \boldsymbol{n} \mathrm{d}\gamma = 0. \tag{1.11}$$

The acoustic linear approximation $(P_i^* - P_i^n) = \left(c^2\right)_i^n \left(\rho_i^{n+1} - \rho_i^n\right)$ is used, and reads $\left(c^2\right)_i^n = c^2(P_i^n, \rho_i^n)$. equation (1.11) thus yields with the pressure variable:

$$\left|\Omega_i^\phi\right| \frac{1}{(c^2)_i^n} \left(P_i^* - P_i^n\right) + \Delta t^n \int_{\Gamma_i} \boldsymbol{Q}^* \cdot \boldsymbol{n} \mathrm{d}\gamma = 0. \tag{1.12}$$

This step allows to predict the pressure P^*, from which the density ρ^{n+1} is deduced. For this purpose, the approximation of the implicit mass flux $\boldsymbol{Q}^* \cdot \boldsymbol{n}$ is, at interfaces:

$$\boldsymbol{Q}^* \cdot \boldsymbol{n} = \boldsymbol{Q}^n \cdot \boldsymbol{n} - \Delta t^n \boldsymbol{\nabla} P^* \cdot \boldsymbol{n}. \tag{1.13}$$

This discretization (1.13) is based on the simplified momentum balance:

$$\partial_t \boldsymbol{Q} + \boldsymbol{\nabla} P = 0. \tag{1.14}$$

Remark 3.1. *The relation* $\rho_i^{n+1} = \rho_i^n + \frac{1}{(c^2)_i^n}\left(P_i^* - P_i^n\right)$ *must be used for the update of the density to conserve the mass over time.*

Remark 3.2. *This first step can be viewed as an acoustic step: assuming a constant time step, equations (1.11) and (1.13), at the previous and current time level, yields the discrete wave equation below:*

$$\frac{\rho^{n+1} - 2\rho^n + \rho^{n-1}}{\Delta t^2} - \operatorname{div}\left(\left(c^2\right)^n \boldsymbol{\nabla}\rho^{n+1}\right) = 0.$$

Indeed, the semi-discrete acoustic linear system can be written:

$$\begin{cases} \dfrac{\rho^{n+1} - \rho^n}{\Delta t} + \operatorname{div}(\boldsymbol{Q^*}) = 0, \\ \dfrac{\boldsymbol{Q}^* - \boldsymbol{Q}^n}{\Delta t} + \boldsymbol{\nabla} P^*(\rho^{n+1}) = 0. \end{cases}$$

Combining the two equations yields:

$$\frac{\rho^{n+1} - \rho^n}{\Delta t} + \operatorname{div}(\boldsymbol{Q^n}) - \operatorname{div}(\Delta t \boldsymbol{\nabla} P^*(\rho^{n+1})) = 0.$$

Assuming that the mass flux $\boldsymbol{Q^n}$ *complies with the mass balance at the previous time step* t^n*:*

$$\frac{\rho^n - \rho^{n-1}}{\Delta t} + \operatorname{div}(\boldsymbol{Q^n}) = 0,$$

the wave equation, at the discrete level, can be thus obtained:

$$\frac{\rho^{n+1} - 2\rho^n + \rho^{n-1}}{\Delta t^2} - \operatorname{div}(\boldsymbol{\nabla} P^*(\rho^{n+1})) = 0.$$

Using the acoustic linear approximation, $\boldsymbol{\nabla} P^*(\rho^{n+1}) = (c^2)^n \boldsymbol{\nabla}\rho^{n+1}$*, yields:*

$$\frac{\rho^{n+1} - 2\rho^n + \rho^{n-1}}{\Delta t^2} - \operatorname{div}\left(\left(c^2\right)^n \boldsymbol{\nabla}\rho^{n+1}\right) = 0.$$

3.2 Momentum balance

In this step, the velocity is implicit, whereas the density and the pressure are known from equation (1.12) of the mass balance step, and the total energy is frozen. Integration of the momentum equation gives:

$$\begin{aligned} \left|\Omega_i^\phi\right|\left(\mathbf{Q}_i^{n+1} - \mathbf{Q}_i^n\right) + \Delta t^n \int_{\Gamma_i} (\boldsymbol{Q}^* \cdot \boldsymbol{n})\mathbf{u}^{n+1}\mathrm{d}\gamma + \Delta t^n \int_{\Gamma_i} P^* \boldsymbol{n}\mathrm{d}\gamma \\ - \Delta t^n \left|\Omega_i^\phi\right| \rho_i^{n+1} \boldsymbol{f}_i^n = 0. \end{aligned} \tag{1.15}$$

This second step provides, for all Ω_i, the unknown velocity $\mathbf{u}_i^{n+1}$. Thus the momentum is inferred by $\mathbf{Q}_i^{n+1} = \rho_i^{n+1}\mathbf{u}_i^{n+1}$.

3.3 Energy balance

The total energy is implicit while the pressure, the density and the velocity are explicit from the previous steps. The total energy E_i^{n+1} is updated with the following implicit scheme:

$$\left|\Omega_i^\phi\right| \left(E_i^{n+1} - E_i^n\right) + \Delta t^n \int_{\Gamma_i} (\boldsymbol{Q}^* \cdot \boldsymbol{n}) \frac{E^{n+1} + P^*}{\rho^{n+1}} \mathrm{d}\gamma \\ - \Delta t^n \left|\Omega_i^\phi\right| \left(\rho_i^{n+1} \boldsymbol{f}_i^n \cdot \mathbf{u}_i^{n+1} + \rho_i^{n+1} \Phi_{v,i}^n\right) = 0. \tag{1.16}$$

Finally, this third step provides the internal energy: $\epsilon_i^{n+1} = \dfrac{E_i^{n+1}}{\rho_i^{n+1}} - \dfrac{1}{2}\left(\mathbf{u}_i^{n+1} \cdot \mathbf{u}_i^{n+1}\right)$, and the pressure is thus corrected with the EOS: $\mathcal{P}(\rho, \epsilon)$, for all cells Ω_i:

$$P_i^{n+1} = \mathcal{P}(\rho_i^{n+1}, \epsilon_i^{n+1}).$$

4 Space scheme

A collocated finite volume method (all the variables are cell-based) is used to discretize in space the integral formulation of the conservation laws, equation (1.5). At each step, a numerical flux is written to evaluate the different boundary integrals. We focus on the fluid and solid interior cell faces of the mesh defined in section 2.2 (see FIGURE 1.3). The boundary conditions of the computational domain Ω are treated in section 4.4. The space scheme is described for structured and orthogonal meshes, involving some simplifications particularly for the pressure gradient approximation in equation (1.13).

4.1 Mass balance

In the time semi-discrete mass balance equation (1.12) given below, an expression of the mass flux needs to be specified:

$$\left|\Omega_i^\phi\right| \frac{1}{(c^2)_i^n} \left(P_i^* - P_i^n\right) + \Delta t^n \int_{\Gamma_i} \boldsymbol{Q}^* \cdot \boldsymbol{n} \mathrm{d}\gamma = 0.$$

Note that the normal mass flux to the wall is null, $(\boldsymbol{Q} \cdot \boldsymbol{n})_{\Gamma^w} = \rho \boldsymbol{u} \cdot \boldsymbol{n}\big|_w = 0$, and thus:

$$\int_{\Gamma_i^w} \boldsymbol{Q}^* \cdot \boldsymbol{n} \mathrm{d}\gamma = 0.$$

Equation (1.13), *i.e.* the simplified momentum balance, allows to decompose the integral over the fluid face into two integrals:

$$\int_{\Gamma_i} \boldsymbol{Q}^* \cdot \boldsymbol{n} \mathrm{d}\gamma = \int_{\Gamma_i^\phi} \boldsymbol{Q}^* \cdot \boldsymbol{n} \mathrm{d}\gamma = \underbrace{\int_{\Gamma_i^\phi} \boldsymbol{Q}^n \cdot \boldsymbol{n} \mathrm{d}\gamma}_{1} - \underbrace{\int_{\Gamma_i^\phi} \Delta t^n \boldsymbol{\nabla} P^* \cdot \boldsymbol{n} \mathrm{d}\gamma}_{2}. \tag{1.17}$$

4.1.1 Evaluation of the explicit mass flux

Integral 1 of equation (1.17) is discretized for all cells Ω_i by summing up on all fluid interfaces Γ_{ij}^{ϕ} of Ω_i^{ϕ}, with $j \in N(i)$. The convective numerical flux is defined as follows:

$$\int_{\Gamma_i^{\phi}} \boldsymbol{Q}^n \cdot \boldsymbol{n} \mathrm{d}\gamma = \sum_{j \in N(i)} \int_{\Gamma_{ij}^{\phi}} \boldsymbol{Q}^n \cdot \boldsymbol{n} \mathrm{d}\gamma = \sum_{j \in N(i)} \left(\rho_{ij}^n\right)^{upw} \left(\mathbf{u}^n \cdot \boldsymbol{n}\right)_{ij} S_{ij}^{\phi}, \tag{1.18}$$

where $\boldsymbol{n}_{ij}$ is the unit normal vector at the fluid interface Γ_{ij}^{ϕ} from Ω_i^{ϕ} to Ω_j^{ϕ}. The transported quantity ρ_{ij}^n is estimated by the standard first order upwind scheme:

$$\left(\rho_{ij}^n\right)^{upw} = \beta_{ij}^n \rho_i^n + (1 - \beta_{ij}^n)\rho_j^n,$$

with:

$$\beta_{ij}^n = \begin{cases} 1 & \text{if } \left(\mathbf{u}^n \cdot \boldsymbol{n}\right)_{ij} \geq 0, \\ 0 & \text{otherwise.} \end{cases}$$

The normal velocity at the fluid interface is linearly interpolated between the two neighbouring cells:

$$\left(\mathbf{u}^n \cdot \boldsymbol{n}\right)_{ij} = \left(\alpha_{ij} \mathbf{u}_i^n + (1 - \alpha_{ij})\, \mathbf{u}_j^n\right) \cdot \boldsymbol{n}_{ij},$$

where:

$$\alpha_{ij} = \frac{h_{ij/j}}{h_{ij/i} + h_{ij/j}},$$

and $h_{ij/i}$ stands for the distance from the gravity centre of the cell Ω_i to the interface Γ_{ij}^{ϕ} (remember that we assumed an orthogonal structured grid).

4.1.2 Evaluation of the mass flux implicit contribution

As previously, integral 2 of equation (1.17) is decomposed into a sum on all fluid faces of the cell Ω_i. Structured and orthogonal meshes are only considered, which allows a simple gradient scheme. Numerically and despite the potential presence of sub-elements into the cell, the value of the pressure P_i in the cell Ω_i is supposed uniform. The pressure gradient at the face is approximated with a "two-point flux approximation" scheme, standard for admissible meshes [57]:

$$\boldsymbol{\nabla} P \cdot \boldsymbol{n_{ij}} = \left.\frac{\partial P}{\partial \boldsymbol{n}}\right|_{\Gamma_{ij}^{\phi}} = \frac{P_j - P_i}{h_{ij/i} + h_{ij/i}}.$$

Thus, the scheme yields:

$$\int_{\Gamma_i^{\phi}} \Delta t^n \boldsymbol{\nabla} P^* \cdot \boldsymbol{n} \mathrm{d}\gamma = \sum_{j \in N(i)} \int_{\Gamma_{ij}^{\phi}} \Delta t^n \boldsymbol{\nabla} P^* \cdot \boldsymbol{n} \mathrm{d}\gamma = \sum_{j \in N(i)} \frac{\Delta t^n}{h_{ij/i} + h_{ij/j}} \left(P_j^* - P_i^*\right) S_{ij}^{\phi}. \tag{1.19}$$

We conclude that the mass flux is approximated, at each fluid interface, by:

$$\int_{\Gamma_i^{\phi}} \boldsymbol{Q}^* \cdot \boldsymbol{n} \mathrm{d}\gamma = \sum_{j \in N(i)} \left(\rho_{ij}^n\right)^{upw} \left(\mathbf{u}^n \cdot \boldsymbol{n}\right)_{ij} S_{ij}^{\phi} - \sum_{j \in N(i)} \frac{\Delta t^n}{h_{ij/i} + h_{ij/j}} \left(P_j^* - P_i^*\right) S_{ij}^{\phi}. \tag{1.20}$$

4.2 Momentum balance

In this section, the semi-discrete momentum balance (1.15), solved with the velocity $\mathbf{u}^{n+1}$, is discretized in space:

$$\left|\Omega_i^\phi\right|\left(\rho_i^{n+1}\mathbf{u}_i^{n+1}-\rho_i^n\mathbf{u}_i^n\right)+\Delta t^n\int_{\Gamma_i}\mathbf{u}^{n+1}(\boldsymbol{Q}^*\cdot\boldsymbol{n})\mathrm{d}\gamma+\Delta t^n\int_{\Gamma_i}P^*\boldsymbol{n}\mathrm{d}\gamma \\ -\Delta t^n\left|\Omega_i^\phi\right|\rho_i^{n+1}\boldsymbol{f}_i^n=0.$$

At this step, the density ρ_i^{n+1} and the force $\boldsymbol{f}_i^n$ are known. We must define the numerical flux for both integrals of equation (1.15):

$$\int_{\Gamma_i}\mathbf{u}^{n+1}(\boldsymbol{Q}^*\cdot\boldsymbol{n})\mathrm{d}\gamma, \tag{1.21}$$

$$\text{and}\quad\int_{\Gamma_i}P^*\boldsymbol{n}\mathrm{d}\gamma. \tag{1.22}$$

4.2.1 Evaluation of the convective flux in the momentum equation

The integral (1.21) is decomposed on the wall faces Γ_i^w and the fluid faces Γ_i^ϕ of the cell Ω_i:

$$\int_{\Gamma_i}\mathbf{u}^{n+1}(\boldsymbol{Q}^*\cdot\boldsymbol{n})\mathrm{d}\gamma=\underbrace{\int_{\Gamma_i^w}\mathbf{u}^{n+1}(\boldsymbol{Q}^*\cdot\boldsymbol{n})\mathrm{d}\gamma}_{=0}+\int_{\Gamma_i^\phi}\mathbf{u}^{n+1}(\boldsymbol{Q}^*\cdot\boldsymbol{n})\mathrm{d}\gamma.$$

To evaluate the fluid part in this relation, the numerical flux is summed up on all fluid interfaces Γ_{ij}^ϕ of the cell Ω_i as follows:

$$\int_{\Gamma_i^\phi}\mathbf{u}^{n+1}(\boldsymbol{Q}^*\cdot\boldsymbol{n})\mathrm{d}\gamma=\sum_{j\in N(i)}\int_{\Gamma_{ij}^\phi}\mathbf{u}^{n+1}(\boldsymbol{Q}^*\cdot\boldsymbol{n})\mathrm{d}\gamma=\sum_{j\in N(i)}\left(\mathbf{u}_{ij}^{n+1}\right)^{upw}(\boldsymbol{Q}^*\cdot\boldsymbol{n})_{ij}\,S_{ij}^\phi. \tag{1.23}$$

The mass flux $(\boldsymbol{Q}^*\cdot\boldsymbol{n})_{ij}\,S_{ij}^\phi$ has already been computed at the previous step by equation (1.20):

$$(\boldsymbol{Q}^*\cdot\boldsymbol{n})_{ij}\,S_{ij}^\phi=\int_{\Gamma_{ij}^\phi}\boldsymbol{Q}^*\cdot\boldsymbol{n}\mathrm{d}\gamma.$$

The value of the convected velocity $\left(\mathbf{u}_{ij}^{n+1}\right)^{upw}$ at the fluid interface is computed with a upwind scheme:

$$\left(\mathbf{u}_{ij}^{n+1}\right)^{upw}=\lambda_{ij}^n\mathbf{u}_i^{n+1}+(1-\lambda_{ij}^n)\mathbf{u}_j^{n+1},$$

with:

$$\lambda_{ij}^n=\begin{cases}1 & \text{if } (\boldsymbol{Q}^*\cdot\boldsymbol{n})_{ij}\geq 0,\\ 0 & \text{otherwise.}\end{cases}$$

4.2.2 Evaluation of the pressure force in the momentum equation

The pressure value P_i^* for all cells Ω_i is known from the mass conservation step. The integral decomposition on Γ_i^ϕ and Γ_i^w is thus explicit in time:

$$\int_{\Gamma_i}P^*\boldsymbol{n}\mathrm{d}\gamma=\int_{\Gamma_i^w}P^*\boldsymbol{n}\mathrm{d}\gamma+\int_{\Gamma_i^\phi}P^*\boldsymbol{n}\mathrm{d}\gamma.$$

For the fluid interfaces Γ_{ij}^{ϕ}, the pressure contribution is a linear interpolation between neighbouring cells values, that is to say:

$$P_{ij}^{*} = \frac{h_{ij/i}P_i^{*} + h_{ij/j}P_j^{*}}{h_{ij/i} + h_{ij/j}} = (1-\alpha_{ij})P_i^{*} + \alpha_{ij}P_j^{*}.$$

Remark 4.1. *Note that the interpolation coefficients $1-\alpha_{ij}$ are unusual. Indeed a standard interpolation formula would have yielded α_{ij} instead of $1-\alpha_{ij}$. This stems from the fact that the discrete pressure gradient is built as the transpose of the velocity divergence operator by duality with respect to the L^2 inner product [55].*

For the solid faces (interior walls) of Γ_i^{w}, two approximations of the wall pressure P^{w} are considered.

- *First approximation of the wall pressure*

The contribution of the wall pressure P^{w} is decentred in taking directly the cell centre value:

$$P^{w} = P_i^{*}. \tag{1.24}$$

Eventually, summing up on all cell faces, the pressure gradient may be written as follows:

$$\begin{aligned}
\int_{\Gamma_i} P^{*}\boldsymbol{n}\mathrm{d}\gamma = \left|\Omega_i^{\phi}\right| \boldsymbol{\nabla}_i P^{*} &= \sum_{j\in N(i)} P_{ij}^{*}\boldsymbol{n}_{ij}S_{ij}^{\phi} + \int_{\Gamma_i^{w}} P^{w}\boldsymbol{n}\mathrm{d}\gamma \\
&= \sum_{j\in N(i)} P_{ij}^{*}\boldsymbol{n}_{ij}S_{ij}^{\phi} + P_i^{*}\left(-\sum_{j\in N(i)} \boldsymbol{n}_{ij}S_{ij}^{\phi}\right) \\
&= \sum_{j\in N(i)} \left(P_{ij}^{*} - P_i^{*}\right)\boldsymbol{n}_{ij}S_{ij}^{\phi}.
\end{aligned}$$

In the last relation, we used the fact that the integral of the normal vector on a closed boundary vanishes:

$$\int_{\Gamma_i} \boldsymbol{n}\mathrm{d}\gamma = 0 = \sum_{j\in N(i)} \boldsymbol{n}_{ij}S_{ij}^{\phi} + \int_{\Gamma_i^{w}} \boldsymbol{n}\mathrm{d}\gamma.$$

- *Second approximation of the wall pressure*

Another choice for the evaluation of the wall pressure P^{w} is to use the "mirror state" technique defined in [58]. A virtual cell is considered in the solid obstacle with the normal $\boldsymbol{n}$ and the wall pressure is obtained by solving a Riemann problem, see 1.B:

$$P^{w} = P^{Riemann}\left(\mathbf{W}^{n+1}, \widehat{\mathbf{W}}^{n+1}\right), \tag{1.25}$$

where

$$\widehat{\mathbf{W}}^{n+1} = \left[\rho_i^{n+1}, -\rho_i^{n+1}\mathbf{u}_i^{n+1}\cdot\boldsymbol{n}, E_i^{*}\right]^{\mathsf{T}}$$

is the mirror state of

$$\mathbf{W}^{n+1} = \left[\rho_i^{n+1}, \rho_i^{n+1}\mathbf{u}_i^{n+1}\cdot\boldsymbol{n}, E_i^{*}\right]^{\mathsf{T}}.$$

For the Euler equations (1.1) and for any EOS, the general form of the solution of this problem is:

$$P^{Riemann}\left(\mathbf{W}^{n+1}, \widehat{\mathbf{W}}^{n+1}\right) = P_i^{*}\left(1 + f\left(M^{*}\right)\right),$$

where M^* is the local Mach number based on the normal velocity to the wall:

$$M^* = \frac{\mathbf{u}_i^{n+1} \cdot \boldsymbol{n}}{c(P_i^*, \rho_i^{n+1})}.$$

The expression of the function f depends on the Riemann solver and the EOS of the fluid, see [58], but in any cases: $f(0) = 0$.

In order to compute the pressure integral contribution, the function f is linearized in using its Taylor expansion at the first order with respect to M^*, supposed to be small compared to 1:

$$P^w = P_i^* \left(1 + \hat{\gamma}\, M^*\right), \tag{1.26}$$

where $\hat{\gamma} = f'(0)$.

Remark 4.2. *For the EOS of an ideal gas, $\hat{\gamma} = \gamma$, and for the EOS of a stiffened gas, $\hat{\gamma} = \gamma\left(1 + \frac{\Pi_\infty}{P}\right)$.*

Consequently, the wall pressure integral evaluation becomes:

$$\begin{aligned}\int_{\Gamma_i^w} P^* \boldsymbol{n} \mathrm{d}\gamma &= \int_{\Gamma_i^w} P_i^* \left(1 + \hat{\gamma}\, M^*\right) \boldsymbol{n} \mathrm{d}\gamma \\ &= P_i^* \left(\int_{\Gamma_i^w} \boldsymbol{n} \mathrm{d}\gamma\right) + P_i^* \frac{\hat{\gamma}}{c(P_i^*, \rho_i^{n+1})} \left(\int_{\Gamma_i^w} \boldsymbol{n}\boldsymbol{n}^\mathsf{T} \mathrm{d}\gamma\right) \mathbf{u}_i^{n+1}.\end{aligned}$$

The pressure gradient is thus discretized in space as:

$$\begin{aligned}\int_{\Gamma_i} P^* \boldsymbol{n} \mathrm{d}\gamma = \left|\Omega_i^\phi\right| \boldsymbol{\nabla}_i P^* &= \sum_{j \in N(i)} P_{ij}^* \boldsymbol{n}_{ij} S_{ij}^\phi + \int_{\Gamma_i^w} P^w \boldsymbol{n} \mathrm{d}\gamma \\ &= \sum_{j \in N(i)} \left(P_{ij}^* - P_i^*\right) \boldsymbol{n}_{ij} S_{ij}^\phi + \boldsymbol{K}_i \mathbf{u}_i^{n+1},\end{aligned}$$

where: $\boldsymbol{K}_i = \frac{\hat{\gamma} P_i^*}{c(P_i^*, \rho_i^{n+1})} \int_{\Gamma_i^w} \boldsymbol{n}\boldsymbol{n}^\mathsf{T} \mathrm{d}\gamma$ is a symmetric positive tensor (see appendix 1.C for its computation).

Remark 4.3. *The first order term, $\boldsymbol{K}\mathbf{u}$, corresponds to a pressure drag force or form drag force due to the obstacle shape. This term dissipates kinetic energy and is not taken into account in the approximation (1.24).*

The resolution of the Riemann problem (1.25) seems more physically grounded than the first choice (1.24) of the cell pressure, particularly when the cell normal velocity to the wall is not close to zero. If the flow is locally tangent to the wall *i.e.* $M^* = 0$, then the second approximation boils down to the first one.

4.3 Energy balance

The space scheme is built from the semi-discrete equation (1.16) of the total energy conservation:

$$\begin{aligned}\left|\Omega_i^\phi\right| \left(E_i^{n+1} - E_i^n\right) + \Delta t^n \int_{\Gamma_i} (\boldsymbol{Q}^* \cdot \boldsymbol{n}) \frac{E^{n+1} + P^*}{\rho^{n+1}} \mathrm{d}\gamma \\ - \Delta t^n \left|\Omega_i^\phi\right| \left(\rho_i^{n+1} \boldsymbol{f}_i^n \cdot \mathbf{u}_i^{n+1} + \rho_i^{n+1} \Phi_{v,i}^n\right) = 0.\end{aligned}$$

The density ρ^{n+1}, the pressure P^* and the velocity $\mathbf{u}^{n+1}$ have been already computed in the previous steps, and the external force $\boldsymbol{f}^n$ and the term source Φ_v^n are given. Thus the last part of equation (1.16) is explicit. The flux integral remains to be evaluated, once again by decomposing it on the fluid and solid faces:

$$\int_{\Gamma_i}(\boldsymbol{Q}^*\cdot\boldsymbol{n})\frac{E^{n+1}+P^*}{\rho^{n+1}}\mathrm{d}\gamma=\underbrace{\int_{\Gamma_i^w}(\boldsymbol{Q}^*\cdot\boldsymbol{n})\frac{E^{n+1}+P^*}{\rho^{n+1}}\mathrm{d}\gamma}_{=0}+\int_{\Gamma_i^\phi}(\boldsymbol{Q}^*\cdot\boldsymbol{n})\frac{E^{n+1}+P^*}{\rho^{n+1}}\mathrm{d}\gamma. \tag{1.27}$$

The fluid part in the integral (1.27) is approximated for each cell Ω_i by a numerical flux. Using the definitions of section 2.2, the flux is decomposed into a sum on all fluid interfaces of Γ_i^ϕ:

$$\begin{aligned}\int_{\Gamma_i^\phi}(\boldsymbol{Q}^*\cdot\boldsymbol{n})\frac{E^{n+1}+P^*}{\rho^{n+1}}\mathrm{d}\gamma&=\sum_{j\in N(i)}\int_{\Gamma_{ij}^\phi}(\boldsymbol{Q}^*\cdot\boldsymbol{n})\frac{E^{n+1}+P^*}{\rho^{n+1}}\mathrm{d}\gamma\\&=\sum_{j\in N(i)}\left(\frac{E^{n+1}}{\rho^{n+1}}\right)_{ij}^{upw}(\boldsymbol{Q}^*\cdot\boldsymbol{n})_{ij}\,S_{ij}^\phi+\sum_{j\in N(i)}\left(\frac{P^*}{\rho^{n+1}}\right)_{ij}^{upw}(\boldsymbol{Q}^*\cdot\boldsymbol{n})_{ij}\,S_{ij}^\phi.\end{aligned} \tag{1.28}$$

The fluid face values of $\left(\frac{E^{n+1}}{\rho^{n+1}}\right)_{ij}^{upw}$ and $\left(\frac{P^*}{\rho^{n+1}}\right)_{ij}^{upw}$ are given by an upwind scheme as described previously:

$$\begin{aligned}\left(\frac{E^{n+1}}{\rho^{n+1}}\right)_{ij}^{upw}&=\lambda_{ij}^n\frac{E_i^{n+1}}{\rho_i^{n+1}}+(1-\lambda_{ij}^n)\frac{E_j^{n+1}}{\rho_j^{n+1}},\\\left(\frac{P^*}{\rho^{n+1}}\right)_{ij}^{upw}&=\lambda_{ij}^n\frac{P_i^*}{\rho_i^{n+1}}+(1-\lambda_{ij}^n)\frac{P_j^*}{\rho_j^{n+1}},\end{aligned}$$

where:

$$\lambda_{ij}^n=\begin{cases}1 & \text{if } (\boldsymbol{Q}^*\cdot\boldsymbol{n})_{ij}\geq 0,\\0 & \text{otherwise.}\end{cases}$$

4.4 Wall boundary condition

Rigid wall boundary conditions on $\partial\Omega^w$, the wall boundary of the computational domain Ω, are taken into account by using the "mirror state" technique, see 1.B and [59, 60, 58]. For the EOS of an ideal gas or stiffened gas, the exact solution of this Riemann problem is calculated. Hence the condition applied at a wall boundary face Γ_{b_i} of the boundary of Ω_i is such that the convective mass flux is null ($\boldsymbol{Q}_{b_i}^*\cdot\boldsymbol{n}_{b_i}=0$) and the predicted pressure is, for the EOS of an ideal gas, either:

- for $\mathbf{u}_i^n\cdot\boldsymbol{n}_{b_i}\leq 0$, rarefaction configuration:

$$\begin{cases}P_{b_i}^*=P_i^*\left(1+\dfrac{\gamma-1}{2}\dfrac{\mathbf{u}_i^n\cdot\boldsymbol{n}_{b_i}}{c_i^n}\right)^{\frac{2\gamma}{\gamma-1}} & \text{if } -\frac{2}{\gamma-1}<\frac{\mathbf{u}_i^n\cdot\boldsymbol{n}_{b_i}}{c_i^n}\leq 0,\\P_{b_i}^*=0 & \text{otherwise,}\end{cases}$$

- for $\mathbf{u}_i^n\cdot\boldsymbol{n}_{b_i}>0$, shock configuration:

$$P_{b_i}^*=P_i^*\left(1+\gamma\frac{\mathbf{u}_i^n\cdot\boldsymbol{n}_{b_i}}{c_i^n}\left(1+\frac{(\gamma+1)^2}{16}\left(\frac{\mathbf{u}_i^n\cdot\boldsymbol{n}_{b_i}}{c_i^n}\right)^2\right)^{\frac{1}{2}}+\frac{\gamma(\gamma+1)}{4}\left(\frac{\mathbf{u}_i^n\cdot\boldsymbol{n}_{b_i}}{c_i^n}\right)^2\right).$$

Furthermore, the wall boundary value of the pressure for the EOS of a stiffened gas is inferred from the formula given in 1.B.

5 Main properties of the scheme

5.1 Properties of the pressure prediction step

This section aims at proving that the numerical scheme preserves the positivity of both the discrete density and the predicted pressure.

The discrete equation coming from the time and space scheme of equation (1.11) of the mass conservation is written with the notations introduced in section 2.2 as follows:

$$\left|\Omega_i^\phi\right| \frac{(P_i^* - P_i^n)}{(c^2)_i^n} + \Delta t^n \sum_{j\in N(i)} \left(\beta_{ij}^n \rho_i^n + (1-\beta_{ij}^n)\rho_j^n\right) (\mathbf{u}^n \cdot \boldsymbol{n})_{ij} S_{ij}^\phi - \sum_{j\in N(i)} \frac{(\Delta t^n)^2}{h_{ij/i} + h_{ij/j}} \left(P_j^* - P_i^*\right) S_{ij}^\phi = 0. \tag{1.29}$$

Equation (1.29) yields a linear system:

$$\mathbf{A}\,\mathbf{X} = \mathbf{B},$$

with the vector $\mathbf{X} = (P_i^*)_{i\in\{1,\dots,N_{cell}\}}$, where N_{cell} is the total number of cell (degrees of freedom). $\forall\, i \in \{1,\dots,N_{cell}\}$, the diagonal matrix coefficients are:

$$A_{ii} = \begin{cases} \dfrac{\left|\Omega_i^\phi\right|}{(c^2)_i^n} + (\Delta t^n)^2 \displaystyle\sum_{j\in N(i)} \frac{S_{ij}^\phi}{h_{ij/i} + h_{ij/j}} & \text{if } \left|\Omega_i^\phi\right| > 0, \\ 1 & \text{otherwise,} \end{cases}$$

$\forall\, i, j \in \{1,\dots,N_{cell}\}$ with $j \neq i$, the off-diagonal coefficients are:

$$A_{ij} = \begin{cases} -\dfrac{(\Delta t^n)^2}{h_{ij/i} + h_{ij/j}} S_{ij}^\phi & \text{if } j \in N(i) \text{ and } \left|\Omega_i^\phi\right| > 0, \\ 0 & \text{otherwise.} \end{cases}$$

The right hand side coefficients are:

$$B_i = \begin{cases} \left|\Omega_i^\phi\right| \dfrac{P_i^n}{(c^2)_i^n} - \Delta t^n \displaystyle\sum_{j\in N(i)} \left(\beta_{ij}^n \rho_i^n + (1-\beta_{ij}^n)\rho_j^n\right) (\mathbf{u}^n \cdot \boldsymbol{n})_{ij} S_{ij}^\phi & \text{if } \left|\Omega_i^\phi\right| > 0, \\ P_i^n & \text{otherwise.} \end{cases}$$

Remark 5.1. *If the measure of the fluid part of the cell Ω_i is null, then all faces are considered as solid, i.e.: if $\left|\Omega_i^\phi\right| = 0$, then $\forall\, j \in N(i)$, $S_{ij}^\phi = 0$. We conclude that: $B_i = P_i^n$ and hence $P_i^* = P_i^n$.*

Property 5.1. *[Positivity of the density and the predicted pressure] Assume that the EOS is such that $\rho > 0$, $P > 0$ and $\hat{\gamma} = \frac{\rho c^2}{P} > 1$. If the initial conditions are such that, for all Ω_i, $\rho_i^n > 0$ and $P_i^n > 0$, then the density ρ_i^{n+1} and the pressure P_i^* will remain positive for all Ω_i, provided that the time step Δt^n complies with the CFL-like condition:*

$$\left|\Omega_i^\phi\right| \geq \hat{\gamma} \Delta t^n \sum_{j\in N(i)} \beta_{ij}^n \left(\mathbf{u}^n \cdot \boldsymbol{n}\right)_{ij} S_{ij}^\phi. \tag{1.30}$$

The CFL-like condition (1.30) allows to define the CFL^+ condition if $\left|\Omega_i^\phi\right| > 0$:

$$CFL^+ := \hat{\gamma} \Delta t^n \max_{i\in\{1,\dots,N_{cell}\}} \frac{1}{\left|\Omega_i^\phi\right|} \sum_{j\in N(i)} \beta_{ij}^n \left(\mathbf{u}^n \cdot \boldsymbol{n}\right)_{ij} S_{ij}^\phi \leq 1. \tag{1.31}$$

Proof. The proof is that $\mathbf{A}$ is a M-matrix and $\mathbf{B}$ is positive.

- $\mathbf{A}$ is a M-matrix: the time step $\Delta t^n > 0$, $\forall\, i \in \{1, ..., N_{cell}\}$, $(c^2)_i^n > 0$ and $\left|\Omega_i^\phi\right| \geq 0$. Moreover, $\forall\, j \in N(i)$, $S_{ij}^\phi \geq 0$ and $h_{ij/i} + h_{ij/j} > 0$. Thus all diagonal coefficients of the matrix $\mathbf{A}$ are strictly positive ($A_{ii} > 0$), and all off-diagonal coefficients are negative or null ($A_{ij} \leq 0$ for $j \neq i$).

  $\forall\, i \in \{1, ..., N_{cell}\}$, $\mathbf{A}$ is strictly diagonally dominant by lines:

$$|A_{ii}| - \sum_{j \neq i} |A_{ij}| = A_{ii} + \sum_{j \in N(i)} A_{ij}$$
$$= \begin{cases} \frac{\left|\Omega_i^\phi\right|}{(c^2)_i^n} > 0 & \text{if } \left|\Omega_i^\phi\right| > 0, \\ 1 & \text{otherwise.} \end{cases}$$

  Thus $\mathbf{A}$ is a M-matrix *i.e.* invertible and the $\mathbf{A}^{-1}$ coefficients are positive:

$$\forall\, i, j \in \{1, ..., N_{cell}\},\ \left(\mathbf{A}^{-1}\right)_{ij} \geq 0.$$

- $\mathbf{B}$ is positive: if $\left|\Omega_i^\phi\right| > 0$, the coefficient B_i yields:

$$B_i = \left[\frac{\left|\Omega_i^\phi\right|}{(c^2)_i^n} - \Delta t^n \sum_{j \in N(i)} \beta_{ij}^n \frac{\rho_i^n}{P_i^n} (\mathbf{u}^n \cdot \boldsymbol{n})_{ij} S_{ij}^\phi\right] P_i^n - \Delta t^n \sum_{j \in N(i)} (1 - \beta_{ij}^n) \rho_j^n (\mathbf{u}^n \cdot \boldsymbol{n})_{ij} S_{ij}^\phi. \quad (1.32)$$

  By considering equation (1.32), the coefficient B_i is a positive combination of P_i^n and ρ_j^n if the CFL-like condition (1.30) holds. Thus the vector $\mathbf{B}$ is positive:

$$\forall\, i \in \{1, ..., N_{cell}\},\ B_i \geq 0.$$

  Given that:

$$\mathbf{X} = \mathbf{A}^{-1}\mathbf{B},$$

  we conclude, for all Ω_i, $X_i = P_i^* \geq 0$.

  Likewise the density ρ^{n+1} remains positive under the condition (1.30). Indeed, to be conservative, we have set for all $i \in \{1, ..., N_{cell}\}$ (see section 3) :

$$\rho_i^{n+1} - \rho_i^n = \frac{P_i^* - P_i^n}{(c^2)_i^n} \Rightarrow \rho_i^{n+1} = \frac{P_i^*}{(c_i^2)^n} + \rho_i^n \frac{(\hat{\gamma}_i^n - 1)}{\hat{\gamma}_i^n},$$

  which completes the proof: $\rho_i^{n+1} > 0$, since $\hat{\gamma}_i^n = \hat{\gamma} > 1$.

Remark 5.2. *For an ideal gas, $\hat{\gamma} = \gamma \approx 1$ (notably $\gamma = 1.4$ for a diatomic gas). The CFL-like condition (1.30) is close to the standard CFL_u condition (1.33), based on the material transport.*

$$CFL_u := \Delta t^n \max_{i \in \{1, ..., N_{cell}\}} \frac{1}{\left|\Omega_i^\phi\right|} \sum_{j \in N(i)} \beta_{ij}^n \left(\mathbf{u}^n \cdot \boldsymbol{n}\right)_{ij} S_{ij}^\phi \leq 1. \quad (1.33)$$

Remark 5.3. *For a liquid with a physical EOS, $\hat{\gamma} \gg 1$. This CFL-like condition (1.30) becomes more limiting than the standard CFL_u condition (1.33) on the velocity for an explicit upwind scheme. A way to maintain the standard CFL_u constraint is to substitute the mass balance linear scheme by a non-linear scheme (see 1.A).*

Remark 5.4. *For the stiffened gas EOS, Property 5.1 does not apply. Indeed negative pressures greater than $-\Pi_\infty$ are meaningful. In this case, we may prove the following result, Property 5.2.*

Property 5.2. *[Admissible state of the density and the predicted pressure for the stiffened gas EOS] Assume a stiffened gas EOS (1.2), which is such that $\rho > 0$ and $P + \Pi_\infty > 0$. If the initial conditions are such that, for all Ω_i, $\rho_i^n > 0$ and $P_i^n + \Pi_\infty > 0$, then the density ρ_i^{n+1} and the pressure $P_i^* + \Pi_\infty$ will remain positive for all Ω_i, provided that the time step Δt^n complies with the modified CFL^+ condition:*

$$CFL^+ := \gamma \Delta t^n \max_{i \in \{1,\dots,N_{cell}\}} \frac{1}{\left|\Omega_i^\phi\right|} \sum_{j \in N(i)} \beta_{ij}^n \left(\mathbf{u}^n \cdot \boldsymbol{n}\right)_{ij} S_{ij}^\phi \leq 1. \tag{1.34}$$

Proof. The proof is identical to the one of Property 5.1 thanks to the suitable change of variables, for all Ω_i, $\widetilde{P}_i = P_i + \Pi_\infty$ in the discrete mass balance equation (1.29).

Remark 5.5. *The CFL^+ condition (1.34) remains always close to the CFL_u condition (1.33), since, for the stiffened gas EOS, γ is usually in the range $(1, 10]$.*

Remark 5.6 (Conservativity in time and space). *The algorithm is conservative in time and in space. It is important to emphasize that, for all $i \in \{1, ..., N_{cell}\}$, the density ρ_i^{n+1} needs to be updated only as follows:*

$$\rho_i^{n+1} = \rho_i^n + \frac{1}{(c_i^2)^n} \left(P_i^* - P_i^n\right).$$

Conservativity of the algorithm allows to find the correct shock solutions in pure fluid cases. This is verified in presence of discontinuities in [45]. The convergence order, determined from the Riemann problem of the shock tube test case, is $\frac{1}{2}$ for contact discontinuities, and 1 for shock waves and rarefaction waves.

5.2 Properties of the pressure correction step

This section aims at proving that the numerical scheme preserves the positivity of the discrete internal energy and hence of the corrected pressure.

Property 5.3. *[Positivity of the internal energy] Assume that the EOS is such that $\rho > 0$ and $\epsilon > 0$. If the initial conditions are such that, for all Ω_i, $\rho_i^n > 0$ and $\epsilon_i^n > 0$, then the internal energy ϵ_i^{n+1} will remain positive for all Ω_i, provided that the time step Δt^n complies with the CFL-like condition:*

$$\left|\Omega_i^\phi\right| \geq \frac{\Delta t^n}{\rho_i^n \epsilon_i^n} \sum_{j \in N(i)} \left(\left(\frac{P^*}{\rho^{n+1}}\right)_{ij}^{upw} \left(\boldsymbol{Q}^* \cdot \boldsymbol{n}\right)_{ij} - \left(P_{ij}^* - P_i^*\right) \boldsymbol{n}_{ij} \cdot \mathbf{u}_i^{n+1} \right) S_{ij}^\phi. \tag{1.35}$$

The CFL-like condition (1.35) allows to define the CFL_ϵ^+ condition, if $\left|\Omega_i^\phi\right| > 0$:

$$CFL_\epsilon^+ := \Delta t^n \max_{i \in \{1,\dots,N_{cell}\}} \frac{1}{\left|\Omega_i^\phi\right|} \frac{a_i^*}{\rho_i^n \epsilon_i^n} \leq 1, \tag{1.36}$$

with $a_i^* := \displaystyle\sum_{j \in N(i)} \left(\left(\frac{P^*}{\rho^{n+1}}\right)_{ij}^{upw} \left(\boldsymbol{Q}^* \cdot \boldsymbol{n}\right)_{ij} - \left(P_{ij}^* - P_i^*\right) \boldsymbol{n}_{ij} \cdot \mathbf{u}_i^{n+1} \right) S_{ij}^\phi.$

Proof. The proof consists in deriving a discrete kinetic energy balance. Subtracting this balance to the total energy balance (1.16) allows to obtain a discrete internal energy balance and to deduce a condition of positivity on the right hand side of the associated linear system.

- Discrete kinetic energy balance

The derivation of the kinetic energy balance in the continuous case is mimicked: we multiply the momentum equation by the velocity and use the mass balance. Multiplying the discrete momentum balance (1.15) by the velocity $\mathbf{u}_i^{n+1}$ for all Ω_i, $i \in \{1, ..., N_{cell}\}$, yields:

$$\left|\Omega_i^\phi\right| \frac{\rho_i^{n+1}\mathbf{u}_i^{n+1} - \rho_i^n \mathbf{u}_i^n}{\Delta t^n} \cdot \mathbf{u}_i^{n+1} + \sum_{j \in N(i)} (\boldsymbol{Q}^* \cdot \boldsymbol{n})_{ij} \, (\mathbf{u}_{ij}^{n+1})^{upw} \cdot \mathbf{u}_i^{n+1} S_{ij}^\phi + \sum_{j \in N(i)} \left(P_{ij}^* - P_i^*\right) \boldsymbol{n}_{ij} \cdot \mathbf{u}_i^{n+1} S_{ij}^\phi = 0. \tag{1.37}$$

Using the identity: $2\ \mathbf{u}_i^n \cdot \mathbf{u}_i^{n+1} = \left|\mathbf{u}_i^{n+1}\right|^2 + \left|\mathbf{u}_i^n\right|^2 - \left|\mathbf{u}_i^{n+1} - \mathbf{u}_i^n\right|^2$, the unsteady term of equation (1.37) reads:

$$2\left(\rho_i^{n+1}\left|\mathbf{u}_i^{n+1}\right|^2 - \rho_i^n \mathbf{u}_i^n \cdot \mathbf{u}_i^{n+1}\right) = 2\rho_i^{n+1}\left|\mathbf{u}_i^{n+1}\right|^2 - \rho_i^n \left|\mathbf{u}_i^n\right|^2 + \rho_i^n \left|\mathbf{u}_i^{n+1} - \mathbf{u}_i^n\right|^2 - \rho_i^n \left|\mathbf{u}_i^{n+1}\right|^2,$$

multiplying the mass balance (1.11) by $\frac{1}{2}\left|\mathbf{u}_i^{n+1}\right|^2$,

$$\frac{\left|\Omega_i^\phi\right|}{2\Delta t^n}\rho_i^n \left|\mathbf{u}_i^{n+1}\right|^2 = \frac{\left|\Omega_i^\phi\right|}{2\Delta t^n}\rho_i^{n+1}\left|\mathbf{u}_i^{n+1}\right|^2 + \sum_{j \in N(i)} (\boldsymbol{Q}^* \cdot \boldsymbol{n})_{ij} \frac{1}{2}\left|\mathbf{u}_i^{n+1}\right|^2 S_{ij}^\phi,$$

and substituting this relation in equation (1.37) yields:

$$\frac{\left|\Omega_i^\phi\right|}{2\Delta t^n}\left(\rho_i^{n+1}\left|\mathbf{u}_i^{n+1}\right|^2 - \rho_i^n\left|\mathbf{u}_i^n\right|^2\right) + \sum_{j \in N(i)} (\boldsymbol{Q}^* \cdot \boldsymbol{n})_{ij}\left((\mathbf{u}_{ij}^{n+1})^{upw} \cdot \mathbf{u}_i^{n+1} - \frac{1}{2}\left|\mathbf{u}_i^{n+1}\right|^2\right) S_{ij}^\phi + \frac{\left|\Omega_i^\phi\right|}{2\Delta t^n}\rho_i^n \left|\mathbf{u}_i^{n+1} - \mathbf{u}_i^n\right|^2 + \sum_{j \in N(i)} \left(P_{ij}^* - P_i^*\right) \boldsymbol{n}_{ij} \cdot \mathbf{u}_i^{n+1} S_{ij}^\phi = 0. \tag{1.38}$$

The convective flux can be rewritten for the upwind discretization (1.23) as:

$$(\boldsymbol{Q}^* \cdot \boldsymbol{n})_{ij}\left((\mathbf{u}_{ij}^{n+1})^{upw} \cdot \mathbf{u}_i^{n+1} - \frac{1}{2}\left|\mathbf{u}_i^{n+1}\right|^2\right) = (\boldsymbol{Q}^* \cdot \boldsymbol{n})_{ij}\frac{1}{2}\left|(\mathbf{u}_{ij}^{n+1})^{upw}\right|^2 - \underbrace{(1 - \lambda_{ij}^n)\,(\boldsymbol{Q}^* \cdot \boldsymbol{n})_{ij}}_{\leq 0}\frac{1}{2}\left|\mathbf{u}_i^{n+1} - \mathbf{u}_j^{n+1}\right|^2.$$

The coefficient λ_{ij}^n has been defined in section 4.2.1. Eventually substituting this latter equality in equation (1.38) yields the following discrete kinetic energy balance for all Ω_i:

$$\frac{\left|\Omega_i^\phi\right|}{2\Delta t^n}\left(\rho_i^{n+1}\left|\mathbf{u}_i^{n+1}\right|^2 - \rho_i^n\left|\mathbf{u}_i^n\right|^2\right) + \sum_{j \in N(i)} (\boldsymbol{Q}^* \cdot \boldsymbol{n})_{ij}\frac{1}{2}\left|(\mathbf{u}_{ij}^{n+1})^{upw}\right|^2 S_{ij}^\phi + \sum_{j \in N(i)} \left(P_{ij}^* - P_i^*\right) \boldsymbol{n}_{ij} \cdot \mathbf{u}_i^{n+1} S_{ij}^\phi + R_i^2 = 0, \tag{1.39}$$

with $R_i^2 = \dfrac{\left|\Omega_i^\phi\right|}{2\Delta t^n}\rho_i^n \left|\mathbf{u}_i^{n+1} - \mathbf{u}_i^n\right|^2 - \displaystyle\sum_{j\in N(i)} (1-\lambda_{ij}^n)\,(\boldsymbol{Q}^*\cdot\boldsymbol{n})_{ij}\,\frac{1}{2}\left|\mathbf{u}_i^{n+1} - \mathbf{u}_j^{n+1}\right|^2 S_{ij}^\phi \geq 0$, since $\rho_i^n > 0$ for all Ω_i.

- Discrete internal energy balance

Subtracting the discrete kinetic energy balance (1.39) to the discrete total energy balance (1.16) yields the following local discrete internal energy balance for all Ω_i:

$$\frac{\left|\Omega_i^\phi\right|}{\Delta t^n}\left(\rho_i^{n+1}\epsilon_i^{n+1} - \rho_i^n\epsilon_i^n\right) + \sum_{j\in N(i)} (\boldsymbol{Q}^*\cdot\boldsymbol{n})_{ij}\left(\epsilon_{ij}^{n+1}\right)^{upw} S_{ij}^\phi + \sum_{j\in N(i)}\left((\boldsymbol{Q}^*\cdot\boldsymbol{n})_{ij}\left(\frac{P^*}{\rho^{n+1}}\right)_{ij}^{upw} - \left(P_{ij}^* - P_i^*\right)\boldsymbol{n}_{ij}\cdot\mathbf{u}_i^{n+1}\right) S_{ij}^\phi = R_i^2. \tag{1.40}$$

The upwind discretization of the internal energy equation (1.40) infers that the associated linear system matrix is a M-matrix, *i.e.* invertible and its inverse is positive. Thus the internal energy ϵ_i^{n+1} remains positive as long as the explicit-in-time term is positive. Since $R_i^2 \geq 0$, the sufficient condition of the positivity of ϵ_i^{n+1} is for all Ω_i:

$$\frac{\left|\Omega_i^\phi\right|}{\Delta t^n}\rho_i^n\epsilon_i^n + \sum_{j\in N(i)}\left(\left(P_{ij}^* - P_i^*\right)\boldsymbol{n}_{ij}\cdot\mathbf{u}_i^{n+1} - \left(\frac{P^*}{\rho^{n+1}}\right)_{ij}^{upw}(\boldsymbol{Q}^*\cdot\boldsymbol{n})_{ij}\right) S_{ij}^\phi \geq 0,$$

which completes the proof.

Remark 5.7. *The positivity of the pressure holds under the CFL-like conditions (1.30) and (1.35): for all Ω_i, $P_i^{n+1} = \mathcal{P}(\rho_i^{n+1}, \epsilon_i^{n+1}) \geq 0$, since $\rho_i^{n+1} > 0$ under the CFL^+ condition (1.30) and $\epsilon_i^{n+1} \geq 0$ under the CFL_ϵ^+ condition (1.35).*

Remark 5.8. *if $\left|\Omega_i^\phi\right| = 0$, then $\forall\, j \in N(i)$, $S_{ij}^\phi = 0$. We thus conclude that $\rho_i^{n+1} = \rho_i^n$ and $\epsilon_i^{n+1} = \epsilon_i^n$ (and so $P_i^{n+1} = P_i^n$) for all Ω_i.*

Remark 5.9. *For the stiffened gas EOS, Property 5.3 does not apply. The inequality $\rho\epsilon - \Pi_\infty \geq 0$, equivalent to $P + \Pi_\infty \geq 0$ with $\gamma > 1$, must be verified. The change of variables is set here $\widetilde{\rho\epsilon} = \rho\epsilon - \Pi_\infty$ and $\widetilde{P} = P + \Pi_\infty$, given that $\widetilde{P} = (\gamma-1)\widetilde{\rho\epsilon}$. In this case, we may prove the following result, Property 5.4.*

Property 5.4. *[Admissible state of the internal energy for the stiffened gas EOS] Assume a stiffened gas EOS (1.2), which is such that $\rho > 0$ and $\widetilde{\rho\epsilon} = \rho\epsilon - \Pi_\infty > 0$. If the initial conditions are such that for all Ω_i, $\rho_i^n > 0$ and $\widetilde{\rho\epsilon}_i^n > 0$, then $\widetilde{\rho\epsilon}_i^{n+1}$ will remain positive for all Ω_i, provided that the time step Δt^n complies with the modified CFL_ϵ^+ condition:*

$$CFL_\epsilon^+ := (\gamma-1)\Delta t^n \max_{i\in\{1,\dots,N_{cell}\}} \frac{1}{\left|\Omega_i^\phi\right|}\frac{\tilde{a}_i^*}{\widetilde{P}_i^n} \leq 1, \tag{1.41}$$

with $\tilde{a}_i^* := \displaystyle\sum_{j\in N(i)}\left(\left(\frac{\widetilde{P}^*}{\rho^{n+1}}\right)_{ij}^{upw}(\boldsymbol{Q}^*\cdot\boldsymbol{n})_{ij} - \left(\widetilde{P}_{ij}^* - \widetilde{P}_i^*\right)\boldsymbol{n}_{ij}\cdot\mathbf{u}_i^{n+1}\right) S_{ij}^\phi.$

Proof. The proof is identical to the one of Property 5.3 thanks to the suitable change of variables (see Remark 5.9), for all Ω_i, $\widetilde{P}_i = P_i + \Pi_\infty$ and $\widetilde{\rho\epsilon}_i = \rho_i \epsilon_i - \Pi_\infty$ in the proof of Property 5.3 and thus in the discrete internal energy balance equation (1.40).

Remark 5.10. *Note that, when considering a locally constant pressure, the CFL_ϵ^+ condition (1.41) boils down to:*

$$(\gamma - 1)\Delta t^n \max_{i \in \{1,\dots,N_{cell}\}} \frac{1}{\left|\Omega_i^\phi\right|} \sum_{j \in N(i)} \frac{(\boldsymbol{Q}^* \cdot \boldsymbol{n})_{ij}}{\left(\rho_{ij}^{n+1}\right)^{upw}} S_{ij}^\phi \leq 1,$$

the CFL_ϵ^+ number (1.41) is thus approximately equal to $(\gamma-1)CFL_u$, and $(\gamma-1)$ is of the same order of magnitude as one.

6 Numerical results

6.1 Verification test cases: one-dimensional Riemann problems

6.1.1 Sod shock tube

This section is dedicated to the verification case of the basic configuration without obstacles: the so-called Sod shock tube, which is a one-dimensional Riemann problem. The computational domain is $\Omega = (-200, 200)$ and consists of a one-dimensional tube with a membrane in the middle which separates two different constant fluid states. At the time $t = 0$, the membrane bursts. The ideal gas EOS is considered with $\gamma = 1.4$ (diatomic gas). The numerical solution is compared with the exact solution, which is composed of a 1-rarefaction wave followed by a 2-contact discontinuity and a 3-shock wave. This solution is derived in [20].

All meshes used to solve this Riemann problem are uniform. The meshes contain N cells with $N = 800, 1600, 3200, 6400, 12800, 25600$ or 51200 cells. The CFL_u number, based on the material velocity u and defined by equation (1.33), is equal to 0.1.

In the sequel, the space step dx is defined in m, the density ρ in $kg.m^{-3}$, the velocity u in $m.s^{-1}$ and the pressure P in Pa.

Initial conditions are, for the left and right states:

$$\begin{cases} (\rho_L, u_L, P_L) = \left(1, 0, 10^5\right), \\ (\rho_R, u_R, P_R) = \left(0.125, 0, 10^4\right). \end{cases} \tag{1.42}$$

For a qualitative study, the profiles of density, velocity, pressure and enthalpy are presented in FIGURE 1.4 at a time $t = 0.3\ s$ such that all waves are visible in the computational domain. The exact profiles are recovered with numerical diffusion for the rarefaction, contact discontinuity and shock waves. To check the convergence order, we plot in FIGURE 1.5 the logarithm of the relative L^1 error[1] as a function of the logarithm of the mesh size N (see TABLE 1.1). The numerical rates of convergence are about 0.6 for the density, 0.9 for the velocity and the pressure, and slightly more than 0.5 for the enthalpy (see TABLE 1.2). Theoretically the convergence order is 1 for a rarefaction wave and shock wave, and $\frac{1}{2}$ for a contact discontinuity. This verification shows the ability of the fractional step scheme to correctly capture discontinuous solutions.

dx	N	ρ	u	P	h
5.0e-1	800	8.497e-3	9.778e-3	5.308e-3	9.099e-3
2.5e-1	1600	5.427e-3	5.627e-3	3.010e-3	6.180e-3
1.25e-1	3200	3.472e-3	3.078e-3	1.679e-3	4.169e-3
6.25e-2	6400	2.237e-3	1.668e-3	9.272e-4	2.831e-3
3.125e-2	12800	1.456e-3	9.269e-3	5.095e-4	1.943e-3
1.5625e-2	25600	9.571e-4	5.070e-4	2.780e-4	1.342e-3
7.8125e-3	51200	6.354e-4	2.660e-4	1.496e-4	9.273e-4

TABLE 1.1 – L^1 *error for variables* (ρ, u, P, h) *for all the considered meshes for the Sod shock-tube.*

6.1.2 Riemann problem with a stiffened gas EOS

This verification test case is a one-dimensional Riemann problem with a stiffened gas EOS. The stiffened gas parameters are computed for a liquid water at a 165 *bar* pressure and 583.15 K

[1] The discrete relative L^1 error is defined as: $e_{L^1(\Omega)}(\varphi) = \frac{\sum_{i=1}^{N_{cell}} \left|\varphi_i^{exact} - \varphi_i^{computed}\right| |\Omega_i|}{\sum_{i=1}^{N_{cell}} \left|\varphi_i^{exact}\right| |\Omega_i|}$.

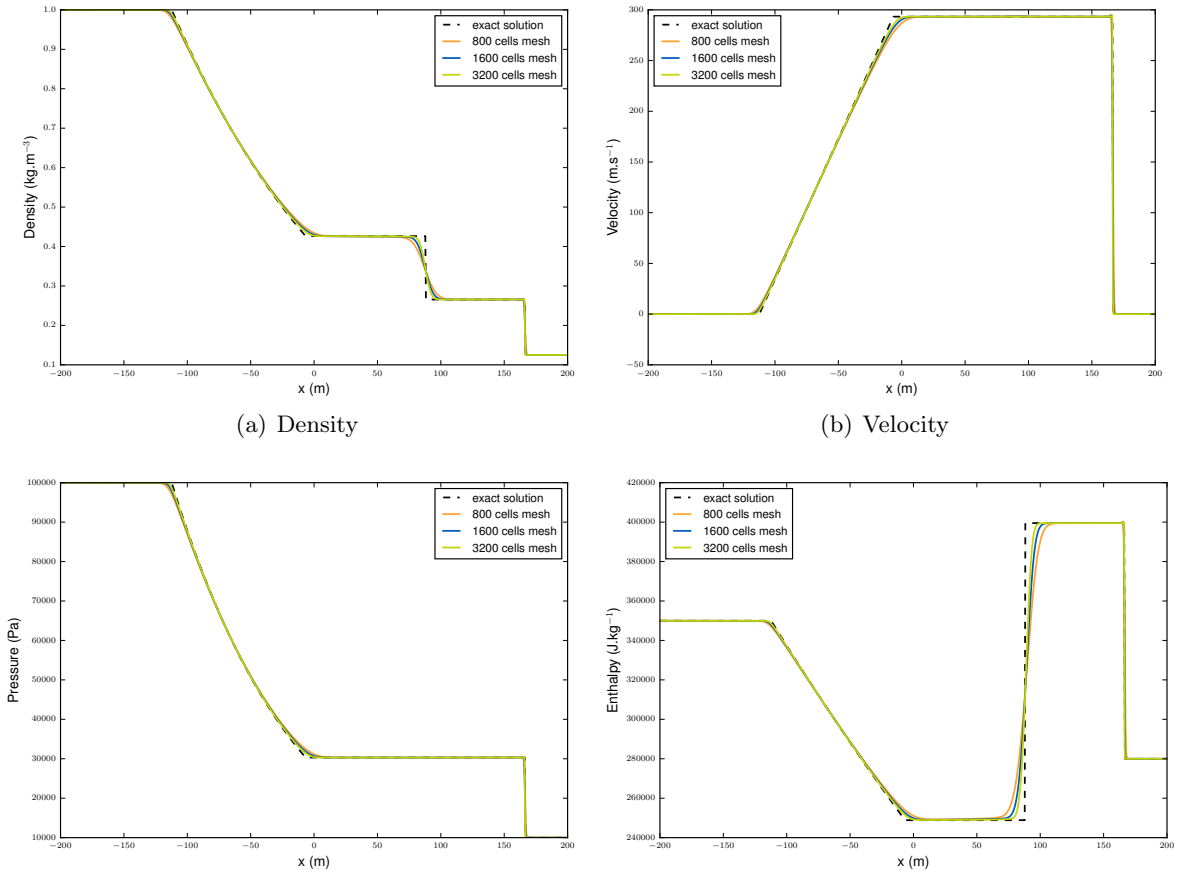

(a) Density (b) Velocity

(c) Pressure (d) Enthalpy

FIGURE 1.4 – *Comparison of the numerical solutions for 800, 1600 and 3200 cells with the exact solution for the Sod shock-tube at* $t = 0.3$ *s.*

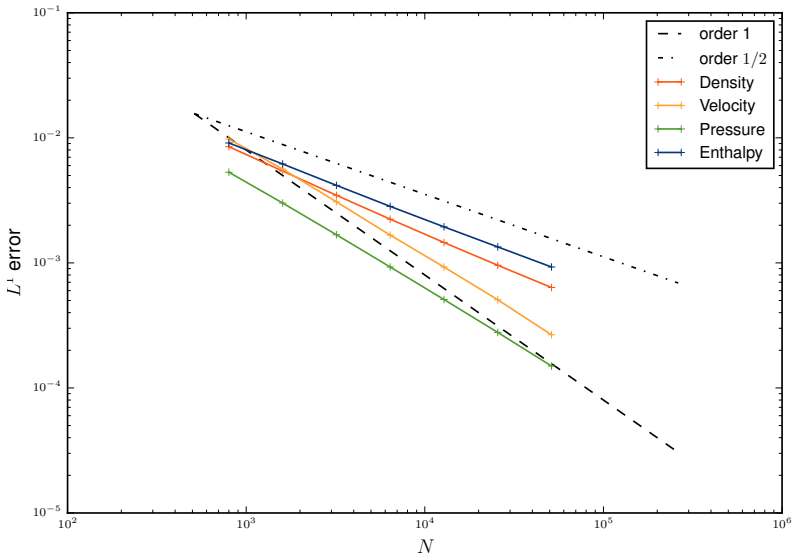

FIGURE 1.5 – L^1 *convergence curves for the Sod shock-tube.*

dx	N	ρ cnv. order	u cnv. order	P cnv. order	h cnv. order
5.0e-1	800				
2.5e-1	1600	0.6467	0.7972	0.8185	0.5582
1.25e-1	3200	0.6444	0.8703	0.8436	0.5679
6.25e-2	6400	0.6341	0.8839	0.8562	0.5586
3.125e-2	12800	0.6196	0.8477	0.8638	0.5429
1.5625e-2	25600	0.6054	0.8703	0.8743	0.5337
7.8125e-3	51200	0.5910	0.9306	0.8940	0.5334

TABLE 1.2 – L^1 *convergence order for variables* (ρ, u, P, h) *for all the considered meshes for the Sod shock-tube.*

temperature: $\gamma_{SG} = 1.85768$ and $\Pi_\infty = 4.243468 \times 10^8$ Pa. Initial conditions are, for the left and right states:

$$\begin{cases} (\rho_L, u_L, P_L) = \left(800, 0, 1.65 \times 10^7\right), \\ (\rho_R, u_R, P_R) = \left(797, 6.827, 5.0 \times 10^6\right). \end{cases} \tag{1.43}$$

This test case corresponds to a low Mach number flow. The Mach number is such that: $M = \frac{|u|}{c} \in \left[0, 10^{-2}\right]$. The exact solution is composed of a 1-rarefaction wave followed by a 2-contact discontinuity and a 3-shock wave. The uniform meshes contain $N = 800$, 1600, 3200, 6400, 12800, 25600 and 51200 cells. For the first test, CFL_u is equal to 0.0084, *i.e.* $CFL^+ = 0.015$ (CFL^+ defined by equation (1.31)). The second test is run with CFL_u equal to 0.54 ($CFL^+ = 1$). The simulation ending time is 0.1 s. As expected, the numerical simulation matches the exact profile with numerical diffusion at discontinuities (see FIGURE 1.6 and TABLE 1.3). The greater is the CFL_u value, the greater is the diffusion, excepted for the contact discontinuity profile which maintains sharp (see FIGURE 1.8 and TABLE 1.5). In accordance with the theory for a stiffened gas EOS, we note that the L^1 convergence order is $\frac{1}{2}$ for all waves (see TABLE 1.4, 1.6 and FIGURE 1.7, 1.9).

The semi-implicit pressure correction scheme allows to release the explicit stability constraint due to the acoustic waves and thus to increase the CFL_u value.

Test case 1 with $CFL^+ = 0.015$

dx	N	ρ	u	P	h
5.0e-01	800	1.927e-04	2.546e-02	1.534e-02	1.684e-04
2.5e-01	1600	1.352e-04	1.786e-02	1.073e-02	1.182e-04
1.25e-01	3200	9.449e-05	1.244e-02	7.477e-03	8.260e-05
6.25e-02	6400	6.570e-05	8.634e-03	5.189e-03	5.744e-05
3.125e-02	12800	4.534e-05	5.943e-03	3.571e-03	3.965e-05
1.5625e-02	25600	3.100e-05	4.049e-03	2.433e-03	2.712e-05
7.8125e-03	51200	2.093e-05	2.722e-03	1.635e-03	1.832e-05

TABLE 1.3 – L^1 *error for variables* (ρ, u, P, h) *for all the considered meshes for a Riemann problem with a SG EOS* ($CFL^+ = 0.015$).

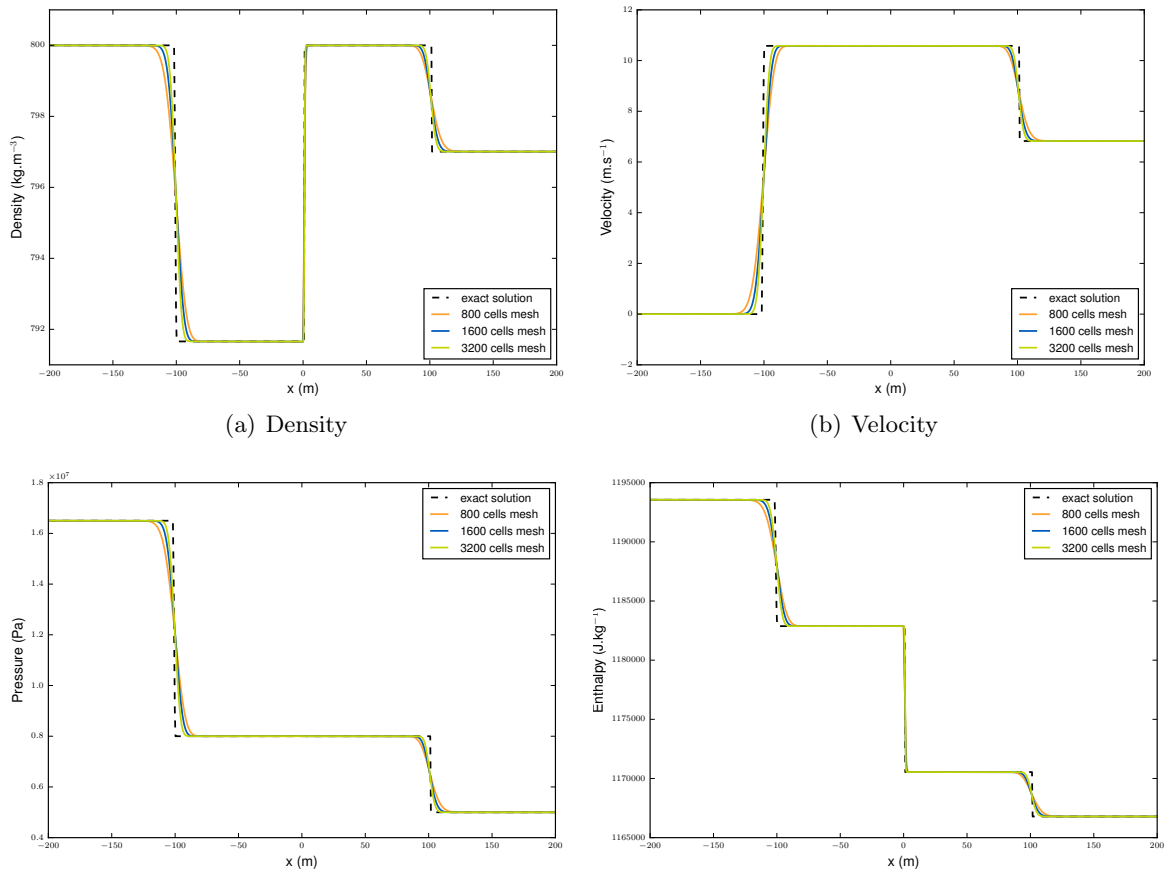

(a) Density (b) Velocity

(c) Pressure (d) Enthalpy

FIGURE 1.6 – *Comparison of the numerical solutions for 800, 1600 and 3200 cells with the exact solution for a Riemann problem with a SG EOS at* $t = 0.1$ *s* $(CFL^+ = 0.015)$.

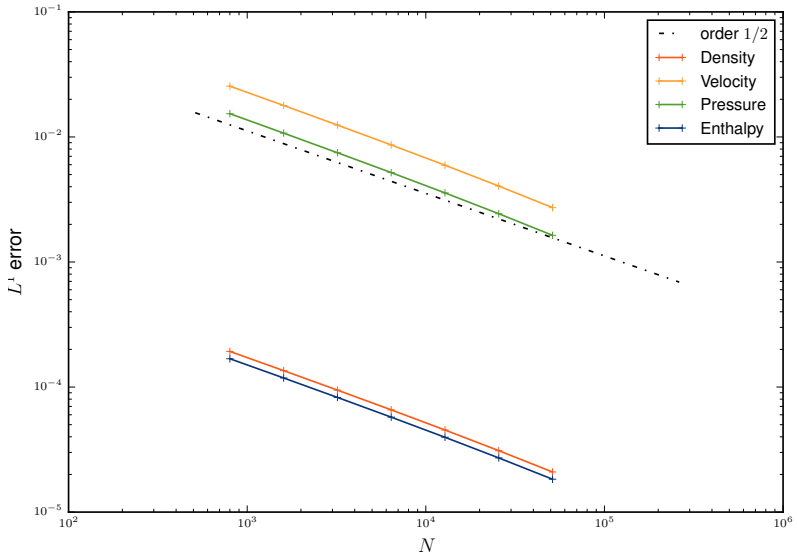

FIGURE 1.7 – L^1 *convergence curves for a Riemann problem with a SG EOS* $(CFL^+ = 0.015)$.

dx	N	ρ cnv. order	u cnv. order	P cnv. order	h cnv. order
5.0e-1	800				
2.5e-1	1600	0.5110	0.5120	0.5157	0.5107
1.25e-1	3200	0.5171	0.5209	0.5211	0.5168
6.25e-2	6400	0.5243	0.5274	0.5270	0.5240
3.125e-2	12800	0.5353	0.5389	0.5392	0.5349
1.5625e-2	25600	0.5486	0.5535	0.5536	0.5480
7.8125e-3	51200	0.5665	0.5731	0.5733	0.5658

TABLE 1.4 – *L^1 convergence order for variables (ρ, u, P, h) for all the considered meshes for a Riemann problem with a SG EOS ($CFL^+ = 0.015$).*

Test case 2 with $CFL^+ = 1$

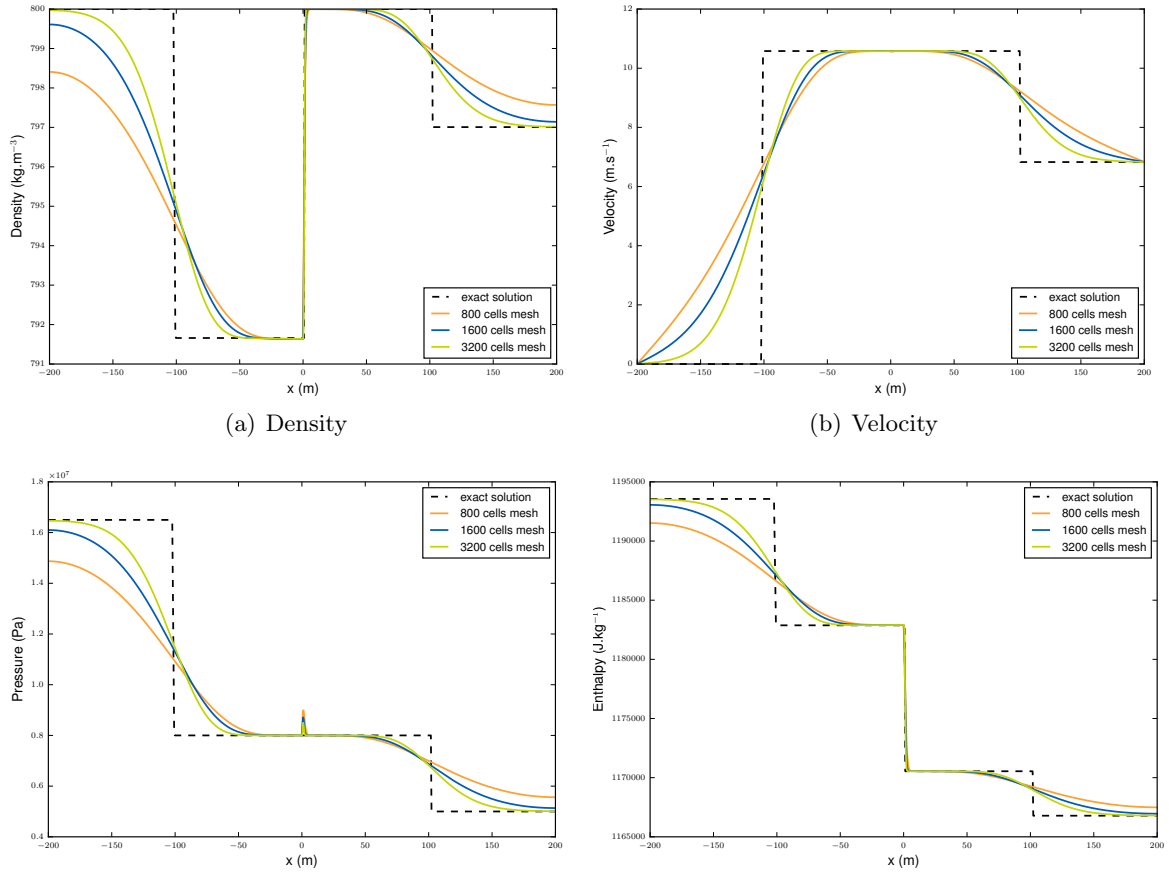

(a) Density (b) Velocity

(c) Pressure (d) Enthalpy

FIGURE 1.8 – *Comparison of the numerical solutions for 800, 1600 and 3200 cells with the exact solution for a Riemann problem with a SG EOS at $t = 0.1$ s ($CFL^+ = 1$).*

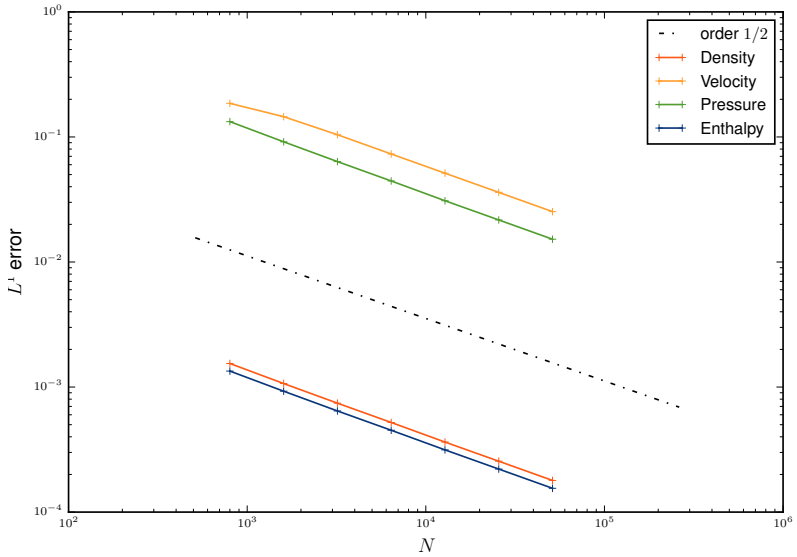

FIGURE 1.9 – L^1 *convergence curves for a Riemann problem with a SG EOS* ($CFL^+ = 1$).

dx	N	ρ	u	P	h
5.0e-1	800	1.543e-03	1.857e-01	1.326e-01	1.342e-03
2.5e-1	1600	1.067e-03	1.453e-01	9.145e-02	9.263e-04
1.25e-1	3200	7.431e-04	1.042e-01	6.355e-02	6.440e-04
6.25e-2	6400	5.208e-04	7.307e-02	4.447e-02	4.512e-04
3.125e-2	12800	3.631e-04	5.132e-02	3.090e-02	3.144e-04
1.5625e-2	25600	2.552e-04	3.604e-02	2.169e-02	2.209e-04
7.8125e-3	51200	1.791e-04	2.528e-02	1.521e-02	1.550e-04

TABLE 1.5 – L^1 *error for variables* (ρ, u, P, h) *for all the considered meshes for a Riemann problem with a SG EOS* ($CFL^+ = 1$).

dx	N	ρ cnv. order	u cnv. order	P cnv. order	h cnv. order
5.0e-1	800				
2.5e-1	1600	0.5327	0.3542	0.5364	0.5343
1.25e-1	3200	0.5214	0.4797	0.5250	0.5245
6.25e-2	6400	0.5129	0.5116	0.5149	0.5132
3.125e-2	12800	0.5202	0.5097	0.5253	0.5211
1.5625e-2	25600	0.5089	0.5010	0.5103	0.5094
7.8125e-3	51200	0.5108	0.5115	0.5118	0.5111

TABLE 1.6 – L^1 *convergence order for variables* (ρ, u, P, h) *for all the considered meshes for a Riemann problem with a SG EOS* ($CFL^+ = 1$).

6.2 Verification test case: one-dimensional shock tube interaction with a wall

The aim here is to simulate the interaction between a shock wave generated by a subsonic shock tube experiment and a wall. The shock tube experiment has been presented in the previous

section 6.1. In this second test case, the computational domain contains a wall boundary on the right located at $x = x_1$; here, a wall boundary condition is applied. The 3-shock wave is reflected by the wall, and then the reflected shock interacts with the 2-contact discontinuity at time t_1 in $x = x^* = x_1 - \sigma_3(t_1 - t_0) = x_0 + u_1 t_1$, where t_0 denotes the time when the initial 3-shock wave hits the wall and u_1 and σ_3 the celerity of the contact discontinuity and the reflected shock wave respectively. The computed configurations are:

- the interaction of the initial shock wave with the wall,
- the interaction of the initial contact discontinuity with the reflected shock wave.

The localisation of the different constant fluid states is given in FIGURE 1.10. The state (3) is created by the shock wave reflection on the wall and the states (4) and (5) are created by the interaction of the contact discontinuity (1) and the reflected shock (3).

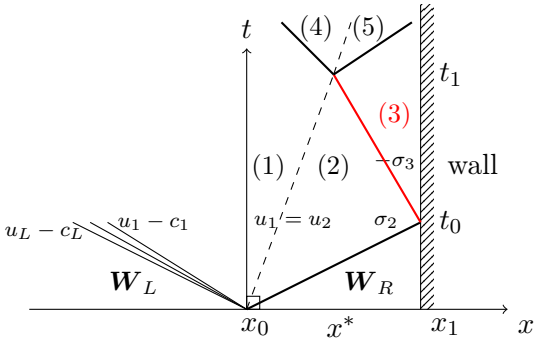

FIGURE 1.10 – *Wave interactions with the wall (subsonic case: $u_1 - c_1 < 0$).*

1.D presents the calculation of the analytic solution (hence computing exact values for $\boldsymbol{W}_3$, $\boldsymbol{W}_4$ and $\boldsymbol{W}_5$) based on an exact solving of two distinct Riemann problems. In the following section, the numerical solution is compared with this analytic solution in order to check the numerical scheme error and to investigate convergence rates.

6.2.1 Shock wave reflection on a wall with an ideal gas EOS

The computational domain is initialized with the Sod shock-tube configuration. The membrane between initial left and right states is located at $x_0 = 50\ m$. Initial conditions are:

$$\begin{cases} (\rho_L, u_L, P_L) = \left(1, 0, 10^5\right) \\ (\rho_R, u_R, P_R) = \left(0.125, 0, 10^4\right) \end{cases} \tag{1.44}$$

and: $P = (\gamma - 1)\,\rho\epsilon$, with $\gamma = \frac{7}{5}$.
The convergence study is performed with Cartesian regular meshes. The mesh contains N cells with $N = 800$, 1600, 3200, 6400, 12800, 25600 or 51200. The material CFL_u number is equal to 1.

The computation final time is 0.35 s such that the reflected shock wave has been generated by the wall. The different numerical profiles are in good agreement with the exact solution (dark dashed line) see FIGURE 1.11. The L^1 convergence orders are recovered: close to $\frac{1}{2}$ for the density, and 1 for the pressure and velocity (see FIGURE 1.12 and TABLE 1.8). For $N = 12800$, the numerical wall pressure after the reflection on the wall is $P_{wall}^{num} = 78037.840\ Pa$ to be compared with the theoretical value $P_{wall}^{exact} = 78038.054\ Pa$ (arising from 1.D). The relative error is 2.7×10^{-6}.

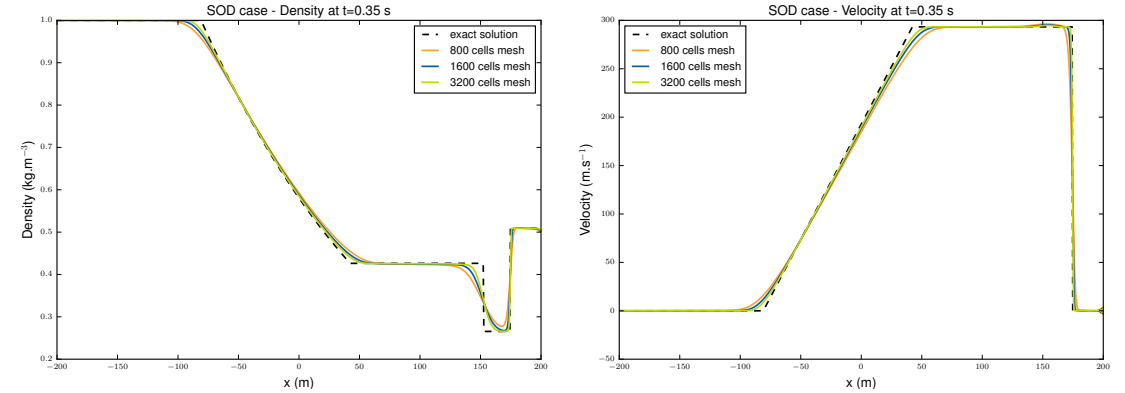

(a) Density

(b) Velocity

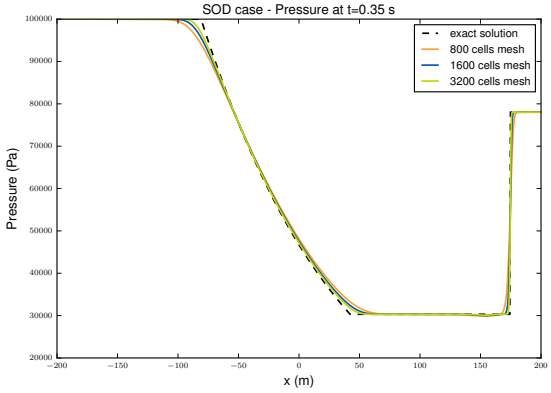

(c) Pressure

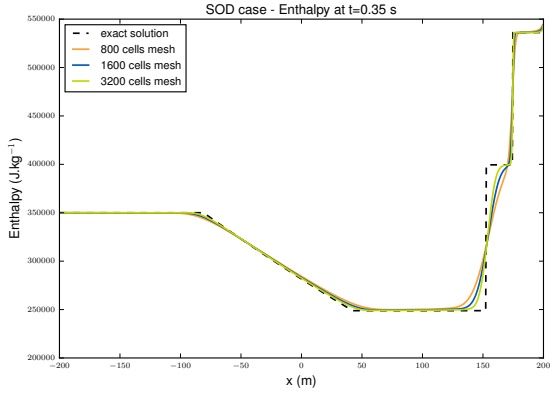

(d) Enthalpy

FIGURE 1.11 – *Comparison of the numerical solutions for 800, 1600 and 3200 cells with the exact solution of the Sod shock-tube reflection case at* $t = 0.35$ *s.*

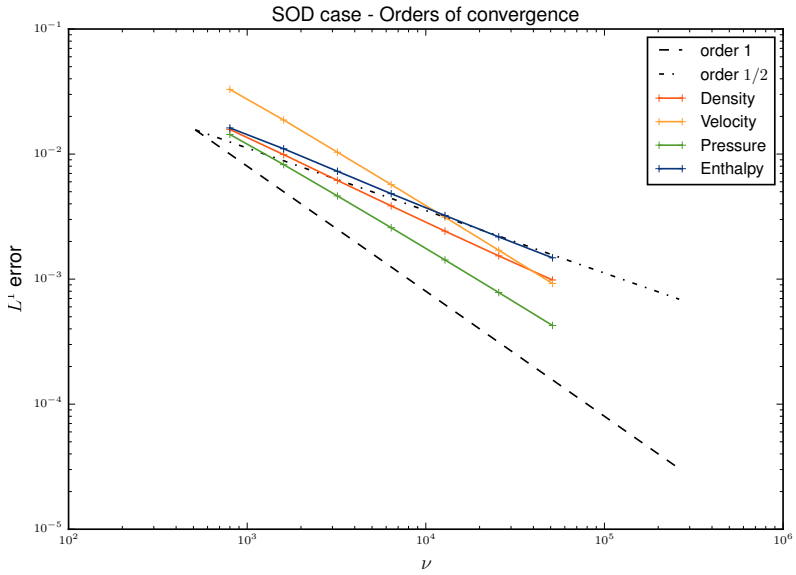

FIGURE 1.12 – L^1 *convergence curves of the Sod shock-tube reflection case.*

dx	N	ρ	u	P	h
5.0e-1	800	1.573e-2	3.290e-2	1.435e-2	1.619e-2
2.5e-1	1600	9.900e-3	1.872e-2	8.239e-3	1.1023e-2
1.25e-1	3200	6.155e-3	1.034e-2	4.625e-3	7.284e-3
6.25e-2	6400	3.849e-3	5.702e-3	2.577e-3	4.821e-3
3.125e-2	12800	2.419e-3	3.125e-3	1.424e-3	3.227e-3
1.5625e-2	25600	1.534e-3	1.702e-3	7.810e-4	2.175e-3
7.8125e-3	51200	9.839e-4	9.223e-4	4.257e-4	1.480e-3

TABLE 1.7 – L^1 *error for variables* (ρ, u, P, h) *for all considered meshes of the Sod shock-tube reflection case.*

dx	N	ρ cnv. order	u cnv. order	P cnv. order	h cnv. order
5.0e-1	800				
2.5e-1	1600	0.6684	0.8133	0.8009	0.5541
1.25e-1	3200	0.6857	0.8560	0.8331	0.5978
6.25e-2	6400	0.6771	0.8591	0.8435	0.5954
3.125e-2	12800	0.6701	0.8674	0.8560	0.5791
1.5625e-2	25600	0.6568	0.8764	0.8664	0.5694
7.8125e-3	51200	0.6411	0.8842	0.8756	0.5550

TABLE 1.8 – L^1 *convergence order for variables* (ρ, u, P, h) *for all considered meshes of the Sod shock-tube reflection case.*

6.2.2 Interaction of the initial contact discontinuity with the reflected shock wave for an ideal gas EOS

The computational domain is still initialized with the Sod shock-tube configuration.

But now, the computation final time is 0.42 s such that the reflected shock wave has interacted with the initial contact discontinuity. Numerical diffusion affects obtained profiles, but these latter are in quite good agreement with the exact solution (dark dashed line), see FIGURE 1.13 and TABLE 1.9. The L^1 convergence orders are close to 0.5 for the density, and close to 0.6 for the pressure and the velocity (see FIGURE 1.14 and TABLE 1.10). For $N = 12800$, the numerical wall pressure is $P_{wall}^{num} = 78038.0843\ Pa$ to be compared with the theoretical value $P_{wall}^{exact} = 78038.3071\ Pa$ (arising from 1.D). The relative error is 2.9×10^{-6}.

dx	N	ρ	u	P	h
5.0e-1	800	5.143e-02	5.508e-02	3.673e-02	3.938e-02
2.5e-1	1600	3.680e-02	3.631e-02	2.332e-02	2.774e-02
1.25e-1	3200	2.562e-02	2.294e-02	1.468e-02	1.906e-02
6.25e-2	6400	1.781e-02	1.495e-02	9.649e-03	1.322e-02
3.125e-2	12800	1.209e-02	9.426e-03	6.181e-03	9.107e-03
1.5625e-2	25600	8.247e-03	6.062e-03	4.003e-03	6.290e-03
7.8125e-3	51200	5.569e-03	3.766e-03	2.507e-03	4.320e-03

TABLE 1.9 – L^1 *error for variables* (ρ, u, P, h) *for all the considered meshes for the Sod shock-tube interaction case.*

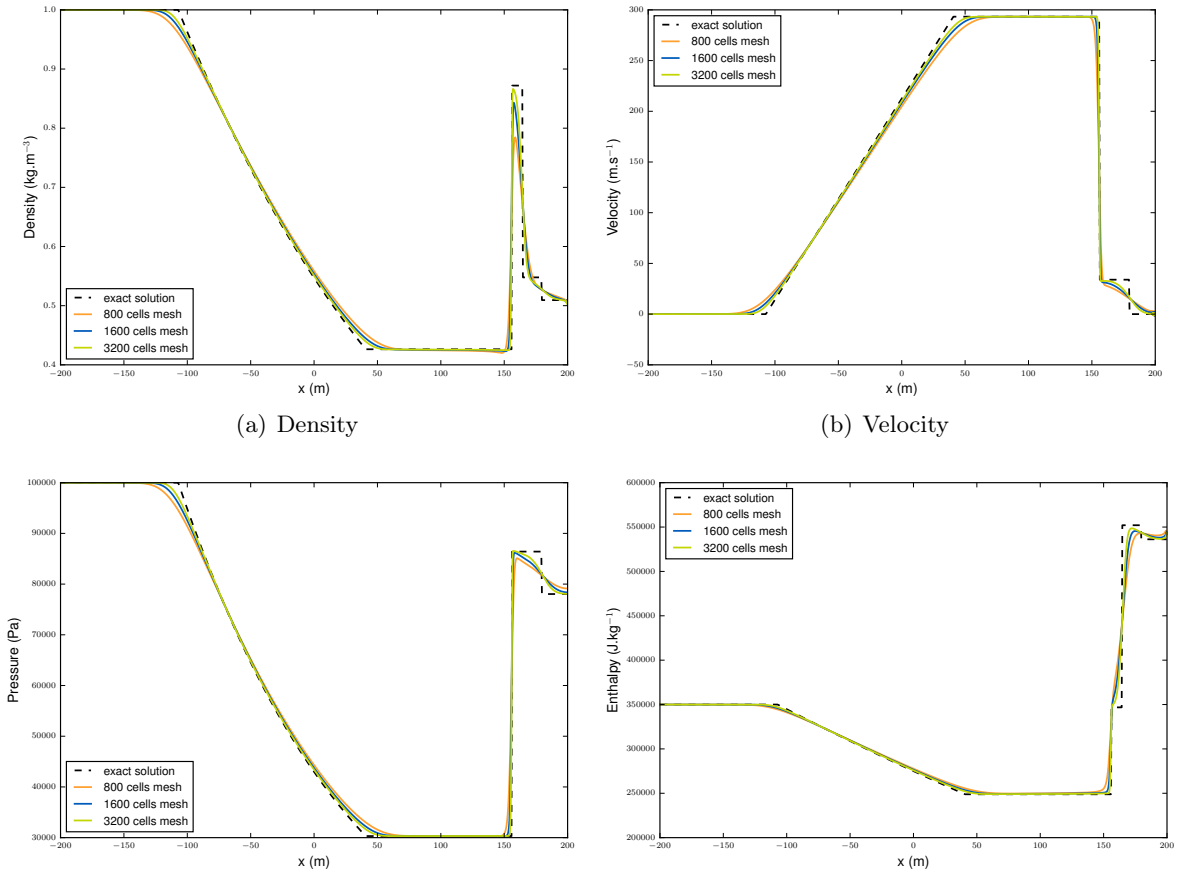

(a) Density (b) Velocity

(c) Pressure (d) Enthalpy

FIGURE 1.13 – *Comparison of the numerical solutions for 800, 1600 and 3200 cells with the exact solution for the Sod shock-tube interaction case at* $t = 0.42$ *s.*

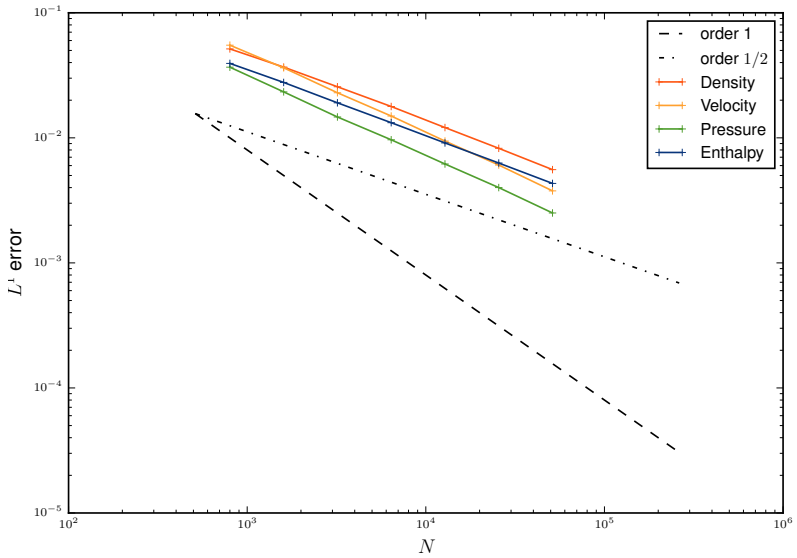

FIGURE 1.14 – L^1 *convergence curves of for Sod shock-tube interaction case.*

dx	N	ρ cnv. order	u cnv. order	P cnv. order	h cnv. order
5.0e-1	800				
2.5e-1	1600	0.4829	0.6012	0.6557	0.5056
1.25e-1	3200	0.5226	0.6626	0.6671	0.5411
6.25e-2	6400	0.5244	0.6182	0.6057	0.5281
3.125e-2	12800	0.5594	0.6649	0.6427	0.5377
1.5625e-2	25600	0.5516	0.6368	0.6269	0.5338
7.8125e-3	51200	0.5663	0.6868	0.6748	0.5419

TABLE 1.10 – L^1 *convergence order for variables* (ρ, u, P, h) *for all the considered meshes for the Sod shock-tube interaction case.*

6.2.3 Shock wave reflection on a wall for a stiffened gas EOS

The verification test case is still a shock tube experiment that interacts with a wall, now considering a stiffened gas EOS. The stiffened gas parameters are:

$$\gamma_{SG} = 5 \quad \text{and} \quad \Pi_\infty = 1.345951 \times 10^8 \ Pa.$$

The membrane is located at $x_0 = 50\ m$. Initial conditions are:

$$\begin{cases} (\rho_L, u_L, P_L) = \left(762.8, 0, 1.65 \times 10^7\right), \\ (\rho_R, u_R, P_R) = \left(762.8, 0, 1.55 \times 10^7\right). \end{cases} \tag{1.45}$$

This test case corresponds to a low Mach number flow. Indeed the Mach number varies from 0 to 10^{-3}. The convergence study is performed with the same uniform meshes. CFL_u is equal to 0.005 (*i.e.* $CFL_{u+c} \approx 5$). The CFL_u value is chosen small enough to capture accurately the shock wave profile. The computation final time is 0.21 s such that the reflected shock wave has been generated by interaction with the wall. The field values of the shock after the wall reflection fit the exact solution (see FIGURE 1.15 and TABLE 1.11). The expected L^1 convergence orders are recovered: approximately 0.5 for the density, the pressure and the velocity (see FIGURE 1.16 and TABLE 1.12). For $N = 12800$ cells, the numerical wall pressure after the reflection on the wall is $P_{wall}^{num} = 16500348\ Pa$ to be compared with the theoretical value $P_{wall}^{exact} = 16500335\ Pa$ (arising from 1.D). The relative error is 7.8×10^{-7}.

dx	N	ρ	u	P	h
5.0e-1	800	5.401e-05	1.059e-01	2.504e-03	2.147e-04
2.5e-1	1600	3.857e-05	7.607e-02	1.776e-03	1.525e-04
1.25e-1	3200	2.714e-05	5.377e-02	1.253e-03	1.076e-04
6.25e-2	6400	1.915e-05	3.793e-02	8.840e-04	7.589e-05
3.125e-2	12800	1.351e-05	2.673e-02	6.230e-04	5.350e-05
1.5625e-2	25600	9.501e-06	1.880e-02	4.382e-04	3.763e-05
7.8125e-3	51200	6.668e-06	1.319e-02	3.075e-04	2.641e-05

TABLE 1.11 – L^1 *error for variables* (ρ, u, P, h) *for all considered meshes for the shock-tube reflection case with a SG EOS.*

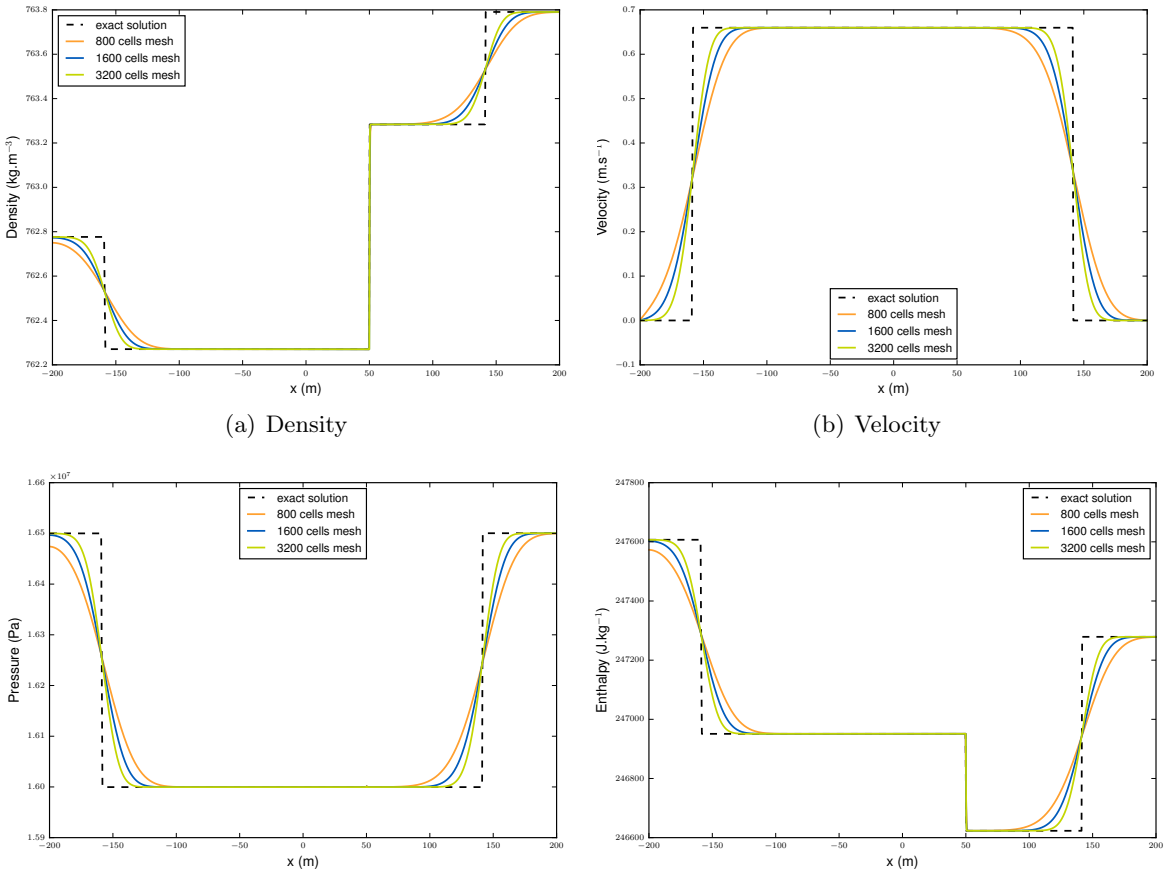

(a) Density (b) Velocity

(c) Pressure (d) Enthalpy

FIGURE 1.15 – *Comparison of the numerical solutions for 800, 1600 and 3200 cells with the exact solution for the shock-tube reflection case with a SG EOS at* $t = 0.21$ *s.*

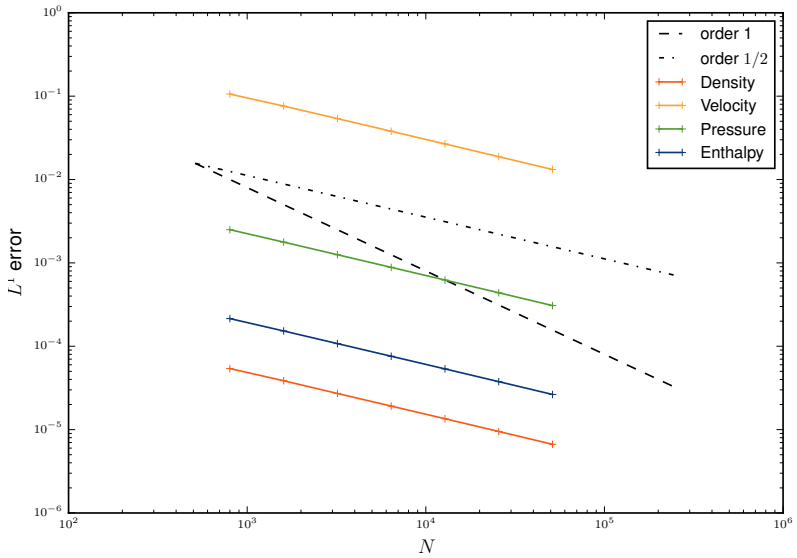

FIGURE 1.16 – L^1 *convergence curves for the shock-tube reflection case with a SG EOS.*

dx	N	ρ cnv. order	u cnv. order	P cnv. order	h cnv. order
5.0e-1	800				
2.5e-1	1600	0.4855	0.4778	0.4958	0.4934
1.25e-1	3200	0.5073	0.5006	0.5025	0.5037
6.25e-2	6400	0.5028	0.5034	0.5037	0.5034
3.125e-2	12800	0.5040	0.5049	0.5047	0.5045
1.5625e-2	25600	0.5075	0.5078	0.5078	0.5077
7.8125e-3	51200	0.5107	0.5110	0.5110	0.5109

TABLE 1.12 – L^1 *convergence order for variables* (ρ, u, P, h) *for all considered meshes for the shock-tube reflection case with a SG EOS.*

6.3 Integral formulation validation test case

EDF R&D has set up research programmes in order to investigate accidental situations in a major context of nuclear safety and security expertise for PWR (Pressurized Water Reactor) conditions, including RIA (Reactivity Initiated Accident) [48].

The aim of the current test case is to assess the integral formulation with obstacles, while mimicking the RIA situation. Thus, the numerical test case consists in simulating a fluid flow induced by the fuel during a RIA fast transient, where a shock wave impacts a fuel assembly, gathering a few rods. Actually, the desired physical quantity is the resultant pressure force on fuel rods in order to evaluate the mechanical properties of the rod cladding. Both the CFD fluid approach, where the mesh perfectly matches the rods, and the new integral approach, where fluid cells are obstructed by the rods, are used in this study. Results are thus compared to validate the integral approach. The CFD study provides the reference values.

6.3.1 Case description

The numerical test consists in a shock wave impacting rigid obstacles. The compressible fluid is assumed to be inviscid, and the flow is unsteady. The two-dimensional computational domain Ω is a large tube with a membrane in the middle which separates two discontinuous constant fluid states $\boldsymbol{W}_L$ and $\boldsymbol{W}_R$ initially at rest. Both tube ends are closed by walls. Symmetry boundary conditions are imposed at the top and the bottom of the computational domain to enforce a periodic condition in the y-direction. An obstructed area composed of four solid rods is set on the right of the shock tube membrane. A sketch of the test case is displayed in FIGURE 1.17. The obstacles are squares of 1 *cm* edge. We perform several computations with Cartesian meshes:

- The reference $2D$ CFD computation using a fine fluid mesh including 87 millions of square cells, such that 2000 cells mesh the height h of the tube (see FIGURE 1.17).

- The integral formulation computations using coarse porous meshes with square cells. N_h cells mesh the height h of the tube: $N_h = \mathbf{1}$, 2, 3, 4, 5 or 6. Thus the obstructed pattern of size $h \times L/8$ is meshed with $3.5 \times N_h^2$ square cells (see FIGURE 1.17). The total number of cells in Ω is: $N_{cell} = 8 \times 3.5 \times N_h^2$.

The first mesh size ($N_h = \mathbf{1}$) is representative of the one used for a "component" computation with THYC or FLICA-4 codes for instance. Unlike with the CFD computation where the solid boundary is explicitly meshed (a wall boundary condition is enforced on the obstacle surface), the obstacles with the integral approach are included or partially included in the cells. The simulation is performed with a stiffened gas EOS modelling the liquid water thermodynamic in

the PWR core. The stiffened gas parameters are:

$$\gamma_{SG} = 1.66512803 \quad \text{and} \quad \Pi_\infty = 3.7258761468 \times 10^8 Pa.$$

Initial conditions are, for left and right states:

$$\begin{cases} (\rho_L, u_L, P_L) = \left(713.187, 0, 200 \times 10^5\right), \\ (\rho_R, u_R, P_R) = \left(729.614, 0, 155 \times 10^5\right). \end{cases} \tag{1.46}$$

CFL^+ is equal to 0.006 (*i.e.* $CFL_{u+c} \approx 1$). The CFL^+ value is chosen small enough to capture accurately shock and rarefaction waves. The final time is 0.17 ms. Hence the fast waves (rarefaction and shock waves) do not hit the left and right wall boundaries. The CFD unsteady pressure field is plotted in FIGURE 1.18.

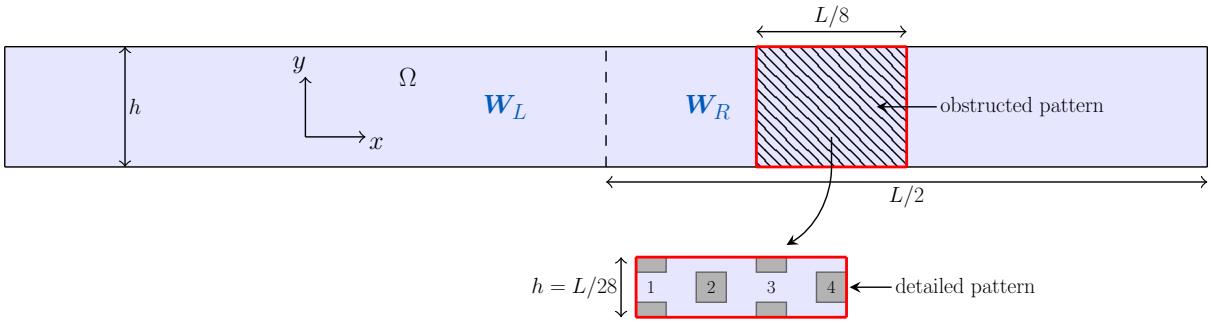

FIGURE 1.17 – *Sketch of the Ω domain of size $h \times L$ obstructed by four internal solid rods (in grey) and periodic in the y-direction. The pressure shock wave propagates from the middle of the domain towards the right end.*

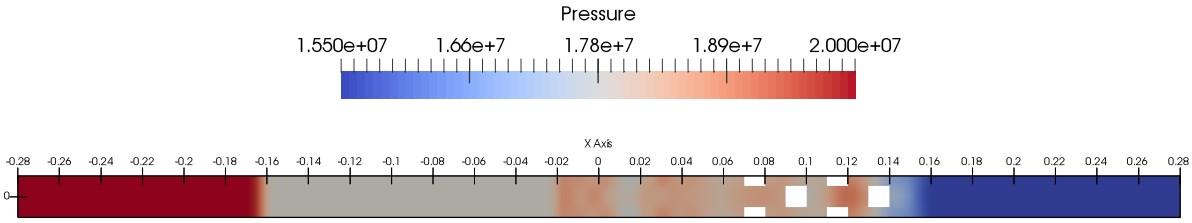

FIGURE 1.18 – *Pressure field obtained with the local CFD approach (870 000 cells), $t_{final} =$ 0.17 ms.*

Note that explicit-in-time schemes, such as the one described in [41] would lower computational cost results for the same level of accuracy in this case, where the acoustic CFL_{u+c} number is close to one, in order to be accurate on pressure loads associated with fast waves. However this test case validates the ability of the semi-implicit algorithm to deal with unsteady situations involving sharp genuinely non-linear shocks.

6.3.2 Numerical results

In order to validate the integral approach for the fluid variables, the unsteady profiles of the density, the x-velocity component and the pressure, for the coarse mesh integral approach computations, are compared, at $t_{final} = 0.17$ ms, with the local CFD profiles in FIGURE 1.19. These one-dimensional profiles, along the x-direction, are obtained as a volume-average of the

fluid fields in the y-direction. We retrieve the plateau values for the pressure, the velocity and the density for $x \in [-0.15, -0.05]$. These values are exactly those obtained when solving the one-dimensional Riemann problem associated with the current initial conditions (1.46). The profiles in the obstructed area, for $x \in [0.07, 0.14]$, give satisfactory profiles for the fluid variables, when compared with the CFD reference.

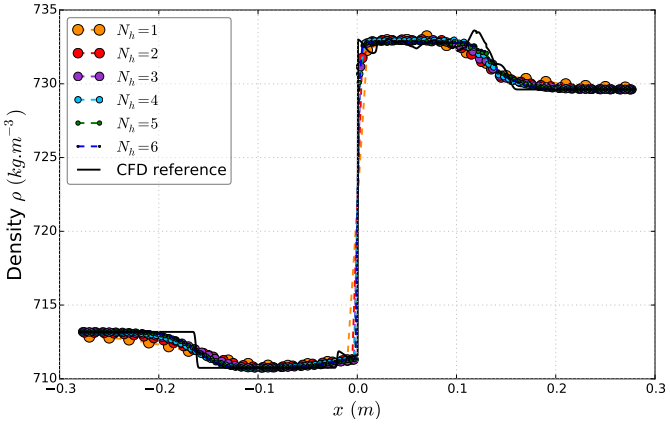

(a) Density

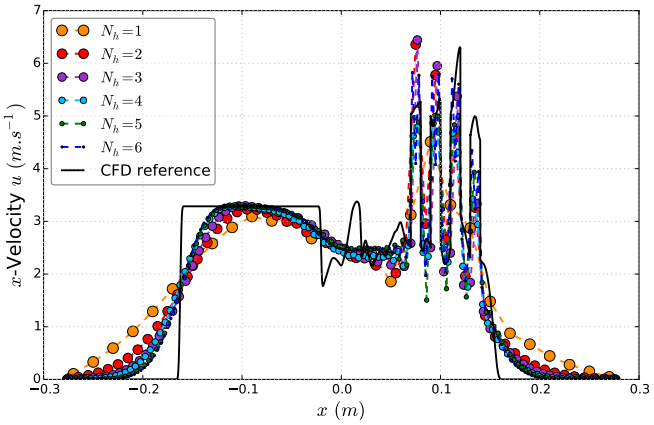

(b) x-Velocity

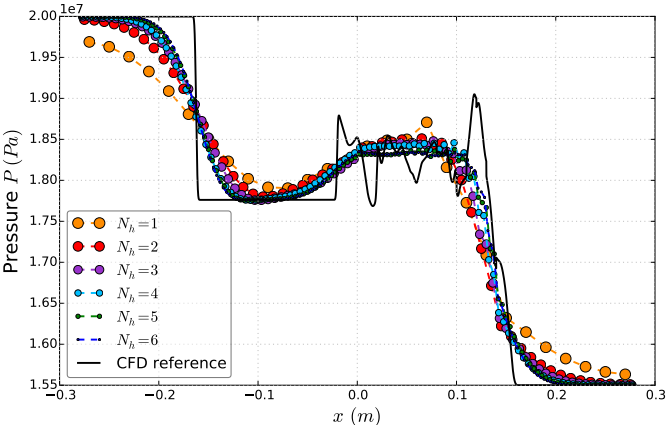

(c) Pressure

FIGURE 1.19 – *Fluid fields, at t_{final} = 0.17 ms, averaged in the y-direction using the* ***integral*** *approach with different* ***coarse*** *meshes – comparison with the CFD reference (black line).*

In order to compare the integral approach and the local approach on the quantity of interest, the pressure force exerted by the pressure shock wave on the surface of the four rods is computed from the numerical simulations with both the integral approach and the CFD reference simulation. FIGURE 1.20 presents a mesh refinement study for the pressure force using several meshes ($N_{cell} = 87 \times 10^4$, 3.48×10^6, 13.92×10^6 or 87×10^6). The maximal relative difference between the finest and the coarsest CFD mesh is 14%. The finest CFD computation with $N_{cell} = 87 \times 10^6$ is the reference.

The x-component of the pressure force $F_x(t)$ is defined as:

$$F_x(t) = \left(\int_{\Gamma^w} P(\boldsymbol{x}, t)\ \boldsymbol{n} \mathrm{d}\gamma \right) \cdot \boldsymbol{e}_x,$$

where for the integral approach $P(\boldsymbol{x}, t^n)|_{\Gamma^w}$ is equal to P_i^n for all wall interfaces in the cell Ω_i, according to the 0^{th}-order approximation (1.24). For each mesh, the pressure force as a function of time $F_x(t)$ is plotted in FIGURE 1.21; in addition the time integral of the force, called impulsion, as a function of time is given in FIGURE 1.22. The impulsion is defined as:

$$J_x(t) = \int_0^t F_x(\tau) d\tau.$$

The results reveal that:

- For all computations, the maximal resultant force with the integral approach is underestimated for the rods 1, 2, 3, 4 and their sum, when compared with the CFD reference; however the resultant force with the integral approach has the same order of magnitude as the one with the CFD reference. Note that the maximal value of the sum of the forces exerted on the rods is less underestimated than the one exerted rod by rod, see FIGURE 1.21. Besides, we observe that the convergence towards the CFD reference computation is not monotonous for coarse porous meshes.

- The impulsion approximation on the coarse meshes is slightly overestimated for all computations when compared with the CFD reference, see FIGURE 1.22.

- As expected, FIGURE 1.23 shows that the integral approach converges towards the CFD approach when refining the mesh.

- FIGURE 1.24 and 1.25 show the quantities of interest (force and impulsion) computed with the 1^{st}-order approximation (1.26) of the wall pressure in the algorithm, and using the post-treatment: $P(\boldsymbol{x}, t)|_{\Gamma^w} = P_i + \rho_i c_i \mathbf{u}_i \cdot \boldsymbol{n}$ on the wall boundary of the cell Ω_i. The latter values are actually different from those obtained with the 0^{th}-order approximation on very coarse meshes (see FIGURE 1.26); as expected, they are almost identical on very fine meshes, since $\mathbf{u}_i \cdot \boldsymbol{n}$ tends to zero close to the wall. Moreover, when compared with the CFD reference, the maximal value of the sum of the forces exerted on the rods and the impulsion, using the 1^{st}-order approximation (1.26), are overestimated on very coarse meshes.

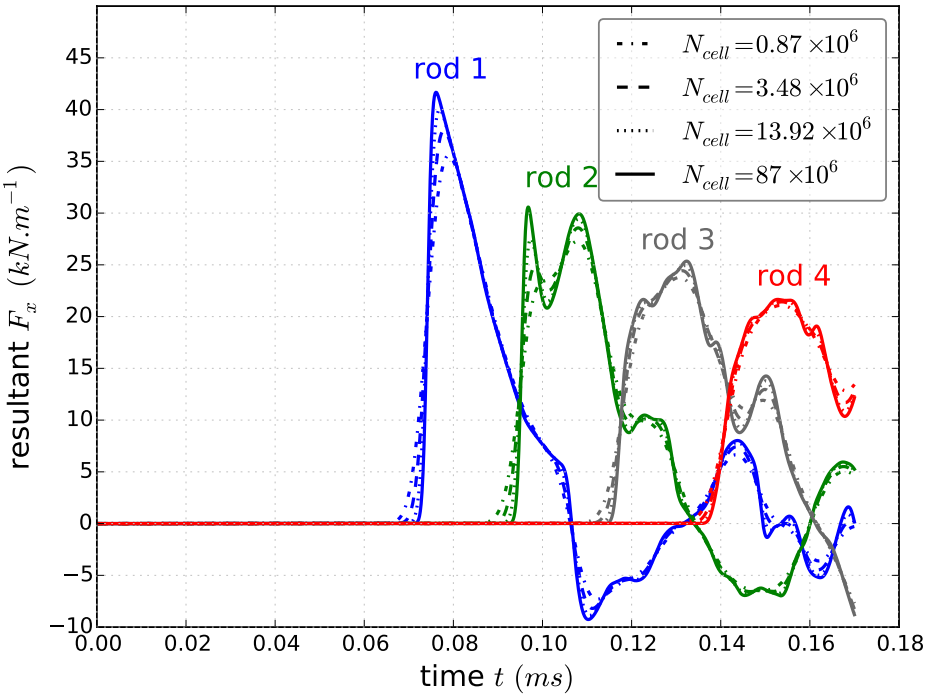

FIGURE 1.20 – *Resultant pressure force $F_x(t)$ using different meshes with N_{cell} cells –* ***CFD*** *approach.*

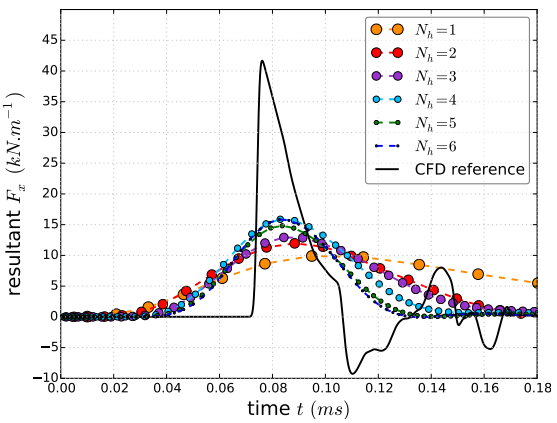

(a) Rod 1

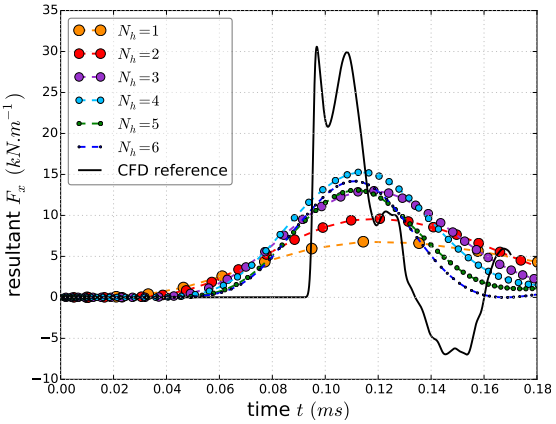

(b) Rod 2

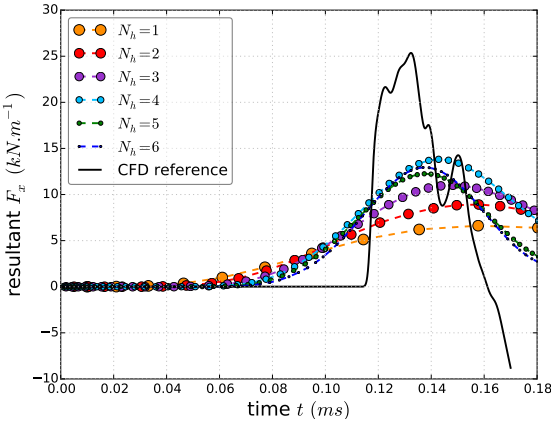

(c) Rod 3

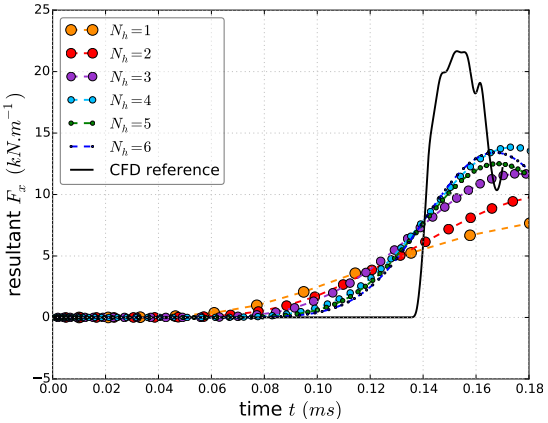

(d) Rod 4

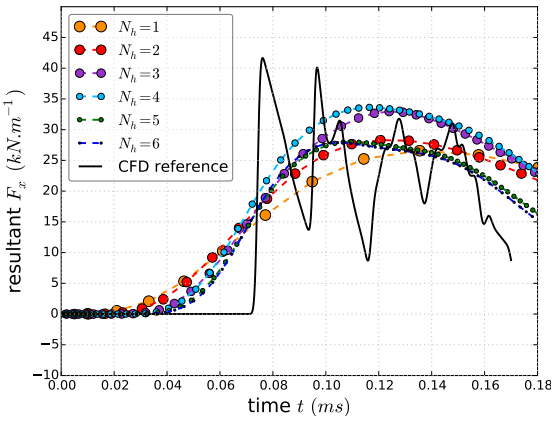

(e) Rods sum

FIGURE 1.21 – *Resultant pressure force $F_x(t)$ using the **integral** approach with different **coarse** meshes – comparison with the CFD reference (black line).*

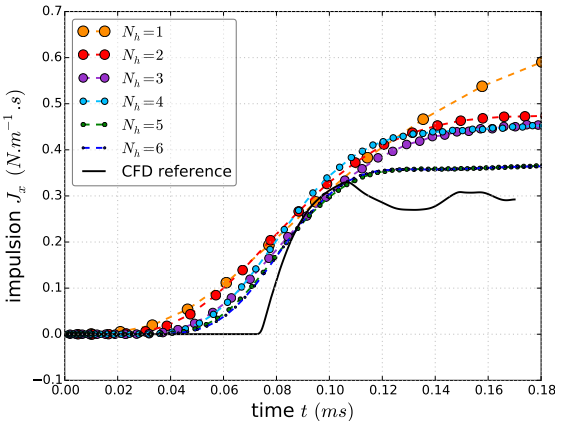

(a) Rod 1

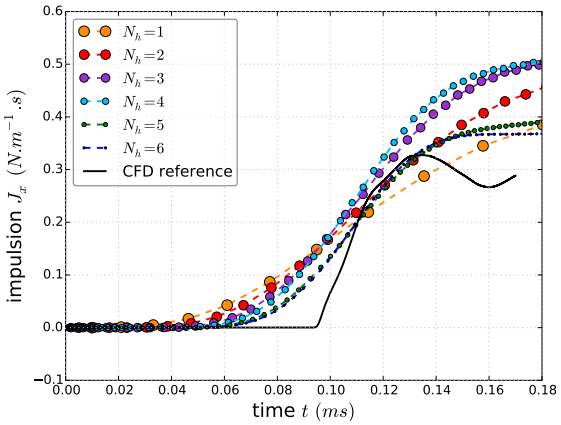

(b) Rod 2

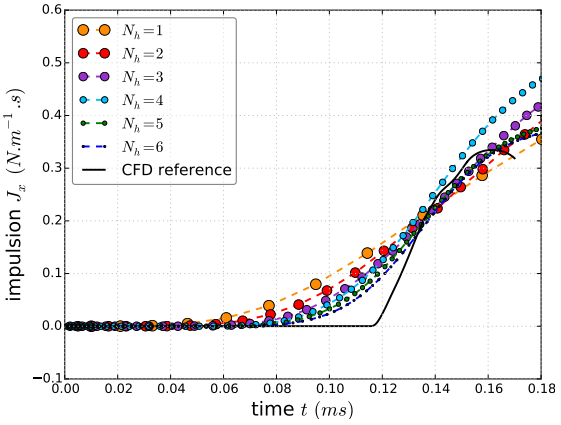

(c) Rod 3

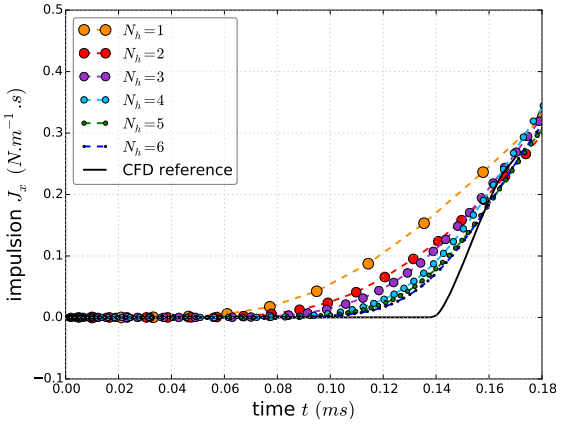

(d) Rod 4

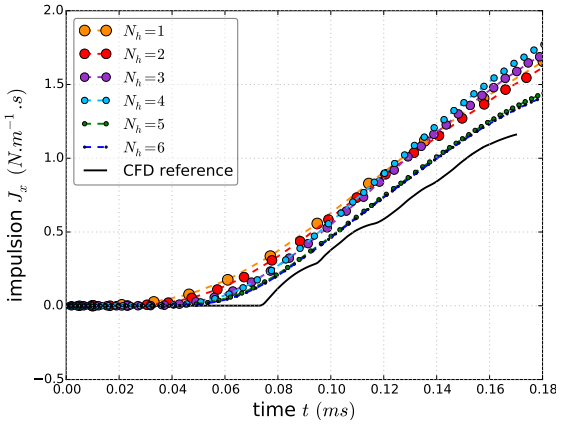

(e) Rods sum

FIGURE 1.22 – *Pressure force impulsion $J_x(t)$ using the **integral** approach with different **coarse** meshes – comparison with the CFD reference (black line).*

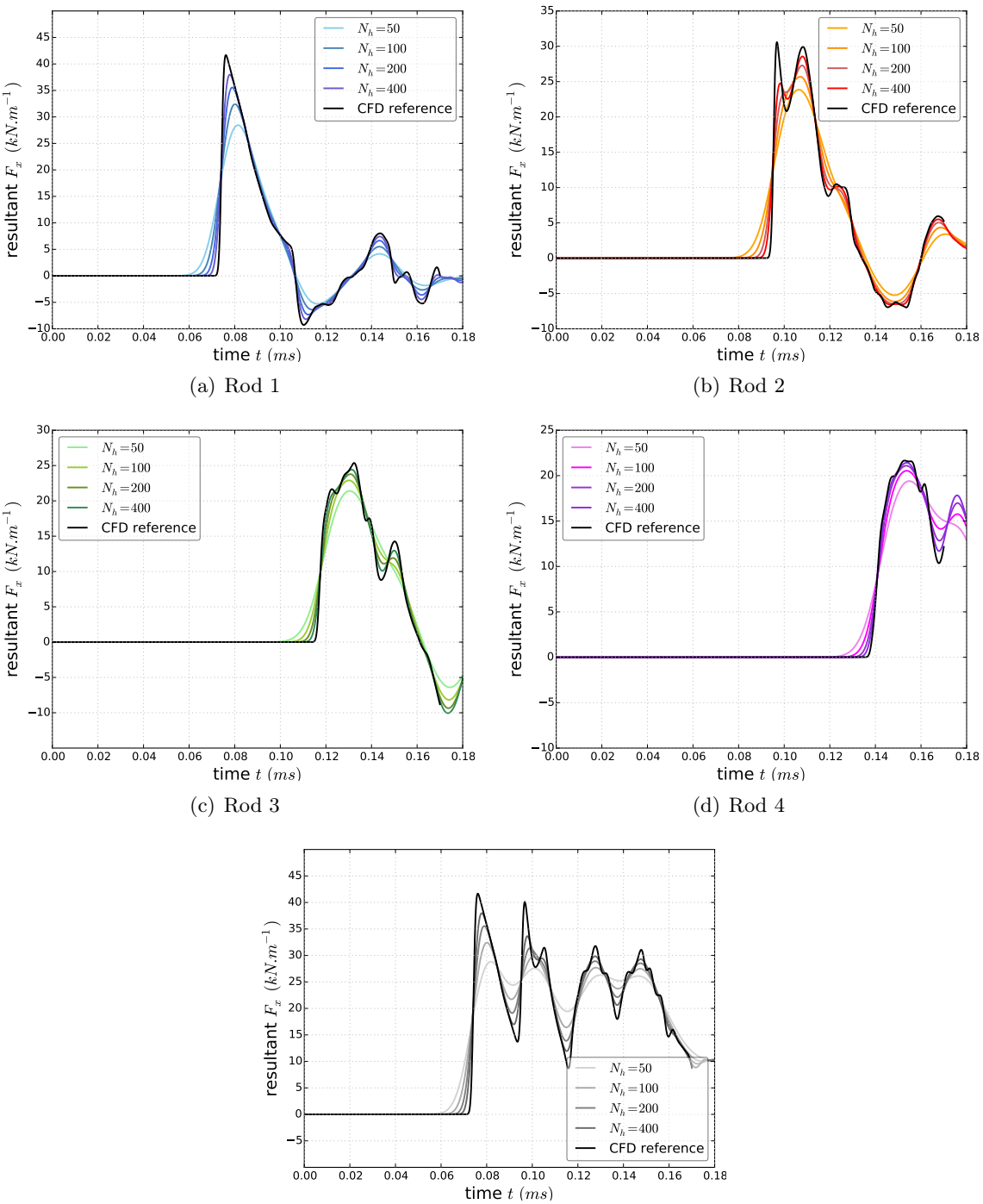

(a) Rod 1

(b) Rod 2

(c) Rod 3

(d) Rod 4

(e) Rods sum

FIGURE 1.23 – *Resultant pressure force $F_x(t)$ using the **integral** approach with different **fine** meshes – comparison with the CFD reference (black line).*

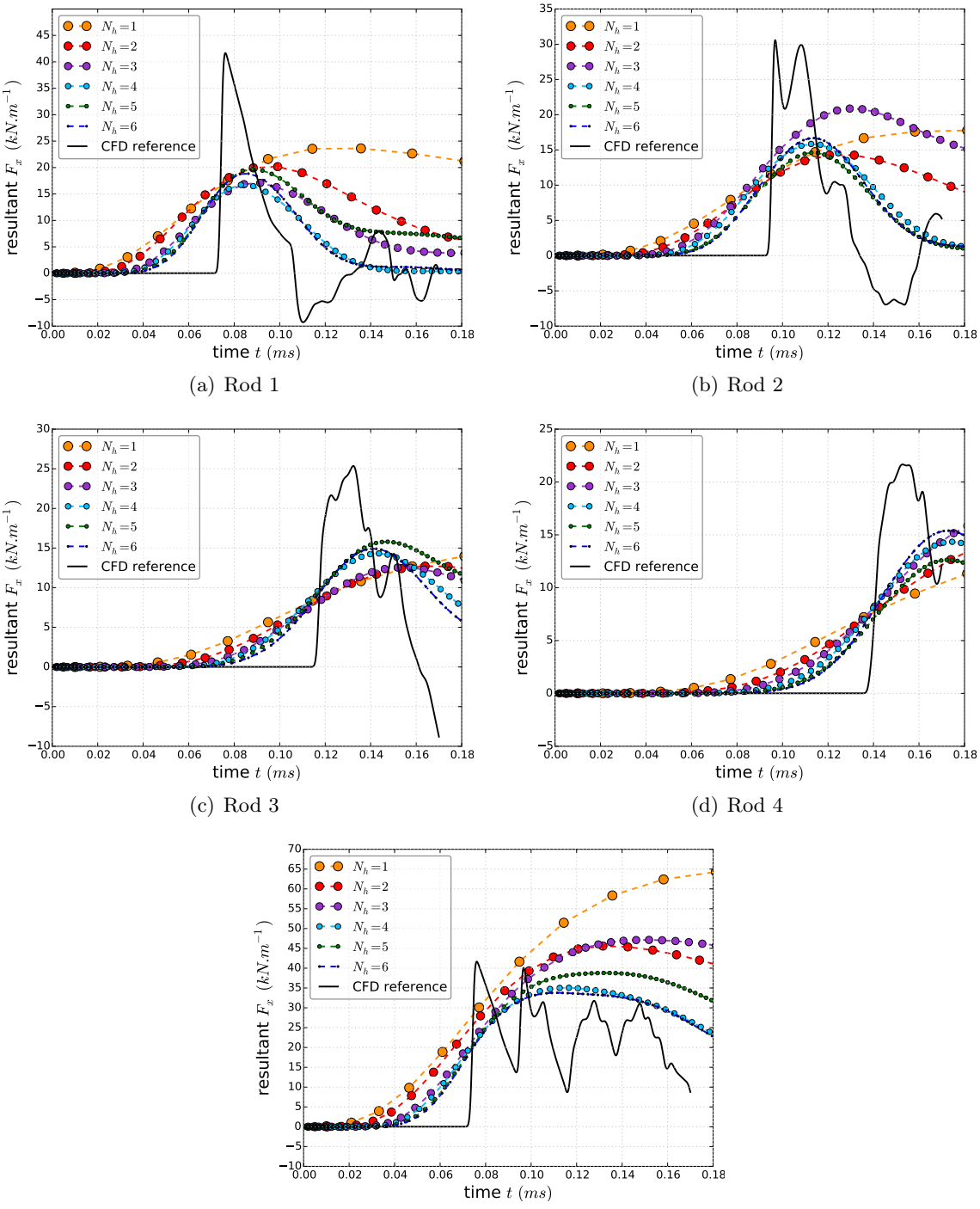

(a) Rod 1

(b) Rod 2

(c) Rod 3

(d) Rod 4

(e) Rods sum

FIGURE 1.24 – *Resultant pressure force $F_x(t)$ using the **integral** approach with different **coarse** meshes and **the** 1^{st}**-order approximation** of the wall pressure – comparison with the CFD reference (black line).*

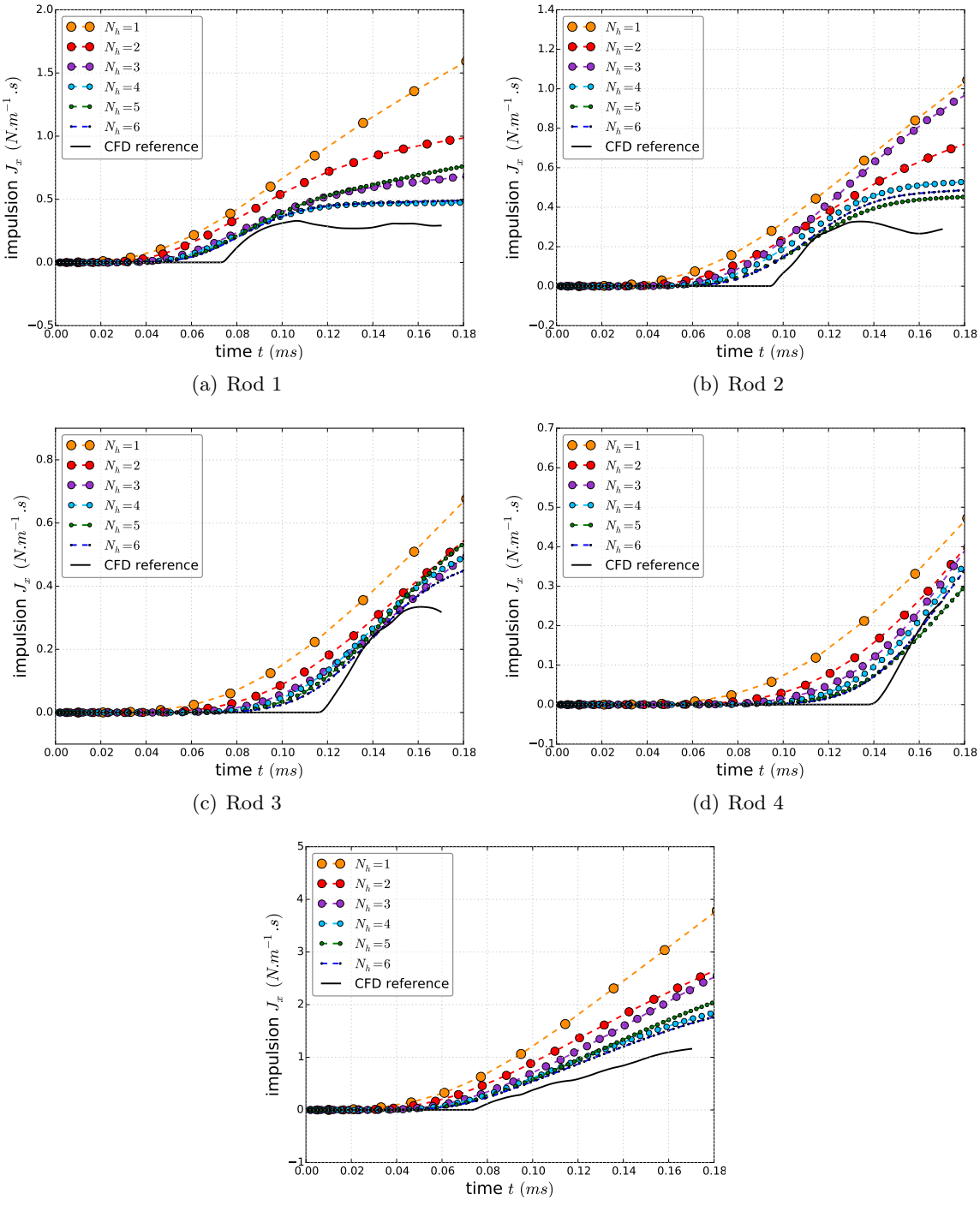

(a) Rod 1

(b) Rod 2

(c) Rod 3

(d) Rod 4

(e) Rods sum

FIGURE 1.25 – *Pressure force impulsion $J_x(t)$ using the **integral** approach with different **coarse** meshes and **the** 1^{st}**-order approximation** of the wall pressure – comparison with the CFD reference (black line).*

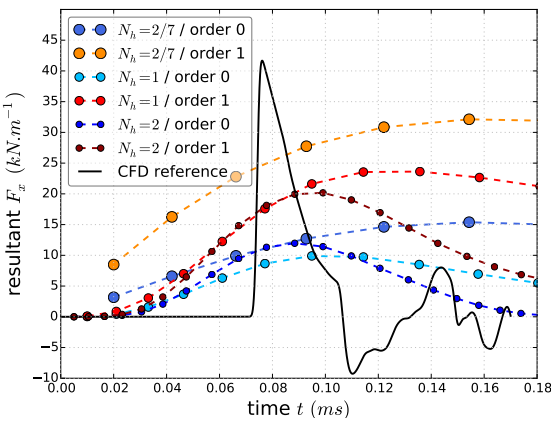

(a) Rod 1

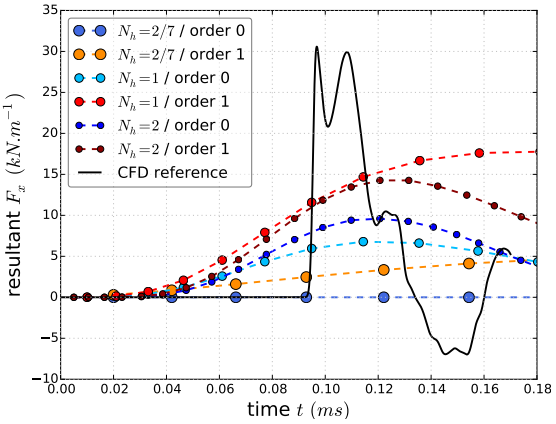

(b) Rod 2

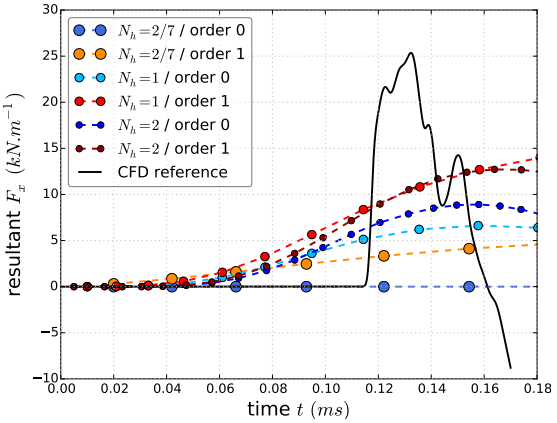

(c) Rod 3

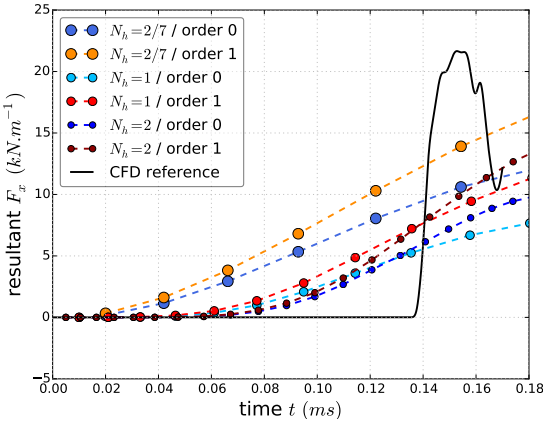

(d) Rod 4

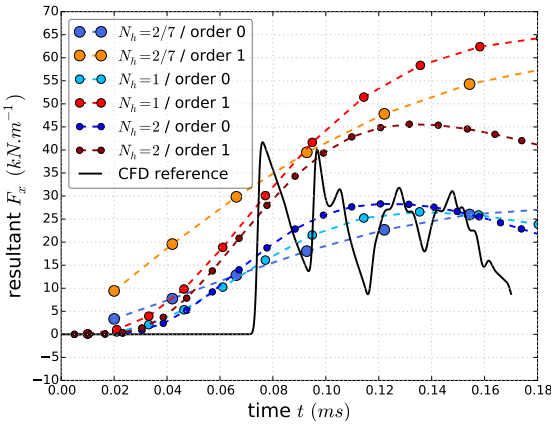

(e) Rods sum

FIGURE 1.26 – *Resultant pressure force $F_x(t)$ using the **integral** approach with three **very coarse** meshes – **comparison of the 0^{th}-order approximation with the 1^{st}-order approximation** of the wall pressure.*

7 Conclusion

The multi-dimensional integral formulation has been introduced to approximate solutions of the Euler equations in a domain cluttered up by small solid obstacles compared with the global size of the domain. Thus, the obstacles may not be explicitly meshed in the computational domain. The integral formulation uses an original pressure-correction method in a collocated semi-implicit finite volume conservative scheme. The preservation of the positivity of the density and the internal energy under a CFL condition, based on the material velocity, is proved.

Numerical verification tests presented herein are shock tube problems, for gas or liquid, either in a free domain or in a domain closed by a wall reflecting the incident shock wave. These tests indicate a stable and consistent behaviour of the algorithm, for Mach numbers ranging from 10^{-3} to 1. Indeed, the numerical scheme enables to capture correct shock waves and contact discontinuities, and also to reproduce the correct pressure, density and velocity profiles in rarefaction waves. We emphasize that the numerical rate of convergence is similar to those obtained with classical exact or approximate Riemann solvers.

The numerical validation test, representative of a safety industrial experiment, shows the ability of the integral approach, with porous coarse meshes, to obtain integral quantities, such that forces acting on tube bundles, with the same order of magnitude than the fine CFD solution. The zero and the first order approximation of the wall pressure in the integral approach are tested. Furthermore, the integral approach naturally converges towards the CFD approach when the mesh is refined.

Hence, by simply defining mesh geometric quantities like fluid volumes and fluid surfaces, the integral formulation allows to unify the porous and the fluid representation by construction. Thus a wide range of computational meshes, from the coarsest porous mesh for the "component" scale to the finest fluid mesh for the "local" scale, can be continuously treated. The current integral approach is an alternative to the standard porous approach in order to compute fluid flows in an obstructed medium, including the sharp transition between a free and an obstructed medium, as it occurs when the fluid flow enters the PWR core. Numerical tests involving comparisons with results performed with the component scale software THYC, using the standard porous approach, will be carried out in the near future.

Current work aims at extending the integral formulation to compressible and incompressible viscous fluid flows governed by the Navier-Stokes equations. Viscous effects would be taken into account thanks to wall functions which vanish when the mesh is refined.

1.A Mass balance non linear scheme for liquid

The mass balance step of the fractional step algorithm (see section 3.1) is modified for a real Equation Of State (EOS) of a liquid.

1.A.1 Time scheme

At the time step Δt^n, pressure and density are implicit, while entropy is always considered frozen, $s^{n+1} = s^n$. Integration of the mass balance equation between t^n and t^{n+1} and over Ω_i^ϕ gives the following implicit time scheme:

$$\left|\Omega_i^\phi\right| \left(\rho_i^{n+1} - \rho_i^n\right) + \Delta t^n \int_{\Gamma_i^\phi} \boldsymbol{Q}^* \cdot \boldsymbol{n} \mathrm{d}\gamma = 0, \tag{1.47}$$

where the implicit mass flux $\boldsymbol{Q}^*$ is computed as (see equation (1.13)):

$$\boldsymbol{Q}^* \cdot \boldsymbol{n} = \boldsymbol{Q}^n \cdot \boldsymbol{n} - \Delta t^n \boldsymbol{\nabla} P^* \cdot \boldsymbol{n}.$$

The relation between pressure and density is henceforth non linear: $\rho_i^{n+1} = \rho(P_i^*, s_i^n)$. equation (1.47) is written with the unknown pressure P_i^* as follows:

$$\left|\Omega_i^\phi\right| \left(\frac{\rho(P_i^*, s_i^n)}{P_i^*} - (\Delta t^n)^2 \operatorname{div} \boldsymbol{\nabla}\right) P_i^* = \left|\Omega_i^\phi\right| \rho_i^n - \Delta t^n \int_{\Gamma_i^\phi} \boldsymbol{Q}^n \cdot \boldsymbol{n} \mathrm{d}\gamma. \tag{1.48}$$

Remark 1.A.1. *The relation $\rho_i^{n+1} = \rho\left(P_i^*, s_i^n\right)$ must be used for the update of the density to conserve mass over time.*

1.A.2 Space scheme

The space discretization of the mass balance equation (1.48) is identical to the scheme described in section 4.1. The explicit mass flux is discretized by a upwind scheme:

$$\int_{\Gamma_i^\phi} \boldsymbol{Q}^n \cdot \boldsymbol{n} \mathrm{d}\gamma = \sum_{j \in N(i)} \left(\rho_{ij}^n\right)^{upw} \left(\mathbf{u}^n \cdot \boldsymbol{n}\right)_{ij} S_{ij}^\phi, \tag{1.49}$$

with:

$$\left(\rho_{ij}^n\right)^{upw} = \beta_{ij}^n \rho_i^n + (1 - \beta_{ij}^n)\rho_j^n, \quad \beta_{ij}^n = \begin{cases} 1 & \text{if } \left(\mathbf{u}^n \cdot \boldsymbol{n}\right)_{ij} \geq 0, \\ 0 & \text{otherwise,} \end{cases}$$

and the pressure gradient is discretized with a two-point flux approximation:

$$\int_{\Gamma_i^\phi} \boldsymbol{\nabla} P^* \cdot \boldsymbol{n} \mathrm{d}\gamma = \sum_{j \in N(i)} \frac{1}{h_{ij/i} + h_{ij/j}} \left(P_j^* - P_i^*\right) S_{ij}^\phi. \tag{1.50}$$

Thus the pressure prediction scheme holds:

$$\begin{aligned} \left|\Omega_i^\phi\right| \left(\frac{\rho(P_i^*, s_i^n)}{P_i^*}\right) P_i^* - (\Delta t^n)^2 \sum_{j \in N(i)} \frac{1}{h_{ij/i} + h_{ij/j}} \left(P_j^* - P_i^*\right) S_{ij}^\phi \\ = \left|\Omega_i^\phi\right| \rho_i^n - \Delta t^n \sum_{j \in N(i)} \left(\rho_{ij}^n\right)^{upw} \left(\mathbf{u}^n \cdot \boldsymbol{n}\right)_{ij} S_{ij}^\phi. \end{aligned} \tag{1.51}$$

Equation (1.51) yields a non-linear algebraic system:

$$\mathbf{M}\,\mathbf{X} = \mathbf{B}',$$

with the vector $\mathbf{X} = (P_i^*)_{i\in\{1,...,N_{cell}\}}$ and N_{cell} the total number of cell (or degrees of freedom). $\forall\, i \in \{1, ..., N_{cell}\}$, the diagonal operator coefficients are:

$$M_{ii} = \begin{cases} \left|\Omega_i^\phi\right| \left(\dfrac{\rho(P_i^*, s_i^n)}{P_i^*}\right) + (\Delta t^n)^2 \displaystyle\sum_{j\in N(i)} \frac{S_{ij}^\phi}{h_{ij/i} + h_{ij/j}} & \text{if } \left|\Omega_i^\phi\right| > 0, \\ 1 & \text{otherwise.} \end{cases}$$

$\forall\, i, j \in \{1, ..., N_{cell}\}$ with $j \neq i$, the off-diagonal coefficients are:

$$M_{ij} = \begin{cases} -\dfrac{(\Delta t^n)^2}{h_{ij/i} + h_{ij/j}} S_{ij}^\phi & \text{if } j \in N(i) \text{ and } \left|\Omega_i^\phi\right| > 0, \\ 0 & \text{otherwise.} \end{cases}$$

The right hand side coefficients are:

$$B_i' = \begin{cases} \left|\Omega_i^\phi\right| \rho_i^n - \Delta t^n \displaystyle\sum_{j\in N(i)} \left(\rho_{ij}^n\right)^{upw} (\mathbf{u}^n \cdot \boldsymbol{n})_{ij} S_{ij}^\phi & \text{if } \left|\Omega_i^\phi\right| > 0, \\ P_i^n & \text{otherwise.} \end{cases}$$

1.A.3 Property of positivity

The non linear operator $\mathbf{M}$ is coercive (therefore invertible) if the pressure is positive, *i.e.* for all i, $P_i^* \geq 0$. The sufficient condition of positivity of both the pressure and the density is the classical CFL-like condition (1.52) only based on the mass flux rather than the thermodynamic coefficient $\hat{\gamma} = \frac{\rho c^2}{P} > 1$.

Property 1.A.1 (Positivity of the density and the pressure). *If the initial conditions are such that $\rho_i^n > 0$ and $P_i^n > 0$, then the density ρ_i^{n+1} and the pressure P_i^* will remain positive for all i, provided that the time step Δt^n complies with the CFL-like condition (1.52):*

$$\left|\Omega_i^\phi\right| \geq \Delta t^n \sum_{j\in N(i)} \beta_{ij}^n \left(\mathbf{u}^n \cdot \boldsymbol{n}\right)_{ij} S_{ij}^\phi. \tag{1.52}$$

Proof. The proof is similar to the proof of Property 5.1 in section 5. The inverse operator $\mathbf{M}^{-1}$ is positive ($M_{ij}^{-1} \geq 0$) and the right hand side vector $\mathbf{B}'$ is also positive ($B_i' \geq 0$) if Condition (1.52) holds, implying $P_i^* \geq 0$. Besides, density ρ_i^{n+1} is computed as a positive function of the pressure $\rho_i^{n+1} = \rho\left(P_i^*, s_i^n\right) \geq 0$, which completes the proof.

1.B Riemann problem with mirror state

A popular method to treat numerically solid wall boundary conditions is the "mirror state" technique. It consists in defining a virtual state $\widehat{\mathbf{W}_i^n}$ outside the multidimensional fluid domain, which is deduced from the state $\mathbf{W}_i^n$ in the nearest wall cell with the same density, pressure, but opposite normal velocity. The half Riemann problem consists in solving an exact one-dimensional Riemann problem with respect to this virtual state in the normal direction to the wall (see FIGURE 1.27).

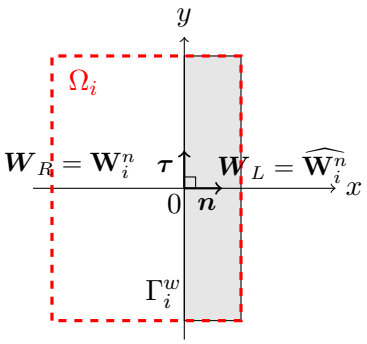

FIGURE 1.27 – *Riemann problem with mirror state in the immersed obstacle into the cell* Ω_i.

This problem is used to compute the wall pressure with *a priori* any EOS where $\boldsymbol{n}$ is the outward normal from the cell to the wall and $\boldsymbol{\tau}$ a tangent vector to the wall. Since Euler system (1.1) is invariant under frame rotation and translation along the $\boldsymbol{\tau}$ direction, the wall pressure is the solution of the local one-dimensional Riemann problem (1.53) in the $\boldsymbol{n}$-direction:

$$\left\{ \begin{array}{l} \partial_t \boldsymbol{W} + \partial_{\boldsymbol{n}} \left(\boldsymbol{F}_{\boldsymbol{n}} \left(\boldsymbol{W} \right) \right) = 0, \ \boldsymbol{x} \cdot \boldsymbol{n} \in \mathbb{R}, \ t \in \mathbb{R}^+, \\ \boldsymbol{W}(\boldsymbol{x} \cdot \boldsymbol{n}, 0) = \left\{ \begin{array}{ll} \boldsymbol{W}_L & \text{if } \boldsymbol{x} \cdot \boldsymbol{n} < 0, \\ \boldsymbol{W}_R & \text{if } \boldsymbol{x} \cdot \boldsymbol{n} > 0, \end{array} \right. \end{array} \right. \tag{1.53}$$

where the left state $\boldsymbol{W}_L$ and the right state $\boldsymbol{W}_R$ are such that:

$$\left\{ \begin{array}{ll} \boldsymbol{W}_L = \mathbf{W}_i^n & \text{(real cell } i\text{)}, \\ \boldsymbol{W}_R = \widehat{\mathbf{W}_i^n} & \text{(virtual cell, mirror of } \mathbf{W}_i^n\text{)}, \end{array} \right. \tag{1.54}$$

and $\boldsymbol{F}_n(\boldsymbol{W}) = \boldsymbol{F}(\boldsymbol{W}) \cdot \boldsymbol{n}$ is the normal flux. For the two-dimensional Euler system:

$$\boldsymbol{W} = \left[\begin{array}{c} \rho \\ \rho \boldsymbol{u} \\ E \end{array} \right] \text{ and } \boldsymbol{F}_n(\boldsymbol{W}) = \left[\begin{array}{c} \rho \boldsymbol{u} \cdot \boldsymbol{n} \\ (\rho \boldsymbol{u} \cdot \boldsymbol{n}) \, \boldsymbol{u} + P \boldsymbol{n} \\ (\boldsymbol{u} \cdot \boldsymbol{n}) \, (E + P) \end{array} \right].$$

Note that $\boldsymbol{u} = [u, v]^\mathsf{T}$, where $u = \boldsymbol{u} \cdot \boldsymbol{n}$ is the normal velocity and $v = \boldsymbol{u} \cdot \boldsymbol{\tau}$ is the tangential velocity.

The discrete conservative variable is $\mathbf{W}_i^n = [\rho_i^n, \rho_i^n u_i^n, \rho_i^n v_i^n, E_i^n]^\mathsf{T}$ and so the corresponding mirror state is $\widehat{\mathbf{W}_i^n} = [\rho_i^n, -\rho_i^n u_i^n, \rho_i^n v_i^n, E_i^n]^\mathsf{T}$. Two possible cases may appear:

- a double symmetric rarefaction wave if $\mathbf{u}_i^n \cdot \boldsymbol{n} \leq 0$,
- a double symmetric shock wave if $\mathbf{u}_i^n \cdot \boldsymbol{n} > 0$.

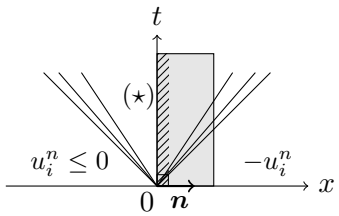

FIGURE 1.28 – *Double symmetric rarefaction with mirror state in the immersed obstacle.*

1.B.1 Double symmetric rarefaction wave: $\mathbf{u}_i^n \cdot \boldsymbol{n} \leq 0$

The computation of the wall state, classically called intermediate state $(\star)$ (see FIGURE 1.28), is based on the symmetry of the problem, implying:

$$u^\star = 0, \tag{1.55}$$

and on the conservation of three Riemann invariants of the 1-wave:

$$\begin{cases} v^\star = v_i^n, & \text{(1.56a)} \\ s(P^\star, \rho^\star) = s(P_i^n, \rho_i^n) = s_i^n, & \text{(1.56b)} \\ u^\star + \displaystyle\int_0^{\rho^\star} \frac{c(\rho, s_i^n)}{\rho} d\rho = u_i^n + \int_0^{\rho_i^n} \frac{c(\rho, s_i^n)}{\rho} d\rho. & \text{(1.56c)} \end{cases}$$

We deduce from equations (1.55) and (1.56c) that: $\displaystyle\int_{\rho^\star}^{\rho_i^n} \frac{c(\rho, s_i^n)}{\rho} d\rho = -u_i^n \geq 0$, allowing to retrieve the density $\rho^\star \leq \rho_i^n$ of the intermediate state, and then the pressure $P^\star$ using equation (1.56b), such that:

$$P^\star = P_i^n \left(1 + f\left(\frac{u_i^n}{c_i^n}\right)\right).$$

The expression of the function f depends on the thermodynamic law of the fluid, but for any EOS:

$$f(0) = 0 \quad \text{and} \quad f(\xi < 0) < 0, \text{ where } \xi = \frac{u_i^n}{c_i^n}.$$

1.B.1.1 Ideal gas EOS

For an ideal gas such that $\rho\epsilon = \frac{P}{\gamma - 1}$, with $\gamma > 1$ the heat capacity ratio:

$$\int_{\rho^\star}^{\rho_i^n} \frac{c(\rho, s_i^n)}{\rho} d\rho = \frac{2}{\gamma - 1}(c_i^n - c^\star) = -u_i^n \quad \text{and} \quad \frac{P^\star}{P_i^n} = \left(\frac{\rho^\star}{\rho_i^n}\right)^\gamma = \left(\frac{c^\star}{c_i^n}\right)^{\frac{2\gamma}{\gamma-1}}$$

$$\Rightarrow \begin{cases} P^\star = P_i^n \left(1 + \dfrac{\gamma - 1}{2} \dfrac{u_i^n}{c_i^n}\right)^{\frac{2\gamma}{\gamma-1}} & \text{if } -\frac{2}{\gamma-1} < \frac{u_i^n}{c_i^n} \leq 0, \\ P^\star = 0 & \text{otherwise.} \end{cases}$$

1.B.1.2 Stiffened gas EOS

For a stiffened gas such that $\rho\epsilon = \frac{P+\gamma\Pi_\infty}{\gamma-1}$, with $\Pi_\infty \geq 0$ the reference pressure:

$$\int_{\rho^\star}^{\rho_i^n} \frac{c(\rho, s_i^n)}{\rho} d\rho = \frac{2}{\gamma-1}(c_i^n - c^\star) = -u_i^n \quad \text{and} \quad \frac{P^\star + \Pi_\infty}{P_i^n + \Pi_\infty} = \left(\frac{\rho^\star}{\rho_i^n}\right)^\gamma = \left(\frac{c^\star}{c_i^n}\right)^{\frac{2\gamma}{\gamma-1}}$$

$$\Rightarrow \begin{cases} P^\star + \Pi_\infty = (P_i^n + \Pi_\infty)\left(1 + \dfrac{\gamma-1}{2}\dfrac{u_i^n}{c_i^n}\right)^{\frac{2\gamma}{\gamma-1}} & \text{if } -\frac{2}{\gamma-1} < \frac{u_i^n}{c_i^n} \leq 0, \\ P^\star = -\Pi_\infty & \text{otherwise.} \end{cases}$$

1.B.1.3 First order expansion of the function f for any EOS

For all $\xi \in \mathbb{R}^-$, the function $f(\xi)$ and its derivative $f'(\xi)$ are evaluated in the neighbourhood of zero in order to get a first order expansion for any EOS.

Noting $f(\xi) = \dfrac{P^\star - P_i^n}{P_i^n}(\xi)$, and using the mean value theorem and equation (1.56b), $\widetilde{\rho} \in [\rho^\star, \rho_i^n]$ exists such that:

$$P^\star - P_i^n = \widetilde{\partial_\rho P|_s}\,(\rho^\star - \rho_i^n)\,.$$

Moreover equation (1.56c) suggests that $\widehat{\rho} \in (\rho^\star, \rho_i^n)$ exists such that:

$$u_i^n = -\int_{\rho^\star}^{\rho_i^n} \frac{c(\rho, s_i^n)}{\rho} d\rho = \frac{\widehat{c(\rho, s_i^n)}}{\rho}\,(\rho^\star - \rho_i^n)\,.$$

We conclude that:

$$f(\xi) = \frac{1}{P_i^n}\widetilde{c^2}\frac{\widehat{\rho}}{c(\rho, s_i^n)}u_i^n = \frac{c_i^n}{P_i^n}\widetilde{c^2}\frac{\widehat{\rho}}{c(\rho, s_i^n)}\xi \underset{\xi\to 0^-}{\sim} \frac{\rho_i^n \left(c_i^2\right)^n}{P_i^n}\xi,$$

since $\rho^\star \to \rho_i^{n-}$ when $\xi \to 0^-$.

Hence the function f is differentiable in $\xi = 0^-$ such that, for any EOS:

$$f(0^-) = 0 \quad \text{and} \quad f'(0^-) = \hat{\gamma}_i^n = \frac{\rho_i^n \left(c_i^2\right)^n}{P_i^n}.$$

1.B.2 Double symmetric shock configuration: $\mathbf{u}_i^n \cdot \boldsymbol{n} > 0$

The computation of the intermediate state $(\star)$ (see FIGURE 1.29) is based on the Rankine-Hugoniot jump relations for a shock (1.57), and also on the symmetry of the problem:

$$\begin{aligned} u^\star &= 0, \\ -\sigma\,[\boldsymbol{W}]_i^\star + [\boldsymbol{F}(\boldsymbol{W})\cdot\boldsymbol{n}]_i^\star &= 0, \end{aligned} \tag{1.57}$$

where for any field φ, the jump is defined as: $[\varphi]_i^\star = \varphi^\star - \varphi_i^n$ and σ is the speed of the shock wave.

This system of jump relations (1.57) gives:

$$\begin{cases} [v]_i^\star = 0, & \text{(1.58a)} \\ [\epsilon]_i^\star + \dfrac{P_i + P^\star}{2}\left[\dfrac{1}{\rho}\right]_i^\star = 0, & \text{(1.58b)} \\ \rho_i\rho^\star\left([u]_i^\star\right)^2 - [P]_i^\star\,[\rho]_i^\star = 0, & \text{(1.58c)} \end{cases}$$

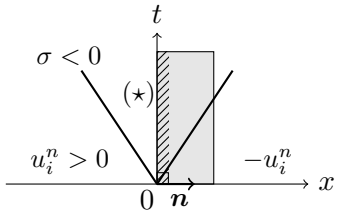

FIGURE 1.29 – *Double symmetric shock with mirror state in the immersed obstacle.*

which allows to determine the intermediate density $\rho^\star > \rho_i^n$ and the intermediate pressure $P^\star$. For any EOS, the pressure reads as follows:

$$P^\star = P_i^n \left(1 + g\left(\frac{u_i^n}{c_i^n}\right)\right).$$

The function g verifies:

$$g(0) = 0 \quad \text{and} \quad g(\xi > 0) > 0, \text{ where } \quad \xi = \frac{u_i^n}{c_i^n}.$$

1.B.2.1 Ideal gas EOS

For an ideal gas, the solution is detailed in [58]. We get the solution of the intermediate state, writing:

$$P^\star = P_i^n \left(1 + \gamma \frac{u_i^n}{c_i^n}\left(1 + \frac{(\gamma+1)^2}{16}\left(\frac{u_i^n}{c_i^n}\right)^2\right)^{\frac{1}{2}} + \frac{\gamma(\gamma+1)}{4}\left(\frac{u_i^n}{c_i^n}\right)^2\right).$$

1.B.2.2 Stiffened gas EOS

For a stiffened gas, the solution of the intermediate state is:

$$P^\star + \Pi_\infty = (P_i^n + \Pi_\infty)\left(1 + \gamma \frac{u_i^n}{c_i^n}\left(1 + \frac{(\gamma+1)^2}{16}\left(\frac{u_i^n}{c_i^n}\right)^2\right)^{\frac{1}{2}} + \frac{\gamma(\gamma+1)}{4}\left(\frac{u_i^n}{c_i^n}\right)^2\right).$$

1.B.2.3 First order expansion of the function g for any EOS

For all $\xi \in \mathbb{R}^+$, the function $g(\xi) = \dfrac{P^\star - P_i^n}{P_i^n}(\xi)$ is evaluated to get a first order expansion for any EOS. The mean value theorem suggests that $\widetilde{\rho} \in (\rho_i^n, \rho^\star)$ and $\widetilde{\epsilon} \in (\epsilon^n, \epsilon^\star)$ exist and such that:

$$P^\star - P_i^n = \widetilde{\partial_\rho P|_\epsilon}\,(\rho^\star - \rho_i^n) + \widetilde{\partial_\epsilon P|_\rho}\,(\epsilon^\star - \epsilon^n) = a\,[\rho]_i^\star + b\,[\epsilon]_i^\star.$$

Thus equation (1.58b) implies:

$$[P]_i^\star = \left(a + b\frac{P_i^n + P^\star}{2\rho_i^n \rho^\star}\right)[\rho]_i^\star,$$

and equation (1.58c) gives:

$$([P]_i^\star)^2 = \rho_i^n \rho^\star \left(a + b\frac{P_i^n + P^\star}{2\rho_i^n \rho^\star}\right)(u_i^n)^2.$$

Thus, we conclude:

$$g(x) = \frac{c_i^n}{P_i^n}\left(\rho_i^n \rho^\star \left(a + b\frac{P_i^n + P^\star}{2\rho_i^n \rho^\star}\right)\right)^{\frac{1}{2}} \xi.$$

Since $\partial_\rho P|_\epsilon + \partial_\epsilon P|_\rho \frac{P}{\rho^2} = c^2$, the equivalent when $\rho^\star \to \rho_i^{n+}$ is:

$$g(x) \underset{\xi \to 0^+}{\sim} \frac{\rho_i^n \left(c_i^2\right)^n}{P_i^n} \xi.$$

Hence the function g is differentiable in $\xi = 0^+$ and such that, for any EOS:

$$g(0^+) = 0 \quad \text{and} \quad g'(0^+) = \hat{\gamma}_i^n = \frac{\rho_i^n \left(c_i^2\right)^n}{P_i^n}.$$

Property 1.B.1. *For any EOS such that $P = \mathcal{P}(\rho, \epsilon)$, the fitting between the double symmetric shock solution and the double symmetric rarefaction solution is C^1:*

$$\forall\ \xi \in \mathbb{R},\ \ f(\xi) \equiv g(\xi) + o(\xi)\ \textit{when}\ \xi \to 0, \tag{1.59}$$

and the derivative value is: $f'(0) = g'(0) = \hat{\gamma}_L = \left(\frac{\rho c^2}{P}\right)_L$.

1.C Evaluation of the symmetric positive tensor $\boldsymbol{K}$

The geometric part of symmetric tensor $\boldsymbol{K}$ is described for some obstacles shapes of interest.

$$\boldsymbol{K}_i = \hat{\gamma}_i \frac{P_i}{c_i} \int_{\Gamma_i^w} \boldsymbol{n}\boldsymbol{n}^{\mathsf{T}} \mathrm{d}\gamma \tag{1.60}$$

The pressure P_i, the sound speed c_i and the thermodynamic coefficient $\hat{\gamma}_i$ are explicit, known from the step of mass balance of the fractional step algorithm, see section 3.1. But the wall boundary integral is computed in terms of the geometric shape of the obstacle into the cell Ω_i. The evaluation is equivalent for a set of shapes. For instance, the computation is done per unit length for three immersed obstacles into a given cell in $2D$:

1. Square of side a:

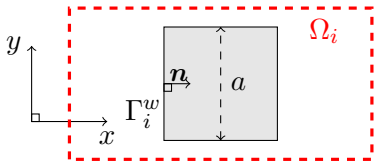

FIGURE 1.30 – *Square (grey obstacle) of side a immersed into cell Ω_i.*

In summing up on the four sides, the linear integral reads in the local system of axes (x, y):

$$\begin{aligned}\int_{\Gamma^w} \boldsymbol{n}\boldsymbol{n}^{\mathsf{T}} \mathrm{d}\gamma &= \begin{bmatrix}1\\0\end{bmatrix}\begin{bmatrix}1 & 0\end{bmatrix} a + \begin{bmatrix}0\\-1\end{bmatrix}\begin{bmatrix}0 & -1\end{bmatrix} a + \begin{bmatrix}-1\\0\end{bmatrix}\begin{bmatrix}-1 & 0\end{bmatrix} a + \begin{bmatrix}0\\1\end{bmatrix}\begin{bmatrix}0 & 1\end{bmatrix} a \\ &= \begin{bmatrix}1 & 0\\0 & 1\end{bmatrix} 2a\end{aligned}$$

2. Rectangle of area $a \times b$:

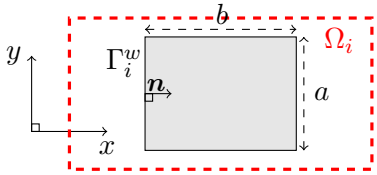

FIGURE 1.31 – *Rectangle (gray obstacle) of area $a \times b$ immersed into cell Ω_i.*

In summing up on the four sides of rectangle, the integral reads:

$$\int_{\Gamma^w} \boldsymbol{n}\boldsymbol{n}^{\mathsf{T}} \mathrm{d}\gamma = \begin{bmatrix}2a & 0\\0 & 2b\end{bmatrix}$$

3. Circle of radius $\frac{a}{2}$:

In integrating on the contour of the circle, the integral reads:

$$\begin{aligned}\int_{\Gamma^w} \boldsymbol{n}\boldsymbol{n}^{\mathsf{T}} \mathrm{d}\gamma &= \int_0^{2\pi} \begin{bmatrix}\cos^2\theta & \cos\theta\sin\theta\\\cos\theta\sin\theta & \sin^2\theta\end{bmatrix} d\theta \frac{a}{2} \\ &= \begin{bmatrix}1 & 0\\0 & 1\end{bmatrix} \frac{\pi}{2} a\end{aligned}$$

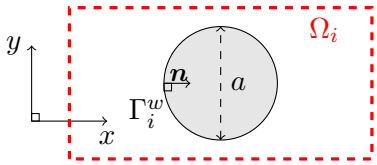

FIGURE 1.32 – *Circle (gray obstacle) of radius $\frac{a}{2}$ immersed into cell Ω_i.*

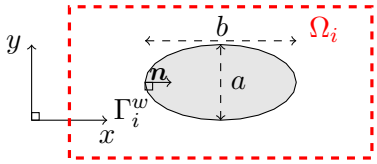

FIGURE 1.33 – *Ellipse (gray obstacle) immersed into cell Ω_i.*

4. Ellipse of semi-minor axis $\frac{a}{2}$ and semi-major axis $\frac{b}{2}$:

   In integrating on the contour of the ellipse, the integral reads:

$$\begin{aligned}\int_{\Gamma^w} \boldsymbol{n}\boldsymbol{n}^{\mathsf{T}} \mathrm{d}\gamma &= \frac{a}{a^2+b^2} \int_0^{2\pi} \begin{bmatrix} a^2\cos^2\theta & ab\cos\theta\sin\theta \\ ab\cos\theta\sin\theta & b^2\sin^2\theta \end{bmatrix} \sqrt{1-e^2 sin^2\theta} d\theta \\ &= \begin{bmatrix} a^2 & 0 \\ 0 & b^2 \end{bmatrix} \frac{2a}{a^2+b^2} \underbrace{\int_0^{\frac{\pi}{2}} \sqrt{1-e^2 sin^2\theta} d\theta}_{E(e)}\end{aligned}$$

   where $e = \sqrt{1-\frac{b^2}{a^2}}$ is the ellipse eccentricity, and the function $E(e)$ is the complete elliptic integral of second kind, which has not closed-form expression in terms of elementary functions.

5. Cross of size a:

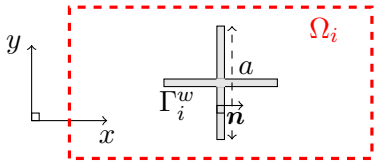

FIGURE 1.34 – *Cross (gray obstacle) of size a immersed into cell Ω_i.*

   In summing up on all edges of the cross, the evaluation is the same than for the square integral:

$$\int_{\Gamma^w} \boldsymbol{n}\boldsymbol{n}^{\mathsf{T}} \mathrm{d}\gamma = \begin{bmatrix} 1 & 0 \\ 0 & 1 \end{bmatrix} 2a$$

6. Cross of size $a \times b$:

   In summing up on all edges of the cross, the evaluation is the same than for the rectangle integral:

$$\int_{\Gamma^w} \boldsymbol{n}\boldsymbol{n}^{\mathsf{T}} \mathrm{d}\gamma = \begin{bmatrix} 2a & 0 \\ 0 & 2b \end{bmatrix}$$

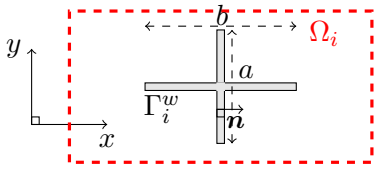

FIGURE 1.35 – *Cross (gray obstacle) of size $a \times b$ immersed into cell Ω_i.*

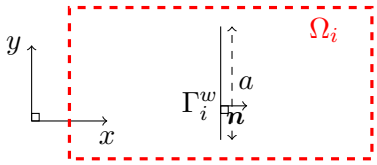

FIGURE 1.36 – *Infinitely thin plate (gray obstacle) immersed into cell Ω_i.*

7. Infinitely thin plate of length a:

   In summing up on the two faces of the plate, the integral gives:

$$\begin{aligned}\int_{\Gamma^w} \boldsymbol{n}\boldsymbol{n}^{\mathsf{T}} \mathrm{d}\gamma &= \begin{bmatrix}1\\0\end{bmatrix}\begin{bmatrix}1 & 0\end{bmatrix} a + \begin{bmatrix}-1\\0\end{bmatrix}\begin{bmatrix}-1 & 0\end{bmatrix} a \\ &= \begin{bmatrix}1 & 0\\0 & 0\end{bmatrix} 2a\end{aligned}$$

8. Infinitely thin drilled plate of full length a:

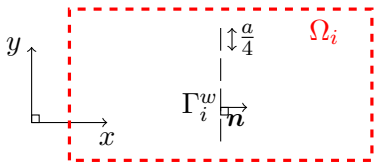

FIGURE 1.37 – *Infinitely thin drilled plate (gray obstacle) immersed into cell Ω_i.*

   In summing up on all faces of length $\frac{a}{4}$ of the drilled plate, the integral gives:

$$\int_{\Gamma^w} \boldsymbol{n}\boldsymbol{n}^{\mathsf{T}} \mathrm{d}\gamma = \begin{bmatrix}1 & 0\\0 & 0\end{bmatrix} 2a$$

9. Drilled plate of full length a and width b:

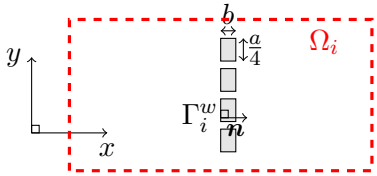

FIGURE 1.38 – *Drilled plate (gray obstacle) immersed into cell Ω_i.*

In summing up on all edges of the drilled plate, the integral reads:

$$\int_{\Gamma^w} \boldsymbol{n}\boldsymbol{n}^{\mathsf{T}} \mathrm{d}\gamma = \begin{bmatrix} 2a & 0 \\ 0 & 8b \end{bmatrix}$$

1.D Analytic solution of a shock tube interaction with a wall

1.D.1 Initial condition: the shock tube

The analytic solution is based on the exact solution of 1D Riemann problems for the Euler equations. The calculation is performed with an ideal gas or a stiffened gas EOS. At the beginning of the computation, the shock tube apparatus contains a membrane ($x = x_0$) separating two different initial constant fluid states at rest: the right state $\boldsymbol{W}_R$ and the left state $\boldsymbol{W}_L$ (see FIGURE 1.39). The tube is closed on the right side: $x = x_1$.

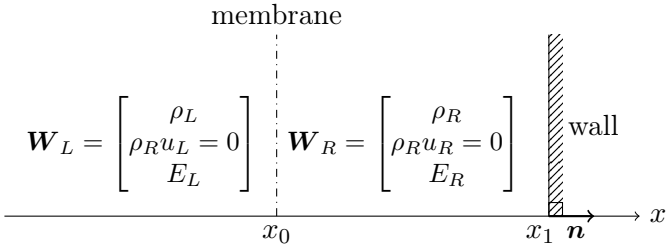

FIGURE 1.39 – *Sketch of the shock tube apparatus, with the initial condition:* $u_L = u_R = 0$ *and* $P_L > P_R$.

The solution of this Riemann problem can be computed using [20] in order to evaluate the two intermediate states $\boldsymbol{W}_1$ and $\boldsymbol{W}_2$ respectively on the left and the right side of the contact discontinuity travelling at speed $u_1 = u_2 > 0$. Since $u_L = u_R = 0$ and $P_L > P_R$, the unique solution is a 1-rarefaction wave that propagates towards the left side, and a 3-shock wave travelling at the celerity σ_2 that moves to the right. We assume in addition that the initial pressure ratio P_L/P_R is such that $u_1 - c_1 < 0$.

1.D.2 Shock wave reflection with the wall for an ideal gas

The shock wave generated by the shock tube hits the wall in $x = x_1$ at time $t = t_0$ (see FIGURE 1.40):

$$t_0 = \frac{x_1 - x_0}{\sigma_2},$$

where σ_2 is the celerity of the 3-shock wave. In order to evaluate the state $\boldsymbol{W}_3$, we need to calculate the Riemann problem for $t > t_0$ with the initial condition (see FIGURE 1.41):

$$\begin{cases} \boldsymbol{W}(x < x_1, t = t_0) = \boldsymbol{W}_2 = [\rho_2, \rho_2 u_2, E_2]^\mathsf{T}, \\ \boldsymbol{W}(x > x_1, t = t_0) = \widehat{\boldsymbol{W}}_2 = [\rho_2, -\rho_2 u_2, E_2]^\mathsf{T}, \end{cases}$$

with $u_2 > 0$, obtained above by solving the shock tube Riemann problem.

This 1D Riemann problem is solved with the primitive variables: $\boldsymbol{Z}_2 = [\rho_2, u_2, P_2]^\mathsf{T}$ and $\widehat{\boldsymbol{Z}}_2 = [\rho_2, -u_2, P_2]^\mathsf{T}$. The new intermediate state (3) (see FIGURE 1.40) with $\boldsymbol{Z}_3 = [\rho_3, u_3, P_3]^\mathsf{T}$ is the reflected shock wave on the wall. The Rankine-Hugoniot jump relations of the Euler equations and the symmetry of the problem give:

$$\begin{cases} u_3 = 0, \\ [\epsilon]_2^3 + \dfrac{P_2 + P_3}{2} \left[\dfrac{1}{\rho}\right]_2^3 = 0, \\ \rho_2 \rho_3 \left([u]_2^3\right)^2 - [P]_2^3 [\rho]_2^3 = 0. \end{cases}$$

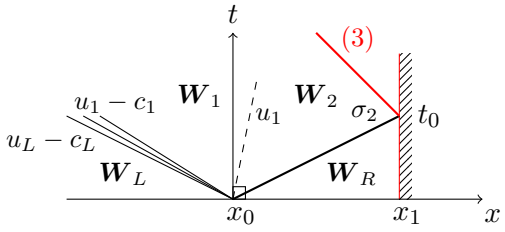

FIGURE 1.40 – *Reflection of the shock wave on the wall (subsonic case: $u_1 - c_1 < 0$) at $t = t_0$.*

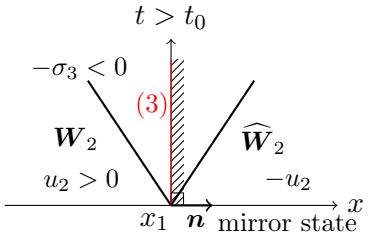

FIGURE 1.41 – *Riemann problem for $t > t_0$: double symmetric shock wave with a mirror state.*

For an ideal gas EOS, $P = (\gamma - 1)\rho\epsilon$, it implies the following equation with respect to $z = \dfrac{\rho_3}{\rho_2}$:

$$g(z) = \frac{(z-1)^2}{z(\beta - z)} = \frac{1}{\beta + 1}\frac{\rho_2 u_2^2}{P_2} := b, \tag{1.63}$$

using the standard notation $\beta = \frac{\gamma+1}{\gamma-1} > 1$. There exists a unique solution $z_0 \in [1, \beta)$ of equation (1.63):

$$z_0 = \frac{2 + b\beta + \sqrt{\Delta}}{2(1+b)}, \tag{1.64}$$

with the positive discriminant $\Delta = b\beta\left(b\beta + 4\left(1 - \frac{1}{\beta}\right)\right)$.
The state $\boldsymbol{Z}_3 = [\rho_3, u_3, P_3]^\mathsf{T}$ is thus known.

1.D.3 Interaction of the contact discontinuity with the reflected shock wave for an ideal gas

The initial contact discontinuity created by the shock tube interacts with the reflected shock wave in $x = x^*$ at the time $t = t_1$ (see FIGURE 1.42), such that:

$$(u_1 + \sigma_3)t_1 = x_1 - x_0 + \sigma_3 t_0, \tag{1.65}$$

with $\sigma_3 > 0$.

For $t > t_1$, there exists a unique solution of the Riemann problem since the initial condition:

$$\begin{cases} \boldsymbol{W}(x < x^*, t = t_1) = \boldsymbol{W}_1, \\ \boldsymbol{W}(x > x^*, t = t_1) = \boldsymbol{W}_3, \end{cases}$$

is such that: $u_3 - u_1 = -u_1 < 0 < \frac{2}{\gamma-1}(c_1 + c_3)$. Since $u_1 > u_3 = 0$ and $P_1 = P_2 < P_3$ (pressure increases through a shock), the unique solution of this Riemann solution cannot involve a 1-rarefaction wave. The solutions can be either:

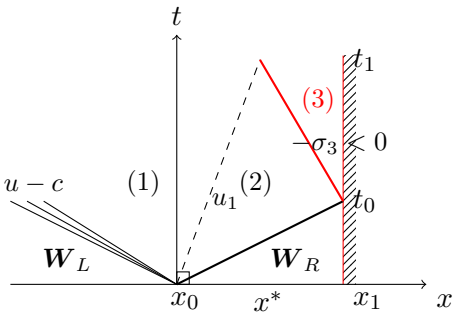

FIGURE 1.42 – *Interaction of the reflected shock wave with the initial contact discontinuity (subsonic case: $u_1 - c_1 < 0$).*

1. a 1-shock / 3-rarefaction configuration,
2. a 1-shock / 3-shock configuration.

1.D.3.1 1-Shock / 3-rarefaction solution

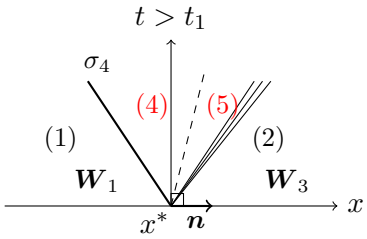

FIGURE 1.43 – *Riemann problem: 1-shock / 3-rarefaction.*

We wish to compute intermediate states $\boldsymbol{W}_4$ and $\boldsymbol{W}_5$ (see FIGURE 1.43). We recall that we have $u_3 = 0$ and $P_3 > P_1$. Moreover the unknowns are such that $u_4 = u_5$ and $P_4 = P_5$. The jump relations for the 1-shock yield:

$$\begin{cases} (u_1 - u_4)^2 = (P_1 - P_4)(\tau_4 - \tau_1), \\ \mu_1 = \dfrac{P_4}{P_1} = \dfrac{\beta z_1 - 1}{\beta - z_1} > 1, \end{cases}$$

with $z_1 = \dfrac{\rho_4}{\rho_1} = \dfrac{\tau_1}{\tau_4} > 1$, $\tau = \frac{1}{\rho}$ is the specific volume. We derive:

$$z_1 = \frac{1 + \beta\mu_1}{\beta + \mu_1} \quad \text{and} \quad u_1 - u_4 = \sqrt{\tau_1 P_1}\sqrt{\beta - 1}\,(\mu_1 - 1)\,\frac{1}{\sqrt{1 + \beta\mu_1}}.$$

The Riemann invariants of the 3-rarefaction are:

$$\begin{cases} u_3 - \dfrac{2}{\gamma - 1}c_3 = u_5 - \dfrac{2}{\gamma - 1}c_5 \quad \text{with} \quad c = \sqrt{\gamma P \tau}, \\ s_3(P_3, \tau_3) = s_5(P_5, \tau_5) \Rightarrow P_3 \tau_3^{\gamma} = P_5 \tau_5^{\gamma}. \end{cases}$$

The whole set of relations implies:

$$u_4 = u_5 = u_5 - u_3 = \frac{2}{\gamma - 1} c_3 \left(\mu_2^{\frac{\gamma-1}{2\gamma}} - 1 \right) \leq 0,$$

since the 3-wave is a rarefaction wave, so $\mu_2 = \frac{P_5}{P_3} \leq 1$. The final scalar equation with respect to μ_1 that needs to be solved is:

$$l(\mu_1) = u_1 - u_3 = u_1,$$

where the function l is defined by $l(\mu_1) = A_1 \frac{\mu_1 - 1}{\sqrt{1+\beta\mu_1}} + \frac{2}{\gamma-1} c_3 \left(\left(\frac{\mu_1}{a}\right)^{\frac{\gamma-1}{2\gamma}} - 1 \right)$, with:

$$A_1 = \sqrt{\tau_1 P_1}\sqrt{\beta - 1} \quad \text{and} \quad a = \frac{P_3}{P_1} \geq 1.$$

We remark that $\frac{\mu_1}{\mu_2} = a$, since $P_5 = P_4$.
In the current wave configuration, $\mu_1 \in (1, a]$, since $\mu_1 = \frac{P_4}{P_1} > 1$ and $\mu_2 = \frac{\mu_1}{a} \leq 1$ thus $\mu_1 \leq a$. The function $l(\mu_1)$ is strictly increasing over the interval $(1, a]$ from $l(1) < 0$ to $l(a) > 0$. Thus, if $u_1 \in (0, l(a)]$, the unique solution is the present configuration with a 1-shock / 3-rarefaction configuration, else, if $u_1 > l(a)$, the solution is the 1-shock / 3-shock configuration as detailed below.

1.D.3.2 1-Shock / 3-shock solution

The jump relations for the 3-shock give:

$$\begin{cases} (u_5 - u_3)^2 = (u_4 - u_3)^2 = (P_5 - P_3)(\tau_3 - \tau_5), \\ \mu_2 = \dfrac{P_5}{P_3} = \dfrac{\beta z_2 - 1}{\beta - z_2} > 1. \end{cases}$$

Similarly, it follows $z_2 = \dfrac{1 + \beta\mu_2}{\beta + \mu_2}$. So the scalar non-linear equation to be solved for the 1-shock / 3-shock configuration is:

$$q(\mu_2) = A_1 \frac{a\mu_2 - 1}{\sqrt{1 + a\beta\mu_2}} + A_2 \frac{\mu_2 - 1}{\sqrt{1 + \beta\mu_2}} = u_1 - u_3 = u_1,$$

with $A_2 = \sqrt{\tau_3 P_3}\sqrt{\beta - 1}$ and $\mu_2 = \dfrac{P_5}{P_3} > 1$.
This equation has a unique solution if and only if $u_1 > A_1 \dfrac{a - 1}{\sqrt{1 + a\beta}}$.

Hence, two configurations are identified:

- if $u_1 > A_1 \dfrac{(a-1)}{\sqrt{1+a\beta}}$ the solution is the 1-shock–3-shock configuration with $\mu_2 > 1$ such that $q(\mu_2) = u_1$,
- if $0 < u_1 \leq A_1 \dfrac{(a-1)}{\sqrt{1+a\beta}}$, the solution is the 1-shock–3-rarefaction configuration with $\mu_1 \in [1, a]$ such that $l(\mu_1) = u_1$.

This completely determines states $\boldsymbol{W}_4$ and $\boldsymbol{W}_5$.

1.D.4 Shock wave reflection with the wall for a stiffened gas EOS

The calculation of the analytic solution is now performed with a stiffened gas thermodynamic law.

The method of calculation is the same as with an ideal gas EOS. A 1D Riemann problem is solved, thanks to the jump relations. For a stiffened gas, the EOS is:

$$P + \gamma\Pi_\infty = (\gamma - 1)\rho\epsilon.$$

This implies:

$$c^2 = \gamma(P + \Pi_\infty)\tau \quad \text{and} \quad s = (P + \Pi_\infty)\tau^\gamma.$$

The jump relations for a 1-shock and the symmetry of the problem give:

$$\begin{cases} u_3 = 0, & (1.70a) \\ \left([u]_2^3\right)^2 + [P + \Pi_\infty]_2^3 [\tau]_2^3 = 0, & (1.70b) \\ [\epsilon]_2^3 + \dfrac{P_2 + P_3}{2} [\tau]_2^3 = 0. & (1.70c) \end{cases}$$

Equation (1.70c) is equivalent to:

$$[\tau(P + \Pi_\infty)]_2^3 + (\gamma - 1)\frac{P_2 + \Pi_\infty + P_3 + \Pi_\infty}{2} [\tau]_2^3 = 0.$$

The change of variable $\widetilde{P} = P + \Pi_\infty$ thus yields:

$$\begin{cases} \left([u]_2^3\right)^2 + \left[\widetilde{P}\right]_2^3 [\tau]_2^3 = 0, \\ \dfrac{\tau_2 + \tau_3}{2} \left[\widetilde{P}\right]_2^3 + \gamma\dfrac{\widetilde{P}_2 + \widetilde{P}_3}{2} [\tau]_2^3 = 0. \end{cases}$$

The same system than for the ideal gas EOS is recovered. The solution is then identical. The unknown is always the ratio $z = \frac{\rho_3}{\rho_2}$ and the equation to be solved is:

$$g(z) = \frac{(z-1)^2}{z(\beta - z)} = \frac{\gamma - 1}{2\gamma}\frac{\rho_2 u_2^2}{\widetilde{P}_2} := b.$$

The unique solution of this equation is called $z_0 > 1$ and the relation $\dfrac{P_3 + \Pi_\infty}{P_2 + \Pi_\infty} = \dfrac{\beta z_0 - 1}{\beta - z_0}$ allows to retrieve the pressure variable:

$$P_3 - P_2 = (P_2 + \Pi_\infty)(\beta + 1)\frac{z_0 - 1}{\beta - z_0}.$$

Remark 1.D.1 (low velocity situation). *In the case of low Mach number, $b \ll 1$, then a first order approximation of the solution is:*

$$z_0 \approx 1 + \sqrt{b(\beta - 1)},$$

thus $P_3 - P_2 = (P_2 + \Pi_\infty)\,\gamma\dfrac{|u_2|}{c_2}$ and if $P_2 \ll \Pi_\infty$, the relative difference is close to $\dfrac{P_3 - P_2}{P_2} \approx \gamma\dfrac{\Pi_\infty}{P_2}\dfrac{|u_2|}{c_2}$.

References

[3] F. Barre and M. Bernard. "The CATHARE code strategy and assessment". In: *Nuclear Engineering and Design* 124(3):257-284 (1990) (cit. on pp. 9, 28).

[4] S. Aubry, C. Caremoli, J. Olive, and P. Rascle. "The THYC three-dimensional thermal-hydraulic code for rod bundles: recent developments and validation tests". In: *Nuclear technology* 112.3 (1995), pp. 331–345 (cit. on pp. 10, 14, 28, 110, 215).

[6] I. Toumi, A. Bergeron, D. Gallo, E. Royer, and D. Caruge. "FLICA-4: A three-dimensional two-phase flow computer code with advanced numerical methods for nuclear applications". In: *Nuclear Engineering and Design* 200 (2000), pp. 139–155 (cit. on pp. 10, 13, 15, 28).

[9] *Code_Saturne 5.2.0 Theory Guide*. EDF R&D. 2018. URL: https://code-saturne.org/cms/sites/default/files/docs/5.2/theory.pdf (cit. on pp. 10, 28, 92, 93, 176).

[16] R. Eymard, T. Gallouët, and R. Herbin. "Finite Volume Methods". In: *Handbook for Numerical Analysis, P.G. Ciarlet, J.L. Lions eds, North Holland* 7 (2006), pp. 713–1020 (cit. on pp. 10, 29, 33, 92, 94, 120, 177).

[20] J. Smoller. *Shock Waves and Reaction-Diffusion Equations*. Vol. 258. A Series of Comprehensive Studies in Mathematics. New York: Springer-Verlag, 1994 (cit. on pp. 11, 12, 47, 82, 119, 127, 181).

[23] Y. Davit, C.G. Bell, H.M. Byrne, L.A.C. Chapman, L.S. Kimpton, K.H.L. Lang G.E. Leonard, J.M. Oliver, N.C. Pearson, R.J. Shipley, S.L. Waters, J.P. Whiteley, B.D. Wood, and M. Quintard. "Homogenization via formal multiscale asymptotics and volume averaging: how do the two techniques compare?" In: *Advances in Water Resources* 62 (2013), pp. 178–206 (cit. on pp. 13, 29).

[25] A.-J. Chorin. "Numerical solution of the Navier-Stokes equations". In: *Mathematics of Computation* 22(104):745–762 (1968) (cit. on pp. 15, 29, 90, 92, 176).

[27] R. Temam. "Sur l'approximation de la solution des équations de Navier-Stokes par la méthode des pas fractionnaires (II)". In: *Archive for Rational Mechanics and Analysis* 33.5 (1969), pp. 377–385 (cit. on pp. 15, 29, 90, 92, 176).

[30] M. Grandotto and P. Obry. "Steam generators two phase flows numerical simulation with liquid and gas momentum equations". In: *Nuclear Science and Engineering* 151 (2005), pp. 313–318. URL: https://hal-cea.archives-ouvertes.fr/cea-00275766 (cit. on pp. 15, 28).

[31] M. Grandotto and P. Obry. "Calculs des écoulements diphasiques dans les échangeurs par une méthode aux éléments finis". In: *Revue Européenne des Eléments Finis* 5.1 (1996), pp. 53–74 (cit. on pp. 15, 28).

[33] M. Belliard. "Méthodes de décomposition de domaine et de frontière immergée pour la simulation des composants nucléaires". Habilitation à Diriger des Recherches. Aix-Marseille Université, 2014. URL: https://tel.archives-ouvertes.fr/tel-01085328 (cit. on pp. 15, 28).

[38] L. Girault and J.-M. Hérard. "Multidimensional computations of a two-fluid hyperbolic model in a porous medium". In: *International Journal on Finite Volumes* 7.1 (2010), pp. 1–33. URL: https://hal.archives-ouvertes.fr/hal-01114209 (cit. on pp. 16, 17, 29).

[41] J.-M. Hérard and X. Martin. "An integral approach to compute compressible fluid flows in domains containing obstacles." In: *International Journal on Finite Volumes* 12.1 (2015), pp. 1–39. URL: https://hal.archives-ouvertes.fr/hal-01166478/ (cit. on pp. 17, 29, 60).

[45] F. Archambeau, J.-M. Hérard, and J. Laviéville. "Comparative study of pressure-correction and Godunov-type schemes on unsteady compressible cases". In: *Computers & Fluids* 38 (2009), pp. 1495–1509 (cit. on pp. 20, 29, 33, 43).

[47] R. Menikoff and B.J. Plohr. "The Riemann problem for fluid flow of real materials". In: *Rev. Mod. Phy.* 61.1 (1989), pp. 75–130 (cit. on pp. 20, 31).

[48] *Institut de Radioprotection et de Sûreté Nucléaire (IRSN), Reactivity-Initiated Accident (RIA)*. 2019. URL: https://www.irsn.fr/FR/connaissances/Installations_nucleaires/Les-centrales-nucleaires/criteres_surete_ria_aprp/Pages/1-accident-reactivite-RIA.aspx (cit. on pp. 20, 28, 30, 59).

[50] *Nuclear Energy Agency (NEA), Loss-Of-Coolant Accident (LOCA)*. 2009. URL: https://www.oecd-nea.org/nsd/reports/2009/nea6846_LOCA.pdf (cit. on p. 28).

[51] *FLACS Software*. GEXCON. 2018. URL: https://www.gexcon.com/products-services/FLACS-Software/22/en (cit. on p. 29).

[52] D.-R. Van Der Heul, C. Vuik, and P. Wesseling. "A conservative pressure-correction method for flow at all speeds". In: *Computers & Fluids* 32 (2003), pp. 1113–1132 (cit. on pp. 29, 176).

[53] T. Gallouët, L. Gastaldo, J.-C. Latché, and R. Herbin. "An unconditionnally stable pressure correction scheme for compressible barotropic Navier-Stokes equations". In: *ESAIM: Mathematical Modelling and Numerical Analysis* 44.2 (2010), pp. 251–287. URL: https://hal.archives-ouvertes.fr/hal-00179610 (cit. on pp. 29, 176).

[54] W. Kheriji, R. Herbin, and J.-C. Latché. "Pressure correction staggered schemes for barotropic one-phase and two-phase flows". In: *Computers & Fluids* 88 (2013), pp. 524–542. URL: https://hal.archives-ouvertes.fr/hal-00875348 (cit. on pp. 29, 176).

[55] C. Zaza. "Contribution to numerical methods for all Mach flow regimes and to fluid-porous coupling for the simulation of homogeneous two-phase flows in nuclear reactors". PhD thesis. Aix-Marseille Université, 2015. URL: \https://tel.archives-ouvertes.fr/tel-01135355 (cit. on pp. 29, 33, 38, 176, 179).

[56] X. Martin. "Modélisation d'écoulements fluides en milieu encombré d'obstacles". PhD thesis. Aix-Marseille Université, Chapter 3, pages 207–238, 2015. URL: https://tel.archives-ouvertes.fr/tel-01235089 (cit. on pp. 31, 33).

[57] R. Eymard, T. Gallouët, C. Guichard, R. Herbin, and R. Masson. "TP or not TP, that is the question". In: *Computational Geosciences* 18 (Aug. 2014), pp. 285–296. URL: https://hal.archives-ouvertes.fr/hal-00801648 (cit. on pp. 36, 94, 96, 111, 180, 192).

[58] T. Buffard, T. Gallouët, and J.-M. Hérard. "A sequel to a rough Godunov scheme: application to real gases". In: *Computers & Fluids* 29.7 (2000), pp. 813–847 (cit. on pp. 38–40, 76, 121, 127–129, 182).

[59] F. Dubois. "Boundary conditions and the Osher scheme for the Euler equations of gas dynamics." In: *Internal Report CMAP 170, Ecole Polytechnique, Palaiseau, France* (1987) (cit. on pp. 40, 121).

[60] F. Blondel, B. Audebert, T. Pasutto, and M. Stanciu. "Condensation models and boundary conditions for non-equilibrium wet steam flows." In: *International Journal on Finite Volumes* 10 (2013), pp. 1–53 (cit. on pp. 40, 121).

Chapter 2

An Implicit Cell-centred Finite Volume Method for Incompressible Fluid Flows with Fluid Section Jumps

Contents

1 Introduction

An important concern of the industrial computational fluid dynamics is the numerical simulation of steady state flows interior to a channel with variable cross section, such as flows in pipes of an hydraulic system, see FIGURE 2.1, or in congested media as the core of a nuclear reactor, see FIGURE 2.2.

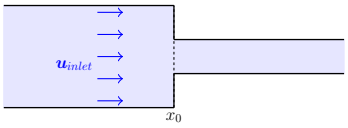

FIGURE 2.1 – *Flow in a pipe with a discontinuous fluid section at $x = x_0$.*

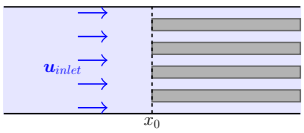

FIGURE 2.2 – *Flow in a congested medium with discontinuous fluid sections at $x = x_0$.*

The present work is devoted to the numerical simulation of channel flow in congested media when its cross sections are subject to sudden variations in space. A critical point is to compute the **steady state** of those flows in presence of **discontinuous cross sections**.

Herein, we propose to use the integral formulation of the flow governing equations described in chapter 1 and in [46, 40] to deal with this flow configuration. The cross section discontinuity is taken into account in the mesh of the computational domain with a reduction of fluid surfaces.

Nevertheless, the existing numerical scheme of the integral formulation, as initially described in chapter 1, does not allow to preserve the steady state on either side of the discontinuous interface. The approximate solution does not match with the steady one-dimensional analytic solution. This discrepancy may be attributed to the fact that the pressure drop at the discontinuous interface is not accounted for in an appropriate way at the discrete level in the momentum balance equation.

The numerical scheme framework is the following: a collocated finite volume scheme in space, using the same control volumes for both the scalar and the vector unknowns, and a pressure-correction scheme in time allowing a semi-implicit time integration thanks to a fractional-step method. This method is relevant to address the issue of slow dynamics at large time steps, thanks to its built-in stability properties. It has been introduced in [25, 26, 27] for incompressible flows and extended to compressible flows in [61, 62]. This method involves an elliptic step for a pressure correction.

Due to the collocated feature of the present scheme, the discretization in space requires cell value interpolations to approximate the face values. Those interpolations assume smooth fields which are not satisfied at this interface: fields are actually discontinuous.

The proposed method is to alter the collocated finite volume scheme in space in order to take up this discontinuous cross section issue by ensuring the steady state at the discrete level. Since the problem is not specific to the scheme of the compressible Euler equations, we focus initially on the incompressible Euler equations governing inviscid incompressible fluid flows.

In this chapter, we introduce another interpolation of the pressure and the velocity at the interface based on the steady balances over a dual mesh attached to the face of the primal mesh of the computational domain. It allows to enforce the preservation of the discontinuous steady state for flow configurations when fluid section jumps at the interface.

The chapter is organized as follows. The incompressible Euler equations (the classical model for inviscid incompressible fluid flows) are first presented. Next, the multi-dimensional integral formulation, presented in chapter 1, is applied to these equations. Its time and spatial discretizations are then described through a semi-implicit-in-time and collocated finite volume numerical scheme using a fractional step method. Second, an extension of the collocated space scheme is proposed in order to build a numerical method which recovers the steady state flow with discontinuous cross section. Third, the numerical method is thus verified on an analytic test case considering a steady plane channel flow with a discontinuous constriction of its cross section. Finally it is closed with a conclusion.

2 Model: flow governing equations

The Euler equations for incompressible fluid flows are considered on a finite time interval $(0,T)$, $T \in \mathbb{R}_+^*$ and in an open connected bounded domain $\Omega \subset \mathbb{R}^d$ ($d = 1, 2$ or 3):

$$\begin{cases} \partial_t \boldsymbol{Q} + \mathbf{div}\,(\boldsymbol{u} \otimes \boldsymbol{Q}) + \boldsymbol{\nabla} P = 0 \quad \text{in } \Omega \times (0,T)\,, \\ \mathrm{div}\,(\boldsymbol{Q}) = 0, \end{cases} \tag{2.1}$$

where $\boldsymbol{u} : \Omega \times (0,T) \to \mathbb{R}^3$ is the velocity and $P : \Omega \times (0,T) \to \mathbb{R}$ the pressure of the fluid. $\boldsymbol{Q} = \rho_0 \boldsymbol{u}$ denotes the momentum per unit volume. This system must be supplemented by the initial condition $\boldsymbol{u}(\boldsymbol{x}, t = 0) = \boldsymbol{u}_0(\boldsymbol{x})$ in Ω and by boundary conditions on $\partial\Omega$ for the velocity or the pressure. Herein, we assume that the density $\rho_0 > 0$ is a constant reference density.

3 Integral formulation

The integral formulation, described in chapter 1 [46] and in [40], is applied to the incompressible Euler equations. Set of equations (2.1) is integrated over fixed control volumes Ω_i, $i \in \mathbb{N}$, which may potentially contain many disjoint solid obstacles. Before proceeding further, we recall that obstacles may be completely or partially included in Ω_i. Part of a control volume boundary may coincide with the surface of an obstacle, see FIGURE 2.3 for an example of an obstructed cell. The whole volume occupied by fluid within Ω_i is denoted by Ω_i^ϕ.

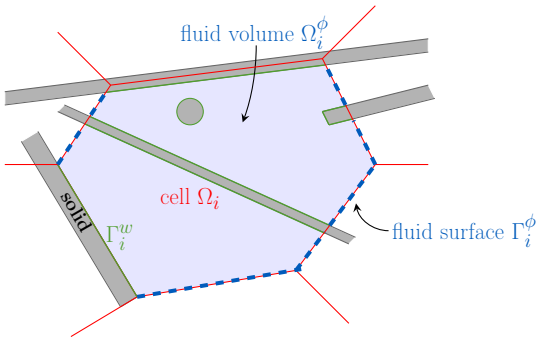

FIGURE 2.3 – *Sketch of a cell including fluid and solid.*

The mean value of a quantity $\boldsymbol{\varphi}(\boldsymbol{x}, t)$, with $\boldsymbol{x} \in \Omega$ and $t \in \mathbb{R}^+$, within each cell Ω_i of the

mesh of Ω, is:

$$\boldsymbol{\varphi}_i(t) = \frac{1}{\left|\Omega_i^\phi\right|} \int_{\Omega_i^\phi} \boldsymbol{\varphi}(\boldsymbol{x}, t) \mathrm{d}\boldsymbol{x}. \tag{2.2}$$

Applying the same methodology as in chapter 1 for the incompressible Euler equations gives, in integrating equations (2.1) over a bounded time interval $[t_0, t_1] \subset (0, T)$ and space with respect to the fluid part of the cell Ω_i, for all $i \in \{1, ..., N\}$:

$$\begin{cases} \left|\Omega_i^\phi\right| \rho_0 \left(\boldsymbol{u}_i\left(t_1\right) - \boldsymbol{u}_i\left(t_0\right)\right) + \displaystyle\int_{t_0}^{t_1} \int_{\Gamma_i} \left(\boldsymbol{u}\left(\boldsymbol{x}, t\right) \boldsymbol{Q}(\boldsymbol{x}, t) \cdot \boldsymbol{n}(\boldsymbol{x}) + P\left(\boldsymbol{x}, t\right) \boldsymbol{n}(\boldsymbol{x})\right) \mathrm{d}\gamma(\boldsymbol{x}) dt = 0, \\ \displaystyle\int_{\Gamma_i} \boldsymbol{Q}(\boldsymbol{x}, t) \cdot \boldsymbol{n}(\boldsymbol{x}) \mathrm{d}\gamma(\boldsymbol{x}) = 0, \end{cases} \tag{2.3}$$

where $\Gamma_i = \partial\Omega_i^\phi$ denotes the whole boundary of the fluid cell Ω_i^ϕ and $\boldsymbol{n}(\boldsymbol{x})$ its unit outward normal vector.

The slip condition at the wall $\boldsymbol{u} \cdot \boldsymbol{n}|_w = 0$ means that the mass flux is equal to zero through the wall boundary Γ_i^w. Thus, the pressure integral on the wall boundary is the unique contribution. Integral formulation (2.3) yields by decomposing on the fluid Γ_i^ϕ and wall Γ_i^w boundaries, for all Ω_i:

$$\begin{cases} \left|\Omega_i^\phi\right| \rho_0 \left(\boldsymbol{u}_i(t_1) - \boldsymbol{u}_i(t_0)\right) + \displaystyle\int_{t_0}^{t_1} \int_{\Gamma_i^\phi} \left(\boldsymbol{u}(\boldsymbol{Q} \cdot \boldsymbol{n}) + P\boldsymbol{n}\right) \mathrm{d}\gamma dt + \int_{t_0}^{t_1} \int_{\Gamma_i^w} P\boldsymbol{n} \mathrm{d}\gamma dt = 0, \\ \displaystyle\int_{\Gamma_i^\phi} \boldsymbol{Q} \cdot \boldsymbol{n} \mathrm{d}\gamma = 0. \end{cases} \tag{2.4}$$

Set of equations (2.4) is rewritten by summing up on the interfaces of Ω_i:

$$\begin{cases} \left|\Omega_i^\phi\right| \rho_0 \left(\boldsymbol{u}_i(t_1) - \boldsymbol{u}_i(t_0)\right) + \displaystyle\int_{t_0}^{t_1} \left(\sum_{j \in N(i)} \int_{\Gamma_{ij}^\phi} \left(\boldsymbol{u}(\boldsymbol{Q} \cdot \boldsymbol{n}) + P\boldsymbol{n}\right) \mathrm{d}\gamma \right) dt + \int_{t_0}^{t_1} \int_{\Gamma_i^w} P\boldsymbol{n} \mathrm{d}\gamma dt = 0, \\ \displaystyle\sum_{j \in N(i)} \int_{\Gamma_{ij}^\phi} \boldsymbol{Q} \cdot \boldsymbol{n} \mathrm{d}\gamma = 0. \end{cases} \tag{2.5}$$

We recall that the subscript ij refers to the interfaces between the neighbouring control volumes Ω_i and Ω_j, with $j \in N(i)$ and $N(i)$ defines the set of neighbouring cells of Ω_i.

4 Discretization

The incompressible Euler equations are solved with a first order semi-implicit in time collocated finite volume method, using the same control volumes for both the scalar and the vector unknowns [16]. The algorithm, described below and integrated in the open-source *Code_Saturne* software [9], corresponds to SIMPLEC (Semi-Implicit Method for Pressure Linked Equations-Consistent) algorithm [63], commonly used to solve the incompressible Navier-Stokes equations, and falls within the class of pressure-correction algorithm, so-called projection methods introduced in [25, 26, 27] and revisited in [28]. A fractional-step method, involving a prediction and a correction of the velocity, is used to solve the conservation of momentum coupled with the incompressibility constraint, Equation (2.1). Numerical fluxes are evaluated by finite volume space schemes, considering one mean fluid value $\mathbf{u}_i^n$ per cell Ω_i at each discrete time t^n; $\mathbf{u}_i^n$ is an approximation of $\boldsymbol{u}_i(t^n)$. Many standard first or second order finite volume schemes are

available as upwind, centred with or without limiters, SOLU, see the theory manual [9] for more details. We are considering here only an upwind scheme for the sake of simplicity, without loss of generality (the coding is made for all the available schemes).

4.1 Time scheme

The time discretization of Equation (2.5) is based on a fractional step time scheme with an implicit first order Euler integration for each step.

$\Delta t = t^{n+1} - t^n$ denotes the time step, between two successive times t^n and t^{n+1} of the time interval $(0, T)$.

Each time step is then divided in two steps. Starting with the initial condition $\mathbf{u}^n$ and P^n for all $n \in \mathbb{N}$, the momentum balance equation (2.6) is first solved and provides a predicted velocity $\tilde{\mathbf{u}}$, with a linearisation of the convective flux:

$$\rho_0 \frac{\tilde{\mathbf{u}} - \mathbf{u}^n}{\Delta t} + \mathbf{div}\ (\tilde{\mathbf{u}} \otimes \boldsymbol{Q}^n) + \boldsymbol{\nabla} P^n = 0. \tag{2.6}$$

The continuity equation is taken into account during the second step: the mass flux at the faces is corrected by solving a discrete Poisson equation (2.7) on the pressure temporal increment:

$$\begin{cases} \text{div}\ \left(\boldsymbol{Q}^{n+1}\right) = 0, \\ \dfrac{\boldsymbol{Q}^{n+1} - \rho_0 \tilde{\mathbf{u}}}{\Delta t} + \boldsymbol{\nabla}\left(P^{n+1} - P^n\right) = 0. \end{cases} \tag{2.7}$$

Equation (2.7) is used to update both the mass flux at the faces and the discrete velocity, $\mathbf{u}^{n+1} = \frac{\boldsymbol{Q}^{n+1}}{\rho_0}$.

Remark 4.1. *Note that second order in time schemes, as the Cranck-Nicolson method, can be also used, see [9].*

4.1.1 Prediction step: momentum balance

A predicted velocity field $\tilde{\mathbf{u}}$ is obtained by solving the momentum balance equation (2.6) with a semi-implicit scheme; the velocity is implicit, while the pressure is explicit. The time scheme of the integral formulation of the momentum equation gives for any cell Ω_i:

$$\left|\Omega_i^\phi\right| \rho_0 \left(\tilde{\mathbf{u}}_i - \mathbf{u}_i^n\right) + \Delta t \int_{\Gamma_i^\phi} (\tilde{\boldsymbol{u}} - \boldsymbol{u}^n)\,(\boldsymbol{Q}^n \cdot \boldsymbol{n}) \mathrm{d}\gamma = -\Delta t \int_{\Gamma_i^\phi} \boldsymbol{u}^n (\boldsymbol{Q}^n \cdot \boldsymbol{n}) \mathrm{d}\gamma - \Delta t \int_{\Gamma_i^\phi \cup \Gamma_i^w} P^n \boldsymbol{n} \mathrm{d}\gamma. \tag{2.8}$$

We note that at the right hand side of equation (2.8) appears the steady-state momentum balance. This first step provides, for all Ω_i, the unknown $\tilde{\mathbf{u}}_i$, by solving a linear system (using, by default, a block Gauss-Seidel solver). This predicted velocity has an *a priori* non-zero divergence.

4.1.2 Correction step: mass balance

The second step, equation (2.7), corrects the velocity at faces to impose the incompressibility constraint over the time interval Δt. The integral formulation of the mass flux reads over this time interval, for any cell Ω_i:

$$\int_{\Gamma_i^\phi} \boldsymbol{Q}^{n+1} \cdot \boldsymbol{n} \mathrm{d}\gamma = 0. \tag{2.9}$$

The mass flux $\boldsymbol{Q}^{n+1} \cdot \boldsymbol{n}$ is computed from semi-discrete simplified momentum equation (2.10) at the fluid interfaces, with $\delta P_i = P_i^{n+1} - P_i^n$ the pressure temporal increment:

$$\boldsymbol{Q}^{n+1} \cdot \boldsymbol{n} = \rho_0 \tilde{\boldsymbol{u}} \cdot \boldsymbol{n} - \Delta t \boldsymbol{\nabla} \delta P \cdot \boldsymbol{n}. \tag{2.10}$$

Thus the integration of Equation (2.10) gives semi-discrete Poisson equation (2.11):

$$-\int_{\Gamma_i^\phi} \Delta t \boldsymbol{\nabla} \delta P \cdot \boldsymbol{n} = -\int_{\Gamma_i^\phi} \rho_0 \tilde{\boldsymbol{u}} \cdot \boldsymbol{n}. \tag{2.11}$$

This second step provides, for all cells Ω_i, the unknown δP_i by solving a linear system. Thus, the pressure is updated such that: $P_i^{n+1} = P_i^n + \delta P_i$.

4.1.3 Velocity update

Finally, the velocity is corrected with equation (2.7), which corresponds to the semi-discrete simplified momentum equation (2.10) written at cells:

$$\mathbf{u}_i^{n+1} = \tilde{\mathbf{u}}_i - \frac{\Delta t}{\left|\Omega_i^\phi\right| \rho_0} \int_{\Gamma_i^\phi \cup \Gamma_i^w} \delta P \boldsymbol{n} \mathrm{d}\gamma. \tag{2.12}$$

Remark 4.2. *The pressure increment is used in the projection step of the velocity to recover an implicit scheme of the momentum equation on the pressure by summing Equation (2.8) and (2.12).*

$$\left|\Omega_i^\phi\right| \rho_0 \left(\mathbf{u}_i^{n+1} - \mathbf{u}_i^n\right) + \Delta t \int_{\Gamma_i^\phi} \tilde{\boldsymbol{u}} (\boldsymbol{Q}^n \cdot \boldsymbol{n}) \mathrm{d}\gamma + \Delta t \int_{\Gamma_i^\phi \cup \Gamma_i^w} P^{n+1} \boldsymbol{n} \mathrm{d}\gamma = 0. \tag{2.13}$$

Remark 4.3. *The prediction-correction method can be extended by using a PISO (Pressure-Implicit with Splitting of Operators) like algorithm with sub-iterations of equations (2.8), (2.11) and (2.12) over the time interval (t^n, t^{n+1}) in order to update the discrete velocity in the momentum balance equation.*

4.2 Space scheme

In the following, integral formulation (2.5) is discretised in space with a first order cell-centred finite volume scheme. Numerical fluxes are evaluated from the discrete variables to compute the different boundary integrals. We focus on the numerical fluxes on the boundary of a cell intersected by solids. The space scheme is detailed for admissible meshes in the sense of [16, 57], implying some simplifications for the increment pressure gradient approximation used in equation (2.7).

4.2.1 Prediction step: momentum balance

First the approximation of the convective flux is detailed. The numerical flux is summed on all the fluid interfaces Γ_{ij}^ϕ of the cell Ω_i and approximated here by an upwind scheme.

$$\left|\Omega_i^\phi\right| \mathbf{div}_i(\tilde{\mathbf{u}} \otimes \boldsymbol{Q}^n) = \int_{\Gamma_i^\phi} \tilde{\boldsymbol{u}} (\boldsymbol{Q}^n \cdot \boldsymbol{n}) \mathrm{d}\gamma = \sum_{j \in N(i)} \int_{\Gamma_{ij}^\phi} \tilde{\boldsymbol{u}} (\boldsymbol{Q}^n \cdot \boldsymbol{n}) \mathrm{d}\gamma = \sum_{j \in N(i)} \tilde{\boldsymbol{u}}_{ij}^{upw} \left(\boldsymbol{Q}^n \cdot \boldsymbol{n}\right)_{ij} S_{ij}^\phi. \tag{2.14}$$

The mass flux is known from the previous time step such that $\sum_{j \in N(i)} \left(\boldsymbol{Q}^n \cdot \boldsymbol{n}\right)_{ij} S_{ij}^\phi = 0$, and the implicit convected velocity at the fluid interfaces is:

$$\tilde{\mathbf{u}}_{ij}^{upw} = \lambda_{ij}^n \tilde{\mathbf{u}}_i + (1 - \lambda_{ij}^n) \tilde{\mathbf{u}}_j, \tag{2.15}$$

with:

$$\lambda_{ij}^n = \begin{cases} 1 & \text{if } (\boldsymbol{Q}^n \cdot \boldsymbol{n})_{ij} \geq 0, \\ 0 & \text{otherwise.} \end{cases}$$

Second, the approximation of the pressure gradient is detailed. The boundary integral is decomposed on the fluid interfaces and the walls for all cells Ω_i:

$$\left|\Omega_i^\phi\right| \boldsymbol{\nabla}_i P^n = \int_{\Gamma_i} P^n \boldsymbol{n} \mathrm{d}\gamma = \int_{\Gamma_i^w} P^n \boldsymbol{n} \mathrm{d}\gamma + \int_{\Gamma_i^\phi} P^n \boldsymbol{n} \mathrm{d}\gamma = \int_{\Gamma_i^w} P_w^n \boldsymbol{n} \mathrm{d}\gamma + \sum_{j \in N(i)} P_{ij}^n S_{ij}^\phi.$$

The fluid interface pressure is computed by a linear interpolation of the neighbouring cell pressures:

$$P_{ij}^n = \frac{h_{ij/j} P_i^n + h_{ij/i} P_j^n}{h_{ij/i} + h_{ij/j}} = \alpha_{ij} P_i^n + (1 - \alpha_{ij}) P_j^n. \tag{2.16}$$

with:

$$\alpha_{ij} = \frac{h_{ij/j}}{h_{ij/i} + h_{ij/j}}, \tag{2.17}$$

and $h_{ij/i}$ (respectively $h_{ij/j}$) stands for the distance from the mass centre of the cell Ω_i (respectively Ω_j) to the interface Γ_{ij}^ϕ.

For the interior walls of Γ_i^w, a simple alternative for the wall pressure P_w^n approximation is to take the cell value:

$$P_w^n = P_i^n. \tag{2.18}$$

Eventually, the pressure force reads:

$$\begin{aligned} \left|\Omega_i^\phi\right| \boldsymbol{\nabla}_i P^n = \int_{\Gamma_i} P^n \boldsymbol{n} \mathrm{d}\gamma &= \sum_{j \in N(i)} P_{ij}^n \boldsymbol{n}_{ij} S_{ij}^\phi + P_i^n \int_{\Gamma_i^w} \boldsymbol{n} \mathrm{d}\gamma \\ &= \sum_{j \in N(i)} P_{ij}^n \boldsymbol{n}_{ij} S_{ij}^\phi + P_i^n \left(- \sum_{j \in N(i)} \boldsymbol{n}_{ij} S_{ij}^\phi \right) \\ &= \sum_{j \in N(i)} \left(P_{ij}^n - P_i^n \right) \boldsymbol{n}_{ij} S_{ij}^\phi. \end{aligned}$$

Remark 4.4. *We have used the fact that the integral of the normal vector on a closed boundary vanishes:*

$$\int_{\Gamma_i} \boldsymbol{n} \mathrm{d}\gamma = 0 = \sum_{j \in N(i)} \boldsymbol{n}_{ij} S_{ij}^\phi + \int_{\Gamma_i^w} \boldsymbol{n} \mathrm{d}\gamma.$$

4.2.2 Correction step: mass balance

The semi-discrete Poisson equation (2.11) is discretised in space by a centred scheme.

- Explicit mass flux approximation:

$$\left|\Omega_i^\phi\right| \mathrm{div}_i(\rho_0 \tilde{\boldsymbol{u}}) = \int_{\Gamma_i^\phi} \rho_0 \tilde{\boldsymbol{u}} \cdot \boldsymbol{n} \mathrm{d}\gamma = \sum_{j \in N(i)} \int_{\Gamma_{ij}^\phi} \rho_0 \tilde{\boldsymbol{u}} \cdot \boldsymbol{n} \mathrm{d}\gamma = \sum_{j \in N(i)} \rho_0 \tilde{\boldsymbol{u}}_{ij}^{cent} \cdot \boldsymbol{n}_{ij} S_{ij}^\phi, \tag{2.19}$$

where $\boldsymbol{n}_{ij}$ is the unit outward normal vector at the fluid interface Γ_{ij}^ϕ from Ω_i^ϕ to Ω_j^ϕ. The normal velocity at the fluid interfaces is linearly interpolated between the two neighbouring cell values:

$$\tilde{\boldsymbol{u}}_{ij}^{cent} \cdot \boldsymbol{n}_{ij} = \left(\alpha_{ij} \tilde{\mathbf{u}}_i + (1 - \alpha_{ij}) \tilde{\mathbf{u}}_j \right) \cdot \boldsymbol{n}_{ij}. \tag{2.20}$$

- Pressure gradient increment approximation:

The pressure gradient increment at the fluid interface is approximated with a "two-point flux approximation" scheme, which is consistent for admissible meshes, see [57]:

$$\boldsymbol{\nabla}\delta P \cdot \boldsymbol{n}_{ij} = \left.\frac{\partial \delta P}{\partial \boldsymbol{n}}\right|_{\Gamma_{ij}^{\phi}} = \frac{\delta P_j - \delta P_i}{h_{ij/i} + h_{ij/j}}. \tag{2.21}$$

Thus, the scheme yields for the Laplacian operator:

$$\begin{aligned} -\left|\Omega_i^{\phi}\right| \operatorname{div}_i(\Delta t \boldsymbol{\nabla}\delta P) = -\int_{\Gamma_i^{\phi}} \Delta t \boldsymbol{\nabla}\delta P \cdot \boldsymbol{n} \mathrm{d}\gamma &= -\sum_{j\in N(i)} \int_{\Gamma_{ij}^{\phi}} \Delta t \boldsymbol{\nabla}\delta P \cdot \boldsymbol{n} \mathrm{d}\gamma \\ &= -\sum_{j\in N(i)} \frac{\Delta t}{h_{ij/i} + h_{ij/j}} \left(\delta P_j - \delta P_i\right) S_{ij}^{\phi}. \end{aligned} \tag{2.22}$$

Once discrete Poisson equation (2.23) is solved:

$$-\sum_{j\in N(i)} \frac{\Delta t}{h_{ij/i} + h_{ij/j}} \left(\delta P_j - \delta P_i\right) S_{ij}^{\phi} = -\sum_{j\in N(i)} \rho_0 \tilde{\boldsymbol{u}}_{ij}^{cent} \cdot \boldsymbol{n}_{ij} S_{ij}^{\phi}, \tag{2.23}$$

we deduce the updated mass flux at each fluid interface, satisfying the free-divergence constraint at the discrete level:

$$\sum_{j\in N(i)} \left(\boldsymbol{Q}^{n+1} \cdot \boldsymbol{n}\right)_{ij} S_{ij}^{\phi} = \sum_{j\in N(i)} \rho_0 \tilde{\boldsymbol{u}}_{ij}^{cent} \cdot \boldsymbol{n}_{ij} S_{ij}^{\phi} - \sum_{j\in N(i)} \frac{\Delta t}{h_{ij/i} + h_{ij/j}} \left(\delta P_j - \delta P_i\right) S_{ij}^{\phi} = 0. \tag{2.24}$$

4.2.3 Velocity update

Equation (2.12) is discretized in space as for the pressure force in equation (2.8), with a centred scheme:

$$\int_{\Gamma_i^{\phi} \cup \Gamma_i^{w}} \delta P \boldsymbol{n} \mathrm{d}\gamma = \sum_{j\in N(i)} \left(\delta P_{ij}^{cent} - \delta P_i\right) \boldsymbol{n}_{ij} S_{ij}^{\phi}, \tag{2.25}$$

with:

$$\delta P_{ij}^{cent} = (1 - \alpha_{ij}) \delta P_i^n + \alpha_{ij} \delta P_j^n.$$

The update of the discrete velocity then writes:

$$\mathbf{u}_i^{n+1} = \tilde{\mathbf{u}}_i - \frac{\Delta t}{\left|\Omega_i^{\phi}\right| \rho_0} \sum_{j\in N(i)} \left(\delta P_{ij}^{cent} - \delta P_i\right) \boldsymbol{n}_{ij} S_{ij}^{\phi}. \tag{2.26}$$

4.3 Summing up: discrete incompressible Euler equations

The discrete incompressible Euler equations are summed up for any cell Ω_i, $i \in \{1, ..., N\}$:

$$\rho_0 \frac{\tilde{\mathbf{u}}_i - \mathbf{u}_i}{\Delta t} + \mathbf{div}_i((\tilde{\boldsymbol{u}} - \boldsymbol{u}^n) \otimes \boldsymbol{Q}^n) = -\boldsymbol{\nabla}_i P^n - \mathbf{div}_i(\boldsymbol{u}^n \otimes \boldsymbol{Q}^n), \tag{2.27}$$

$$\begin{cases} -\operatorname{div}_i(\Delta t \boldsymbol{\nabla}\delta P) = -\operatorname{div}_i(\rho_0 \tilde{\boldsymbol{u}}), \\ \left(\boldsymbol{Q}^{n+1} \cdot \boldsymbol{n}\right)_{ij} S_{ij}^{\phi} = \rho_0 \tilde{\boldsymbol{u}}_{ij}^{cent} \cdot \boldsymbol{n}_{ij} S_{ij}^{\phi} - \Delta t \ \boldsymbol{\nabla}\delta P \cdot \boldsymbol{n}_{ij} S_{ij}^{\phi}, \ \forall\, j \in N(i), \end{cases} \tag{2.28}$$

$$P_i^{n+1} = P_i^n + \delta P_i,$$

$$\mathbf{u}_i^{n+1} = \tilde{\mathbf{u}}_i - \frac{\Delta t}{\rho_0} \boldsymbol{\nabla}_i(\delta P). \tag{2.29}$$

5 Space discretization for discontinuous fluid sections

5.1 one-dimensional analytic solution

The problem of the steady plane channel flow with a section jump is considered, as depicted in FIGURE 2.4. The left fluid section is denoted by S_L, while the right fluid section is S_R. The bulk velocity u_L, on the left side, is known, and also the pressure P_R, on the right side. The analytical solution is computed by integrating the steady Euler incompressible equations (2.1) in space with respect to the computational fluid domain Ω^ϕ (in blue in FIGURE 2.4). In addition, the velocity u_L and the pressure P_R are assumed to be uniform in the transverse directions to the x-direction.

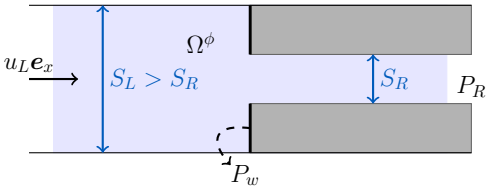

FIGURE 2.4 – *Channel flow with a constriction.*

The mass conservation gives:

$$u_L S_L = u_R S_R, \tag{2.30}$$

and the steady momentum balance gives ($S_L \geq S_R$):

$$\left(\rho_0 u_R^2 + P_R\right) S_R - \left(\rho_0 u_L^2 + P_L\right) S_L + P_w \left(S_L - S_R\right) = 0. \tag{2.31}$$

We deduce the right velocity u_R and the pressure jump $P_R - P_L$ in terms of $\Delta P^w = P_w - P_L$:

$$P_R - P_L = \frac{\rho_0 u_L S_L}{S_R}\left(u_L - u_R\right) + \Delta P^w \left(1 - \frac{S_L}{S_R}\right) = \left(\frac{\rho_0 u_L^2 S_L}{S_R} + \Delta P^w\right)\left(1 - \frac{S_L}{S_R}\right). \tag{2.32}$$

The pressure drop $P_R - P_L$ is due to the discontinuous section of the channel. The value of the difference ΔP^w is customizable, depending on the desired fluid model.

In the sequel, ΔP^w is assumed equal to zero, that is $P_w = P_L$. It is a standard approximation, allowing to obtain singular head loss in a channel with a constriction for real fluid, see [64] for more details about head losses.

Another estimation of the wall pressure based on the kinetic energy conservation is proposed in appendix 2.C. In this case, as expected for an ideal fluid governed by the incompressible Euler equations, the hydraulic head is then conserved.

Herein, the aim is to retrieve these analytic steady states (2.30) and (2.32) at the discrete level.

5.2 Inconsistency of the legacy scheme: one-dimensional approximate steady solution

Assuming a steady state, the steady integral formulation (2.5) is discretised with the legacy spatial scheme described below in section 4.2.

For the sake of simplicity, the time upperscript "n" is omitted.

The computational domain Ω is meshed with two uniform Cartesian cells Ω_L and Ω_R, see FIGURE 2.5, such that $\Omega = \Omega_L \cup \Omega_R$. The fluid section, S_{LR}^ϕ, at the interface LR between the two neighbouring cells Ω_L and Ω_R is equal to the right section, S_R.

At the left inlet boundary, the velocity is imposed $u_{in} = u_0$ (Dirichlet condition), while an homogeneous Neumann condition on the pressure is prescribed $\partial_{\boldsymbol{n}} P|_{in} = 0$. At the right outlet boundary, the pressure is imposed $P_{out} = P_0$, while an homogeneous Neumann condition on the velocity is prescribed $\partial_{\boldsymbol{n}} u|_{out} = 0$.

In this section, φ_L denotes (respectively φ_R) the discrete value of any variable φ in the cell Ω_L (respectively Ω_R).

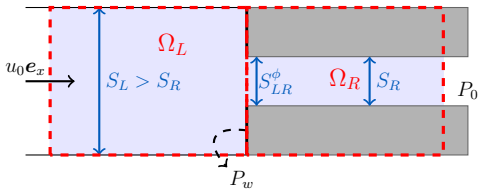

FIGURE 2.5 – *Mesh of the channel with a constriction* ($u_L > 0$).

The computation is decomposed in three steps, we write:

- the discrete mass balance, $\operatorname{div} \boldsymbol{Q} = 0$ for the cells Ω_L and Ω_R,
- Equation (2.28), the steady simplified momentum equation (correction) for the interface "in", "out" and "LR",
- Equation (2.27), the steady momentum equation (prediction) for the cells Ω_L and Ω_R.

First, the discrete mass balance holds, for the cell Ω_L:

$$-Q_{in} S_L + Q_{LR} S^\phi_{LR} = 0,$$

and for the cell Ω_R:

$$-Q_{LR} S^\phi_{LR} + Q_{out} S_R = 0. \tag{2.33}$$

Moreover, the inlet boundary condition gives $Q_{in} = \rho_0 u_0$. So, the mass conservation in Ω reads:

$$\rho_0 u_0 S_L = Q_{LR} S^\phi_{LR} = Q_{out} S_R. \tag{2.34}$$

Second, equation (2.28) gives at the discontinuous interface LR ($S^\phi_{LR} = S_R$):

$$Q_{LR} S^\phi_{LR} = Q_{LR} S_R = \rho_0 \frac{u_R + u_L}{2} S_R, \tag{2.35}$$

and at the outlet boundary, the scheme is upwind $u_{out} = u_R$:

$$Q_{out} S_R = \rho_0 u_R S_R. \tag{2.36}$$

We deduce the left and right discrete velocity:

$$u_L = u_R = u_0 \frac{S_L}{S_R}. \tag{2.37}$$

So, according to the exact solution (2.30), we have wrong discrete velocities, since $u_L \neq u_0$ if $S_L \neq S_R$ and $u_R = u_L$, see FIGURE 2.6.

Third, the discrete steady momentum balance (2.27) reads, for the cell Ω_L:

$$-Q_{in} u_{in} S_L + Q_{LR} u^{upw}_{LR} S^\phi_{LR} + P^{cent}_{LR} S^\phi_{LR} + P_w (S_L - S^\phi_{LR}) - P_{in} S_L = 0.$$

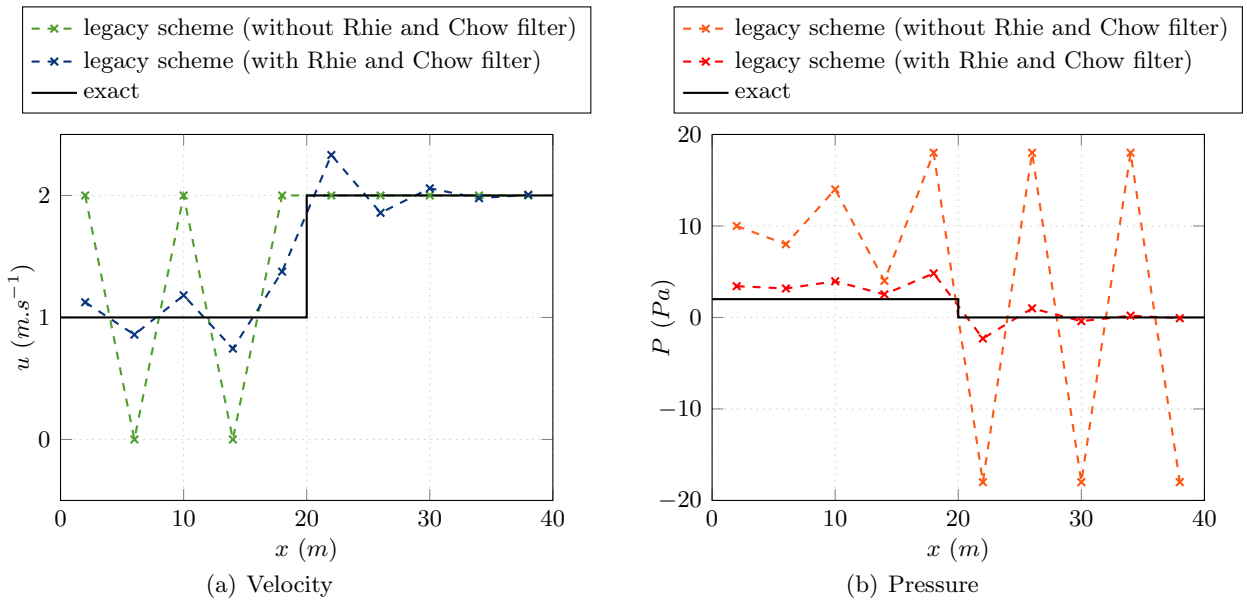

(a) Velocity (b) Pressure

FIGURE 2.6 – *Steady approximate solutions with the legacy scheme.*

The inlet boundary condition on the pressure gives $P_{in} = P_L$ and the wall pressure is assumed to be $P_w = P_L$:

$$-Q_{in}u_{in}S_L + Q_{LR}u_{LR}^{upw}S_{LR}^{\phi} + (P_{LR}^{cent} - P_L)S_{LR}^{\phi} = 0.$$

Given that the mass conservation, $Q_{in}u_{in} = Q_{LR}S_{LR}^{\phi} = \rho_0 u_0 S_L$, and the inlet condition, $u_{in} = u_0$, we deduce:

$$\frac{P_R - P_L}{2}S_R = \rho_0 u_0 S_L(u_0 - u_L),$$

After simple simplifications, we obtain the following relation:

$$P_R - P_L = 2\rho_0 u_0^2 \frac{S_L}{S_R}\left(1 - \frac{S_L}{S_R}\right). \tag{2.38}$$

For the cell Ω_R, the steady momentum balance (2.27) writes:

$$-Q_{LR}u_{LR}^{upw}S_{LR}^{\phi} + Q_{out}u_{out}S_R + (P_{out} - P_{LR}^{cent})S_R = 0,$$

Using the mass conservation $Q_{LR}S_{LR}^{\phi} = Q_{out}S_R$, $u_R = u_L = u_{out}$ and the outlet boundary condition $P_{out} = P_0$, we find:

$$P_0 S_R = \frac{P_L + P_R}{2}S_R,$$

Thus, for $S_R \neq 0$:

$$P_0 = \frac{P_L + P_R}{2}.$$

From equation (2.38), we deduce $P_R \neq P_0$ if $S_L \neq S_R$. The exact solution (2.32) is not recovered, see FIGURE 2.6.

Finally, equations (2.37) and (2.38) give wrong discrete values, in the sense that it is not consistent with equations (2.30) and(2.32) (for the pressure jump at the interface).

In conclusion, the space scheme at the interfaces, described in section 4.2, *i.e.* the spatial interpolation, does not allow to recover, at the discrete level, the one-dimensional analytic solution of the steady channel flow with discontinuous sections. It is due to the fact that the linear

interpolation to estimate the face values of the velocity and the pressure is only relevant for smooth fields in Ω, at least $C^0(\Omega)$.

In the sequel, a new space scheme is proposed to recover the analytic piecewise constant solution using the local steady balances in dual sub cells.

5.3 A new scheme preserving steady state with fluid section jumps

The new scheme consists in modifying the interpolation at the interfaces in order to evaluate numerical fluxes, in the case of a fluid section jump, with the local steady balances in the dual pyramid of each cell.

5.3.1 Dual mesh

A dual mesh, associated to the faces of the primal mesh, is defined with the diamond cells. For each interface ij of the primal cell Ω_i, the two pyramids $\widehat{\Omega}_{i/ij}$ and $\widehat{\Omega}_{j/ij}$ are built, in red in FIGURE 2.7, satisfying $\Omega_i = \cup_{j\in N(i)}\widehat{\Omega}_{i/ij}$.

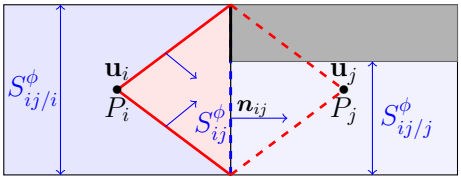

FIGURE 2.7 – *Dual cell and pyramid* $\widehat{\Omega}_{i/ij}$.

Thus, the fluid dual-surface vector $\boldsymbol{S}^\phi_{ij/i}$ is defined as the fluid surface of the face of the diamond cell in Ω_i such that:

$$\boldsymbol{S}^\phi_{ij/i} = -\int_{(\partial\widehat{\Omega}_{i/ij})^\phi\setminus\Gamma^\phi_{ij}} \boldsymbol{n}\mathrm{d}\gamma. \tag{2.39}$$

The mean value over the dual pyramid $\widehat{\Omega}^\phi_{i/ij}$ is also defined as:

$$\boldsymbol{\varphi}_{i/ij} = \frac{1}{\left|\widehat{\Omega}^\phi_{i/ij}\right|}\int_{\widehat{\Omega}^\phi_{i/ij}} \boldsymbol{\varphi}(\boldsymbol{x})\mathrm{d}\boldsymbol{x}. \tag{2.40}$$

5.3.2 Local discrete mass balance

The mass balance is integrated over the fluid part of the pyramid $\widehat{\Omega}^\phi_{i/ij}$ and holds:

$$\left|\widehat{\Omega}^\phi_{i/ij}\right| \mathrm{div}_{\,i/ij}(\boldsymbol{u}) = \int_{\widehat{\Omega}^\phi_{i/ij}} \mathrm{div}\,\boldsymbol{u}\ \mathrm{d}\boldsymbol{x} = 0, \tag{2.41}$$

giving at the discrete level,

$$\boldsymbol{u}_{ij/i}\cdot\boldsymbol{n}_{ij}S^\phi_{ij} = \mathbf{u}_i\cdot\boldsymbol{S}^\phi_{ij/i}. \tag{2.42}$$

This relation attaches the discrete velocity at cell to the velocity at face in taking into account the ratio of fluid section.

We thus define the velocity vector in the dual pyramid as:

$$\boldsymbol{u}_{ij/i} = \mathbf{u}_i\cdot\frac{\boldsymbol{S}^\phi_{ij/i}}{S^\phi_{ij}}\boldsymbol{n}_{ij} + (\mathbf{Id} - \boldsymbol{n}_{ij}\otimes\boldsymbol{n}_{ij})\,\mathbf{u}_i. \tag{2.43}$$

5.3.3 Local discrete steady momentum balance

Section jumps imply velocity jumps at interface, and therefore a non-zero convective acceleration term in the steady momentum balance, over the fluid part of the pyramid $\widehat{\Omega}^{\phi}_{i/ij}$.

Let us define $\boldsymbol{f}_{i/ij}$, in the pyramid $\widehat{\Omega}^{\phi}_{i/ij}$, the opposite of the discrete convective acceleration due to section jumps:

$$\boldsymbol{f}_{i/ij} = -\frac{\left|\widehat{\Omega}^{\phi}_{i/ij}\right|}{h_{ij/i} S^{\phi}_{ij}} \mathbf{div}_{\,i/ij}\left(\boldsymbol{u} \otimes \boldsymbol{Q}\right). \tag{2.44}$$

The convective term reads:

$$\begin{aligned}\left|\widehat{\Omega}^{\phi}_{i/ij}\right| \mathbf{div}_{\,i/ij}\left(\boldsymbol{u} \otimes \boldsymbol{Q}\right) = \int_{\widehat{\Omega}^{\phi}_{i/ij}} \mathbf{div}\ \left(\boldsymbol{u} \otimes \boldsymbol{Q}\right) \mathrm{d}\boldsymbol{x} &= \int_{(\partial\widehat{\Omega}_{i/ij})^{\phi}\setminus\Gamma^{\phi}_{ij}} \boldsymbol{u}(\boldsymbol{Q}\cdot\boldsymbol{n})\mathrm{d}\gamma + \int_{\Gamma^{\phi}_{ij}} \boldsymbol{u}(\boldsymbol{Q}\cdot\boldsymbol{n})\mathrm{d}\gamma \\ &= -\mathbf{u}_i(\boldsymbol{Q}_i\cdot\boldsymbol{S}^{\phi}_{ij/i}) + \mathbf{u}_{ij/i}\left(\boldsymbol{Q}\cdot\boldsymbol{n}\right)_{ij} S^{\phi}_{ij} \\ &= \left(\boldsymbol{u}_{ij/i} - \mathbf{u}_i\right)\left(\boldsymbol{Q}\cdot\boldsymbol{n}\right)_{ij} S^{\phi}_{ij},\end{aligned}$$

since the local mass balance is verified over the pyramid $\widehat{\Omega}^{\phi}_{i/ij}$:

$$\boldsymbol{Q}_i \cdot \boldsymbol{S}^{\phi}_{ij/i} = \left(\boldsymbol{Q}\cdot\boldsymbol{n}\right)_{ij} S^{\phi}_{ij}.$$

Thus, using equation (2.42), the projection of equation (2.44) in the $\boldsymbol{n}_{ij}$-direction gives:

$$\boldsymbol{f}_{i/ij}\cdot\boldsymbol{n}_{ij} = -\frac{1}{h_{ij/i}}\left(\boldsymbol{Q}\cdot\boldsymbol{n}\right)_{ij}\left(\frac{\boldsymbol{S}^{\phi}_{ij/i}}{S^{\phi}_{ij}} - \boldsymbol{n}_{ij}\right)\cdot\mathbf{u}_i. \tag{2.45}$$

We note that this convective acceleration per unit volume (2.45), normal to the face, is only non-zero for a fluid section jump.

Then, this convective acceleration (2.45) should be balanced by part of the pressure gradient to satisfy the local discrete steady momentum balance (2.27) over the cell Ω_i, when the fluid section, between the cells Ω_i and Ω_j, is discontinuous.

5.3.4 Pressure interpolation at the interface

The interpolated pressure at face is modified to take into account the fluid section jump at the interface, and thus to recover the steady momentum balance.

We assume that the pressure field $P(\boldsymbol{x},t)$, $\boldsymbol{x}\in\Omega$ and $t>0$, can be decomposed into two parts, as follows:

$$P(\boldsymbol{x},t) = P^s(\boldsymbol{x},t) + P^d(\boldsymbol{x},t), \tag{2.46}$$

- P^s is a smooth part, at least $C^1(\Omega)$,
- P^d is a continuous part, not necessary $C^1(\Omega)$. Its discrete gradient over the dual pyramid $\widehat{\Omega}^{\phi}_{i/ij}$ is $\boldsymbol{f}_{i/ij}$.

At the discrete level, the pressure is also assumed to be split into two parts, over the primal cell Ω_i and Ω_j and the associated diamond cell:

$$\begin{cases} P_i = P^s_i + P^d_i, \\ P_j = P^s_j + P^d_j, \quad \text{and} \quad P_{ij} = P^s_{ij} + P^d_{ij}. \end{cases} \tag{2.47}$$

Thus each part of the pressure at the primal faces P^s_{ij} or P^d_{ij} is approximated separately.

The pressure P_{ij}^s at each interface is defined by using a linear interpolation between the discrete pressures P_i and P_j:

$$P_{ij}^s = \alpha_{ij} P_i^s + (1 - \alpha_{ij}) P_j^s. \tag{2.48}$$

We note that the approximation (2.48) is consistent for smooth field in Ω, at least $C^0(\Omega)$.

The pressure $P^d(\boldsymbol{x} \in \widehat{\Omega}_{i/ij}^{\phi})$ is built as a linear function, locally $\mathbb{P}_1$ per pyramid $\widehat{\Omega}_{i/ij}^{\phi}$, with $P^d(\boldsymbol{x}_i) = P_i^d$ and $P^d(\boldsymbol{x}_{\mathtt{f}_{ij}}) = P_{ij}^d$, where $\boldsymbol{x}_{\mathtt{f}_{ij}}$ is the mass centre of the face.

We identify the convective acceleration (2.44) with the pressure gradient per dual pyramid $\widehat{\Omega}_{i/ij}^{\phi}$ and $\widehat{\Omega}_{j/ij}^{\phi}$:

$$\boldsymbol{\nabla}_{i/ij} P^d = \boldsymbol{f}_{i/ij} \text{ and } \boldsymbol{\nabla}_{j/ij} P^d = \boldsymbol{f}_{j/ij}.$$

The pressure P^d is then defined by a first order expansion in the dual pyramid $\widehat{\Omega}_{i/ij}$:

$$P^d(\boldsymbol{x}) = P_i^d + \boldsymbol{f}_{i/ij} \cdot (\boldsymbol{x} - \boldsymbol{x}_i), \ \forall \boldsymbol{x} \in \widehat{\Omega}_{i/ij}^{\phi}, \tag{2.49}$$

Likewise, for the pressure in the dual pyramid $\widehat{\Omega}_{j/ij}$:

$$P^d(\boldsymbol{x}) = P_j^d + \boldsymbol{f}_{j/ij} \cdot (\boldsymbol{x} - \boldsymbol{x}_j), \ \forall \boldsymbol{x} \in \widehat{\Omega}_{j/ij}^{\phi}. \tag{2.50}$$

Then, using the decomposition (2.46) at the interface $P_{ij} = P_{ij}^s + P_{ij}^d$ and equation (2.48), the pressure at interface reads:

$$P_{ij} = P_{ij}^s + P_{ij}^d = \alpha_{ij} P_i^s + (1 - \alpha_{ij}) P_j^s + P_{ij}^d.$$

Yet, using decomposition (2.46) in the cell, $P_i^s = P_i - P_i^d$ and $P_j^s = P_j - P_j^d$, we find:

$$P_{ij} = \alpha_{ij} P_i + (1 - \alpha_{ij}) P_j - \alpha_{ij} P_i^d - (1 - \alpha_{ij}) P_j^d + P_{ij}^d.$$

Finally, equations (2.49) and (2.50) allow to deduce the expression of the pressure at the interface of mass center $\boldsymbol{x}_{\mathtt{f}_{ij}}$:

$$P_{ij} = \alpha_{ij} P_i + (1 - \alpha_{ij}) P_j + \alpha_{ij} \boldsymbol{f}_{i/ij} \cdot (\boldsymbol{x}_{\mathtt{f}_{ij}} - \boldsymbol{x}_i) + (1 - \alpha_{ij}) \boldsymbol{f}_{j/ij} \cdot (\boldsymbol{x}_{\mathtt{f}_{ij}} - \boldsymbol{x}_j). \tag{2.51}$$

The first part is the legacy linear interpolation (2.16) for a continuous pressure and the second is a correction to account for the steady state at an interface with section jump.

Equation (2.51) can rewrite:

$$P_{ij} = \alpha_{ij} \left(P_i + \boldsymbol{f}_{i/ij} \cdot (\boldsymbol{x}_{\mathtt{f}_{ij}} - \boldsymbol{x}_i) \right) + (1 - \alpha_{ij}) \left(P_j + \boldsymbol{f}_{j/ij} \cdot (\boldsymbol{x}_{\mathtt{f}_{ij}} - \boldsymbol{x}_j) \right). \tag{2.52}$$

5.3.5 Velocity interpolation at the interface

The approximation of the normal velocity at face, projected in the $\boldsymbol{n}_{ij}$-direction (the normal direction to the face ij), is modified in order to comply with the local dual mass balance (2.42), as follows:

$$\boldsymbol{u}_{ij} \cdot \boldsymbol{n}_{ij} = \frac{\lambda_{ij} \mathbf{u}_i \cdot \boldsymbol{S}_{ij/i}^{\phi} + (1 - \lambda_{ij}) \mathbf{u}_j \cdot \boldsymbol{S}_{ij/j}^{\phi}}{S_{ij}^{\phi}}. \tag{2.53}$$

For the upwind scheme:

$$\lambda_{ij} = \begin{cases} 1 & \text{if } (\boldsymbol{Q} \cdot \boldsymbol{n})_{ij} \geq 0, \\ 0 & \text{otherwise,} \end{cases}$$

while for the centred scheme: $\lambda_{ij} = \alpha_{ij}$.

Thus the interpolated velocity at the interface can be rewritten:

$$\boldsymbol{u}_{ij} = \lambda_{ij} \boldsymbol{u}_{ij/i} + (1 - \lambda_{ij}) \boldsymbol{u}_{ij/j}. \tag{2.54}$$

5.4 Summary of the new space scheme

For any cell Ω_i, the interpolation at interface are modified, for all $j \in N(i)$, at each time step t^n:

- the convective flux is corrected in the normal direction to the interface with a section jump:

$$\left|\Omega_i^\phi\right| \mathbf{div}_i(\boldsymbol{Q}^n \otimes \tilde{\boldsymbol{u}}) = \sum_{j\in N(i)} \left(\lambda_{ij}^n \tilde{\boldsymbol{u}}_{ij/i} + (1-\lambda_{ij}^n)\tilde{\boldsymbol{u}}_{ij/j}\right) (\boldsymbol{Q}^n \cdot \boldsymbol{n})_{ij}\, S_{ij}^\phi, \tag{2.55}$$

with:

$$\tilde{\boldsymbol{u}}_{ij/i} = \tilde{\mathbf{u}}_i \cdot \frac{\boldsymbol{S}_{ij/i}^\phi}{S_{ij}^\phi} \boldsymbol{n}_{ij} + (\mathbf{Id} - \boldsymbol{n}_{ij} \otimes \boldsymbol{n}_{ij})\, \tilde{\mathbf{u}}_i,$$

and:

$$\tilde{\boldsymbol{u}}_{ij/j} = \tilde{\mathbf{u}}_j \cdot \frac{\boldsymbol{S}_{ij/j}^\phi}{S_{ij}^\phi} \boldsymbol{n}_{ij} + (\mathbf{Id} - \boldsymbol{n}_{ij} \otimes \boldsymbol{n}_{ij})\, \tilde{\mathbf{u}}_j.$$

- The discrete pressure gradient writes:

$$\left|\Omega_i^\phi\right| \boldsymbol{\nabla}_i P^n = \sum_{j\in N(i)} \left(P_{ij}^n - P_i^n\right) \boldsymbol{n}_{ij} S_{ij}^\phi, \tag{2.56}$$

with $P_{ij}^n = \alpha_{ij} P_i^n + (1-\alpha_{ij}) P_j^n + \alpha_{ij} \boldsymbol{f}_{i/ij}^n \cdot (\boldsymbol{x}_{\mathtt{f}_{ij}} - \boldsymbol{x}_i) + (1-\alpha_{ij}) \boldsymbol{f}_{j/ij}^n \cdot (\boldsymbol{x}_{\mathtt{f}_{ij}} - \boldsymbol{x}_j)$, where:

$$\boldsymbol{f}_{i/ij}^n = -\frac{1}{h_{ij/i}} (\boldsymbol{Q}^n \cdot \boldsymbol{n})_{ij} \left(\frac{\boldsymbol{S}_{ij/i}^\phi}{S_{ij}^\phi} - \boldsymbol{n}_{ij} \right) \cdot \mathbf{u}_i^n\, \boldsymbol{n}_{ij},$$

and:

$$\boldsymbol{f}_{j/ij}^n = -\frac{1}{h_{ij/j}} (\boldsymbol{Q}^n \cdot \boldsymbol{n})_{ij} \left(\frac{\boldsymbol{S}_{ij/j}^\phi}{S_{ij}^\phi} - \boldsymbol{n}_{ij} \right) \cdot \mathbf{u}_j^n\, \boldsymbol{n}_{ij}.$$

- The discrete velocity divergence writes:

$$\left|\Omega_i^\phi\right| \mathrm{div}_i(\rho_0 \tilde{\boldsymbol{u}}) = \sum_{j\in N(i)} \rho_0 \tilde{\boldsymbol{u}}_{ij} \cdot \boldsymbol{n}_{ij} S_{ij}^\phi = \sum_{j\in N(i)} \rho_0 \left(\alpha_{ij}^n \tilde{\boldsymbol{u}}_{ij/i} + (1-\alpha_{ij}^n)\tilde{\boldsymbol{u}}_{ij/j}\right) \cdot \boldsymbol{n}_{ij} S_{ij}^\phi, \tag{2.57}$$

- and the discrete pressure gradient increment is:

$$\left|\Omega_i^\phi\right| \boldsymbol{\nabla}_i \delta P = \sum_{j\in N(i)} \left(\delta P_{ij} - \delta P_i\right) \boldsymbol{n}_{ij} S_{ij}^\phi, \tag{2.58}$$

with $\delta P_{ij} = \alpha_{ij} \delta P_i + (1-\alpha_{ij}) \delta P_j + \alpha_{ij} \delta \boldsymbol{f}_{i/ij} \cdot (\boldsymbol{x}_{\mathtt{f}_{ij}} - \boldsymbol{x}_i) + (1-\alpha_{ij}) \delta \boldsymbol{f}_{j/ij} \cdot (\boldsymbol{x}_{\mathtt{f}_{ij}} - \boldsymbol{x}_j)$, where:

$$\delta \boldsymbol{f}_{i/ij} = -\frac{1}{h_{ij/i}} (\boldsymbol{Q}^n \cdot \boldsymbol{n})_{ij} \left(\frac{\boldsymbol{S}_{ij/i}^\phi}{S_{ij}^\phi} - \boldsymbol{n}_{ij} \right) \cdot \left(\tilde{\mathbf{u}}_i - \mathbf{u}_i^n\right) \boldsymbol{n}_{ij},$$

and:

$$\delta \boldsymbol{f}_{j/ij} = -\frac{1}{h_{ij/j}} (\boldsymbol{Q}^n \cdot \boldsymbol{n})_{ij} \left(\frac{\boldsymbol{S}_{ij/j}^\phi}{S_{ij}^\phi} - \boldsymbol{n}_{ij} \right) \cdot \left(\tilde{\mathbf{u}}_j - \mathbf{u}_j^n\right) \boldsymbol{n}_{ij}.$$

5.5 Consistency of the new scheme: one-dimensional approximate steady solution

We start again with the previous one-dimensional channel flow with a section jump, see FIGURE 2.5. Assuming a steady state, the steady integral formulation (2.5) is discretised with the new space scheme described above in section 5.3.

First, the discrete mass balance still holds in the computational domain Ω with $Q_{in} = \rho_0 u_0$:

$$\rho_0 u_0 S_L = Q_{in} S_L = Q_{LR} S_{LR}^{\phi} = Q_{out} S_R.$$

Second, equation (2.28) with the new scheme gives at the interface LR ($S_{LR}^{\phi} = S_R$):

$$Q_{LR} S_{LR}^{\phi} = Q_{LR} S_R = \rho_0 \frac{u_{LR/L} + u_{LR/R}}{2} S_R = \frac{\rho}{2} \left(u_L \frac{S_L}{S_R} + u_R \right) S_R. \tag{2.59}$$

and equation (2.28) gives at the outlet boundary with the upwind scheme $u_{out} = u_R$:

$$Q_{out} S_R = \rho_0 u_R S_R. \tag{2.60}$$

We deduce the left and right discrete velocity:

$$u_R = u_0 \frac{S_L}{S_R} \quad \text{and} \quad u_L = u_0. \tag{2.61}$$

According to the exact solution (2.30), the correct discrete velocities are thus computed.

Third, the discrete steady momentum balance (2.27) reads with the new scheme, for the cell Ω_L:

$$-Q_{in} u_{in} S_L + Q_{LR} S_{LR}^{\phi} u_{LR/L} + \left(P_{LR}^{cent} + h_{LR/L} \frac{(f_{L/LR} + f_{R/LR})}{2} \right) S_{LR}^{\phi} + P_w (S_L - S_{LR}^{\phi}) - P_{in} S_L = 0.$$

The new scheme reads with $S_{LR}^{\phi} = S_R$:

$$u_{LR/L} = u_L \frac{S_L}{S_R}, \; f_{L/LR} = -\frac{Q_{LR} u_L}{h_{LR/L}} \left(\frac{S_L}{S_R} - 1 \right), \quad \text{and} \quad f_{R/LR} = 0,$$

The mass conservation, the inlet boundary condition, $P_{in} = P_L$, and the wall pressure estimation, $P_w = P_L$, give:

$$Q_{LR} S_R \left(u_L \frac{S_L}{S_R} - u_0 \right) + \left(\frac{P_L + P_R}{2} - \frac{1}{2} Q_{LR} u_L \left(\frac{S_L}{S_R} - 1 \right) - P_L \right) S_R = 0.$$

After some simplifications, by using (2.61), $u_L = u_0$, and $Q_{LR} S_R = \rho_0 u_0 S_L$, we obtain the following relation:

$$\rho_0 u_0^2 S_L \left(\frac{S_L}{S_R} - 1 \right) - \frac{1}{2} \rho_0 u_0^2 S_L \left(\frac{S_L}{S_R} - 1 \right) + \frac{P_R - P_L}{2} S_R = 0.$$

Thus, the right discrete pressure drop is recovered ($S_R \neq 0$), see equation (2.32):

$$P_R - P_L = \rho_0 u_0^2 \frac{S_L}{S_R} \left(1 - \frac{S_L}{S_R} \right). \tag{2.62}$$

Likewise, the steady momentum balance (2.27) writes in the cell Ω_R:

$$-Q_{LR}S^{\phi}_{LR}u_{LR/L} + Q_{out}u_{out}S_R + \left(P_{out} - P^{cent}_{LR} - h_{LR/L}\frac{\left(f_{L/LR} + f_{R/LR}\right)}{2}\right)S_R = 0,$$

The new scheme again gives:

$$u_{LR/L} = u_R,\ f_{L/LR} = -\frac{Q_{LR}u_L}{h_{LR/L}}\left(\frac{S_L}{S_R} - 1\right),\ \text{and}\ \ f_{R/LR} = 0.$$

Thus, using the mass conservation, $Q_{LR}S^{\phi}_{LR} = Q_{out}S_R$, and $u_R = u_{out}$, we obtain:

$$-Q_{LR}S^{\phi}_{LR}u_{LR,L} + Q_{out}u_{out}S_R = 0,$$

and with the outlet boundary condition, $P_{out} = P_0$:

$$P_0S_R - \frac{P_R + P_L}{2}S_R + \frac{1}{2}Q_{LR}S_Ru_L\left(\frac{S_L}{S_R} - 1\right).$$

Thus, using equation (2.62), the following relation holds for $S_R \neq 0$:

$$P_0 = P_R. \tag{2.63}$$

Finally, equations (2.61), (2.62) and (2.63) give the right discrete values, in the sense that it is consistent with equations (2.30) (for the bulk velocity) and(2.32) (for the pressure jump at the interface).

6 Numerical results

This section is dedicated to the verification of the numerical scheme on configurations including fluid section jumps, when the approximate solution is steady.

6.1 Verification test case: plane steady-state flow in a channel with a discontinuous fluid section

The aim is to simulate a plane steady-state inviscid fluid flow in a channel with a discontinuous fluid section, see FIGURE 2.8, for which the exact solution is known; the velocity and pressure fields are piecewise constant.

The two-dimensional fluid computational domain Ω^ϕ consists of a plane channel with a constriction ($S_R < S_L$). At the channel middle, the fluid section is suddenly reduced; thus, the fluid moves from a free domain towards an obstructed domain.

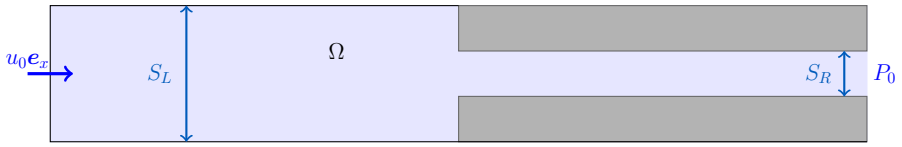

FIGURE 2.8 – *Channel with constriction ($S_R < S_L$).*

The one-dimensional computational domain $\Omega = (0, 40\ m)$ is meshed with a uniform Cartesian grid with N cells, $N = 10, 80$ or 1280 (see FIGURE 2.9). The jump section is located at $x = 0\ m$. The section ratio is $\frac{S_L}{S_R} = 2$.

The initial conditions are: $\forall\ x \in \Omega$, $u(x, t = 0) = 0\ m.s^{-1}$ and $P(x, t = 0) = 0\ Pa$.

The computations are performed with a constant time step complying with $CFL_u = \frac{u\Delta t}{\Delta x} \leq 1$.

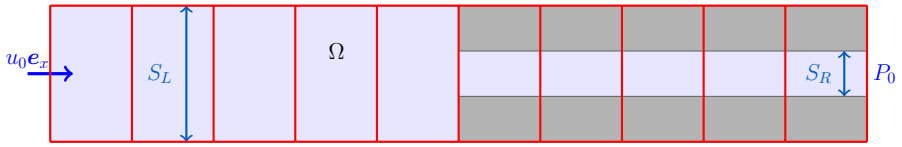

FIGURE 2.9 – *Mesh of the channel with constriction ($S_R < S_L$), $N = 10$.*

6.1.1 Exact solution

For an imposed bulk velocity u_0 at the inlet and a reference pressure at the outlet, the velocity is multiplied by the section ratio $\frac{S_L}{S_R}$ and the pressure drops of ΔP. The left and right steady states are deduced from equations (2.30) and (2.32):

$$\begin{cases} u_L = u_0;\ P_L = P_0 - \Delta P \text{ with } \Delta P = \rho_0 u_0^2 \dfrac{S_L}{S_R}\left(1 - \dfrac{S_L}{S_R}\right), \\ u_R = \dfrac{S_L}{S_R} u_0;\ P_R = P_0. \end{cases}$$

Herein, we still assume that the wall pressure is: $P_w = P_L$, implying $\Delta P^w = 0\ Pa$.

Numerical Application (see TABLE 2.1): with a fluid section ratio $\frac{S_L}{S_R} = 2$, a density $\rho_0 = 1\ kg.m^{-3}$ and a bulk velocity $u_0 = 1\ m.s^{-1}$: we then obtain a velocity jump $u_R - u_L = 1\ m.s^{-1}$ and a pressure drop $\Delta P = -2\ Pa$.

$\frac{S_L}{S_R}$	2	10	100
$u_R\ (m.s^{-1})$	2	10	100
$-\Delta P\ (Pa)$	2	90	9900

TABLE 2.1 – *Exact solutions for different fluid section constrictions.*

6.1.2 Boundary conditions

The boundary conditions on $\partial\Omega = \partial\Omega^{in} \cup \partial\Omega^{out} \cup \partial\Omega^{wall}$ are:

- on $\partial\Omega^{in}$: Dirichlet condition on the velocity,
- on $\partial\Omega^{out}$: Dirichlet condition on the pressure,
- on $\partial\Omega^{wall}$: slip condition implying $\boldsymbol{u} = u\,\boldsymbol{e}_x$.

Then the numerical boundary conditions, applied at boundary faces f_b, are described in TABLE 2.2.

	velocity u	pressure P	pressure increment δP
inlet	$u_{f_b} = u_0 = 1$	$\partial_{\boldsymbol{n}} P = 0$	$\partial_{\boldsymbol{n}} \delta P = 0$
outlet	$\partial_{\boldsymbol{n}} u = 0$	$P_{f_b} = P_0 = 0$	$\delta P_{f_b} = 0$
wall	$\boldsymbol{u} \cdot \boldsymbol{n} = 0$ and $\partial_{\boldsymbol{n}} u = 0$	$\partial_{\boldsymbol{n}} P = 0$	$\partial_{\boldsymbol{n}} \delta P = 0$

TABLE 2.2 – *Boundary conditions for channel flow with discontinuous section.*

6.1.3 Results

At steady state, the analytical piecewise constant fields are recovered with the machine precision for the velocity and the solver precision (10^{-12}) for the pressure (see FIGURE 2.10). The discrete L^2 error[1] is 10^{-12}.

In the case of $\frac{S_L}{S_R} = 2$, for instance, with $N = 10$, the time convergence is reached after 63 iterations. The L^2 time residuals for the velocity and the pressure are zero (machine precision is obtained). The discrete pressure errors, in function of the cell centres x_i, are given in TABLE 2.3.

For the other cases, the velocity and pressure profiles are given in FIGURES 2.11 and 2.12 and the discrete pressure error in TABLES 2.4 and 2.5.

$x_i\ (m)$	2	6	10	14	18	22	26	30	34	38
$P_i - P_{exact}\ (Pa)$	0	0	0	0	0	-2.9e-12	-3.1e-13	-3.3e-13	-7.9e-13	-3.8e-13

TABLE 2.3 – *Steady-state discrete pressure error for* $\frac{S_L}{S_R} = 2$.

Remark 6.1. *The computations are performed with a corrective term, the adapted Rhie & Chow filter, in equation (2.23) for the correction step, see appendix 2.A. This filter has to be adapted for the modified space scheme at the interfaces with fluid section jumps.*

[1] The discrete relative L^2 error is defined as: $e_{L^2(\Omega)}(\varphi) = \sqrt{\frac{\sum_{i=1}^{N} \left|\varphi_i^{exact} - \varphi_i^{computed}\right|^2 |\Omega_i|}{\sum_{i=1}^{N} \left|\varphi_i^{exact}\right|^2 |\Omega_i|}}$.

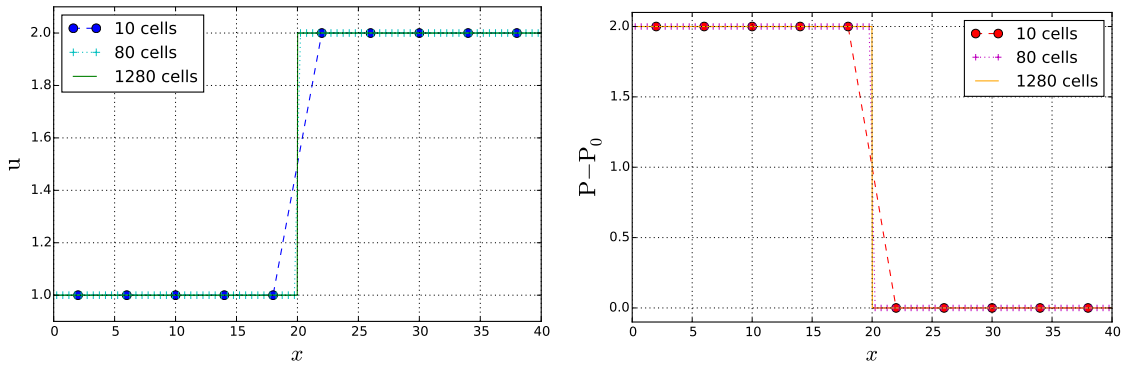

(a) Velocity (b) Pressure

FIGURE 2.10 – *Steady approximate solutions for* $\frac{S_L}{S_R} = 2$.

x_i (m)	2	6	10	14	18	22	26	30	34	38
$P_i - P_{exact}$ (Pa)	0	0	0	0	0	–5.37e-11	-2.79e-10	-3.42e-10	-2.94e-10	-1.20e-10

TABLE 2.4 – *Steady-state discrete pressure error for* $\frac{S_L}{S_R} = 10$.

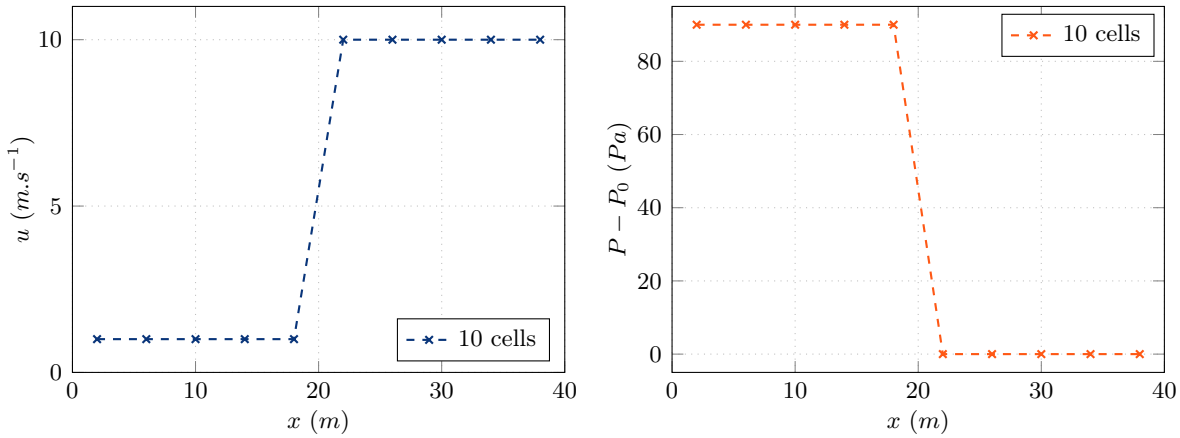

(a) Velocity (b) Pressure

FIGURE 2.11 – *Steady approximate solutions for* $\frac{S_L}{S_R} = 10$.

x_i (m)	2	6	10	14	18	22	26	30	34	38
$P_i - P_{exact}$ (Pa)	0	0	0	0	0	-5.58e-9	4.52e-9	5.93e-9	4.78e-9	1.80e-9

TABLE 2.5 – *Steady-state discrete pressure error for* $\frac{S_L}{S_R} = 100$.

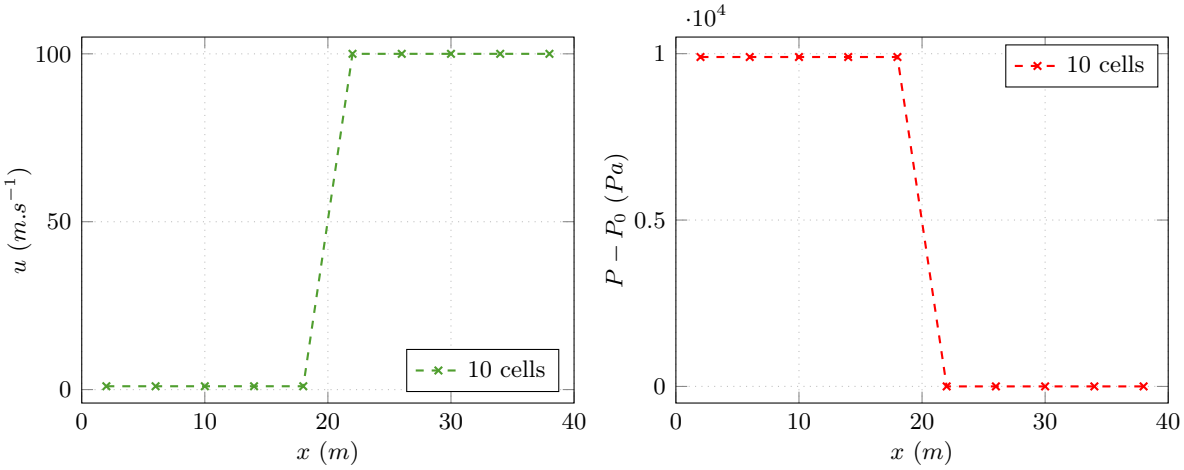

(a) Velocity

(b) Pressure

FIGURE 2.12 – *Steady approximate solutions for* $\frac{S_L}{S_R} = 100$.

7 Conclusion

The multi-dimensional integral formulation has been extended to approximate solutions of the incompressible Euler equations in a medium with fluid section jumps on coarse meshes. The discontinuous geometry of the fluid section does not need to be explicitly meshed by using a wall boundary condition.

The integral formulation is discretised by a semi-implicit collocated finite volume scheme using an incremental pressure projection method. The proposed space scheme corrects the interpolation at the interface of both the velocity and the pressure. This technique is based on the discrete local steady balance equations on a dual sub-mesh, similarly to a staggered scheme.

Numerical verification tests show the ability of the scheme to recover the analytic steady-state flow solution. The test case consists of the discontinuous cross section channel flow. Indeed, the analytic piecewise constant solution is recovered on a collocated mesh with the correct pressure drop and acceleration at the discontinuous interface. Even if only illustrated on a one-dimensional case, this scheme is applicable to multi-dimensional computations and its impact will decrease when refining the mesh in all directions. Additional *ad hoc* head loss correlations could be added to the present developments.

Besides, this methodology aims at being extended to compressible fluid flows (see section 2.B). A new pressure-correction scheme, corresponding to an extension of this incompressible algorithm, has been developed in appendix B and should be tested for fluid section jumps. Thus, the numerical results should be compared with the results performed with the software THYC at the component scale [4].

2.A Filtration of the numerical spatial oscillations

The Rhie & Chow filter is used to avoid the checkerboard effect, see for more information [65, 66, 67].

2.A.1 Reminder about the Rhie & Chow filter

2.A.1.1 Presence of spurious checkerboard modes

Collocated finite volume schemes can introduce spurious modes, due the fact that the discrete pressure and velocity are computed at the same control volume.

We refer now to the space scheme described in section 4.2.

Assuming, for instance, a Cartesian grid: when considering, at the time step t^n, a piecewise constant pressure field in the computational domain Ω such that, for all cell Ω_i, $i \in \{1, ..., N_{cell}\}$:

$$P_i = (-1)^i,$$

then the finite volume cell gradient is equal to zero:

$$\left|\Omega_i^\phi\right| \boldsymbol{\nabla}_i P^n = \sum_{j \in N(i)} \left(P_{ij}^n - P_i^n\right) \boldsymbol{n}_{ij} S_{ij}^\phi = 0.$$

Moreover, a discrete velocity complying with the incompressibility constraint:

$$\sum_{j \in N(i)} \rho_0 \tilde{\boldsymbol{u}}_{ij} \cdot \boldsymbol{n}_{ij} S_{ij}^\phi = 0,$$

gives a zero pressure increment, implying $P_i^{n+1} = P_i^n$, for any Ω_i. Thus, the discrete pressure with checkerboard modes will be not corrected for the following time iterations.

This discrete gradient is not compatible with the continuous gradient in Ω (the discrete operator kernel is not reduced to the constant filed in Ω).

2.A.1.2 Modification of the pressure correction step: space filter

To address this problem, a supplementary term is added to the explicit mass flux at the time step t^n, in the right hand side of the discrete Poisson equation (2.23), solving the pressure increment for all Ω_i. This term consists in adding the difference between the cell discrete pressure gradient (interpolated at the interface) and the face compatible pressure gradient. Thus, equation (2.23) is modified as follows:

$$-\sum_{j \in N(i)} \Delta t \boldsymbol{\nabla} \delta P \cdot \boldsymbol{n}_{ij} S_{ij}^\phi = -\sum_{j \in N(i)} \rho_0 \tilde{\boldsymbol{u}}_{ij} \cdot \boldsymbol{n}_{ij} S_{ij}^\phi - \sum_{j \in N(i)} \underbrace{\left(\Delta t \{\boldsymbol{\nabla}.P^n\}_{ij} - \Delta t \boldsymbol{\nabla} P^n\right)}_{\text{filtering term}} \cdot \boldsymbol{n}_{ij} S_{ij}^\phi, \quad (2.64)$$

where the linear interpolation of the discrete pressure gradient at the interface ij reads:

$$\{\boldsymbol{\nabla}.P^n\}_{ij} = \alpha_{ij} \boldsymbol{\nabla}_i P^n + (1 - \alpha_{ij}) \boldsymbol{\nabla}_j P^n.$$

This correction leads to solve the discrete Poisson equation (2.23) with the compatible gradient, using a TPFA [57], on the discrete pressure:

$$-\sum_{j \in N(i)} \Delta t \boldsymbol{\nabla} P^{n+1} \cdot \boldsymbol{n}_{ij} S_{ij}^\phi = -\sum_{j \in N(i)} \left(\rho_0 \tilde{\boldsymbol{u}}_{ij} \cdot \boldsymbol{n}_{ij} + \Delta t \{\boldsymbol{\nabla} P^n\}_{ij} \cdot \boldsymbol{n}_{ij}\right) S_{ij}^\phi \quad (2.65)$$

This technique, corresponding to the Rhie & Chow filter [65], enables to remove the spurious checkerboard modes.

2.A.2 Adaptation of the Rhie & Chow filter for the new space scheme in presence of fluid section jumps

We refer in the sequel to the new space scheme described in section 5.

The Rhie & Chow filter is adapted, for all Ω_i at each time step t^n, in order to take into account the new interpolated pressure at the interface in the calculation of the discrete pressure gradient. The filtering added term, in equation (2.64), is now built with the discrete pressure gradient $\boldsymbol{\nabla}_i P^n - \boldsymbol{f}^n_{i/ij}$, as follows:

$$\sum_{j\in N(i)} \underbrace{\left(\Delta t\{\boldsymbol{\nabla}.P^n - \boldsymbol{f}^n_{./ij}\}_{ij} - \Delta t(\boldsymbol{\nabla} P^n - \boldsymbol{f}^n_{ij})\right)}_{\text{filtering term}} \cdot \boldsymbol{n}_{ij} S^\phi_{ij}, \tag{2.66}$$

with:

$$\{\boldsymbol{\nabla}.P^n - \boldsymbol{f}^n_{./ij}\}_{ij} = \alpha_{ij}(\boldsymbol{\nabla}_i P^n - \boldsymbol{f}^n_{i/ij}) + (1-\alpha_{ij})(\boldsymbol{\nabla}_j P^n - \boldsymbol{f}^n_{j/ij}).$$

where, the discrete pressure gradient (interpolation at the face) is modified using the new space scheme, equation (2.51):

$$\left|\Omega^\phi_i\right| \boldsymbol{\nabla}_i P^n = \sum_{j\in N(i)} \left(\begin{array}{c} \alpha_{ij} P^n_i + (1-\alpha_{ij}) P^n_j - P^n_i \\ +\alpha_{ij} \boldsymbol{f}^n_{i/ij} \cdot (\boldsymbol{x}_{\mathtt{f}_{ij}} - \boldsymbol{x}_i) + (1-\alpha_{ij}) \boldsymbol{f}^n_{j/ij} \cdot (\boldsymbol{x}_{\mathtt{f}_{ij}} - \boldsymbol{x}_j) \end{array} \right) \boldsymbol{n}_{ij} S^\phi_{ij}.$$

Moreover, similarly in section 5, we define $\boldsymbol{f}^n_{ij} \cdot \boldsymbol{n}_{ij}$ at the face as a part of the pressure gradient flux:

$$\boldsymbol{f}^n_{ij} \cdot \boldsymbol{n}_{ij} = \frac{P^d_j - P^d_i}{h_{ij/i} + h_{ij/j}},$$

thus yielding, with a first order expansion of the pressure P^d_{ij} at the interface ij:

$$\begin{aligned} \boldsymbol{f}^n_{ij} \cdot \boldsymbol{n}_{ij} &= \frac{1}{h_{ij/i} + h_{ij/j}} \left(P^d_{ij} + \boldsymbol{f}^n_{j/ij} \cdot (\boldsymbol{x}_j - \boldsymbol{x}_{\mathtt{f}_{ij}}) - P^d_{ij} - \boldsymbol{f}^n_{i/ij} \cdot (\boldsymbol{x}_i - \boldsymbol{x}_{\mathtt{f}_{ij}}) \right) \\ &= \frac{1}{h_{ij/i} + h_{ij/j}} \left(\boldsymbol{f}^n_{j/ij} \cdot (\boldsymbol{x}_j - \boldsymbol{x}_{\mathtt{f}_{ij}}) - \boldsymbol{f}^n_{i/ij} \cdot (\boldsymbol{x}_i - \boldsymbol{x}_{\mathtt{f}_{ij}}) \right). \end{aligned}$$

2.B Scheme in space for the pressure-correction scheme of the compressible Euler equations

In this appendix, the new space scheme built in section 5.3 is adapted to the compressible discrete Euler equations in the framework of the pressure-correction numerical scheme presented in chapter 1 [46] and appendix B. To begin, we consider the barotropic Euler equations with $P = \mathcal{P}(\rho)$, which is only composed of the mass balance and the momentum balance equations. We follow the same step as in section 5.3.

2.B.1 Local discrete steady balances

2.B.1.1 Steady mass balance

The steady mass balance is integrated over the fluid part of the pyramid $\widehat{\Omega}^{\phi}_{i/ij}$ and reads:

$$\int_{\widehat{\Omega}^{\phi}_{i/ij}} \operatorname{div}(\rho \boldsymbol{u}) \, \mathrm{d}\boldsymbol{x} = 0, \tag{2.67}$$

giving at the discrete level,

$$\rho_{ij/i} \boldsymbol{u}_{ij/i} \cdot \boldsymbol{n}_{ij} S^{\phi}_{ij} = \rho_i \mathbf{u}_i \cdot \boldsymbol{S}^{\phi}_{ij/i}. \tag{2.68}$$

We can choose to take the discrete density at cell for the interface value in the pyramid $\widehat{\Omega}^{\phi}_{i/ij}$:

$$\rho_{ij/i} = \rho_i.$$

Thus,

$$\boldsymbol{u}_{ij/i} \cdot \boldsymbol{n}_{ij} S^{\phi}_{ij} = \mathbf{u}_i \cdot \boldsymbol{S}^{\phi}_{ij/i}. \tag{2.69}$$

This relation is the same one as (2.42) and allows to attach the discrete velocity at cell to the velocity at face in taking into account the ratio of fluid section.

2.B.1.2 Steady momentum balance

The convective flux, integrated over the fluid part of the pyramid $\widehat{\Omega}^{\phi}_{i/ij}$, reads:

$$\int_{\widehat{\Omega}^{\phi}_{i/ij}} \mathbf{div}\,(\boldsymbol{u} \otimes \boldsymbol{Q}) \, \mathrm{d}\boldsymbol{x} = \left(\boldsymbol{u}_{ij/i} - \mathbf{u}_i\right) (\boldsymbol{Q} \cdot \boldsymbol{n})_{ij} \, S^{\phi}_{ij}, \tag{2.70}$$

$\boldsymbol{f}_{i/ij} \cdot \boldsymbol{n}_{ij}$, the opposite of the convective acceleration (2.70) over the pyramid $\widehat{\Omega}^{\phi}_{i/ij}$ in the normal direction to the face ij, writes:

$$h_{ij/i} S^{\phi}_{ij} \boldsymbol{f}_{i/ij} \cdot \boldsymbol{n}_{ij} = -\left(\boldsymbol{u}_{ij/i} - \mathbf{u}_i\right) \cdot \boldsymbol{n}_{ij} \, (\boldsymbol{Q} \cdot \boldsymbol{n})_{ij} \, S^{\phi}_{ij}.$$

Using equation (2.68), the expression of the convective acceleration writes:

$$\boldsymbol{f}_{i/ij} \cdot \boldsymbol{n}_{ij} = -\frac{(\boldsymbol{Q} \cdot \boldsymbol{n})_{ij}}{h_{ij/i}} \left(\frac{\rho_i}{\rho_{ij/i}} \frac{\boldsymbol{S}^{\phi}_{ij/i}}{S^{\phi}_{ij}} - \boldsymbol{n}_{ij} \right) \cdot \mathbf{u}_i, \tag{2.71}$$

giving by $\rho_{ij/i} = \rho_i$:

$$\boldsymbol{f}_{i/ij} \cdot \boldsymbol{n}_{ij} = -\frac{(\boldsymbol{Q} \cdot \boldsymbol{n})_{ij}}{h_{ij/i}} \left(\frac{\boldsymbol{S}^{\phi}_{ij/i}}{S^{\phi}_{ij}} - \boldsymbol{n}_{ij} \right) \cdot \mathbf{u}_i. \tag{2.72}$$

This relation is only non-zero for a fluid section jump.

Thus, we recover equation (2.45), which is a part of the discrete local steady momentum balance over the cell Ω_i, when the fluid section S^{ϕ}_{ij} jumps at the interface ij between the cell Ω_i and Ω_j.

2.B.2 Interpolations at the interface

2.B.2.1 Pressure interpolation at the interface in the momentum balance

The interpolated pressure at face is modified, in the same way in section 5.3, see equation (2.52), to take into account the fluid section jump at the interface, and thus to recover the steady momentum balance:

$$P_{ij} = \alpha_{ij}\left(P_i + \boldsymbol{f}_{i/ij}\cdot(\boldsymbol{x}_{\mathtt{f}_{ij}} - \boldsymbol{x}_i)\right) + (1-\alpha_{ij})\left(P_j + \boldsymbol{f}_{j/ij}\cdot(\boldsymbol{x}_{\mathtt{f}_{ij}} - \boldsymbol{x}_j)\right). \tag{2.73}$$

2.B.2.2 Velocity interpolation at the interface in the momentum balance

The approximation of the normal velocity at face, projected in the $\boldsymbol{n}_{ij}$-direction (the normal direction to the face ij), is modified in order to hold the local dual mass balance (2.42), as follows:

$$\boldsymbol{u}_{ij}\cdot\boldsymbol{n}_{ij} = \frac{\lambda_{ij}\mathbf{u}_i\cdot\boldsymbol{S}^{\phi}_{ij/i} + (1-\lambda_{ij})\mathbf{u}_j\cdot\boldsymbol{S}^{\phi}_{ij/j}}{S^{\phi}_{ij}}. \tag{2.74}$$

For the upwind scheme:

$$\lambda_{ij} = \begin{cases} 1 & \text{if } (\boldsymbol{Q}\cdot\boldsymbol{n})_{ij} \geq 0, \\ 0 & \text{otherwise,} \end{cases}$$

while for the centred scheme: $\lambda_{ij} = \alpha_{ij}$.

2.B.2.3 Mass flux interpolation at the interface in the mass balance

The steady mass balance is satisfied in the two dual pyramids $\widehat{\Omega}^{\phi}_{i/ij}$ and $\widehat{\Omega}^{\phi}_{j/ij}$ (attached to the face ij), thus giving:

$$\rho_{ij}\boldsymbol{u}_{ij}\cdot\boldsymbol{n}_{ij}\boldsymbol{S}^{\phi}_{ij} = \rho_i\boldsymbol{u}_i\cdot\boldsymbol{S}^{\phi}_{ij/i} = \rho_j\boldsymbol{u}_j\cdot\boldsymbol{S}^{\phi}_{ij/j},$$

we can linearly interpolate the mass flux as follows:

$$\rho_{ij}\boldsymbol{u}_{ij}\cdot\boldsymbol{n}_{ij}S^{\phi}_{ij} = \alpha_{ij}\rho_i\boldsymbol{u}_i\boldsymbol{S}^{\phi}_{ij/i} + (1-\alpha_{ij})\rho_j\boldsymbol{u}_j\boldsymbol{S}^{\phi}_{ij/j}. \tag{2.75}$$

In conclusion, in this discretisation, the only difference with respect to the incompressible space scheme is the approximation of the explicit mass flux (2.75) in equation (2.28) (ρ is no longer uniform).

2.C A wall pressure estimation satisfying the steady kinetic energy balance equation

First, we recall that the incompressible Euler set of equations satisfies the kinetic energy balance equation:

$$\partial_t \left(\frac{1}{2} \rho \left| \boldsymbol{u} \right|^2 \right) + \operatorname{div} \left(\boldsymbol{u} \left(\frac{1}{2} \rho \left| \boldsymbol{u} \right|^2 + P \right) \right) = 0.$$

2.C.1 Configuration: channel flow with discontinuous fluid sections

The steady incompressible Euler equations is integrated over the domain Ω (in red in FIGURE 2.13) in order to set the steady balance between the left state L (before the section discontinuity) and the right state R (after the section discontinuity). The steady kinetic energy balance is also written in order to obtain a third relation allowing to determine a unique wall pressure.

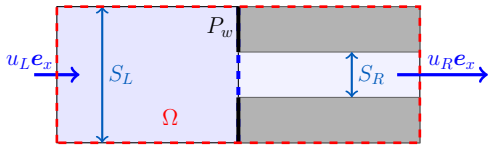

FIGURE 2.13 – *Channel with constriction* $S_L > S_R$

2.C.2 Notations

Let us note $u = \boldsymbol{u} \cdot \boldsymbol{e}_x$ the velocity in the normal-direction to the fluid discontinuous section, and P_w the wall pressure exerted on the discontinuous section.

Moreover, the difference and the average between the left and right states are denoted by:

$$[\cdot]_L^R = \cdot_R - \cdot_L,$$

$$\bar{\cdot} = \frac{1}{2} \left(\cdot_L + \cdot_R \right).$$

2.C.3 Mass balance

Assume that the density is constant $\rho = \rho_0$, the integration of the continuity equation $\int_\Omega \operatorname{div} (\rho_0 \boldsymbol{u}) \, \mathrm{d}\boldsymbol{x} = 0$ yields:

$$\rho_0 \left(uS \right)_L = \rho_0 \left(uS \right)_R = Q_0,$$

which reads:

$$[uS]_L^R = \bar{S} \, [u]_L^R + \bar{u} \, [S]_L^R = 0. \tag{2.76}$$

2.C.4 Steady momentum balance

The integration of the steady momentum balance equation $\int_\Omega \mathbf{div} \left(\rho_0 \boldsymbol{u} \otimes \boldsymbol{u} + P \, \mathbf{Id} \right) \mathrm{d}\boldsymbol{x} = 0$ yields:

$$\rho_0 \left(uS \right)_R u_R - \rho_0 \left(uS \right)_L u_L + P_R S_R - P_L S_L + P_w \left(S_L - S_R \right) = 0,$$

which reads:

$$Q_0 \, [u]_L^R + \bar{P} \, [S]_L^R + \bar{S} \, [P]_L^R - P_w \, [S]_L^R = 0. \tag{2.77}$$

2.C.5 Steady kinetic energy balance

The integration of the steady kinetic energy balance equation $\int_\Omega \operatorname{div}\left(\rho_0 \boldsymbol{u}\frac{\boldsymbol{u}^2}{2}+P\boldsymbol{u}\right)\mathrm{d}\boldsymbol{x}=0$ yields:

$$\rho_0 \left(uS\right)_R \frac{u_R^2}{2} - \rho_0 \left(uS\right)_L \frac{u_L^2}{2} + u_R P_R S_R - u_L P_L S_L = 0,$$

which reads:

$$Q_0 \left[\frac{u^2}{2} + \frac{P}{\rho_0}\right]_L^R = 0, \tag{2.78}$$

or

$$\rho_0 \bar{u} \left[u\right]_L^R + \left[P\right]_L^R = 0. \tag{2.79}$$

It can read as the steady incompressible Euler equations conserve the hydraulic head $\frac{u^2}{2} + \frac{P}{\rho_0}$.

2.C.6 Estimation of the wall pressure preserving the steady kinetic energy balance

From equations (2.77) and (2.79), the following equation is deduced:

$$Q_0 \left[u\right]_L^R - \bar{S}\left(\rho_0 \bar{u} \left[u\right]_L^R\right) + \left(\bar{P} - P_w\right)\left[S\right]_L^R = 0$$

Thus, in using equation (2.76):

$$\left(\left(Q_0 - \rho_0 \bar{S}\bar{u}\right)\bar{u} - \bar{S}\left(\bar{P} - P_w\right)\right)\left[u\right]_L^R = 0 \tag{2.80}$$

The wall pressure P_w is then estimated for $\left[u\right]_L^R \neq 0$ and $\bar{S} \neq 0$:

$$P_w = \bar{P} - \frac{Q_0 - \rho_0 \bar{S}\bar{u}}{\bar{S}}\bar{u} = \bar{P} - \rho_0 \frac{\overline{US} - \bar{S}\bar{u}}{\bar{S}}\bar{u} = \bar{P} - \rho_0 \frac{\left[S\right]_L^R \left[u\right]_L^R}{4\bar{S}}\bar{u} \tag{2.81}$$

Using equation (2.79), another way to write P_w, in function of the left pressure, is:

$$P_w = P_L - \frac{\rho_0}{2}\left[u\right]_L^R \bar{u}\left(1 + \frac{\left[S\right]_L^R}{2\bar{S}}\right). \tag{2.82}$$

References

[4] S. Aubry, C. Caremoli, J. Olive, and P. Rascle. "The THYC three-dimensional thermal-hydraulic code for rod bundles: recent developments and validation tests". In: *Nuclear technology* 112.3 (1995), pp. 331–345 (cit. on pp. 10, 14, 28, 110, 215).

[9] *Code_Saturne 5.2.0 Theory Guide*. EDF R&D. 2018. URL: https://code-saturne.org/cms/sites/default/files/docs/5.2/theory.pdf (cit. on pp. 10, 28, 92, 93, 176).

[16] R. Eymard, T. Gallouët, and R. Herbin. "Finite Volume Methods". In: *Handbook for Numerical Analysis, P.G. Ciarlet, J.L. Lions eds, North Holland* 7 (2006), pp. 713–1020 (cit. on pp. 10, 29, 33, 92, 94, 120, 177).

[25] A.-J. Chorin. "Numerical solution of the Navier-Stokes equations". In: *Mathematics of Computation* 22(104):745–762 (1968) (cit. on pp. 15, 29, 90, 92, 176).

[26] R. Temam. "Sur l'approximation de la solution des équations de Navier-Stokes par la méthode des pas fractionnaires (I)". In: *Archive for Rational Mechanics and Analysis* 32.5 (1969), pp. 135–153 (cit. on pp. 15, 90, 92, 176).

[27] R. Temam. "Sur l'approximation de la solution des équations de Navier-Stokes par la méthode des pas fractionnaires (II)". In: *Archive for Rational Mechanics and Analysis* 33.5 (1969), pp. 377–385 (cit. on pp. 15, 29, 90, 92, 176).

[28] J.-L. Guermond, P. Minev, and J. Shen. "An overview of projection methods for incompressible flows". In: *Computer Methods in Applied Mechanics and Engineering* 195 (Sept. 2006), pp. 6011–6045 (cit. on pp. 15, 92).

[40] X. Martin. "Modélisation d'écoulements fluides en milieu encombré d'obstacles". PhD thesis. Aix-Marseille Université, 2015. URL: https://tel.archives-ouvertes.fr/tel-01235089 (cit. on pp. 17, 90, 91, 176).

[46] C. Colas, M. Ferrand, J.-M. Hérard, J.-C. Latché, and E. Le Coupanec. "An Implicit Integral Formulation to Model Inviscid Fluid Flows in Obstructed Media". In: *Computers & Fluids* 188 (2019), pp. 136–163. URL: https://hal.archives-ouvertes.fr/hal-01969129 (cit. on pp. 20, 22, 90, 91, 113, 121, 176, 179).

[57] R. Eymard, T. Gallouët, C. Guichard, R. Herbin, and R. Masson. "TP or not TP, that is the question". In: *Computational Geosciences* 18 (Aug. 2014), pp. 285–296. URL: https://hal.archives-ouvertes.fr/hal-00801648 (cit. on pp. 36, 94, 96, 111, 180, 192).

[61] F. H. Harlow and A. A. Amsden. "Numerical calculation of almost incompressible flow". In: *Journal of Computational Physics* 3.1 (1968), pp. 80 –93 (cit. on pp. 90, 176).

[62] F. H. Harlow and A. A. Amsden. "A numerical fluid dynamics calculation method for all flow speeds". In: *Journal of Computational Physics* 8 (1971), pp. 197–213 (cit. on pp. 90, 176).

[63] K. C. Karki and S. V. Patankar. "Pressure based calculation procedure for viscous flows at all speeds in arbitrary configurations". In: *AIAA Journal* 27 (Sept. 1989), pp. 1167–1174 (cit. on pp. 92, 177).

[64] I. E. Idel'Cik. "Memento des pertes de charge". In: *Collection de la Direction des Etudes et Recherches d'Electricité de France, Paris: Eyrolles* (1969) (cit. on p. 97).

[65] C. M. Rhie and W. L. Chow. "Numerical study of the turbulent flow past an airfoil with trailing edge separation". In: *AIAA Journal* 21.11 (1983), pp. 1525–1532 (cit. on pp. 111, 181).

[66] S. Zhang, X. Zhao, and S. Bayyuk. "Generalized formulations for the Rhie-Chow interpolation". In: *J. Comput. Phys.* 258.C (Feb. 2014), pp. 880–914. URL: http://dx.doi.org/10.1016/j.jcp.2013.11.006 (cit. on p. 111).

[67] W. Z. Shen, J. Michelsen, and J. N. Sørensen. "An improved Rhie-Chow interpolation for unsteady flow computations". In: *AIAA Journal* 39.12 (2001), pp. 2406–2409 (cit. on p. 111).

Chapter 3

Numerical Error Analysis for Discrete Boundary Conditions of the Euler Equations

Contents

1 Introduction

In this chapter, we leave flow modelling in congested media behind. The work addresses the issue of open numerical boundary conditions to get waves outside of the computational domain.

Concerning fluid dynamic problems, fluid flows are frequently considered in an infinite domain, denoted by Ω_∞, see FIGURE 3.1 corresponding to a one-dimensional case in space.

The solution of the hyperbolic continuous problem is then sought in $\mathbb{R}^d \times (0,T)$, with $d = 1, 2$ or 3 and the time $T \in \mathbb{R}_+^*$, without boundary conditions, see [19, 20]. This solution, expected to be known and unique, is noted $\mathtt{S}_{\Omega_\infty}^{exact}(\boldsymbol{x}, t)$ for $(\boldsymbol{x}, t) \in \mathbb{R}^d \times (0,T)$.

In contrast, the numerical approximations, noted $\mathtt{S}_{\Omega}^{\Delta\boldsymbol{x},\Delta t}(\boldsymbol{x}, t)$ for $(\boldsymbol{x}, t) \in \Omega \times (0,T)$, are performed in a **bounded computational domain** $\Omega \subsetneq \Omega_\infty$ (see FIGURE 3.1) with prescribed inlet/outlet boundary conditions on $\partial\Omega$.

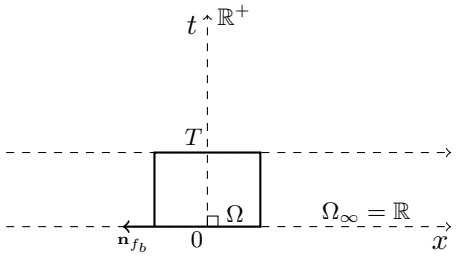

FIGURE 3.1 – *Bounded computational domain $\Omega \subsetneq \Omega_\infty$, with Ω_∞ a spatial infinite domain.*

For this purpose, artificial boundaries have been introduced on (part of) $\partial\Omega$. Then, numerical boundary conditions, depending on the time and space steps, must be prescribed on $\partial\Omega$. When the mesh size and the time step tend to zero, $(\Delta\boldsymbol{x}, \Delta t) \to (0,0)$, we assume that some (unique) converged approximation, noted $\mathtt{S}_\Omega^{0,0}(\boldsymbol{x},t)$ for $(\boldsymbol{x},t) \in \Omega \times (0,T)$, is obtained.

Eventually, we wonder whether $\mathtt{S}_\Omega^{0,0}(\boldsymbol{x},t)$ for $(\boldsymbol{x},t) \in \Omega \times (0,T)$, coincides with the restriction of the exact solution to Ω, $\mathtt{S}_{\Omega_\infty}^{exact}(\boldsymbol{x},t)$ for $(\boldsymbol{x},t) \in \Omega \times (0,T)$, or not ! In the latter case, the converged approximation $\mathtt{S}_\Omega^{0,0}$ will be said to be non **consistent**.

Thus, this chapter focuses on numerical convergence studies for the Euler equations in order to verify the **consistency** (in that sense) and also the order of convergence of the approximate solution taking into account numerical artificial boundary conditions.

Herein, the aim consists in obtaining suitable numerical boundary conditions with an ideal gas or a stiffened gas EOS, in the sense that the L^1-norm of the error, $\left|\mathtt{S}_{\Omega_\infty}^{exact}(\boldsymbol{x},t) - \mathtt{S}_\Omega^{\Delta\boldsymbol{x},\Delta t}(\boldsymbol{x},t)\right|$ for $(\boldsymbol{x},t) \in \Omega \times (0,T)$, tends to zero when refining the mesh. The strategy is the following:

1. propose a formulation of discrete artificial boundary conditions,
2. compute an approximate solution of the problem for which an exact solution is known,
3. verify the numerical convergence of the approximate solution with these boundary conditions to the exact solution.

We emphasize that the technique presented here is devoted to time explicit or semi-implicit Finite Volume Methods, and the suitability of the choice of numerical boundary conditions is discussed.

Euler equations (3.1) are approximated in a bounded domain, $\Omega \times (0,T)$, with a prescribed initial condition:

$$\begin{cases} \partial_t \boldsymbol{W}(\boldsymbol{x},t) + \mathbf{div}\left(\boldsymbol{F}(\boldsymbol{W}(\boldsymbol{x},t))\right) = 0, \quad (\boldsymbol{x},t) \in \Omega \times (0,T)\,, \\ \boldsymbol{W}(\boldsymbol{x},0) = \boldsymbol{W}^0(\boldsymbol{x}). \end{cases} \tag{3.1}$$

The unknown $\boldsymbol{W} = (\rho, \rho\boldsymbol{u}, \rho e)^{\mathsf{T}}$ is the state vector, a function from $\Omega \times (0,T)$ in $\mathbb{R}^{d+2}$ and the given function $\boldsymbol{F} : \mathbb{R}^{d+2} \to \mathbb{R}^{d\times(d+2)}$ is the flux function:

$$\boldsymbol{F}(\boldsymbol{W}) = (\rho\boldsymbol{u}, \rho\boldsymbol{u}\otimes\boldsymbol{u} + P\,\mathbf{Id}, (\rho e + P)\boldsymbol{u})^{\mathsf{T}}\,.$$

In order to complete time evolution continuous problem (3.1), some artificial boundary conditions are added on $\partial\Omega$. Classically [16, 19], a general principle is that the number of boundary conditions needs to be equal to the number of ingoing eigenvalues of the Jacobian matrix on the boundary $\partial\Omega$. However this principle is not easy to apply when the sign of an eigenvalue changes during the simulation or is null [68].

Problem (3.1) with boundary conditions is discretised by using a Finite Volume scheme with the discrete unknown $\mathbf{W}_i^n$ over the cell Ω_i, for $i \in \{1, ..., N\}$ and $n \in \mathbb{N}$:

$$\frac{|\Omega_i|}{\Delta t^n}\left(\mathbf{W}_i^{n+1} - \mathbf{W}_i^n\right) + \sum_{j \in N(i)} \mathbf{F}_{ij}^{num} \cdot \boldsymbol{n}_{ij} S_{ij} + \sum_{f_b \in \mathcal{F}_i^b} \mathbf{F}_{f_b}^{num} \cdot \mathbf{n}_{f_b} S_{f_b} = 0, \tag{3.2}$$

where $\mathbf{F}_{ij}^{num}$ is the numerical flux calculated from the cell values $\mathbf{W}_i$ and $\mathbf{W}_j$, with $j \in N(i)$, set of neighbouring cells. In order to solve problem (3.2), the fluxes on $\partial\Omega$, $\mathbf{F}_{f_b}^{num}$, with $f_b \in \mathcal{F}_i^b$, set of boundary faces, have to be computed. One possible approach is to determine some artificial values in a virtual cell at the exterior of the domain, symmetric of the boundary cell with respect to the boundary face f_b. The boundary flux is then obtained: $\mathbf{F}_{f_b}^{num} = \mathbf{g}(\mathbf{W}_i^n, \mathbf{W}_{ext}^n)$. This numerical flux $\mathbf{g}$ is not necessarily the one used for the interior fluxes, that is at the interface between two inner cells. It can be more precise, such as the exact Godunov flux.

In the general case (*i.e.* considering now not only problem posed over $\mathbb{R}^d$), at the boundaries, three different situations may be encountered.

For the sake of simplicity, the one-dimensional case is considered.

a. Wall boundary condition

A first boundary condition is the rigid wall boundary condition (see chapter 1 or [46] and [58]). The wall condition on $\partial\Omega^w$ is $\boldsymbol{u} \cdot \boldsymbol{n}|_{\partial\Omega^w} = u_w = 0$, which corresponds to the fact that the mass flux is null at the wall. The only component to compute is the wall pressure P_{f_b} at each wall boundary face. The technique consists in solving a Riemann problem at $t = t^n$ with a mirror state in the virtual cell: $\rho_{ext}^n = \rho_i^n$, $\mathbf{u}_{ext}^n = (\mathbf{Id} - 2\boldsymbol{n} \otimes \boldsymbol{n})\,\mathbf{u}_i^n$ and $P_{ext}^n = P_i^n$. The boundary flux $\mathbf{g}(\mathbf{W}_i^n, \mathbf{W}_{ext}^n)$, that is the value of the pressure at the wall, is then obtained. The Godunov flux (or linearised Godunov flux) is suggested, see [58] for explicit approximate Riemann schemes or [46] for semi-implicit scheme.

b. Inlet/outlet boundary condition with a partially known exterior state

Another boundary condition of interest is the inlet condition ($\boldsymbol{u} \cdot \boldsymbol{n}|_{\partial\Omega^{in}} < 0$) or the outlet condition ($\boldsymbol{u} \cdot \boldsymbol{n}|_{\partial\Omega^{out}} > 0$) used for channel or nozzle flows.

A numerical method, often used, is the technique of half Riemann problems as explained in [59, 69] and also used in [60]. The boundary conditions are treated by solving an exact Riemann problem at the boundary faces between the interior state $\mathbf{W}_i^n$ and the virtual state, partially prescribed or known, outside the domain Ω. The calculation depends on the type of boundary conditions (subsonic or supersonic inflow, subsonic or supersonic outflow): the number of ingoing eigenvalues on $\partial\Omega^{in/out}$ gives the number of components to be imposed on the boundary flux or on the virtual state $\mathbf{W}_{ext}^n$. The other components are deduced from the resolution of a Riemann problem (see, for example, FIGURE 3.2 for a subsonic inflow). This method leads, at each time step, to solve a non linear system.

Supposing, without loss of generality, that the inlet and the outlet boundaries are located on the left and right side of the domain, respectively, four configurations are possible depending on the normal local Mach number $\frac{u}{c}$ to the boundary face:

- subsonic inlet condition: two eigenvalues $\{u, u + c\}$ are ingoing in the computational domain Ω. Then two boundary conditions are given (typically external total enthalpy and pressure). The external state $\mathbf{W}_{ext}^n$ and the computed state $\mathbf{W}_i^n$ are connected by a 2-wave and 3-wave going inside Ω (see FIGURE 3.2),

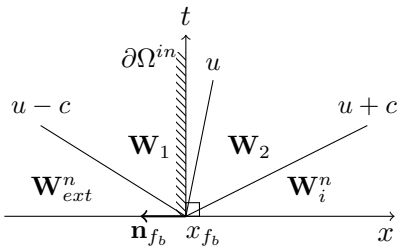

FIGURE 3.2 – *Riemann problem at an inlet boundary face for the subsonic Euler equations.*

- subsonic outlet condition: one eigenvalue $\{u-c\}$ is ingoing in the computational domain Ω. One boundary condition is given (typically the pressure). The external state is deduced in noting that the two states are connected by only a 1-wave going inside Ω,
- supersonic inlet condition: three eigenvalues $\{u-c, u, u+c\}$ are ingoing in the computational domain Ω. The whole external state is given.
- supersonic outlet condition: none eigenvalue is ingoing in the computational domain Ω. The external state is not given. It is determined by the computed state $\mathbf{W}_i^n$, since all the waves go outside of Ω.

c. Inlet/outlet boundary condition with an unknown exterior state

The third class of boundary conditions arises when waves are going out of the computational domain Ω, and when no information is given on the boundary $\partial\Omega$. The boundary condition, used in industrial numerical simulations, is classically the supersonic outlet condition as described above; thus enforcing the boundary cell state to the unknown exterior state $\mathbf{W}_{ext}^n = \mathbf{W}_i^n$.

In this chapter, as said before, **we focus on artificial boundary conditions**, and thus on the point c. Some simple formulations are proposed and tested to deal with these boundary conditions, when no component of $\mathbf{W}_{ext}^n$ is imposed:

***BC*$_0$:** a standard formulation assuming the invariance of the interior state (corresponding to the supersonic outlet condition),

***BC*$_{1r}$:** a formulation for an outgoing rarefaction wave using the structure of Riemann invariants,

***BC*$_{1s}$:** a formulation for an outgoing shock wave relying on the jump relations,

***BC*$_s$:** a formulation for an outgoing shock wave based on another exterior state (to be defined in the sequel).

Three verification test cases are then performed with measure of the discrete L^1 error. These are one-dimensional Riemann problems with outgoing waves, which are simulated and compared with the exact solution calculated on an infinite domain:

case 1: a 1-rarefaction wave going through the left boundary,

case 2: a 3-shock wave going through the right boundary,

case 3: a shock tube with waves going through the left and right boundaries.

The verification cases enable to check whether the approximate solution converges towards the right solution, the unique solution of the Riemann problem. The test cases are performed with two equations of state: an ideal gas EOS and a stiffened gas EOS.

The numerical scheme is an explicit solver: a Godunov-like scheme (VFRoe-ncv scheme).

2 Numerical boundary conditions for outgoing waves

In practice, Euler equations (3.1) are numerically solved in a bounded computational domain Ω. We aim at mimicking an unbounded domain in order to let the waves travel out of the computational domain. The idea is that outgoing waves should be absorbed and not reflected back into the domain. Numerous works propose absorbing (or radiation) boundary conditions, but mainly concern smooth waves and no numerical convergence study is performed. Most approaches for linear or non linear hyperbolic systems rely on the characteristic form of the diagonalized system: the outgoing waves are described by the characteristic equations at the boundaries. We refer to [70, 71, 72, 73] for more details for the Euler equations. These characteristic methods have been extended to the Navier-Stokes equations in [74, 75]. A different method, commonly used for wave problems, is the perfectly matched layer method [76, 77, 78]. This technique, using an absorbing layer, is relevant when solving linearised Euler equations but is more difficult to apply to the non linear system of the Euler or Navier-Stokes equations, see [79]. Another technique, proposed in [80], is the radiative and outflow conditions. This technique alters a part of the domain with a small layer near the boundary where another system of equations is applied. This sponge zone can significantly reduce acoustic wave reflections by absorbing outgoing waves. Nevertheless, the condition is specific to aeroacoustic problems based on linearised Euler equations.

Herein, a boundary is defined as transparent if the limit of the approximate solutions, obtained with a boundary condition, exactly coincides with the exact solution in the unbounded domain. The purpose is to impose numerical non-reflecting boundary conditions at transparent boundaries of the domain Ω in a such way that they allow the wave motion to pass through these boundaries without generating reflections back into the interior of Ω, or at least with a reduced amount of numerical reflections, which should vanish when the mesh of Ω is refined. Convergence studies for smooth and shock non linear waves are numerically performed in a subsonic flow. The proposed boundary conditions only use the computed interior states in the computational domain.

2.1 A formulation assuming the invariance of the interior state (BC_0)

The first boundary condition simply consists in taking the interior value of the state vector into the boundary cell Ω_i at each time step t^n:

$$\mathbf{W}_{ext}^n = \mathbf{W}_i^n, \tag{3.3}$$

thus giving for the primitive variables:

$$\begin{pmatrix} \rho_{ext}^n \\ u_{ext}^n \\ P_{ext}^n \end{pmatrix} = \begin{pmatrix} \rho_i^n \\ u_i^n \\ P_i^n \end{pmatrix}.$$

The boundary flux is thus, more or less, an upwind flux with respect to the propagating direction of the wave front. For a Godunov-like scheme, the numerical boundary flux reads as the numerical flux $\mathbf{g}$ at interface with identical left and right states:

$$\mathbf{F}_{f_b}^{num} = \mathbf{g}(\mathbf{W}_{ext}^n, \mathbf{W}_i^n) = \mathbf{g}(\mathbf{W}_i^n, \mathbf{W}_i^n) = \boldsymbol{F}(\mathbf{W}_i^n) \tag{3.4}$$

This technique does not need any knowledge of the wave structure.

2.2 A formulation for outgoing plane subsonic 1-rarefaction waves using the structure of Riemann invariants (BC_{1r})

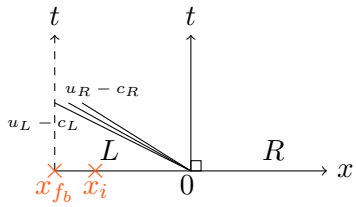

FIGURE 3.3 – *1-rarefaction wave.*

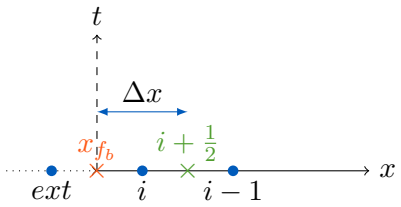

FIGURE 3.4 – *Left boundary with a 1D Cartesian grid.*

The non-reflecting boundary condition for a 1-rarefaction wave going out of the computational domain Ω at x_{f_b}, see FIGURE 3.3, is treated in using the two associated Riemann invariants I_k^1, $k \in \{1, 2\}$. At each time step t^n, they thus allow to connect the interior state $\mathbf{W}_i^n$, of the boundary cell Ω_i, with the boundary state $\mathbf{W}_{ext}^n$, of the exterior virtual cell, see FIGURE 3.4. For sake of simplicity, the upper-script "n" is now omitted, thus:

$$I_k^1(\mathbf{W}_{ext}) = I_k^1(\mathbf{W}_i) \text{ for } k \in \{1, 2\}.$$

For Euler equations (3.1), this is equivalent to:

$$\begin{cases} I_1^1 = s(P_{ext}, \rho_{ext}) = s(P_i, \rho_i) = s_i, & \text{(3.5a)} \\ I_2^1 = u_{ext} + \displaystyle\int_0^{\rho_{ext}} \frac{c(\rho, s_i)}{\rho} d\rho = u_i + \int_0^{\rho_i} \frac{c(\rho, s_i)}{\rho} d\rho, & \text{(3.5b)} \end{cases}$$

with $u = -\boldsymbol{u} \cdot \mathbf{n}_{f_b}$. For an ideal gas EOS such that $\rho\epsilon = \frac{P}{\gamma - 1}$, with $\gamma > 1$, we get at once:

$$\begin{cases} \dfrac{P_{ext}}{\rho_{ext}^\gamma} = \dfrac{P_i}{\rho_i^\gamma}, & \text{(3.6a)} \\ u_{ext} + \dfrac{2}{\gamma - 1} c_{ext} = u_i + \dfrac{2}{\gamma - 1} c_i. & \text{(3.6b)} \end{cases}$$

where the speed of sound is $c = \sqrt{\frac{\gamma P}{\rho}}$, at each time step.

However, a third additional scalar relation is to be provided to set a system of three equations with three unknowns. We now take into account the fact that the profile of the variables is smooth in a rarefaction wave. One of the scalar variables at the boundary has to be estimated. Note that, for an ideal gas EOS, the exact velocity profile is linear in space,

$$u(\xi) = \frac{2}{\gamma + 1} \xi + cste, \text{ where } \xi = \frac{x}{t}.$$

The exterior normal velocity is calculated by a linear extrapolation so that $\partial_{\boldsymbol{n}} u = cste$, *i.e.* in the $\mathbf{n}_{f_b}$-direction, at each time step:

$$\frac{u_{ext} - u_i}{x_{ext} - x_i} = \frac{u_i - u_{i-1}}{x_i - x_{i-1}}. \quad \text{(3.7)}$$

The weight $\omega_{\Delta x} = \frac{x_{ext} - x_i}{x_i - x_{i-1}}$ is defined. For a uniform Cartesian grid, $\omega_{\Delta x} = 1$.

From equations (3.6a), (3.6b) and (3.7), the complete exterior state is thus deduced:

$$\rho_{ext} = \rho_i \left(1 + \omega_{\Delta x} \frac{\gamma - 1}{2} \frac{u_{i-1} - u_i}{c_i}\right)^{\frac{2}{\gamma-1}}, \tag{3.8}$$

$$P_{ext} = P_i \left(1 + \omega_{\Delta x} \frac{\gamma - 1}{2} \frac{u_{i-1} - u_i}{c_i}\right)^{\frac{2\gamma}{\gamma-1}}, \tag{3.9}$$

$$u_{ext} = (1 + \omega_{\Delta x}) u_i - \omega_{\Delta x} u_{i-1}. \tag{3.10}$$

For a stiffened gas EOS such that $\rho\epsilon = \frac{P+\gamma\Pi_\infty}{\gamma-1}$ and thus $c = \sqrt{\frac{\gamma(P+\Pi_\infty)}{\rho}}$, with $\Pi_\infty \geq 0$, the relations are identical except for the pressure:

$$P_{ext} = (P_i + \Pi_\infty) \left(1 + \omega_{\Delta x} \frac{\gamma - 1}{2} \frac{u_{i-1} - u_i}{c_i}\right)^{\frac{2\gamma}{\gamma-1}} - \Pi_\infty. \tag{3.11}$$

The numerical boundary flux reads as the numerical flux $\mathbf{g}$ at interface with the left extrapolated exterior state and the right interior state i over the time interval $\Delta t = t^{n+1} - t^n$:

$$\mathbf{F}_{f_b}^{num} = \mathbf{g}(\mathbf{W}_{ext}^n, \mathbf{W}_i^n). \tag{3.12}$$

2.3 Two formulations for outgoing plane 3-shock waves

2.3.1 A formulation relying on the jump relations (BC_{1s})

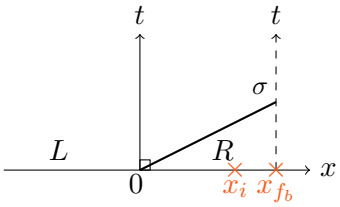

FIGURE 3.5 – *3-shock wave.*

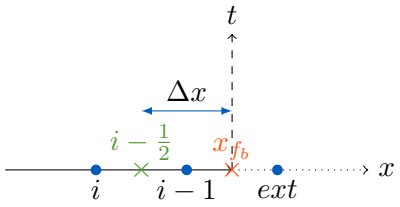

FIGURE 3.6 – *Right boundary with a 1D Cartesian grid.*

For a plane outgoing 3-shock wave, see FIGURE 3.5, the first technique is proposed in order to evaluate the exterior state $\mathbf{W}_{ext}$, similarly as for the rarefaction case. The two shock conditions, *i.e.* the Rankine-Hugoniot jump relations for a 3-shock, are used between the state of the boundary cell i and the exterior state, see FIGURE 3.6, at each time step:

$$\begin{cases} \left([u]_{ext}^i\right)^2 + [P]_{ext}^i \left[\frac{1}{\rho}\right]_{ext}^i = 0, & \text{(3.13a)} \\ [\epsilon]_{ext}^i + \frac{P_{ext} + P_i}{2} \left[\frac{1}{\rho}\right]_{ext}^i = 0, & \text{(3.13b)} \end{cases}$$

where, for any field φ, the jump is defined as $[\varphi]_L^R = \varphi_R - \varphi_L$.

Set $z = \frac{\rho_i}{\rho_{ext}} \in [1, \beta)$, with $\beta = \frac{\gamma + 1}{\gamma - 1}$. From equations (3.13a) and (3.13b), we deduce for an ideal gas EOS:

$$\frac{P_{ext}}{P_i} = \frac{\beta - z}{\beta z - 1}, \tag{3.14}$$

and:

$$[u]_i^{ext} = u_{ext} - u_i = -\sqrt{\frac{P_i}{\rho_i}\left(\frac{\beta - z}{\beta z - 1} - 1\right)(1 - z)}. \tag{3.15}$$

For a stiffened gas EOS, only the relation for the pressure calculation is changed:

$$\frac{P_{ext} + \Pi_\infty}{P_i + \Pi_\infty} = \frac{\beta - z}{\beta z - 1}. \tag{3.16}$$

It remains to provide the exterior density ρ_{ext} at each time step t^n. A possible simple approximate value is:

$$\rho_{ext}^n = \rho_i^{n-1}, \tag{3.17}$$

herein, assuming $CFL = \frac{\sigma \Delta t}{\Delta x} = 0.5$, the transport of the density discontinuity, at the speed of shock wave, is approximated.

Eventually, the numerical boundary flux reads as the numerical flux $\mathbf{g}$ at interface with the left extrapolated exterior state and the right interior state i over the time interval $\Delta t = t^{n+1} - t^n$:

$$\mathbf{F}_{f_b}^{num} = \mathbf{g}(\mathbf{W}_{ext}^n, \mathbf{W}_i^n). \tag{3.18}$$

2.3.2 A formulation based on an imposed exterior state deduced from the initial condition (BC_s)

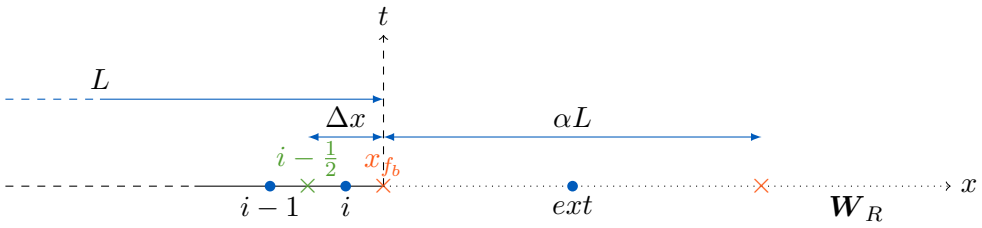

FIGURE 3.7 – *Right boundary with a virtual domain connecting the right state to the interior.*

The boundary cell is connected with the right initial state $\boldsymbol{W}_R$ by a virtual exterior cell of physical size αL, with L the domain length and $\alpha \in \mathbb{R}_+^*$, see FIGURE 3.7. The α coefficient is a parameter of the problem. This exterior state $\mathbf{W}_{ext}^n$ is, at time t^n, not extrapolated from the interior states of the computational domain, but updated with the numerical flux and the known state $\boldsymbol{W}_R$ such that:

$$\mathbf{W}_{ext}^n = \mathbf{W}_{ext}^{n-1} - \frac{\Delta t^{n-1}}{\alpha L}\left(\mathbf{g}(\mathbf{W}_{ext}^{n-1}, \mathbf{W}_R) - \mathbf{g}(\mathbf{W}_i^{n-1}, \mathbf{W}_{ext}^{n-1})\right). \tag{3.19}$$

This technique gives the following asymptotic update of the exterior state $\mathbf{W}_{ext}^n$ when $\alpha \to +\infty$ for a finite time step Δt^{n-1}:

$$\lim_{\alpha \to +\infty} \mathbf{W}_{ext}^n = \mathbf{W}_{ext}^{n-1}, \tag{3.20}$$

The exterior state is steady and therefore equal to its initial state $\mathbf{W}_{ext}^0$, which is the right state $\mathbf{W}_R^0$. The numerical boundary flux thus yields:

$$\mathbf{F}_{f_b}^{num} = \mathbf{g}(\mathbf{W}_i^n, \mathbf{W}_R^0). \tag{3.21}$$

This boundary condition amounts to impose, in the virtual exterior cell, the right state $\mathbf{W}_R$ known from the initial condition of the problem.

3 VFRoe-ncv numerical schemes

The VFRoe-ncv scheme, VFRoe with non conservative variable, for conservation laws of hyperbolic system is succinctly presented, for more details see [58, 81]. We assume that an appropriate EOS holds so that the system is hyperbolic, for instance an ideal gas EOS or a stiffened gas EOS.

$$\begin{cases} \partial_t \boldsymbol{W}(\boldsymbol{x},t) + \mathbf{div}\left(\boldsymbol{F}(\boldsymbol{W}(\boldsymbol{x},t)\right) = 0 \ \text{ in } \Omega \times (0,T)\,, \\ \boldsymbol{W}(\boldsymbol{x},0) = \boldsymbol{W}_0(\boldsymbol{x}). \end{cases} \tag{3.22}$$

VFRoe-ncv is a time-explicit Finite Volume conservative scheme using an approximate Godunov scheme [19, 82, 83, 84]. The approximate mean value of the state $\boldsymbol{W} \in \mathbb{R}^p$ is updated from t^n to t^{n+1} with equation (3.23). The interior numerical flux g is computed at the interface of surface $S_{\mathtt{f}_{ij}}$ between the cell Ω_i and its neighbouring cell Ω_j for $i \in \{1,\ldots,N_{cell}\}$:

$$|\Omega_i|\left(\mathbf{W}_i^{n+1} - \mathbf{W}_i^n\right) + \Delta t^n \sum_{j\in N(i)} \mathbf{g}(\mathbf{W}_i^n, \mathbf{W}_j^n)\cdot \boldsymbol{n}_{ij} S_{ij} + \Delta t^n \sum_{f_b \in \mathcal{F}_b} \mathbf{F}_{f_b}^{num}\cdot \mathbf{n}_{f_b} S_{f_b}, \tag{3.23}$$

$N(i)$ refers to the neighbouring cells of Ω_i, $\boldsymbol{n}_{ij}$ stands for the unit normal vector to the interface, oriented from the cells Ω_i to Ω_j, and $\mathbf{F}_{f_b}^{num}$ stands for the boundary numerical flux. More precisely, the VFRoe-ncv scheme is based on the resolution of a linearised Riemann problems in the $\boldsymbol{n}_{ij}$-direction. The technique consists in calculating the exact intermediate state $\boldsymbol{Y}_{ij}^{\star}$ at each interface ij in order to evaluate the numerical flux:

$$\mathbf{g}(\mathbf{W}_i^n, \mathbf{W}_j^n) = \boldsymbol{F}(\Psi^{-1}(\boldsymbol{Y}_{ij}^{\star})), \tag{3.24}$$

where $\Psi : \boldsymbol{W} \mapsto \Psi(\boldsymbol{W}) = \boldsymbol{Y}$ is a change of variables (Ψ is a smooth invertible function), thus allowing to read the hyperbolic system in a non-conservative form:

$$\partial_t \boldsymbol{Y} + \boldsymbol{B}(\boldsymbol{Y})\partial_{\boldsymbol{n}_{ij}} \boldsymbol{Y} = 0, \tag{3.25}$$

where the Jacobian matrix is $\boldsymbol{B}(\boldsymbol{Y}) = (\partial_{\boldsymbol{Y}}\boldsymbol{W})^{-1}\,\partial_{\boldsymbol{W}}\boldsymbol{F}\;\partial_{\boldsymbol{Y}}\boldsymbol{W} \in \mathbb{R}^{p\times p}$.

At each interface, using invariance under frame rotation, the following **linearised** Riemann problem is solved [20, 19]:

$$\begin{cases} \partial_t \boldsymbol{Y} + \boldsymbol{B}(\widetilde{\boldsymbol{Y}})\boldsymbol{\partial_{n_{ij}}} \boldsymbol{Y} = 0 \ \text{ in } \Omega \times \left(t^n, t^{n+1}\right), \\ \boldsymbol{Y}(\boldsymbol{x}, t^n) = \begin{cases} \boldsymbol{Y}_L = \mathbf{Y}_i^n \text{ if } \boldsymbol{x}\cdot\boldsymbol{n} < 0, \\ \boldsymbol{Y}_R = \mathbf{Y}_j^n \text{ if } \boldsymbol{x}\cdot\boldsymbol{n} < 0, \end{cases} \end{cases} \tag{3.26}$$

where $\widetilde{\boldsymbol{Y}}$ is an average state depending on left and right states, so that $\widetilde{\boldsymbol{Y}}(\mathbf{Y}_i^n, \mathbf{Y}_i^n) = \mathbf{Y}_i^n$. In practice, the arithmetic average between the left and right states, $\overline{\boldsymbol{Y}} = \frac{\boldsymbol{Y}_L + \boldsymbol{Y}_R}{2}$, has been used:

$$\widetilde{\boldsymbol{Y}} = \overline{\boldsymbol{Y}}. \tag{3.27}$$

Let us set $\widetilde{\lambda}_k$, $\widetilde{\boldsymbol{l}}_k$ and $\widetilde{\boldsymbol{r}}_k$, $k \in \{1,\ldots,p\}$, the real eigenvalues arranged in increasing order, the associated left and right eigenvectors of the diagonalizable matrix $\boldsymbol{B}(\widetilde{Y})$ respectively. The exact solution $\boldsymbol{Y}^{\star}(\frac{x}{t}; \boldsymbol{Y}_L, \boldsymbol{Y}_R)$ of the linear Riemann problem (3.26) is then, for $\frac{x}{t} \neq \widetilde{\lambda}_k$, $k \in \{1,\ldots,p\}$, composed of $p+1$ constant states, see FIGURE 3.8:

$$\boldsymbol{Y}^{\star}(\frac{x}{t}; \boldsymbol{Y}_L, \boldsymbol{Y}_R) = \boldsymbol{Y}_L + \sum_{k/\widetilde{\lambda}_k < \frac{x}{t}} \tilde{\alpha}_k \widetilde{\boldsymbol{r}}_k = \boldsymbol{Y}_R - \sum_{k/\widetilde{\lambda}_k > \frac{x}{t}} \tilde{\alpha}_k \widetilde{\boldsymbol{r}}_k, \tag{3.28}$$

noting $\tilde{\alpha}_k = \widetilde{\boldsymbol{l}}_k^{\mathsf{T}}\left(\boldsymbol{Y}_R - \boldsymbol{Y}_L\right)$. The numerical flux (3.24) is thus:

$$\mathbf{g}(\mathbf{W}_i^n, \mathbf{W}_j^n) = \boldsymbol{F}(\Psi^{-1}(\boldsymbol{Y}^{\star}(0; \boldsymbol{Y}_L, \boldsymbol{Y}_R)), \tag{3.29}$$

where the approximate state at the interface ij, *i.e.* for $\frac{x}{t} = 0$, is given by:

$$\boldsymbol{Y}^\star(0; \boldsymbol{Y}_L, \boldsymbol{Y}_R) = \boldsymbol{Y}_L + \sum_{k/\tilde{\lambda}_k<0} \tilde{\alpha}_k \tilde{\boldsymbol{r}}_k = \boldsymbol{Y}_R - \sum_{k/\tilde{\lambda}_k>0} \tilde{\alpha}_k \tilde{\boldsymbol{r}}_k. \tag{3.30}$$

Note that, contrary to the exact Godunov scheme [85], the VFRoe-ncv schemes cannot be interpreted as a projection method. Hence, no theoretical result exists to ensure a good behaviour of the scheme when coping with computations including states near vacuum. An entropy correction is needed for these schemes [58].

The VFRoe-ncv schemes with the non conservative variables

$$\boldsymbol{Y} = \begin{pmatrix} \tau \\ u \\ P \end{pmatrix} \text{ (see [58]), or: } \boldsymbol{Y} = \begin{pmatrix} s \\ u \\ P \end{pmatrix} \text{ (see [86])}$$

are used to approximate solutions of the Euler set of equations.

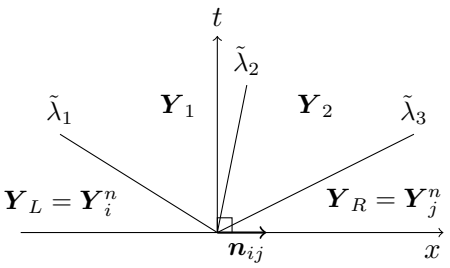

FIGURE 3.8 – *Solution of the linearised Riemann problem for the Euler equations.*

3.1 Entropy correction

When a numerical eigenvalue $\tilde{\lambda}_k$, $k \in \{1, 2, 3\}$, associated with a genuinely non-linear field, vanishes, the numerical fluxes are no more continuous at interfaces. A sonic entropy correction is needed for rarefaction waves in the VFRoe-ncv schemes, which is described in [87].

3.2 VFRoe-ncv with non-conservative variable (τ, u, P)

The VFRoe-ncv scheme [58] is obtained with the non-conservative variable:

$$\boldsymbol{Y} = \begin{pmatrix} \tau \\ u \\ P \end{pmatrix},$$

where $\tau = \frac{1}{\rho}$ is the specific volume. The Euler equations yield for smooth solutions:

$$\partial_t \boldsymbol{Y} + \boldsymbol{B}(\boldsymbol{Y}) \partial_x \boldsymbol{Y} = 0, \tag{3.31}$$

where the Jacobian matrix is:

$$\boldsymbol{B}(\boldsymbol{Y}) = \begin{pmatrix} u & -\tau & 0 \\ 0 & u & \tau \\ 0 & \hat{\gamma} P & u \end{pmatrix},$$

with $\hat{\gamma} = \frac{c^2}{\tau P}$.

The linearisation of system (3.31) is done with (3.27):

$$\boldsymbol{B}(\overline{\boldsymbol{Y}}) = \begin{pmatrix} \overline{u} & -\overline{\tau} & 0 \\ 0 & \overline{u} & \overline{\tau} \\ 0 & \bar{\hat{\gamma}}\overline{P} & \overline{u} \end{pmatrix}.$$

The eigenvalues of the matrix $\boldsymbol{B}(\overline{\boldsymbol{Y}})$ are:

$$\tilde{\lambda}_1 = \overline{u} + \tilde{c}, \quad \tilde{\lambda}_2 = \overline{u} \quad \text{and} \quad \tilde{\lambda}_3 = \overline{u} + \tilde{c},$$

with $\tilde{c}^2 = \bar{\hat{\gamma}}\overline{\tau}\overline{P}$. The associated right eigenvectors are:

$$\tilde{\boldsymbol{r}}_1(\boldsymbol{Y}) = \begin{pmatrix} \overline{\tau} \\ \tilde{c} \\ -\bar{\hat{\gamma}}\overline{P} \end{pmatrix}, \ \tilde{\boldsymbol{r}}_2(\boldsymbol{Y}) = \begin{pmatrix} 1 \\ 0 \\ 0 \end{pmatrix}, \text{ and } \tilde{\boldsymbol{r}}_3(\boldsymbol{Y}) = \begin{pmatrix} \overline{\tau} \\ -\tilde{c} \\ -\bar{\hat{\gamma}}\overline{P} \end{pmatrix},$$

The coefficients $\tilde{\alpha}_1$ and $\tilde{\alpha}_2$ are given by:

$$\tilde{\alpha}_1 = \frac{1}{2\tilde{c}^2}\left(\tilde{c}(u_R - u_L) - \overline{\tau}(P_R - P_L)\right),$$

$$\tilde{\alpha}_3 = -\frac{1}{2\tilde{c}^2}\left(\tilde{c}(u_R - u_L) + \overline{\tau}(P_R - P_L)\right).$$

Thus the two intermediate states read:

$$\boldsymbol{Y}_1 = \begin{pmatrix} \tau_L + \tilde{\alpha}_1\overline{\tau} \\ u_L + \tilde{\alpha}_1\tilde{c} \\ P_L - \tilde{\alpha}_1\bar{\hat{\gamma}}\overline{P} \end{pmatrix}, \text{ and } \boldsymbol{Y}_2 = \begin{pmatrix} \tau_R - \tilde{\alpha}_3\overline{\tau} \\ u_R + \tilde{\alpha}_3\tilde{c} \\ P_R + \tilde{\alpha}_3\bar{\hat{\gamma}}\overline{P} \end{pmatrix},$$

giving:

$$\begin{cases} \tau_1 = \tau_L - \dfrac{\overline{\tau}}{2\bar{\hat{\gamma}}\overline{P}}(P_R - P_L) + \dfrac{\overline{\tau}}{2\tilde{c}}(u_R - u_L), & \text{(3.32a)} \\ \tau_2 = \tau_R + \dfrac{\overline{\tau}}{2\bar{\hat{\gamma}}\overline{P}}(P_R - P_L) + \dfrac{\overline{\tau}}{2\tilde{c}}(u_R - u_L), & \text{(3.32b)} \\ u_1 = u_2 = \overline{u} - \dfrac{\overline{\tau}}{2\tilde{c}}(P_R - P_L), & \text{(3.32c)} \\ P_1 = P_2 = \overline{P} - \dfrac{\tilde{c}}{2\overline{\tau}}(u_R - u_L). & \text{(3.32d)} \end{cases}$$

The approximate state $\boldsymbol{Y}^{\star}_{LR}$ at the interface is deduced and the numerical flux is then calculated by equation (3.24).

The scheme benefits from the following properties, shared by all VFRoe-ncv schemes using variable $\boldsymbol{Y} = (\cdot, u, p)^{\mathsf{T}}$, see [58, 86]:

1. the solution of the linearised Riemann problem satisfies that the 2-Riemann invariants (u, P) are constant across the 2-wave λ_2, since $u_1 = u_2$ and $P_1 = P_2$,

2. assuming that the EOS is such that $\rho\epsilon = f(P) + a\rho + b$, with $a, b \in \mathbb{R}$, then the cell values of the velocity and the pressure are perfectly preserved through the 2-contact discontinuity, when focusing on a single moving contact discontinuity. Note that the family of this latter EOS includes ideal gas and also stiffened gas EOS, see [88] for more details.

3.3 VFRoe-ncv with non-conservative symmetrizing variable (s, u, P)

The Euler equations are rewritten by using symmetrizing variables, see [86], with s the entropy:

$$\boldsymbol{Y} = \begin{pmatrix} s \\ u \\ P \end{pmatrix},$$

giving for smooth solutions:

$$\boldsymbol{M}(\boldsymbol{Y})\partial_t \boldsymbol{Y} + \boldsymbol{S}(\boldsymbol{Y})\partial_x \boldsymbol{Y} = 0, \tag{3.33}$$

with the matrices $\boldsymbol{S}(\boldsymbol{Y})$ and $\boldsymbol{M}(\boldsymbol{Y})$ are defined by:

$$\boldsymbol{S}(\boldsymbol{Y}) = \begin{pmatrix} u & 0 & 0 \\ 0 & u\hat{\gamma}P\rho & \hat{\gamma}P \\ 0 & \hat{\gamma}P & u \end{pmatrix}, \text{ and } \boldsymbol{M}(\boldsymbol{Y}) = \begin{pmatrix} 1 & 0 & 0 \\ 0 & \hat{\gamma}P\rho & 0 \\ 0 & 0 & 1 \end{pmatrix}.$$

$\boldsymbol{S}(\boldsymbol{Y})$ is symmetric and $\boldsymbol{M}(\boldsymbol{Y})$ is symmetric positive definite, provided that both the density and the pressure remain positive. The Jacobian is $\boldsymbol{B}(\boldsymbol{Y}) = \boldsymbol{M}^{-1}(\boldsymbol{Y})\boldsymbol{S}(\boldsymbol{Y})$. The eigenvalues of $\boldsymbol{M}^{-1}(\overline{\boldsymbol{Y}})\boldsymbol{S}(\overline{\boldsymbol{Y}})$ for the linearised problem around the state $\overline{\boldsymbol{Y}}$ are still:

$$\tilde{\lambda}_1 = \overline{u} + \tilde{c}, \quad \tilde{\lambda}_2 = \overline{u} \quad \text{and} \quad \tilde{\lambda}_3 = \overline{u} + \tilde{c},$$

with $\tilde{c}^2 = \bar{\hat{\gamma}}\overline{\tau}\overline{P}$.

The associated right eigenvectors are:

$$\tilde{\boldsymbol{r}}_1(\boldsymbol{Y}) = \begin{pmatrix} 0 \\ \overline{\tau} \\ -\tilde{c} \end{pmatrix}, \ \tilde{\boldsymbol{r}}_2(\boldsymbol{Y}) = \begin{pmatrix} 1 \\ 0 \\ 0 \end{pmatrix}, \text{ and } \tilde{\boldsymbol{r}}_3(\boldsymbol{Y}) = \begin{pmatrix} 0 \\ \overline{\tau} \\ \tilde{c} \end{pmatrix}.$$

The coefficients $\tilde{\alpha}_1$ and $\tilde{\alpha}_2$, for the decomposition on the basis of right eigenvectors, are:

$$\tilde{\alpha}_1 = \frac{1}{2\tilde{c}}\left(\frac{\tilde{c}}{\overline{\tau}}(u_R - u_L) - (P_R - P_L)\right),$$

$$\tilde{\alpha}_3 = \frac{1}{2\tilde{c}}\left(\frac{\tilde{c}}{\overline{\tau}}(u_R - u_L) + (P_R - P_L)\right).$$

Thus the two intermediate states read:

$$\boldsymbol{Y}_1 = \begin{pmatrix} s_L \\ u_L + \tilde{\alpha}_1\overline{\tau} \\ P_L - \tilde{\alpha}_1\tilde{c} \end{pmatrix}, \text{ and } \boldsymbol{Y}_2 = \begin{pmatrix} s_R \\ u_R - \tilde{\alpha}_3\overline{\tau} \\ P_R - \tilde{\alpha}_3\tilde{c} \end{pmatrix},$$

still yielding relations (3.32c) and (3.32d).

The approximate state $\boldsymbol{Y}^{\star}_{LR}$ at the interface is deduced and the numerical flux is then calculated by equation (3.24).

Remark 3.1. *The approximate intermediate value of pressure $P_1 = P_2$ remains positive provided that the initial conditions of the Riemann problem agree with the condition (see [86]):*

$$u_R - u_L < \frac{2\overline{\tau}\overline{P}}{\tilde{c}}. \tag{3.34}$$

Moreover, the approximate intermediate values of density ρ_1 and ρ_2 remain positive provided the latter condition (3.34) is insured.

4 Verification test cases

Three distinct one-dimensional test cases are now considered:

- a pure left-going 1-rarefaction wave (case 1),
- a pure right-going 3-shock wave (case 2),
- a shock tube (case 3).

Herein, we examine whether the approximate solution converges towards the right solution, by choosing one boundary condition formulation detailed before in section 2.

The computations are performed with two analytical equations of state: an ideal gas EOS and a stiffened gas EOS to model a weakly compressible liquid. The rates of convergence of the scheme are numerically measured with the L^1 norm, by refining the mesh with a constant CFL number. The discrete relative L^1 error is defined as, for any variable φ:

$$e_{L^1(\Omega)}(\varphi) = \frac{\sum_{i=1}^{N} \left| \varphi_i^{exact} - \varphi_i^{computed} \right| |\Omega_i|}{\sum_{i=1}^{N} \left| \varphi_i^{exact} \right| |\Omega_i|}.$$

4.1 Left-going 1-rarefaction wave

Numerical results, presented herein, are obtained with a pure rarefaction wave travelling to the left open end of a uniform tube. The initial constant left state and also the right density are chosen. The constant right state is deduced, as detailed below, in order to obtain a pure 1-rarefaction wave.

4.1.1 Exact solution

The exact solution of a pure 1-rarefaction wave, travelling to the left end of the computational domain, is built by solving a 1D Riemann problem for the Euler equations. The 2-contact discontinuity wave and the 3-wave are "ghost" waves. At the beginning of the computation, the shock tube contains a membrane ($x = x_0$) separating two different initial constant fluid states at rest: the right state $\boldsymbol{Y}_R$ and the left state $\boldsymbol{Y}_L$ (see FIGURE 3.9).

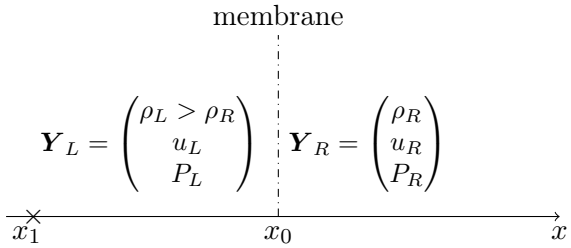

FIGURE 3.9 – *Sketch of the tube apparatus with the initial condition.*

The initial left state is:

$$\boldsymbol{Y}_L = \begin{pmatrix} \rho_L \\ u_L \\ P_L \end{pmatrix},$$

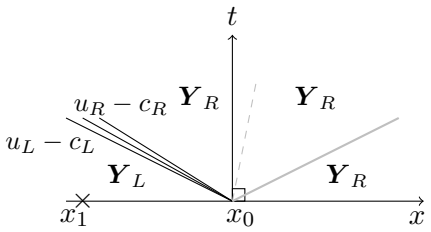

FIGURE 3.10 – *Pure 1-rarefaction wave (subsonic case: $u_L - c_L < 0$).*

and the initial right density ρ_R, whit $\rho_R < \rho_L$, is given.

To complete the initial right state, the velocity u_R and the pressure P_R are calculated by the two k-Riemann invariants of a 1-rarefaction wave:

$$I_k^1(Y_L) = I_k^1(Y_R) \text{ for } k \in \{1, 2\}.$$

Thus, for the Euler equations:

$$\begin{cases} s(P_L, \rho_L) = s(P_R, \rho_R) = s_L, & (3.35a) \\ u_L + \displaystyle\int_0^{\rho_L} \frac{c(\rho, s_L)}{\rho} d\rho = u_R + \int_0^{\rho_R} \frac{c(\rho, s_L)}{\rho} d\rho. & (3.35b) \end{cases}$$

For an ideal gas EOS such that $\rho\epsilon = \frac{P}{\gamma - 1}$, with $\gamma > 1$:

$$\begin{cases} \dfrac{P_L}{\rho_L^\gamma} = \dfrac{P_R}{\rho_R^\gamma}, & (3.36a) \\ u_L + \dfrac{2}{\gamma - 1} c_L = u_R + \dfrac{2}{\gamma - 1} c_R, & (3.36b) \end{cases}$$

where the speed of sound is $c = \sqrt{\frac{\gamma P}{\rho}}$. We deduce from equations (3.36a) and (3.36b) the complete initial right state such that $u_R > u_L$ and $P_R < P_L$:

$$P_R = P_L \left(\frac{\rho_R}{\rho_L} \right)^\gamma, \tag{3.37}$$

$$u_R = u_L + \frac{2}{\gamma - 1} \sqrt{\frac{\gamma P_L}{\rho_L}} \left(1 - \left(\frac{\rho_R}{\rho_L} \right)^{\frac{\gamma - 1}{2}} \right). \tag{3.38}$$

For a stiffened gas EOS such that $\rho\epsilon = \frac{P + \gamma \Pi_\infty}{\gamma - 1}$ and thus $c = \sqrt{\frac{\gamma(P + \Pi_\infty)}{\rho}}$, with $\Pi_\infty \geq 0$, the complete initial right state is simply deduced:

$$P_R = (P_L + \Pi_\infty) \left(\frac{\rho_R}{\rho_L} \right)^\gamma - \Pi_\infty, \tag{3.39}$$

$$u_R = u_L + \frac{2}{\gamma - 1} \sqrt{\frac{\gamma (P_L + \Pi_\infty)}{\rho_L}} \left(1 - \left(\frac{\rho_R}{\rho_L} \right)^{\frac{\gamma - 1}{2}} \right). \tag{3.40}$$

By construction, the unique propagated smooth solution is a pure rarefaction wave such that, for $t > 0$:

$$\boldsymbol{Y}(x,t) = \begin{cases} \boldsymbol{Y}_L & \text{if } \frac{x - x_0}{t} \leq u_L - c_L, \\ \boldsymbol{V}\left(\frac{x - x_0}{t} \right) & \text{if } u_L - c_L \leq \frac{x - x_0}{t} \leq u_R - c_R, \\ \boldsymbol{Y}_R & \text{if } \frac{x - x_0}{t} \geq u_R - c_R, \end{cases} \tag{3.41}$$

where the smooth function connecting the two constant states is, for an ideal gas EOS:

$$\boldsymbol{V}(\xi) = \begin{pmatrix} \rho(\xi) = \rho_L \left(\frac{c(\xi)}{c_L}\right)^{\frac{2}{\gamma-1}} \\ u(\xi) = \frac{2}{\gamma+1}\xi + \frac{2}{\gamma+1}c_L + \frac{\gamma-1}{\gamma+1}u_L \\ P(\xi) = P_L \left(\frac{c(\xi)}{c_L}\right)^{\frac{2\gamma}{\gamma-1}} \end{pmatrix},$$

with:

$$c(\xi) = \frac{2}{\gamma+1}c_L + \frac{\gamma-1}{\gamma+1}u_L - \frac{\gamma-1}{\gamma+1}\xi.$$

For a stiffened gas EOS, the function is similar. The only difference is the pressure expression:

$$P(\xi) = (P_L + \Pi_\infty)\left(\frac{c(\xi)}{c_L}\right)^{\frac{2\gamma}{\gamma-1}} - \Pi_\infty.$$

4.1.2 Numerical results with the VFRoe-ncv scheme

The one-dimensional computational domain is $\Omega = (-200\ m, 200\ m)$. The left boundary is located at $x = x_1 = -200\ m$, see FIGURE 3.9. The numerical approximations, obtained with the VFRoe-ncv (s, u, P) scheme, are compared with the exact solution at three different instants:

- at time $t < t_0$, with $t_0 = \frac{x_1 - x_0}{u_L - c_L}$. The rarefaction wave is inside Ω, not yet at the boundary (the left end).
- at time $t_0 < t < t_1$, with $t_1 = \frac{x_1 - x_0}{u_R - c_R}$. The rarefaction wave is travelling through the boundary (the left end).
- at time $t > t_1$. The rarefaction wave is gone out of Ω.

All meshes used to solve this Riemann problem are uniform. The meshes contain N cells with $N = 800, 1600, 3200, 6400, 12800, 25600$ or 51200. The CFL condition for an explicit scheme is satisfied: $CFL = \frac{|u-c|\Delta t}{\Delta x} = 0.5$.

a. Boundary condition 2.1 (BC_0)

- Verification test case with an ideal gas EOS.

The ideal gas EOS is considered with $\gamma = 1.4$ for a diatomic gas. The initial conditions are:

$$\begin{cases} (\rho_L, u_L, P_L) = \left(1\ kg.m^{-3}, 0\ m.s^{-1}, 10^5\ Pa\right), \\ (\rho_R, u_R, P_R) = \left(0.5\ kg.m^{-3}, 242.17808823988534\ m.s^{-1}, 3.7892701874366379 \times 10^4\ Pa\right). \end{cases} \tag{3.42}$$

The solution is only composed of a 1-rarefaction wave. Profiles are given in FIGURE 3.11 for the exact solution and the VFRoe-ncv approximate solution ($N = 800$) at time $t < t_0$. The "ghost" 2-contact discontinuity is visible on the density profile (a) in FIGURE 3.11. As expected [81], the numerical rates of convergence are slightly greater than 0.8 for density, velocity and pressure. For $t_0 < t < t_1$, the numerical solutions match the exact solution (see FIGURE 3.12). The boundary condition BC_0 is consistent and allows to make the rarefaction wave go out of the computational domain through the boundary at $x_1 = -200\ m$. The convergence orders are still slightly greater than 0.8 for all variables (see TABLE 3.1 and FIGURE 3.13). For $t > t_1$, the rarefaction wave is gone out, the constant initial right state is recovered with a convergence order of approximately 0.9 (see TABLE 3.2 and FIGURE 3.15).

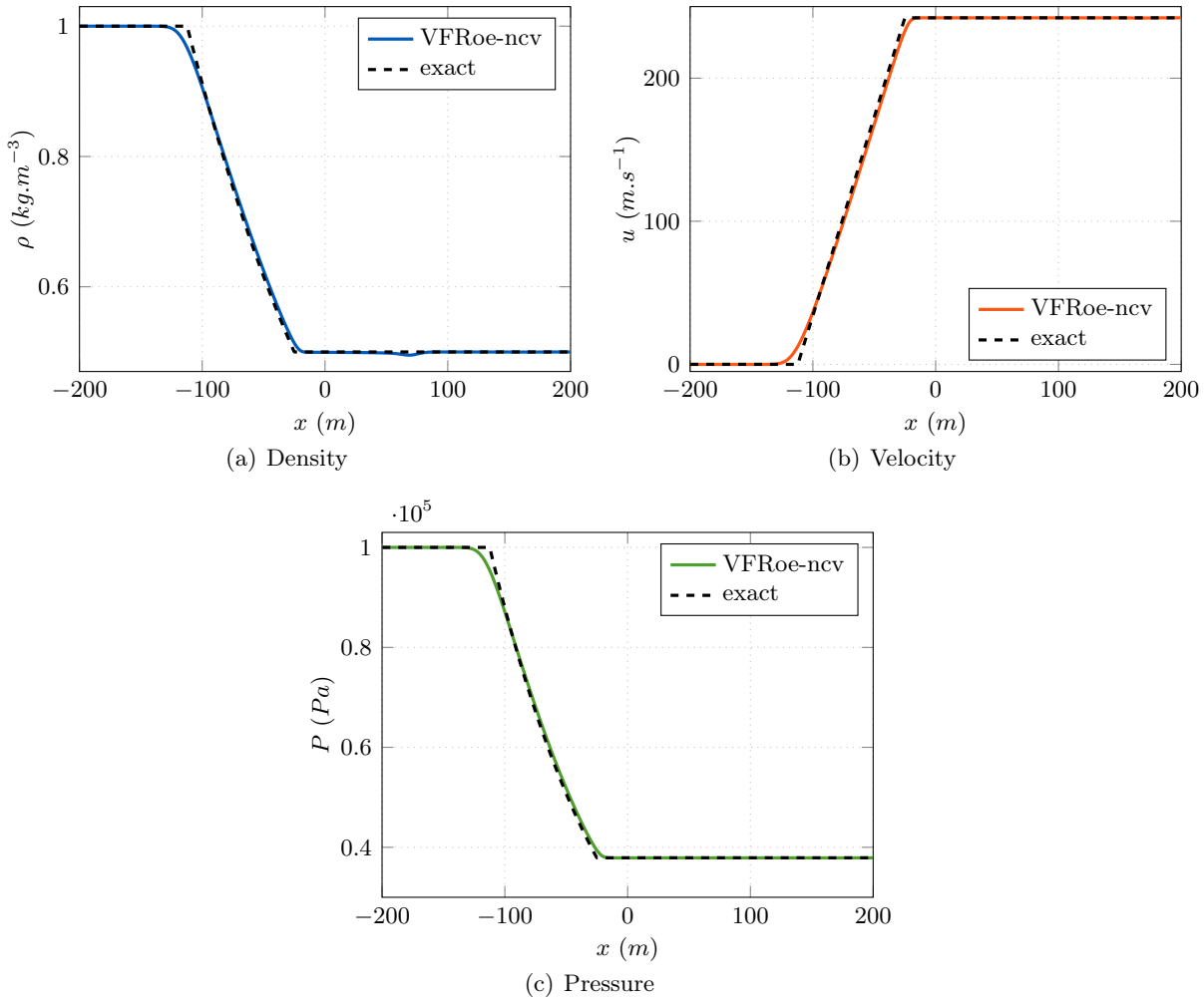

(a) Density (b) Velocity

(c) Pressure

FIGURE 3.11 – *Profiles for the pure rarefaction wave at $t < t_0$ (ideal gas EOS).*

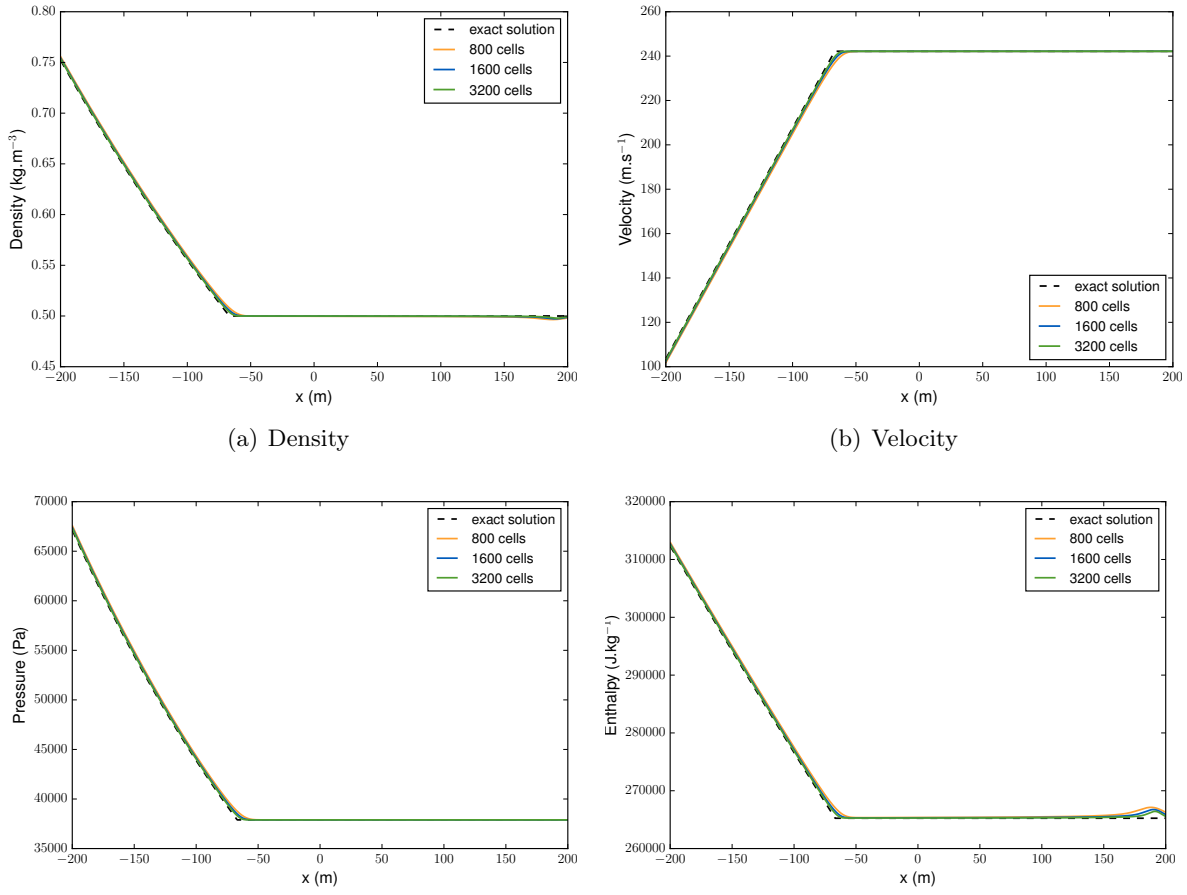

(a) Density

(b) Velocity

(c) Pressure

(d) Enthalpy

FIGURE 3.12 – *BC_0: comparison of the numerical solutions for 800, 1600 and 3200 cells with the exact solution for the pure rarefaction wave at $t_0 < t < t_1$ (ideal gas EOS).*

dx (m)	N	ρ cnv. order	u cnv. order	P cnv. order
5e-1	800			
2.5e-1	1600	0.8221	0.8241	0.8243
1.25e-1	3200	0.8426	0.8403	0.8402
6.25e-2	6400	0.8605	0.8518	0.8516
3.125e-2	12800	0.8774	0.8587	0.8582
1.5625e-2	25600	0.8621	0.8588	0.8579
7.8125e-3	51200	0.8533	0.8491	0.8474

TABLE 3.1 – *BC_0: L^1 convergence orders for the pure rarefaction wave at $t_0 < t < t_1$ (ideal gas EOS).*

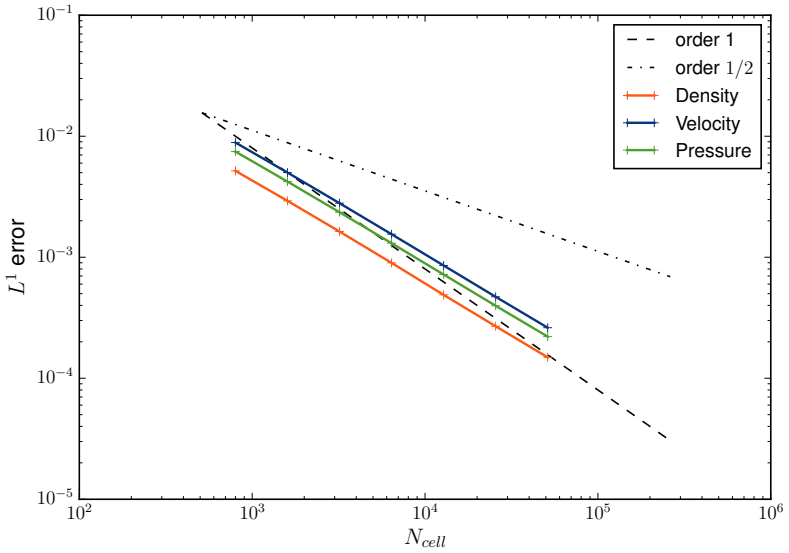

FIGURE 3.13 – *BC_0: L^1 convergence curves for the pure rarefaction wave at $t_0 < t < t_1$ (ideal gas EOS).*

dx (m)	N	ρ cnv. order	u cnv. order	P cnv. order
5e-1	800			
2.5e-1	1600	0.9211	0.9384	0.9383
1.25e-1	3200	0.9395	0.9700	0.9700
6.25e-2	6400	0.9502	1.0061	1.0061
3.125e-2	12800	0.9521	1.0608	1.0609
1.5625e-2	25600	0.9420	1.1687	1.1687
7.8125e-3	51200	0.9134	1.4486	1.4486

TABLE 3.2 – *BC_0: L^1 convergence orders for the pure rarefaction wave at $t > t_1$ (ideal gas EOS).*

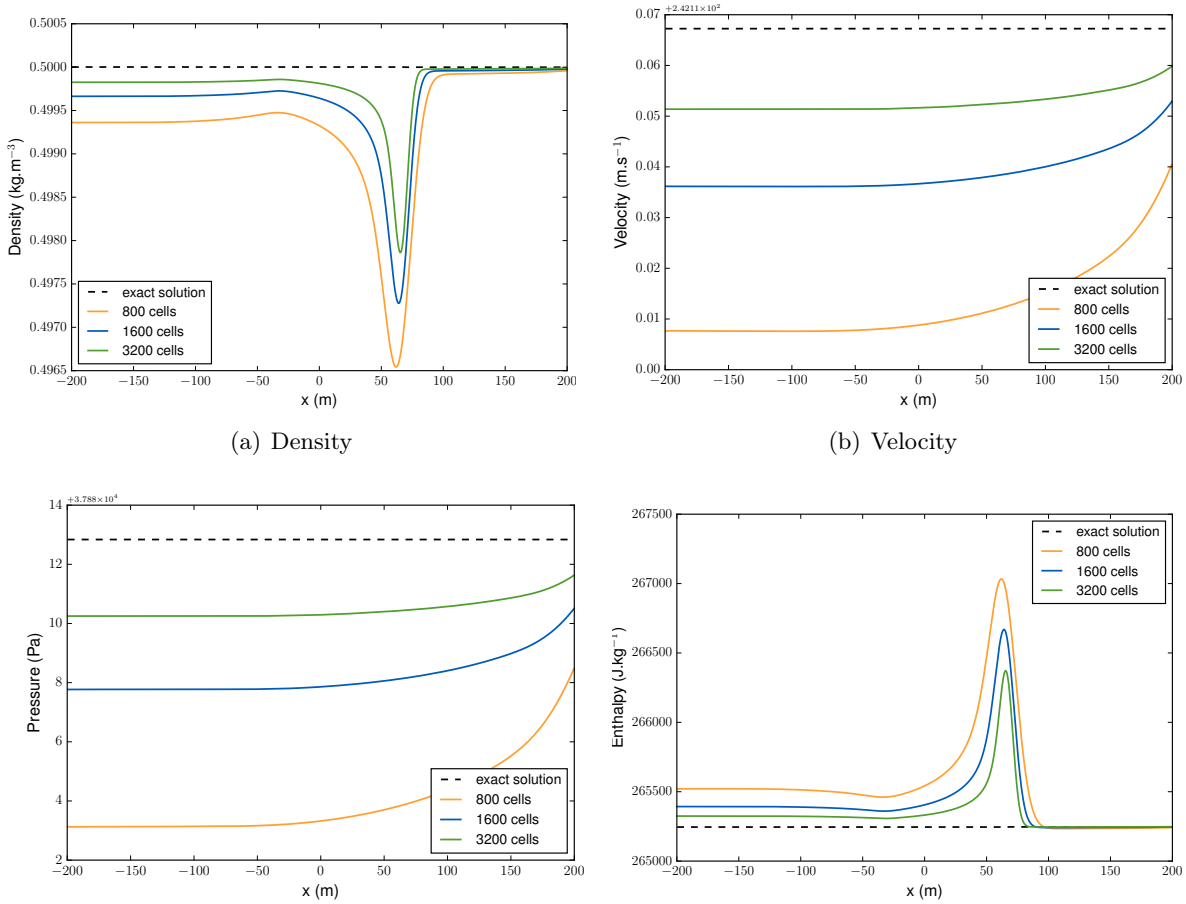

(a) Density (b) Velocity

(c) Pressure (d) Enthalpy

FIGURE 3.14 – *BC_0: comparison of the numerical solutions for 800, 1600 and 3200 cells with the exact solution for the pure rarefaction wave at $t > t_1$ (ideal gas EOS).*

- Verification test case with a stiffened gas EOS.

The stiffened gas EOS, for a liquid water, is considered with

$$\gamma = 1.8576818361693708,$$

and

$$\Pi_\infty = 4.2434683388243169 \times 10^8 \ Pa.$$

The initial conditions are:

$$\begin{cases} (\rho_L, u_L, P_L) = \left(800 \ kg.m^{-3}, 0 \ m.s^{-1}, 165 \times 10^5 \ Pa\right), \\ (\rho_R, u_R, P_R) = \left(797 \ kg.m^{-3}, 3.7982326832 \ m.s^{-1}, 134.338653039146 \times 10^5 \ Pa\right). \end{cases} \tag{3.43}$$

The solution is only composed of a stiff 1-rarefaction wave. Profiles are given in FIGURE 3.16 for the exact solution and the VFRoe-ncv approximate solution ($N = 800$) at time $t < t_0$. The numerical rates of convergence, that are observed for density, velocity and pressure, are greater than 0.5, but still smaller than the expected value 1 (see [81]) which means that a tremendous increase of the number of refined meshes would be necessary to retrieve 1^-. For $t_0 < t < t_1$, the numerical solutions match the exact solution with numerical diffusion (see FIGURE 3.17).

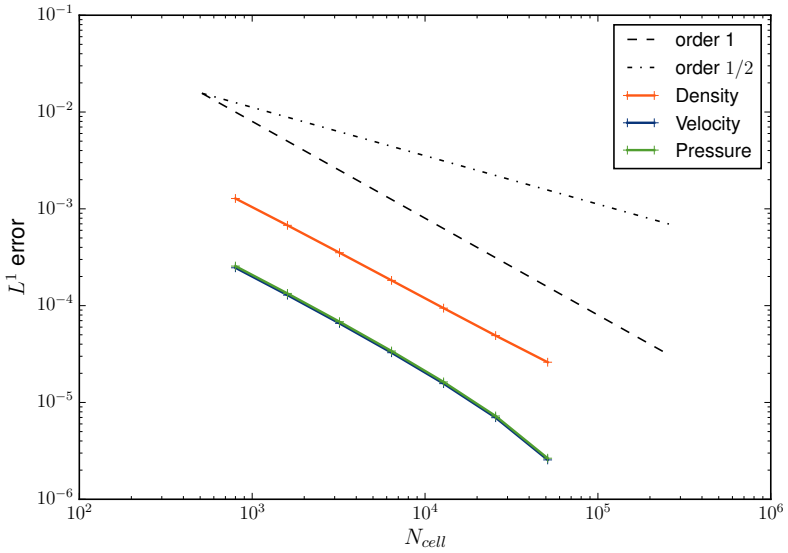

FIGURE 3.15 – *BC_0: L^1 convergence curves for the pure rarefaction wave at $t > t_1$ (ideal gas EOS).*

The boundary condition BC_0 is still consistent. The convergence order is again greater than 0.5 for all variables (see TABLE 3.3 and FIGURE 3.18), but still much smaller than 1^-. For $t > t_1$, the rarefaction wave is gone out, the constant initial right state is recovered with a convergence order of approximately 0.5 (see TABLE 3.4 and FIGURE 3.20).

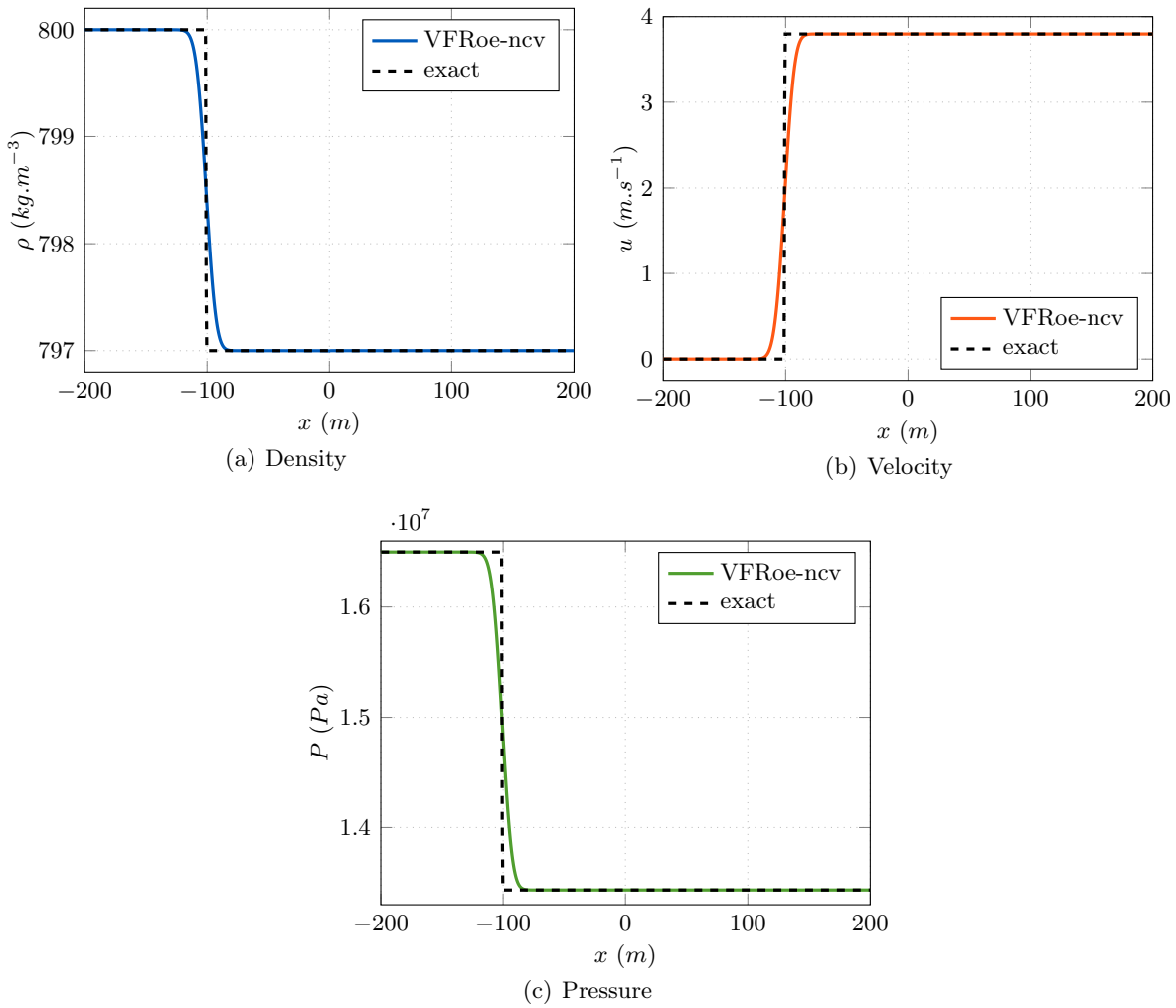

(a) Density

(b) Velocity

(c) Pressure

FIGURE 3.16 – *Profiles for the pure rarefaction wave at $t < t_0$ (stiffened gas EOS).*

$dx\ (m)$	N	ρ cnv. order	u cnv. order	P cnv. order
5e-1	800			
2.5e-1	1600	0.5072	0.5073	0.5075
1.25e-1	3200	0.5107	0.5108	0.5109
6.25e-2	6400	0.5153	0.5154	0.5154
3.125e-2	12800	0.5226	0.5226	0.5227
1.5625e-2	25600	0.5310	0.5311	0.5311
7.8125e-3	51200	0.5430	0.5431	0.5431

TABLE 3.3 – *BC_0: L^1 convergence orders for the pure rarefaction wave at $t_0 < t < t_1$ (stiffened gas EOS).*

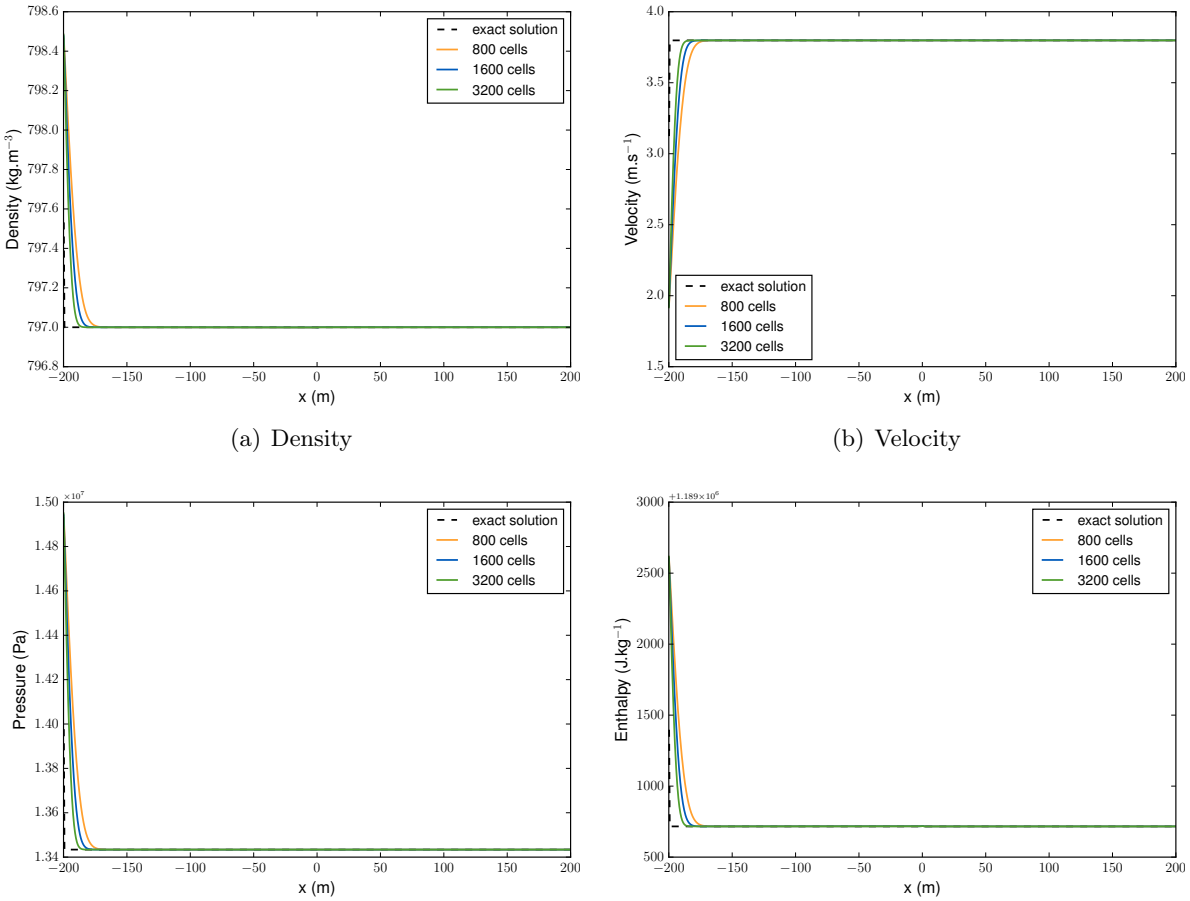

(a) Density (b) Velocity

(c) Pressure (d) Enthalpy

FIGURE 3.17 – *BC_0: Comparison of the numerical solutions for 800, 1600 and 3200 cells with the exact solution for the pure rarefaction wave at $t_0 < t < t_1$ (stiffened gas EOS).*

dx (m)	N	ρ cnv. order	u cnv. order	P cnv. order
5e-1	800			
2.5e-1	1600	0.5225	0.5121	0.5121
1.25e-1	3200	0.5201	0.5141	0.5141
6.25e-2	6400	0.5156	0.5164	0.5164
3.125e-2	12800	0.5142	0.5213	0.5213
1.5625e-2	25600	0.5166	0.5291	0.5291
7.8125e-3	51200	0.5218	0.5402	0.5400
3.90625e-3	102400	0.5296	0.5560	0.5552

TABLE 3.4 – *BC_0: L^1 convergence orders for the pure rarefaction wave at $t > t_1$ (stiffened gas EOS).*

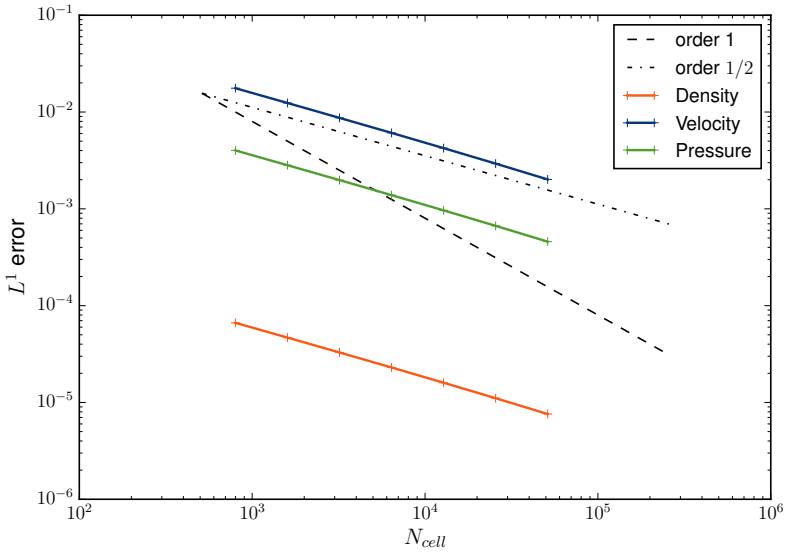

FIGURE 3.18 – BC_0: L^1 *convergence curves for the pure rarefaction wave at* $t_0 < t < t_1$ *(stiffened gas EOS).*

b. Boundary condition 2.2 (BC_{1r})

The same test cases are performed with the boundary condition BC_{1r}. This condition is consistent and allows to make the rarefaction wave go out of the computational domain. The numerical results are very similar to those obtained with the condition BC_0 (see the convergence orders in FIGURE 3.21, TABLE 3.5 and FIGURE 3.22). The fact to take into account the wave invariants does not visibly improve the accuracy of the approximate solutions at the boundary.

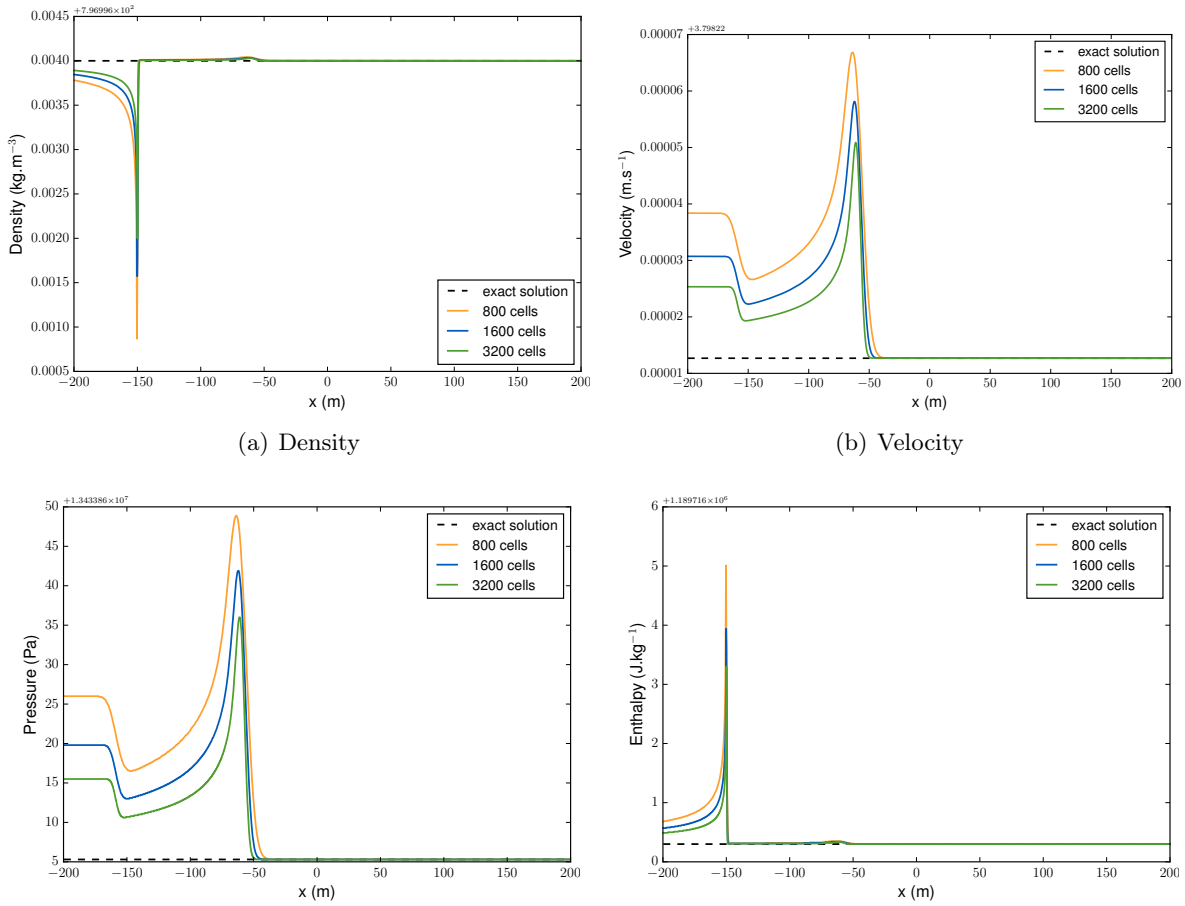

(a) Density (b) Velocity

(c) Pressure (d) Enthalpy

FIGURE 3.19 – *BC_0: comparison of the numerical solutions for 800, 1600 and 3200 cells with the exact solution for the pure rarefaction wave at $t > t_1$ (stiffened gas EOS).*

dx (m)	N	ρ cnv. order	u cnv. order	P cnv. order
5e-1	800			
2.5e-1	1600	0.8221	0.8241	0.8243
1.25e-1	3200	0.8426	0.8406	0.8402
6.25e-2	6400	0.8605	0.8518	0.8516
3.125e-2	12800	0.8774	0.8587	0.8582
1.5625e-2	25600	0.8621	0.8588	0.8579
7.8125e-3	51200	0.8533	0.8491	0.8473

TABLE 3.5 – *BC_{1r}: L^1 convergence orders for the pure rarefaction wave at $t_0 < t < t_1$ (ideal gas EOS).*

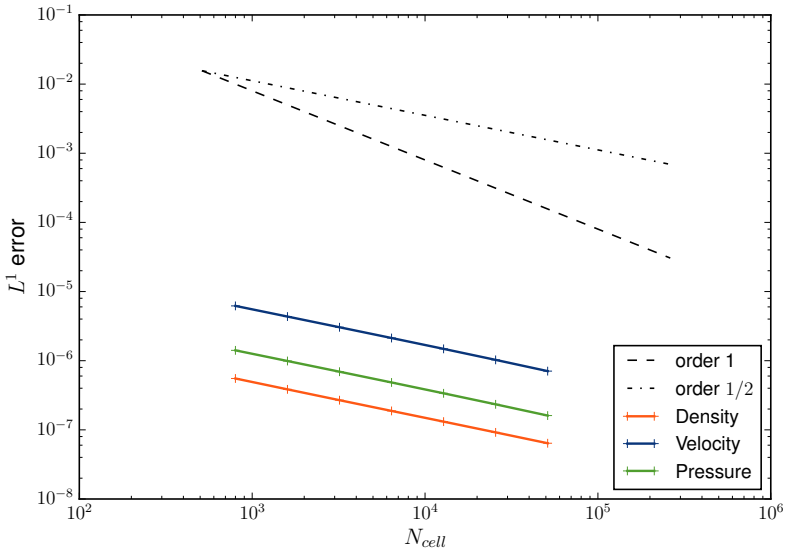

FIGURE 3.20 – *BC_0: L^1 convergence curves for the pure rarefaction wave at $t > t_1$ (stiffened gas EOS).*

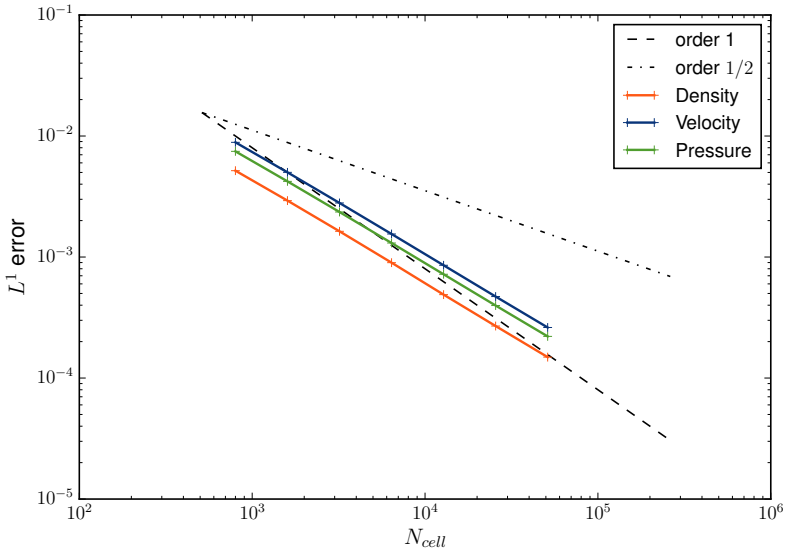

FIGURE 3.21 – *BC_{1r}: L^1 convergence curves for the pure rarefaction wave at $t_0 < t < t_1$ (ideal gas EOS).*

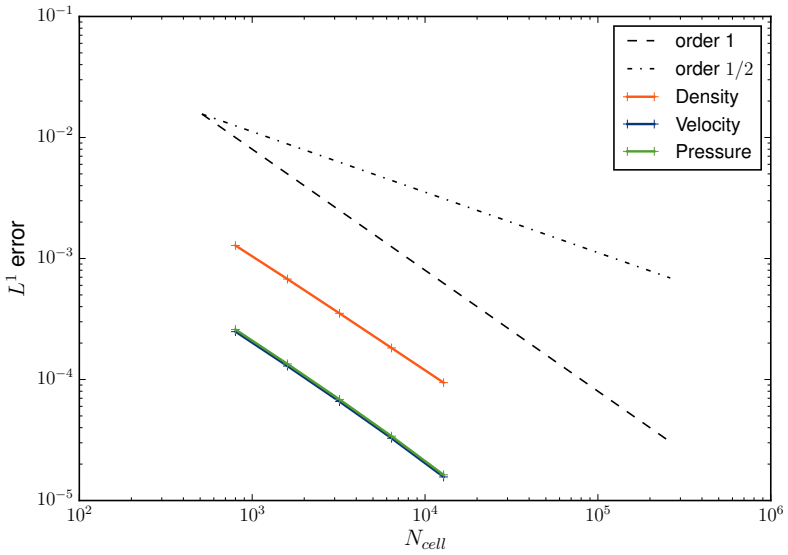

FIGURE 3.22 – *BC_{1r}: L^1 convergence curves for the pure rarefaction wave at $t > t_1$ (ideal gas EOS).*

4.2 Right-going 3-shock wave

4.2.1 Exact solution

In the same way, the exact solution of a pure 3-shock wave, travelling to the right open end of the computational domain, is built by solving a 1D Riemann problem for the Euler equations. The 1-wave and the 2-contact discontinuity wave are "ghost" waves. At the beginning of the computation, the tube contains a membrane ($x = x_0$) separating two different initial constant fluid states at rest: the right state $\boldsymbol{Y}_R$ and the left state $\boldsymbol{Y}_L$ (see FIGURE 3.23).

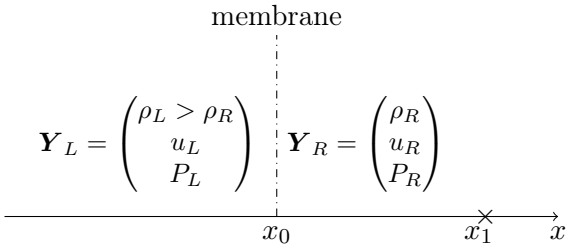

FIGURE 3.23 – *Sketch of the tube apparatus with the initial condition.*

The initial right state is given:

$$\boldsymbol{Y}_R = \begin{pmatrix} \rho_R \\ u_R \\ P_R \end{pmatrix},$$

and the initial left density ρ_L, with $\rho_L > \rho_R$, is given.

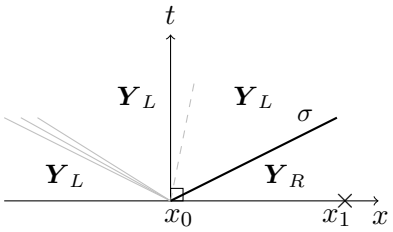

FIGURE 3.24 – *Pure 3-shock wave.*

The right velocity u_R and pressure P_R are calculated from the two Rankine-Hugoniot jump relations of a shock wave, where σ is the speed of the shock wave:

$$-\sigma \left[\boldsymbol{W}\right]_L^R + \left[\boldsymbol{F}(\boldsymbol{W})\right]_L^R = 0,$$

giving for the Euler equations:

$$\begin{cases} \left[\epsilon\right]_L^R + \dfrac{P_L + P_R}{2} \left[\dfrac{1}{\rho}\right]_L^R = 0, & \text{(3.44a)} \\ \rho_L \rho_R \left(\left[u\right]_L^R\right)^2 - \left[P\right]_L^R \left[\rho\right]_L^R = 0, & \text{(3.44b)} \end{cases}$$

thus giving, for an ideal gas EOS such that $\rho\epsilon = \frac{P}{\gamma-1}$, with $\gamma > 1$:

$$\begin{cases} \dfrac{P_L}{P_R} = \dfrac{\beta z - 1}{\beta - z}, & \text{(3.45a)} \\ \rho_L \rho_R \left([u]_L^R \right)^2 - [P]_L^R \, [\rho]_L^R = 0, & \text{(3.45b)} \end{cases}$$

where $\beta = \frac{\gamma+1}{\gamma-1}$ and $1 < z = \frac{\rho_L}{\rho_R} < \beta$. From equations (3.45a) and (3.45b), the complete initial left state is deduced such that $u_L > u_R$, $P_L > P_R$ and also $\beta\rho_R > \rho_L > \rho_R$:

$$P_L = P_R \left(\frac{\beta z - 1}{\beta - z} \right) > 1, \tag{3.46}$$

$$u_L = u_R + \sqrt{(P_R - P_L) \left(\frac{1}{\rho_L} - \frac{1}{\rho_R} \right)}. \tag{3.47}$$

For a stiffened gas EOS such that $\rho\epsilon = \frac{P+\gamma\Pi_\infty}{\gamma-1}$, with $\Pi_\infty \geq 0$, the complete initial right state is simply retrieved:

$$P_R = (P_L + \Pi_\infty) \left(\frac{\beta z - 1}{\beta - z} \right) - \Pi_\infty, \tag{3.48}$$

and the right velocity u_R is still given by (3.47).

By construction, the unique propagated discontinuous solution is a pure shock wave such that:

$$\boldsymbol{Y}(x,t) = \begin{cases} \boldsymbol{Y}_L & \text{if } x - \sigma t < 0, \\ \boldsymbol{Y}_R & \text{otherwise.} \end{cases} \tag{3.49}$$

with $\sigma = \dfrac{\rho_R u_R - \rho_L u_L}{\rho_R - \rho_L}$.

4.2.2 Numerical results with the VFRoe-ncv scheme

The one-dimensional computational domain is still $\Omega = (-200\ m, 200\ m)$. The right boundary is located at $x = x_1 = 200\ m$, see FIGURE 3.23. The numerical approximations are still obtained with the VFRoe-ncv (s, u, P) scheme and compared with the exact solution at two different instants:

- at time $0 < t < t_0$, with $t_0 = \frac{x_1 - x_0}{\sigma}$. The shock wave is inside the computational domain Ω,
- at time $t > t_0$. The shock wave is gone out of Ω.

All meshes used to solve this Riemann problem are uniform. The meshes still contain N cells with $N = 800, 1600, 3200, 6400, 12800, 25600$ or 51200.

The CFL condition is satisfied: $CFL = \frac{\sigma\Delta t}{\Delta x} = 0.5$.

a. Boundary condition 2.1 (BC_0)

- Verification test case with an ideal gas EOS.

The ideal gas EOS is considered with $\gamma = 1.4$ for a diatomic gas. The initial conditions are:

$$\begin{cases} (\rho_L, u_L, P_L) = \left(1\ kg.m^{-3}, 418.3300013267\ m.s^{-1}, 2.75 \times 10^5\ Pa\right), \\ (\rho_R, u_R, P_R) = \left(0.5\ kg.m^{-3}, 0\ m.s^{-1}, 10^5\ Pa\right). \end{cases} \tag{3.50}$$

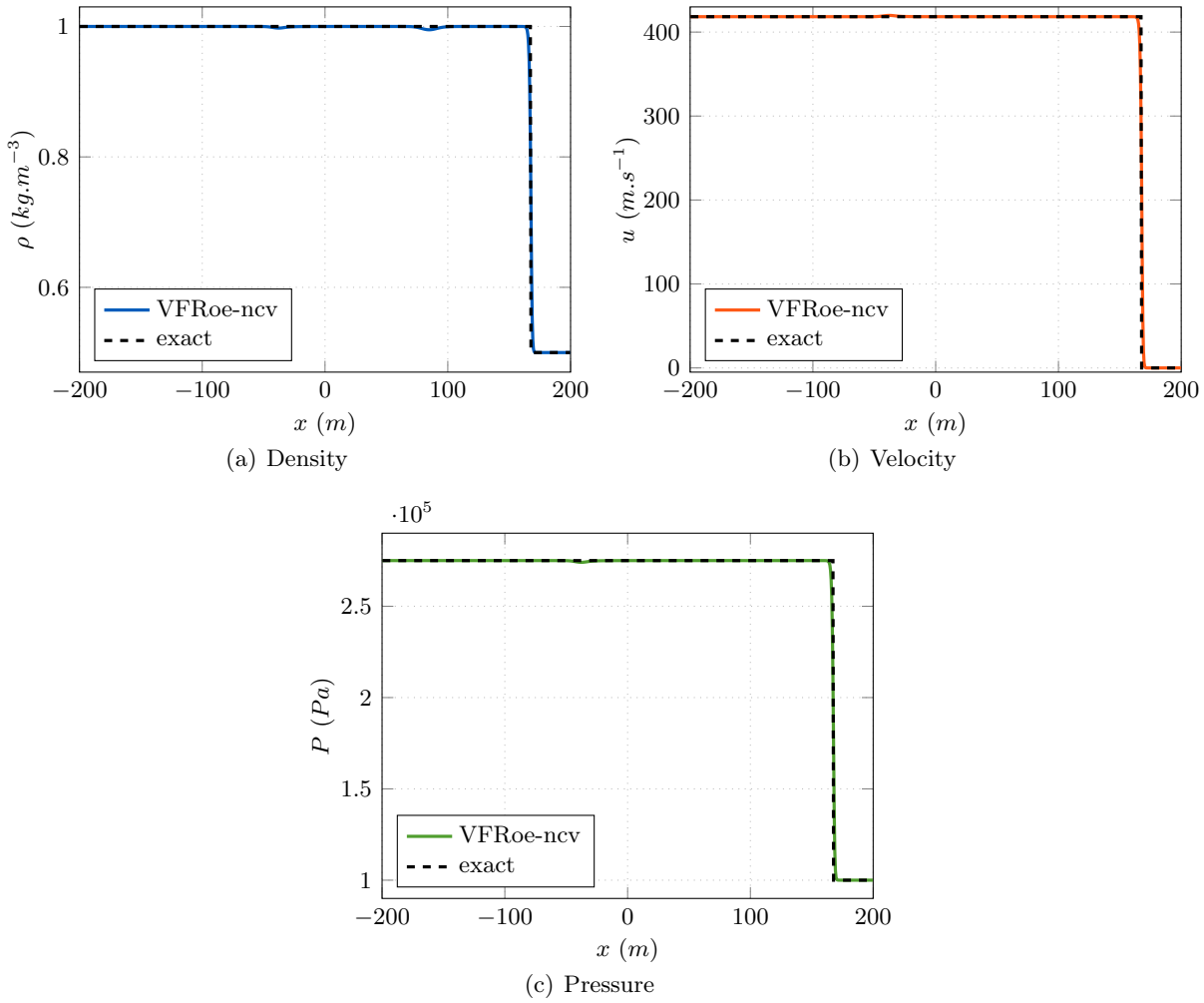

(a) Density

(b) Velocity

(c) Pressure

FIGURE 3.25 – *Profiles for the pure shock wave at $t < t_0$ (ideal gas EOS).*

The solution is only composed of a 3-shock wave. Profiles are given in FIGURE 3.25 for the exact solution and the VFRoe-ncv approximate solution ($N = 800$) at time $t < t_0$. As expected [81], the numerical rates of convergence are slightly greater than 0.8 and smaller than 1^- for density, velocity and pressure. A "ghost" 2-contact discontinuity wave is visible on the density profile (a) in FIGURE 3.25. For $t_0 < t$, boundary condition BC_0 is not consistent, a numeric artificial wave appears in the computational domain at $x_1 = 200\ m$ (see FIGURES 3.26 and 3.27).

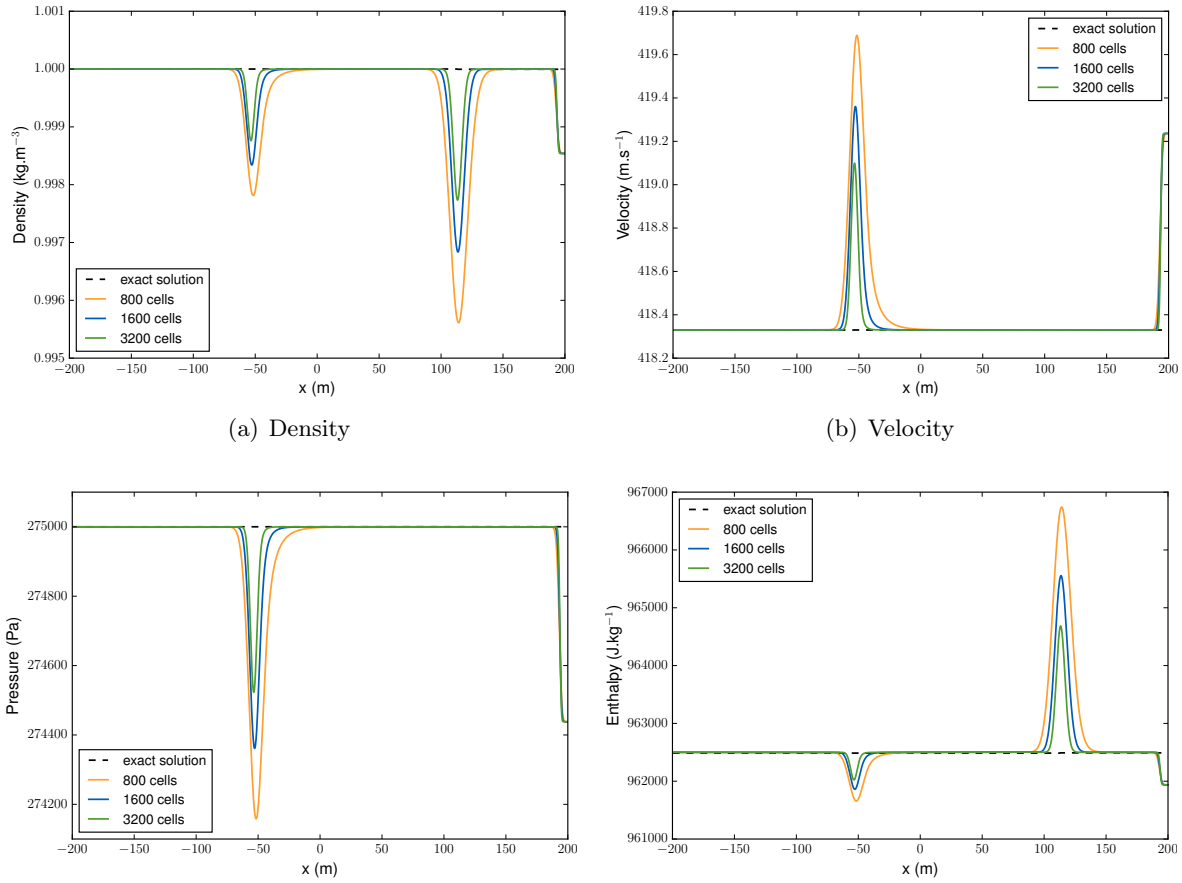

(a) Density (b) Velocity

(c) Pressure (d) Enthalpy

FIGURE 3.26 – *BC_0: comparison of the numerical solutions for 800, 1600 and 3200 cells with the exact solution for the pure shock wave at $t > t_0$ (ideal gas EOS).*

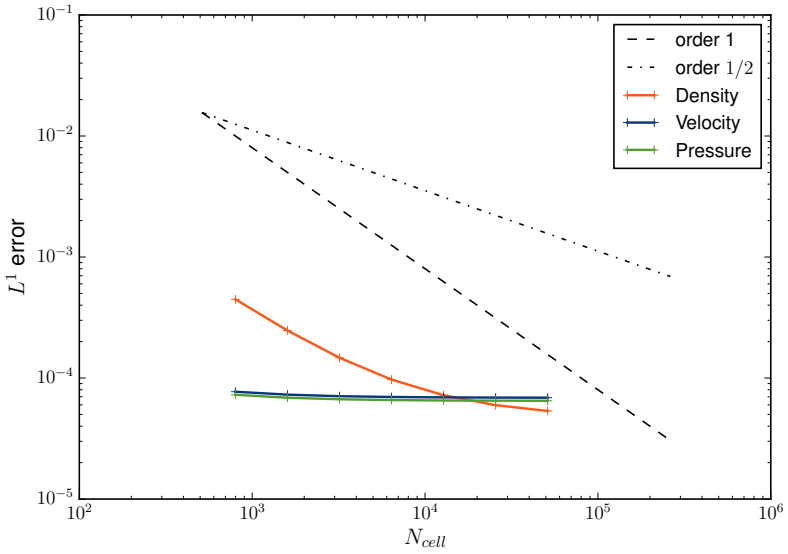

FIGURE 3.27 – *BC_0: L^1 convergence curves for the pure shock wave at $t > t_0$ (ideal gas EOS).*

- Verification test case with a stiffened gas EOS.

The stiffened gas EOS, for a liquid water, is considered with

$$\gamma = 1.8576818361693708,$$

and

$$\Pi_\infty = 4.2434683388243169 \times 10^8 \ Pa.$$

The initial conditions are:

$$\begin{cases} (\rho_L, u_L, P_L) = \left(800 \ kg.m^{-3}, 3.8071952155 \ m.s^{-1}, 185.806144323239 \times 10^5 \ Pa\right), \\ (\rho_R, u_R, P_R) = \left(797 \ kg.m^{-3}, 0 \ m.s^{-1}, 155 \times 10^5 \ Pa\right). \end{cases} \tag{3.51}$$

Profiles are given in FIGURE 3.28 for the exact solution and the VFRoe-ncv approximate solution ($N = 800$) at time $t < t_0$. The numerical rates of convergence are slightly greater than 0.5 for the density, the velocity and the pressure.

For $t > t_0$, the solution perturbation by the boundary condition BC_0 is not clearly apparent (see FIGURES 3.29, 3.30 and TABLE 3.6). However, as for the ideal gas EOS, the approximate solution is not consistent: an artificial reflection of small amplitude still occurs inside the domain, and, for very fine meshes ($N > 10^5$), the convergence order falls to zero.

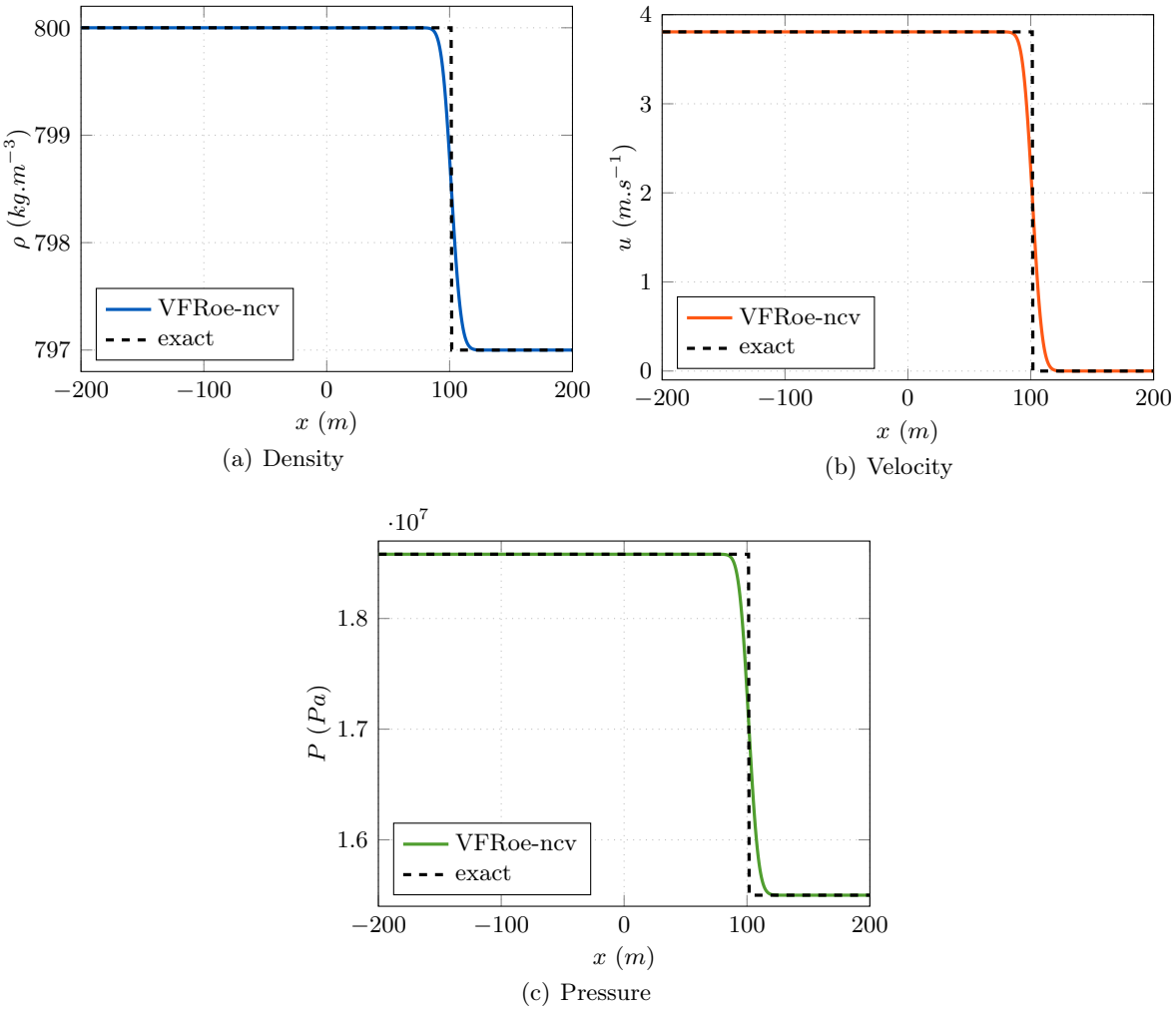

(a) Density

(b) Velocity

(c) Pressure

FIGURE 3.28 – *Profiles for the pure shock wave at $t < t_0$ (stiffened gas EOS).*

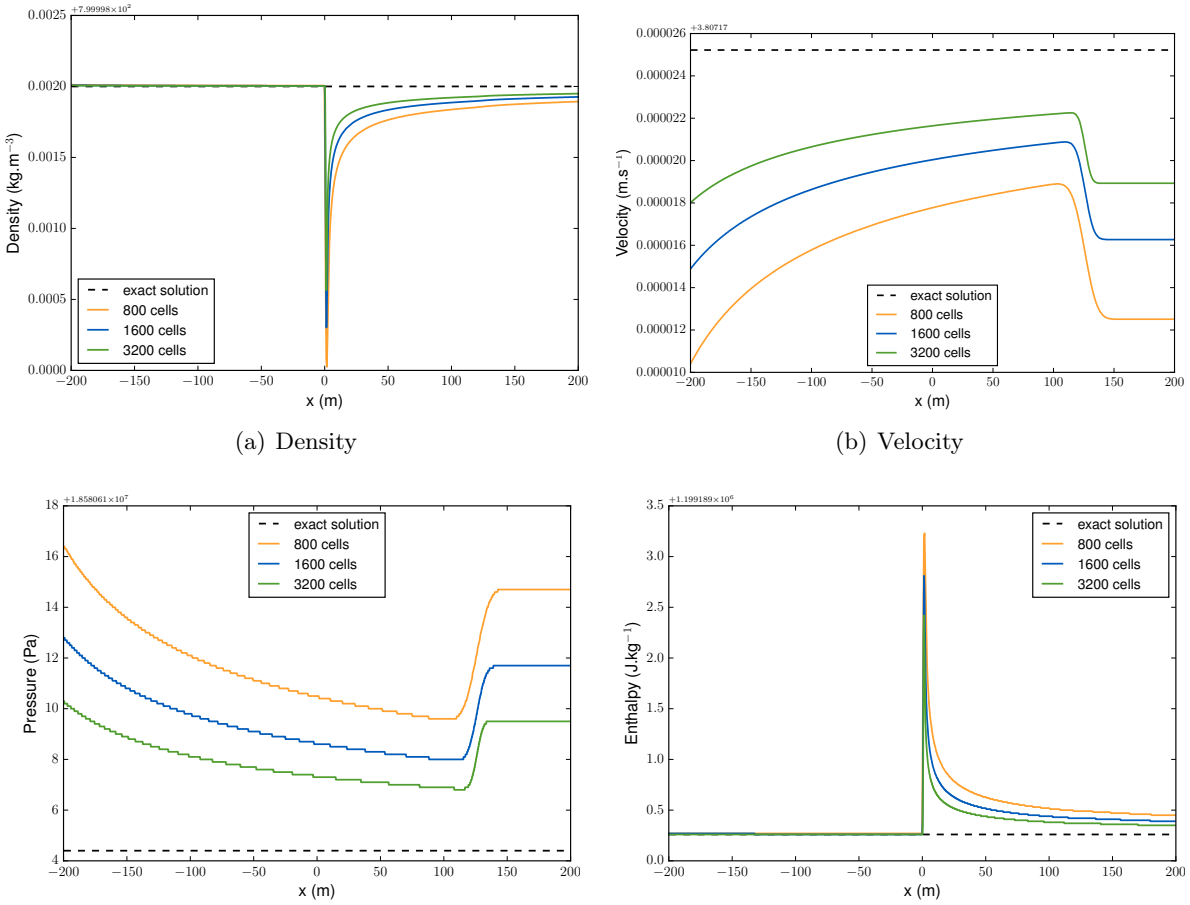

(a) Density (b) Velocity

(c) Pressure (d) Enthalpy

FIGURE 3.29 – *BC_0: comparison of the numerical solutions for 800, 1600 and 3200 cells with the exact solution for the pure shock wave at $t > t_0$ (stiffened gas EOS).*

dx (m)	N	ρ cnv. order	u cnv. order	P cnv. order
5e-1	800			
2.5e-1	1600	0.5137	0.5179	0.5179
1.25e-1	3200	0.5197	0.5230	0.5230
6.25e-2	6400	0.5282	0.5312	0.5312
3.125e-2	12800	0.5404	0.5430	0.5428
1.5625e-2	25600	0.5580	0.5594	0.5588
7.8125e-3	51200	0.5838	0.5801	0.5778

TABLE 3.6 – *BC_0: L^1 convergence orders for the pure shock wave at $t > t_0$ (stiffened gas EOS).*

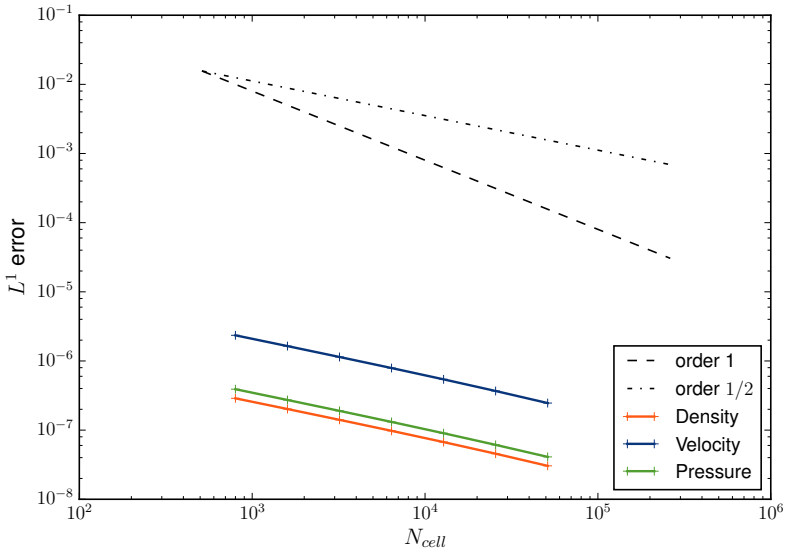

FIGURE 3.30 – *BC_0: L^1 convergence curves for the pure shock wave at $t > t_0$ (stiffened gas EOS).*

b. Boundary condition 2.3.2 (BC_s)

In this section, another Riemann problem is considered for steam water, using an ideal gas EOS with $\gamma_v = 1.084875362318841$. The initial conditions are:

$$\begin{cases} (\rho_L, u_L, P_L) = \left(82.224673154\ kg.m^{-3}, 0\ m.s^{-1}, 1.10^7\ Pa\right), \\ (\rho_R, u_R, P_R) = \left(41.112336577\ kg.m^{-3}, 0\ m.s^{-1}, 5.10^6\ Pa\right). \end{cases} \tag{3.52}$$

The solution is subsonic and composed of a 1-rarefaction wave, a 2-contact discontinuity and a 3-shock wave.

At $t_{final} > t_0$, the shock wave is gone out of the computational domain by the right, while the other waves are still inside the domain.

The BC_s boundary condition (corresponding to equation (3.19)), with a virtual exterior cell connected to the initial right state (ρ_R, u_R, P_R) for a finite value of the parameter $\alpha > 0$, is still not consistent (see FIGURE 3.31). We note that the non-convergence appears for finer meshes when α increases. At the limit $\alpha \to +\infty$, the asymptotic condition BC_s (3.21) allows to ensure the consistency of the approximate solution at the boundary.

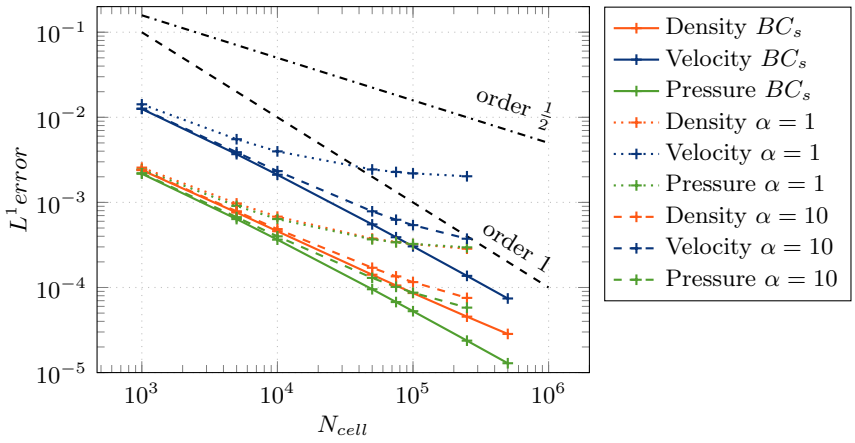

FIGURE 3.31 – *BC_s: L^1 convergence curves for the shock tube at $t > t_0$ (ideal gas EOS).*

5 Conclusion

Some numerical boundary conditions for the Euler equations are studied for wave outgoing from the computational domain. The approach consists in estimating the whole fluid state in a virtual boundary cell in order to compute a boundary flux. Three techniques of estimation are proposed and denoted by: BC_0, BC_1 and BC_s. The BC_0 condition enforces directly the interior boundary cell state to the virtual cell state. The BC_1 condition connects the virtual cell state to the interior boundary cell by using the wave invariants. And the BC_s condition uses the far-field state to reconstruct the virtual cell state.

Numerous analytical test cases with outgoing rarefaction waves or shock waves have allowed to valid or not the proposed numerical boundary conditions, in considering the discrete L^1 error. Some difficulties have been highlighted with an approximate Riemann solver to remain consistent when waves are going out of the computational domain.

The numerical results obtained with the VFRoe-ncv scheme are summarized in TABLE 3.7. The boundary conditions ensuring the convergence of the approximate solution towards the right solution are indicated by "CV" for the different outgoing waves using the ideal gas EOS or the stiffened gas EOS. Otherwise, the convergence towards a wrong solution is indicated by "wrong CV".

BC type	rarefaction wave		shock wave	
	ideal gas	stiffened gas	ideal gas	stiffened gas
BC_0	CV	CV	wrong CV	wrong CV
BC_{1r} or BC_{1s}	CV	CV	wrong CV	wrong CV
BC_s	\	\	CV	CV

TABLE 3.7 – *Synthesis: convergence of the numerical boundary conditions for outgoing waves.*

In conclusion, the BC_0 and BC_{1r} boundary conditions ensure the numerical convergence of the approximate solutions when smooth waves are going out of the computational domain. The BC_{1r} condition does not improve much the accuracy of the results with respect to the BC_0 condition: the discrete L^1-norm of the error is indeed very similar.

In contrast, the formulation BC_0 does not allow to remain consistent for outgoing shock waves: small artificial reflections are produced inside the domain. The numerical tests using the BC_{1s} condition do not appear consistent either.

One possible alternative is the third formulation denoted by BC_s. The consistency is recovered for outgoing shock waves but not for outgoing rarefaction waves. The strategy can be related to [89] where a one-dimensional region is connected to the three-dimensional computational domain to cope with boundary conditions producing artificial oscillations and reflections inside the domain.

Furthermore, these same test cases are currently performed with the pressure correction scheme described in chapter 1 using the BC_0 boundary condition. These exploratory numerical results show that the consistency is not recovered for any outgoing wave (rarefaction or shock wave). Artificial numerical reflections occur inside the domain. This issue deserves further studies in the future.

Acknowledgments This work has benefited from the help of L. Quibel (EDF R&D / Univeristé de Strasbourg), who provided numerical results in FIGURE 3.31.

References

[16] R. Eymard, T. Gallouët, and R. Herbin. "Finite Volume Methods". In: *Handbook for Numerical Analysis, P.G. Ciarlet, J.L. Lions eds, North Holland* 7 (2006), pp. 713–1020 (cit. on pp. 10, 29, 33, 92, 94, 120, 177).

[19] E. Godlewski and P.-A. Raviart. *Numerical approximation of hyperbolic systems of conservation laws*. Vol. 118. Applied Mathematical Sciences. New York: Springer-Verlag, 1996 (cit. on pp. 11, 12, 119, 120, 127, 181).

[20] J. Smoller. *Shock Waves and Reaction-Diffusion Equations*. Vol. 258. A Series of Comprehensive Studies in Mathematics. New York: Springer-Verlag, 1994 (cit. on pp. 11, 12, 47, 82, 119, 127, 181).

[46] C. Colas, M. Ferrand, J.-M. Hérard, J.-C. Latché, and E. Le Coupanec. "An Implicit Integral Formulation to Model Inviscid Fluid Flows in Obstructed Media". In: *Computers & Fluids* 188 (2019), pp. 136–163. URL: https://hal.archives-ouvertes.fr/hal-01969129 (cit. on pp. 20, 22, 90, 91, 113, 121, 176, 179).

[58] T. Buffard, T. Gallouët, and J.-M. Hérard. "A sequel to a rough Godunov scheme: application to real gases". In: *Computers & Fluids* 29.7 (2000), pp. 813–847 (cit. on pp. 38–40, 76, 121, 127–129, 182).

[59] F. Dubois. "Boundary conditions and the Osher scheme for the Euler equations of gas dynamics." In: *Internal Report CMAP 170, Ecole Polytechnique, Palaiseau, France* (1987) (cit. on pp. 40, 121).

[60] F. Blondel, B. Audebert, T. Pasutto, and M. Stanciu. "Condensation models and boundary conditions for non-equilibrium wet steam flows." In: *International Journal on Finite Volumes* 10 (2013), pp. 1–53 (cit. on pp. 40, 121).

[68] T. Gallouët. "Boundary conditions for hyperbolic equations or systems". In: *Numerical Mathematics and Advanced Applications*. Ed. by Miloslav Feistauer, Vít Dolejší, Petr Knobloch, and Karel Najzar. Berlin, Heidelberg: Springer Berlin Heidelberg, 2004, pp. 39–55 (cit. on p. 120).

[69] F. Dubois and P. Le Floch. "Boundary conditions for nonlinear hyperbolic systems of conservation laws". In: *J. Diff Equations* 71.1 (1988), pp. 93–122 (cit. on p. 121).

[70] I. Orlanski. "A simple boundary condition for unbounded hyperbolic flows". In: *Journal of Computational Physics* 21.3 (1976), pp. 251–269 (cit. on p. 123).

[71] B. Engquist and A. Majda. "Absorbing boundary conditions for the numerical simulation of waves". English (US). In: *Mathematics of Computation* 31.139 (1977), pp. 629–651 (cit. on p. 123).

[72] G. W. Hedstrom. "Nonreflecting boundary conditions for nonlinear hyperbolic systems". In: *Journal of Computational Physics* 30 (1979), pp. 222–237 (cit. on p. 123).

[73] K. W. Thompson. "Time dependent boundary conditions for hyperbolic systems". In: *Journal of Computational Physics* 68.1 (1987), pp. 1–24 (cit. on p. 123).

[74] D. H. Rudy and J. C. Strikwerda. "A nonreflecting outflow boundary condition for subsonic Navier-Stokes calculations". In: *Journal of Computational Physics* 36.1 (1980), pp. 55–70 (cit. on p. 123).

[75] T. J. Poinsot and S. K. Lele. "Boundary conditions for direct simulations of compressible viscous flows". In: *Journal of Computational Physics* 101.1 (1992), pp. 104–129 (cit. on p. 123).

[76] J.-P. Berenger. "A perfectly matched layer for the absorption of electromagnetic waves". In: *Journal of Computational Physics* 114.2 (1994), pp. 185–200 (cit. on p. 123).

[77] F. Q. Hu. "On absorbing boundary conditions for linearized Euler equations by a perfectly matched layer". In: *Journal of Computational Physics* 129.1 (1996), pp. 201–219 (cit. on p. 123).

[78] C. K. W. Tam, L. Auriault, and F. Cambuli. "Perfectly matched layer as an absorbing boundary condition for the linearized Euler equations in open and ducted domains". In: *Journal of Computational Physics* 144.1 (1998), pp. 213–234 (cit. on p. 123).

[79] F. Q. Hu, X. D. Li, and D. K. Lin. "Absorbing boundary conditions for nonlinear Euler and Navier-Stokes equations based on the perfectly matched layer technique". In: *Journal of Computational Physics* 227.9 (2008), pp. 4398–4424 (cit. on p. 123).

[80] C. K. W. Tam and Z. Dong. "Radiation and outflow boundary conditions for direct computation of acoustic and flow disturbances in a nonuniform mean flow". In: *Journal of Computational Acoustics* 4.2 (1996), pp. 175–201 (cit. on p. 123).

[81] T. Gallouët, J.-M. Hérard, and N. Seguin. "Some recent Finite Volume schemes to compute Euler equations using real gas EOS". In: *International Journal for Numerical Methods in Fluids* 39 (2002), pp. 1073–1138. URL: https://hal.archives-ouvertes.fr/hal-01290885 (cit. on pp. 127, 133, 137, 147, 182).

[82] A. Harten, P. D. Lax, and B. Van Leer. "On upstream differencing and Godunov-type schemes for hyperbolic conservation laws". In: *SIAM Rev.* 25.1 (1983), pp. 35–61 (cit. on p. 127).

[83] R. J. LeVeque. *Numerical Methods for Conservation Laws*. Birkhäuser-Verlag, Basel, 1990 (cit. on p. 127).

[84] E. F. Toro. *Riemann solvers and numerical methods for fluid dynamics*. Third. Springer-Verlag, Berlin, 2009 (cit. on p. 127).

[85] S. K. Godunov. "A difference method for numerical calculation of discontinuous solutions of the equations of hydrodynamics". In: *Mat. Sb. (N.S.)* 47.89 (1959). In Russian, pp. 271–306 (cit. on p. 128).

[86] T. Gallouët, J.-M. Hérard, and N. Seguin. "On the use of symmetrizing variables for vacuum". In: *Calcolo* 40.3 (2003), pp. 163–194. URL: https://hal.archives-ouvertes.fr/hal-00003439 (cit. on pp. 128–130).

[87] P. Helluy, J.-M. Hérard, H. Mathis, and S. Müller. "A simple parameter-free entropy correction for approximate Riemann solvers". In: *Comptes Rendus Mécanique* 338.9 (July 2010), pp. 493–498. URL: https://hal.archives-ouvertes.fr/hal-00466999 (cit. on p. 128).

[88] T. Gallouët, J.-M. Hérard, and N. Seguin. "A hybrid scheme to compute contact discontinuities in one-dimensional Euler systems". en. In: *ESAIM: Mathematical Modelling and Numerical Analysis - Modélisation Mathématique et Analyse Numérique* 36.6 (2002), pp. 1133–1159. URL: http://www.numdam.org/item/M2AN_2002__36_6_1133_0 (cit. on p. 129).

[89] M. Deininger, U. Iben, and C.-D. Munz. "Coupling of three- and one-dimensional hydraulic flow simulations". In: *Computers & Fluids* 190 (2019), pp. 128 –138 (cit. on p. 154).

Conclusion

Cette thèse porte sur la modélisation et la simulation numérique d'écoulements en milieu encombré. Ce type de problématique est présent dans les circuits thermohydrauliques des réacteurs nucléaires. En effet, le fluide s'écoule dans un milieu encombré de nombreux obstacles solides de petite taille en comparaison à celle du milieu tout entier. Un exemple de milieu encombré est le cœur du réacteur à travers duquel s'écoule le fluide du circuit primaire.

L'approche intégrale, proposée ici, permet de simuler un écoulement dans ce type de configuration en partant de l'échelle composant sur maillage grossier encombré d'obstacles jusqu'à l'échelle locale sur maillage fin. Contrairement à l'approche dite "poreuse" adoptée depuis les années 80 où un modèle moyenné en espace des équations de la mécanique des fluides est adopté, l'approche est directement basée sur les équations de la mécanique des fluides.

Le premier avantage est qu'elle permet de retrouver le cadre des calculs fins CFD, où les obstacles sont pris en compte dans le domaine de calcul fluide au moyen des conditions limites, lorsque le maillage est suffisamment raffiné. Le second est le traitement adéquat, au sens où l'approximation prend en compte naturellement les variations brusques de géométrie d'obstacles.

Rappelons que, à l'heure actuelle, dans l'approche poreuse classique, deux difficultés subsistent dans le cadre de "section discontinue" :

- la définition physique correcte de la perte de charge singulière associée à la discontinuité de section ;

- l'approximation stable (lorsque les rétrécissements de sections sont importants) et consistante avec la perte de charge singulière, de la solution discrète sachant que les schémas "well-balanced" ont des limites de fonctionnement (non-existence de solutions aux interfaces pour de forts ratios de section).

Les travaux menés ont permis de construire une formulation intégrale multidimensionnelle pour un écoulement fluide non visqueux et compressible. Elle est basée sur le modèle des équations d'Euler en régime compressible. La discrétisation est faite en adoptant une stratégie Volumes Finis semi-implicite en temps. Cela permet de relâcher les contraintes de stabilité numérique et donne ainsi la possibilité de mener des calculs à grand pas temps par rapport aux échelles de temps des phénomènes rapides d'ondes de pression dans le fluide.

Dans une première partie, la méthode numérique, basée sur une technique de correction de pression, est tout d'abord vérifiée sur des cas tests analytiques à l'aide d'études de convergence en milieu libre pour un fluide peu compressible. La formulation en milieu encombré sur maillage grossier est validée sur une configuration d'une onde de choc impactant un ensemble d'obstacles immergés dans un liquide. Les résultats sont comparés à un calcul CFD de référence sur maillage fin. Le choix de la discrétisation en espace des termes de pression pariétale sur les obstacles permet d'obtenir de bonnes estimations sur maillage grossier des grandeurs intégrées comme la chute de pression. Cette méthode permet également de retrouver la solution de référence en raffinant le maillage du domaine de calcul.

Dans une seconde partie, la formulation intégrale est étendue pour simuler correctement, en régime incompressible non visqueux, des écoulements stationnaires dans un canal à la traversée d'une discontinuité de la section de passage. Un nouveau schéma numérique en espace est proposé. Il permet de retrouver l'état stationnaire avec la chute de pression correcte à l'interface de discontinuité. Les premiers résultats permettent de se comparer à une solution analytique, obtenue en régime incompressible non visqueux. Le but à terme est de proposer également une formulation permettant de traiter correctement les régimes stationnaires ou quasi-stationnaires pour un fluide peu compressible et visqueux.

Un dernier point, nettement moins intégré à la problématique des milieux encombrés, relatif à la mesure d'erreur de schémas numériques, a été de proposer des conditions limites discrètes pour des frontières ouvertes du domaine de calcul. Plusieurs formulations de conditions limites numériques ont été étudiées en réalisant des études de convergence en maillage. Certaines conditions permettent la sortie des ondes régulières ou de choc du domaine de calcul afin de simuler un domaine ouvert. On s'est initialement intéressé aux équations d'Euler en régime compressible discrétisées avec des schémas explicites en temps. Une perspective est d'étendre ces conditions limites discrètes aux schémas semi-implicites de correction de pression utilisés dans le reste de la thèse.

References

[1] *Institut de Radioprotection et de Sûreté Nucléaire (IRSN), Fonctionnement d'un réacteur nucléaire*. 2019. URL: https://www.irsn.fr/FR/connaissances/Installations_nucleaires/Les-centrales-nucleaires/reacteurs-nucleaires-France/Pages/1-reacteurs-nucleaires-France-Fonctionnement.aspx#.XXUg5_c685k (cit. on p. 8).

[2] *Institut de Radioprotection et de Sûreté Nucléaire (IRSN), Les composants d'un réacteur en détail*. 2019. URL: https://www.irsn.fr/FR/connaissances/Installations_nucleaires/Les-centrales-nucleaires/reacteurs-nucleaires-France/Pages/3-reacteurs-nucleaires-France-Description-detaillee.aspx?dId=82471a77-677a-40cf-8010-5c30f29507df&dwId=231c8e52-c3bd-4187-990e-01a6e97b5418#.XXUlXfc685k (cit. on p. 8).

[3] F. Barre and M. Bernard. "The CATHARE code strategy and assessment". In: *Nuclear Engineering and Design* 124(3):257-284 (1990) (cit. on pp. 9, 28).

[4] S. Aubry, C. Caremoli, J. Olive, and P. Rascle. "The THYC three-dimensional thermal-hydraulic code for rod bundles: recent developments and validation tests". In: *Nuclear technology* 112.3 (1995), pp. 331–345 (cit. on pp. 10, 14, 28, 110, 215).

[5] G. Le Coq, S. Aubry, J. Cahouet, P. Lequesne, G. Nicolas, and S. Pastorini. "The THYC computer code. A finite volume approach for 3 dimensional two-phase flows in tube bundles". In: *Bulletin de la Direction des Etudes et Recherches - Electricité de France. Série A, nucléaire, hydraulique, thermique. In french* 1 (1989), pp. 61–76 (cit. on pp. 10, 13, 14).

[6] I. Toumi, A. Bergeron, D. Gallo, E. Royer, and D. Caruge. "FLICA-4: A three-dimensional two-phase flow computer code with advanced numerical methods for nuclear applications". In: *Nuclear Engineering and Design* 200 (2000), pp. 139–155 (cit. on pp. 10, 13, 15, 28).

[7] M. Grandotto, M. Bernard, J.P. Gaillard, and P. Miranda. *Méthodes numériques utilisées dans le logiciel* TRIO-GENEPI *(Version 1)*. Tech. rep. DER/SCC/LTDE 91-004, CEA, Saclay, 1991 (cit. on pp. 10, 13, 15).

[8] *Logiciel libre Code_Saturne (EDF)*. 2019. URL: https://www.code-saturne.org (cit. on p. 10).

[9] *Code_Saturne 5.2.0 Theory Guide*. EDF R&D. 2018. URL: https://code-saturne.org/cms/sites/default/files/docs/5.2/theory.pdf (cit. on pp. 10, 28, 92, 93, 176).

[10] *Logiciel libre TrioCFD (CEA)*. 2019. URL: http://triocfd.cea.fr (cit. on p. 10).

[11] *Logiciel libre OpenFOAM*. 2019. URL: https://openfoam.org (cit. on p. 10).

[12] *Logiciel propriétaire NEPTUNE_CFD (CEA, EDF, Framatome et IRSN*. 2019. URL: https://www.code-saturne.org/cms/neptune-cfd (cit. on p. 10).

[13] *Logiciel propriétaire ANSYS Fluent*. 2019. URL: https://www.ansys.com/fr-fr/products/fluids/ansys-fluent (cit. on p. 10).

[14] *Logiciel propriétaire STAR-CCM+*. 2019. URL: https://www.plm.automation.siemens.com/global/fr/products/simcenter/STAR-CCM.html (cit. on p. 10).

[15] *Logiciel propriétaire COMSOL Multiphysics*. 2019. URL: https://www.comsol.fr (cit. on p. 10).

[16] R. Eymard, T. Gallouët, and R. Herbin. "Finite Volume Methods". In: *Handbook for Numerical Analysis, P.G. Ciarlet, J.L. Lions eds, North Holland* 7 (2006), pp. 713–1020 (cit. on pp. 10, 29, 33, 92, 94, 120, 177).

[17] E. Guyon, J.-P. Hulin, and L. Petit. *Hydrodynamique Physique*. Ed. by CNRS éditions. 3e. CNRS éditions - EDP sciences, 2012 (cit. on p. 11).

[18] P. Chassaing. *Mécanique des fluides, éléments d'un premier parcours*. 3e édition. Cépaduès, 2010 (cit. on pp. 11, 13, 193).

[19] E. Godlewski and P.-A. Raviart. *Numerical approximation of hyperbolic systems of conservation laws*. Vol. 118. Applied Mathematical Sciences. New York: Springer-Verlag, 1996 (cit. on pp. 11, 12, 119, 120, 127, 181).

[20] J. Smoller. *Shock Waves and Reaction-Diffusion Equations*. Vol. 258. A Series of Comprehensive Studies in Mathematics. New York: Springer-Verlag, 1994 (cit. on pp. 11, 12, 47, 82, 119, 127, 181).

[21] D. Rochette, S. Clain, and T. Buffard. "Numerical scheme to complete a compressible gas flow in variable porosity media". In: *International Journal of Computational Fluid Dynamics* 19.9 (2005), pp. 299–309 (cit. on pp. 13, 16).

[22] L. Girault and J.-M. Hérard. "A two-fluid hyperbolic model in a porous medium." In: *ESAIM : Mathematical Modelling and Numerical Analysis* 44.6 (2010), pp. 1319–1348 (cit. on pp. 13, 16).

[23] Y. Davit, C.G. Bell, H.M. Byrne, L.A.C. Chapman, L.S. Kimpton, K.H.L. Lang G.E. Leonard, J.M. Oliver, N.C. Pearson, R.J. Shipley, S.L. Waters, J.P. Whiteley, B.D. Wood, and M. Quintard. "Homogenization via formal multiscale asymptotics and volume averaging: how do the two techniques compare?" In: *Advances in Water Resources* 62 (2013), pp. 178–206 (cit. on pp. 13, 29).

[24] D. Kröner and M.-D. Thanh. "Numerical solution to compressible flows in a nozzle with variable cross-section". In: *SIAM - J. Numer. Anal.* 43 (2006), pp. 796–824 (cit. on pp. 14, 16).

[25] A.-J. Chorin. "Numerical solution of the Navier-Stokes equations". In: *Mathematics of Computation* 22(104):745–762 (1968) (cit. on pp. 15, 29, 90, 92, 176).

[26] R. Temam. "Sur l'approximation de la solution des équations de Navier-Stokes par la méthode des pas fractionnaires (I)". In: *Archive for Rational Mechanics and Analysis* 32.5 (1969), pp. 135–153 (cit. on pp. 15, 90, 92, 176).

[27] R. Temam. "Sur l'approximation de la solution des équations de Navier-Stokes par la méthode des pas fractionnaires (II)". In: *Archive for Rational Mechanics and Analysis* 33.5 (1969), pp. 377–385 (cit. on pp. 15, 29, 90, 92, 176).

[28] J.-L. Guermond, P. Minev, and J. Shen. "An overview of projection methods for incompressible flows". In: *Computer Methods in Applied Mechanics and Engineering* 195 (Sept. 2006), pp. 6011–6045 (cit. on pp. 15, 92).

[29] I. Toumi. "A weak formulation of Roe's approximate Riemann solver". In: *Journal of Computational Physics* 102.2 (1992), pp. 360 –373 (cit. on p. 15).

[30] M. Grandotto and P. Obry. “Steam generators two phase flows numerical simulation with liquid and gas momentum equations”. In: *Nuclear Science and Engineering* 151 (2005), pp. 313–318. URL: https://hal-cea.archives-ouvertes.fr/cea-00275766 (cit. on pp. 15, 28).

[31] M. Grandotto and P. Obry. “Calculs des écoulements diphasiques dans les échangeurs par une méthode aux éléments finis”. In: *Revue Européenne des Eléments Finis* 5.1 (1996), pp. 53–74 (cit. on pp. 15, 28).

[32] M. Belliard and M. Grandotto. “Computation of two-phase flow in steam generator using domain decomposition and local zoom methods”. In: *Nuclear Engineering and Design* 213.2-3 (2002), pp. 223–239 (cit. on p. 15).

[33] M. Belliard. “Méthodes de décomposition de domaine et de frontière immergée pour la simulation des composants nucléaires”. Habilitation à Diriger des Recherches. Aix-Marseille Université, 2014. URL: https://tel.archives-ouvertes.fr/tel-01085328 (cit. on pp. 15, 28).

[34] M. Grandotto. “Simulation numérique des écoulements diphasiques dans les échangeurs”. Habilitation à Diriger des Recherches. Université de la Méditerranée - Aix-Marseille II, 2006. URL: https://tel.archives-ouvertes.fr/tel-00275746 (cit. on p. 15).

[35] J. Greenberg and A.-Y. Leroux. “A Well-Balanced Scheme for the Numerical Processing of Source Terms in Hyperbolic Equations”. In: *SIAM - J. Numer. Anal.* 33 (1996), pp. 1–16 (cit. on p. 16).

[36] L. Gosse. “A well-balanced scheme using non-conservative products designed for hyperbolic systems of conservation laws with source terms”. In: *Mathematical Models and Methods in Applied Sciences* 11.2 (2001), pp. 339–365 (cit. on p. 16).

[37] S. Clain and D. Rochette. “First and second-order Finite Volume methods for the one-dimensional non-conservative Euler system”. In: *Journal of Computational Physics* 228 (2009), pp. 8214–8248 (cit. on p. 16).

[38] L. Girault and J.-M. Hérard. “Multidimensional computations of a two-fluid hyperbolic model in a porous medium”. In: *International Journal on Finite Volumes* 7.1 (2010), pp. 1–33. URL: https://hal.archives-ouvertes.fr/hal-01114209 (cit. on pp. 16, 17, 29).

[39] J.-M. Hérard and J. Jung. “An interface condition to compute compressible flows in variable cross-section ducts”. In: *Comptes Rendus Mathématique* 354 (2016), pp. 323–327 (cit. on p. 17).

[40] X. Martin. “Modélisation d’écoulements fluides en milieu encombré d’obstacles”. PhD thesis. Aix-Marseille Université, 2015. URL: https://tel.archives-ouvertes.fr/tel-01235089 (cit. on pp. 17, 90, 91, 176).

[41] J.-M. Hérard and X. Martin. “An integral approach to compute compressible fluid flows in domains containing obstacles.” In: *International Journal on Finite Volumes* 12.1 (2015), pp. 1–39. URL: https://hal.archives-ouvertes.fr/hal-01166478/ (cit. on pp. 17, 29, 60).

[42] W. L. Oberkampf and C. J. Roy. *Verification and Validation in Scientific Computing*. Cambridge Univeristy Press, 2010 (cit. on p. 18).

[43] *Guide de l'ASN numéro 28 : Qualification des outils de calcul scientifique utilisés dans la démonstration de sûreté nucléaire - première barrière*. 2017. URL: https://www.asn.fr/Professionnels/Installations-nucleaires/Centrales-nucleaires/Guides-de-l-ASN-dans-le-domaine-des-installations-nucleaires/Guide-de-l-ASN-n-28-Qualification-des-outils-de-calcul-scientifique-utilises-dans-la-demonstration-de-surete-nucleaire (cit. on p. 18).

[44] *Arrêté du 7 février 2012 fixant les règles générales relatives aux installations nucléaires de base*. 2012. URL: https://www.legifrance.gouv.fr/affichTexte.do?cidTexte=JORFTEXT000025338573&dateTexte=20160205 (cit. on p. 18).

[45] F. Archambeau, J.-M. Hérard, and J. Laviéville. "Comparative study of pressure-correction and Godunov-type schemes on unsteady compressible cases". In: *Computers & Fluids* 38 (2009), pp. 1495–1509 (cit. on pp. 20, 29, 33, 43).

[46] C. Colas, M. Ferrand, J.-M. Hérard, J.-C. Latché, and E. Le Coupanec. "An Implicit Integral Formulation to Model Inviscid Fluid Flows in Obstructed Media". In: *Computers & Fluids* 188 (2019), pp. 136–163. URL: https://hal.archives-ouvertes.fr/hal-01969129 (cit. on pp. 20, 22, 90, 91, 113, 121, 176, 179).

[47] R. Menikoff and B.J. Plohr. "The Riemann problem for fluid flow of real materials". In: *Rev. Mod. Phy.* 61.1 (1989), pp. 75–130 (cit. on pp. 20, 31).

[48] *Institut de Radioprotection et de Sûreté Nucléaire (IRSN), Reactivity-Initiated Accident (RIA)*. 2019. URL: https://www.irsn.fr/FR/connaissances/Installations_nucleaires/Les-centrales-nucleaires/criteres_surete_ria_aprp/Pages/1-accident-reactivite-RIA.aspx (cit. on pp. 20, 28, 30, 59).

[49] C. Colas, M. Ferrand, J.-M. Hérard, E. Le Coupanec, and X. Martin. "An Implicit Integral Formulation for the Modeling of Inviscid Fluid Flows in Domains Containing Obstacles". In: *Finite Volumes for Complex Applications 8*. Vol. 200. Springer Proceedings in Mathematics and Statistics. June 2017, pp. 53–61. URL: https://hal.archives-ouvertes.fr/hal-01579372 (cit. on p. 22).

[50] *Nuclear Energy Agency (NEA), Loss-Of-Coolant Accident (LOCA)*. 2009. URL: https://www.oecd-nea.org/nsd/reports/2009/nea6846_LOCA.pdf (cit. on p. 28).

[51] *FLACS Software*. GEXCON. 2018. URL: https://www.gexcon.com/products-services/FLACS-Software/22/en (cit. on p. 29).

[52] D.-R. Van Der Heul, C. Vuik, and P. Wesseling. "A conservative pressure-correction method for flow at all speeds". In: *Computers & Fluids* 32 (2003), pp. 1113–1132 (cit. on pp. 29, 176).

[53] T. Gallouët, L. Gastaldo, J.-C. Latché, and R. Herbin. "An unconditionnally stable pressure correction scheme for compressible barotropic Navier-Stokes equations". In: *ESAIM: Mathematical Modelling and Numerical Analysis* 44.2 (2010), pp. 251–287. URL: https://hal.archives-ouvertes.fr/hal-00179610 (cit. on pp. 29, 176).

[54] W. Kheriji, R. Herbin, and J.-C. Latché. "Pressure correction staggered schemes for barotropic one-phase and two-phase flows". In: *Computers & Fluids* 88 (2013), pp. 524–542. URL: https://hal.archives-ouvertes.fr/hal-00875348 (cit. on pp. 29, 176).

[55] C. Zaza. "Contribution to numerical methods for all Mach flow regimes and to fluid-porous coupling for the simulation of homogeneous two-phase flows in nuclear reactors". PhD thesis. Aix-Marseille Université, 2015. URL: \https://tel.archives-ouvertes.fr/tel-01135355 (cit. on pp. 29, 33, 38, 176, 179).

[56] X. Martin. "Modélisation d'écoulements fluides en milieu encombré d'obstacles". PhD thesis. Aix-Marseille Université, Chapter 3, pages 207–238, 2015. URL: https://tel.archives-ouvertes.fr/tel-01235089 (cit. on pp. 31, 33).

[57] R. Eymard, T. Gallouët, C. Guichard, R. Herbin, and R. Masson. "TP or not TP, that is the question". In: *Computational Geosciences* 18 (Aug. 2014), pp. 285–296. URL: https://hal.archives-ouvertes.fr/hal-00801648 (cit. on pp. 36, 94, 96, 111, 180, 192).

[58] T. Buffard, T. Gallouët, and J.-M. Hérard. "A sequel to a rough Godunov scheme: application to real gases". In: *Computers & Fluids* 29.7 (2000), pp. 813–847 (cit. on pp. 38–40, 76, 121, 127–129, 182).

[59] F. Dubois. "Boundary conditions and the Osher scheme for the Euler equations of gas dynamics." In: *Internal Report CMAP 170, Ecole Polytechnique, Palaiseau, France* (1987) (cit. on pp. 40, 121).

[60] F. Blondel, B. Audebert, T. Pasutto, and M. Stanciu. "Condensation models and boundary conditions for non-equilibrium wet steam flows." In: *International Journal on Finite Volumes* 10 (2013), pp. 1–53 (cit. on pp. 40, 121).

[61] F. H. Harlow and A. A. Amsden. "Numerical calculation of almost incompressible flow". In: *Journal of Computational Physics* 3.1 (1968), pp. 80 –93 (cit. on pp. 90, 176).

[62] F. H. Harlow and A. A. Amsden. "A numerical fluid dynamics calculation method for all flow speeds". In: *Journal of Computational Physics* 8 (1971), pp. 197–213 (cit. on pp. 90, 176).

[63] K. C. Karki and S. V. Patankar. "Pressure based calculation procedure for viscous flows at all speeds in arbitrary configurations". In: *AIAA Journal* 27 (Sept. 1989), pp. 1167–1174 (cit. on pp. 92, 177).

[64] I. E. Idel'Cik. "Memento des pertes de charge". In: *Collection de la Direction des Etudes et Recherches d'Electricité de France, Paris: Eyrolles* (1969) (cit. on p. 97).

[65] C. M. Rhie and W. L. Chow. "Numerical study of the turbulent flow past an airfoil with trailing edge separation". In: *AIAA Journal* 21.11 (1983), pp. 1525–1532 (cit. on pp. 111, 181).

[66] S. Zhang, X. Zhao, and S. Bayyuk. "Generalized formulations for the Rhie-Chow interpolation". In: *J. Comput. Phys.* 258.C (Feb. 2014), pp. 880–914. URL: http://dx.doi.org/10.1016/j.jcp.2013.11.006 (cit. on p. 111).

[67] W. Z. Shen, J. Michelsen, and J. N. Sørensen. "An improved Rhie-Chow interpolation for unsteady flow computations". In: *AIAA Journal* 39.12 (2001), pp. 2406–2409 (cit. on p. 111).

[68] T. Gallouët. "Boundary conditions for hyperbolic equations or systems". In: *Numerical Mathematics and Advanced Applications*. Ed. by Miloslav Feistauer, Vít Dolejší, Petr Knobloch, and Karel Najzar. Berlin, Heidelberg: Springer Berlin Heidelberg, 2004, pp. 39–55 (cit. on p. 120).

[69] F. Dubois and P. Le Floch. "Boundary conditions for nonlinear hyperbolic systems of conservation laws". In: *J. Diff Equations* 71.1 (1988), pp. 93–122 (cit. on p. 121).

[70] I. Orlanski. "A simple boundary condition for unbounded hyperbolic flows". In: *Journal of Computational Physics* 21.3 (1976), pp. 251–269 (cit. on p. 123).

[71] B. Engquist and A. Majda. "Absorbing boundary conditions for the numerical simulation of waves". English (US). In: *Mathematics of Computation* 31.139 (1977), pp. 629–651 (cit. on p. 123).

[72] G. W. Hedstrom. "Nonreflecting boundary conditions for nonlinear hyperbolic systems". In: *Journal of Computational Physics* 30 (1979), pp. 222–237 (cit. on p. 123).

[73] K. W. Thompson. "Time dependent boundary conditions for hyperbolic systems". In: *Journal of Computational Physics* 68.1 (1987), pp. 1–24 (cit. on p. 123).

[74] D. H. Rudy and J. C. Strikwerda. "A nonreflecting outflow boundary condition for subsonic Navier-Stokes calculations". In: *Journal of Computational Physics* 36.1 (1980), pp. 55–70 (cit. on p. 123).

[75] T. J. Poinsot and S. K. Lele. "Boundary conditions for direct simulations of compressible viscous flows". In: *Journal of Computational Physics* 101.1 (1992), pp. 104–129 (cit. on p. 123).

[76] J.-P. Berenger. "A perfectly matched layer for the absorption of electromagnetic waves". In: *Journal of Computational Physics* 114.2 (1994), pp. 185–200 (cit. on p. 123).

[77] F. Q. Hu. "On absorbing boundary conditions for linearized Euler equations by a perfectly matched layer". In: *Journal of Computational Physics* 129.1 (1996), pp. 201–219 (cit. on p. 123).

[78] C. K. W. Tam, L. Auriault, and F. Cambuli. "Perfectly matched layer as an absorbing boundary condition for the linearized Euler equations in open and ducted domains". In: *Journal of Computational Physics* 144.1 (1998), pp. 213–234 (cit. on p. 123).

[79] F. Q. Hu, X. D. Li, and D. K. Lin. "Absorbing boundary conditions for nonlinear Euler and Navier-Stokes equations based on the perfectly matched layer technique". In: *Journal of Computational Physics* 227.9 (2008), pp. 4398–4424 (cit. on p. 123).

[80] C. K. W. Tam and Z. Dong. "Radiation and outflow boundary conditions for direct computation of acoustic and flow disturbances in a nonuniform mean flow". In: *Journal of Computational Acoustics* 4.2 (1996), pp. 175–201 (cit. on p. 123).

[81] T. Gallouët, J.-M. Hérard, and N. Seguin. "Some recent Finite Volume schemes to compute Euler equations using real gas EOS". In: *International Journal for Numerical Methods in Fluids* 39 (2002), pp. 1073–1138. URL: https://hal.archives-ouvertes.fr/hal-01290885 (cit. on pp. 127, 133, 137, 147, 182).

[82] A. Harten, P. D. Lax, and B. Van Leer. "On upstream differencing and Godunov-type schemes for hyperbolic conservation laws". In: *SIAM Rev.* 25.1 (1983), pp. 35–61 (cit. on p. 127).

[83] R. J. LeVeque. *Numerical Methods for Conservation Laws*. Birkhäuser-Verlag, Basel, 1990 (cit. on p. 127).

[84] E. F. Toro. *Riemann solvers and numerical methods for fluid dynamics*. Third. Springer-Verlag, Berlin, 2009 (cit. on p. 127).

[85] S. K. Godunov. "A difference method for numerical calculation of discontinuous solutions of the equations of hydrodynamics". In: *Mat. Sb. (N.S.)* 47.89 (1959). In Russian, pp. 271–306 (cit. on p. 128).

[86] T. Gallouët, J.-M. Hérard, and N. Seguin. "On the use of symmetrizing variables for vacuum". In: *Calcolo* 40.3 (2003), pp. 163–194. URL: https://hal.archives-ouvertes.fr/hal-00003439 (cit. on pp. 128–130).

[87] P. Helluy, J.-M. Hérard, H. Mathis, and S. Müller. "A simple parameter-free entropy correction for approximate Riemann solvers". In: *Comptes Rendus Mécanique* 338.9 (July 2010), pp. 493–498. URL: https://hal.archives-ouvertes.fr/hal-00466999 (cit. on p. 128).

[88] T. Gallouët, J.-M. Hérard, and N. Seguin. “A hybrid scheme to compute contact discontinuities in one-dimensional Euler systems”. en. In: *ESAIM: Mathematical Modelling and Numerical Analysis - Modélisation Mathématique et Analyse Numérique* 36.6 (2002), pp. 1133–1159. URL: http://www.numdam.org/item/M2AN_2002__36_6_1133_0 (cit. on p. 129).

[89] M. Deininger, U. Iben, and C.-D. Munz. “Coupling of three- and one-dimensional hydraulic flow simulations”. In: *Computers & Fluids* 190 (2019), pp. 128 –138 (cit. on p. 154).

[90] A. LALLEMAND. *Écoulements monodimensionnels des fluides compressibles*. B 8 165. Techniques de l’ingénieur, traité Génie énergétique (cit. on pp. 167, 170).

[91] J.L.M. Poiseuille. *Le mouvement des liquides dans les tubes de petits diamètres*. 1844 (cit. on p. 193).

[92] R. Comolet. *Mécanique expérimentale des fluides, Dynamique des fluides réels, turbomachines*. Vol. 2. 4e édition. Masson, 1994 (cit. on p. 193).

Appendix A

De Laval nozzle two-dimensional verification test case: subsonic cases

1 Description

We consider the steady-state, compressible, inviscid, isentropic flow of air in an adiabatic de Laval nozzle (see sketch in FIGURE A.1).

The flow is subsonic in the convergent, then three configurations depending on the pressure at the outlet may occur:

- subsonic flow in the divergent,
- supersonic flow in the divergent,
- shock in the divergent.

Herein, a subsonic flow in the divergent is only considered. Two cases are computed:

1. subsonic flow with a max Mach number $Ma = 0.6$ in the divergent,
2. subsonic flow with a max Mach number $Ma = 0.17$ in the divergent.

The results are compared to the 1D analytical solution derived from the 1D mass, momentum balance equations for an inviscid flow (Euler equations), taking into account the variable section of the nozzle [90].

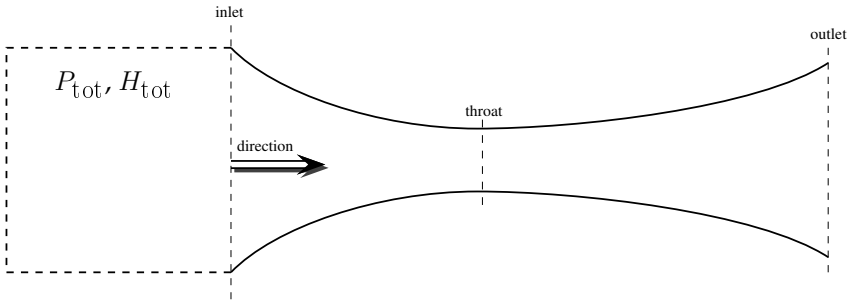

FIGURE A.1 – *Test case geometry.*

This case allows to validate the compressible module of *Code_Saturne* on fully compressible subsonic configurations (Mach number $Ma < 1$).

1.1 Flow parameters

- **Geometric characteristics**

  The 2D nozzle "upper" profile can be easily described by a polygonal path joining the points defined in TABLE A.1.

index	0	1	2	3	4	5
x	0	0.0265	0.0565	0.0996	0.1525	0.32
h	0.06	0.06	0.0519	0.027	0.0153	0.03

TABLE A.1 – *Nozzle variable half section.*

Let us define as well the point C located at $(x_c, y_c) = (0.1446, 0.105)$.

The nozzle variable half section along the x-axis is then analytically defined as follows:

$$h(x) = \begin{cases} h_0, & x \in [x_0, x_1[\\ \sqrt{h_0^2 - (x - x_1)^2}, & x \in [x_1, x_2[\\ \frac{h_3 - h_2}{x_3 - x_2}(x - x_3) + h_3, & x \in [x_2, x_3[\\ y_c - \sqrt{(y_c - h_3)^2 + (x_c - x_3)^2 - (x - x_c)^2}, & x \in [x_3, x_4[\\ \frac{h_5 - h_4}{x_5 - x_4}(x - x_4) + h_4, & x \in [x_4, x_5]. \end{cases}$$

Since the flow is symmetric with respect to the x-axis, only the "upper" half of the nozzle is simulated (see computational domain in FIGURE A.2).

- **Physical characteristics**

  Reference values of density, pressure and temperature are the following ones:

  - reference density: $\rho_0 = 1\ kg.m^{-3}$,
  - reference temperature: $T_{ref} = 293.15\ K$,
  - reference pressure: $P_{ref} = 10^5\ Pa$.

  The following physical properties are kept uniform:

  - dynamic viscosity: $\mu = 1.73 \times 10^{-5}\ kg.m^{-1}.s^{-1}$,
  - thermal conductivity: $\lambda = 0.03\ W.m^{-1}.K^{-1}$,
  - isobaric specific heat: $C_p = 1005\ J.kg^{-1}.K^{-1}$,
  - volume viscosity: $\zeta = 0\ kg.m^{-1}.s^{-1}$.

  It is assumed that the fluid behaves as a perfect gas, with the following parameters:

  - ideal gas constant: $R = 8.31446\ (S.I.)$,
  - molar mass of air: $X_{\text{air}} = 28.966 \times 10^{-3}\ kg.mol^{-1}$.

2 Computation options

Numerical options

The following numerical options are set for all cases:

- *Code_Saturne* compressible algorithm enabled,
- solver precision $\epsilon = 10^{-12}$ for the three computed variables, (pressure, velocity, total energy)
- viscous terms in momentum equations and diffusion term in total energy equation are disabled for velocity and total energy variable,
- time step Δt computed such that $CFL_u = 0.25$.

Meshes

Two meshes composed of triangular prisms with progressive refinement are used (see FIGURE A.2).

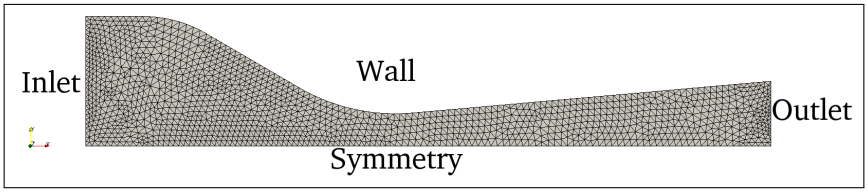

FIGURE A.2 – *Coarse mesh of the de Laval nozzle.*

TABLE A.2 gives the number of cells for each mesh.

Mesh label	N_{cells}
coarse	2812
fine	10778

TABLE A.2 – *Number of cells for each mesh.*

Boundary conditions

The boundary conditions are imposed as presented in FIGURE A.2. Note that symmetry are applied in the z-direction (2D hypothesis).

At the inlet or the outlet, TABLE A.3 gives details about the types of boundary conditions specific to the compressible module applied in each case:

B.C. type	SUBSONIC ($Ma = 0.3$)	SUBSONIC ($Ma = 0.08$)
subsonic inlet	$P_{\text{tot}}, H_{\text{tot}}$ imposed	$P_{\text{tot}}, H_{\text{tot}}$ imposed
subsonic outlet	$P_o = 0.95 \times 10^5\ Pa$	$P_o = 0.995 \times 10^5\ Pa$

TABLE A.3 – *Types of compressible B.C. used in each case.*

The values given for the subsonic inlet (so called reservoir boundary conditions) are as follows:

- $P_{\text{tot}} = 10^5\ Pa$,
- $H_{\text{tot}} = 294465\ J$.

Steady state: time convergence

Convergence is ensured by the evaluation of the L^2 time residual of the computed variables (see FIGURES A.3 and A.8).

3 Numerical results

3.1 Subsonic case 1

FIGURE A.4 shows the profiles of pressure obtained on the two meshes for the subsonic case 1 respectively and compare them to the 1D theoretical solution (cf. [90]). FIGURE A.5 shows the 2D-pressure field on the coarse mesh. FIGURE A.6 shows the profiles of x-velocity obtained

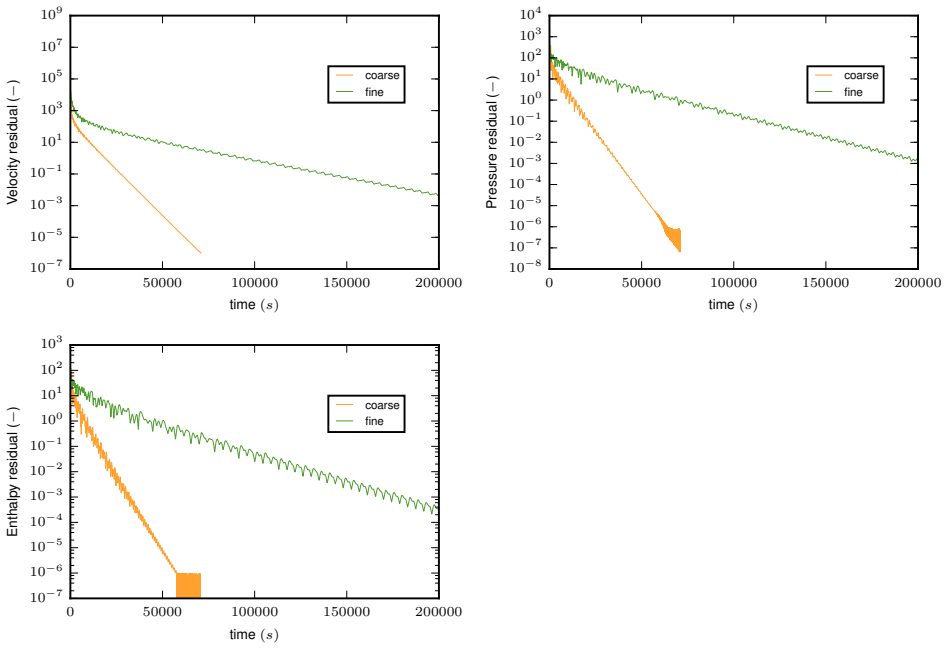

FIGURE A.3 – *Case 1: L^2 residuals.*

on the two meshes for the subsonic case 1 respectively and compare them to the 1D theoretical solution (cf. 1). FIGURE A.7 shows the 2D-Mach number field on the coarse mesh.

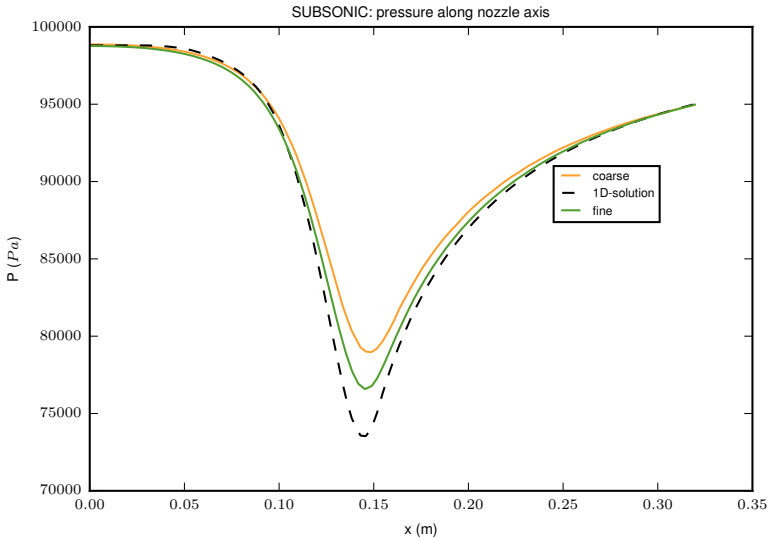

FIGURE A.4 – *Case 1: 1D pressure profile.*

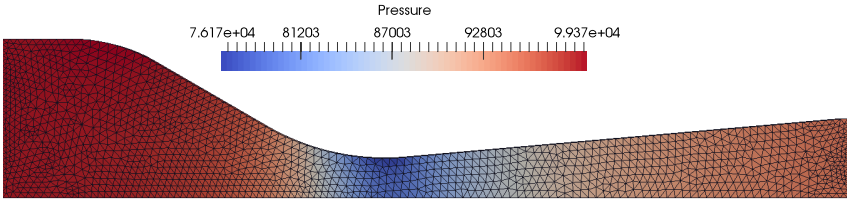

FIGURE A.5 – *Case 1: 2D pressure field.*

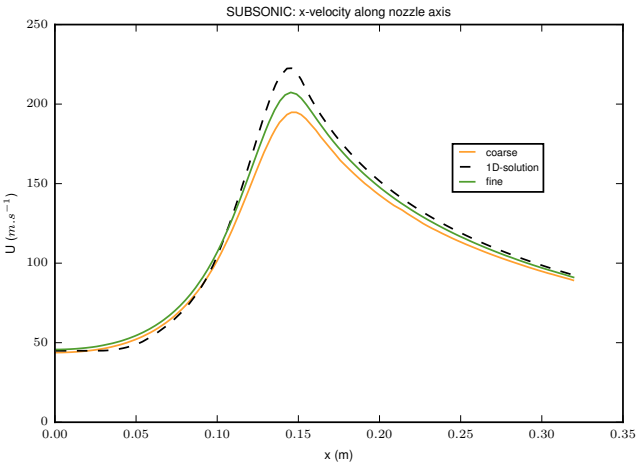

FIGURE A.6 – *Case 1: 1D x-velocity profile.*

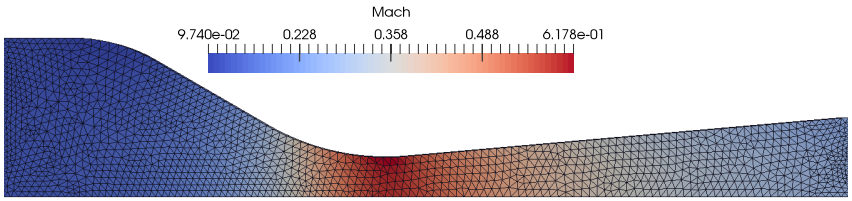

FIGURE A.7 – *Case 1: 2D Mach field.*

3.2 Low subsonic case 2

Likewise, FIGURE A.9 shows the profiles of pressure obtained on the two meshes for the low subsonic case 2 respectively and compare them to the 1D theoretical solution. FIGURE A.10 shows the 2D-pressure field on the coarse mesh. FIGURE A.11 shows the profiles of x-velocity

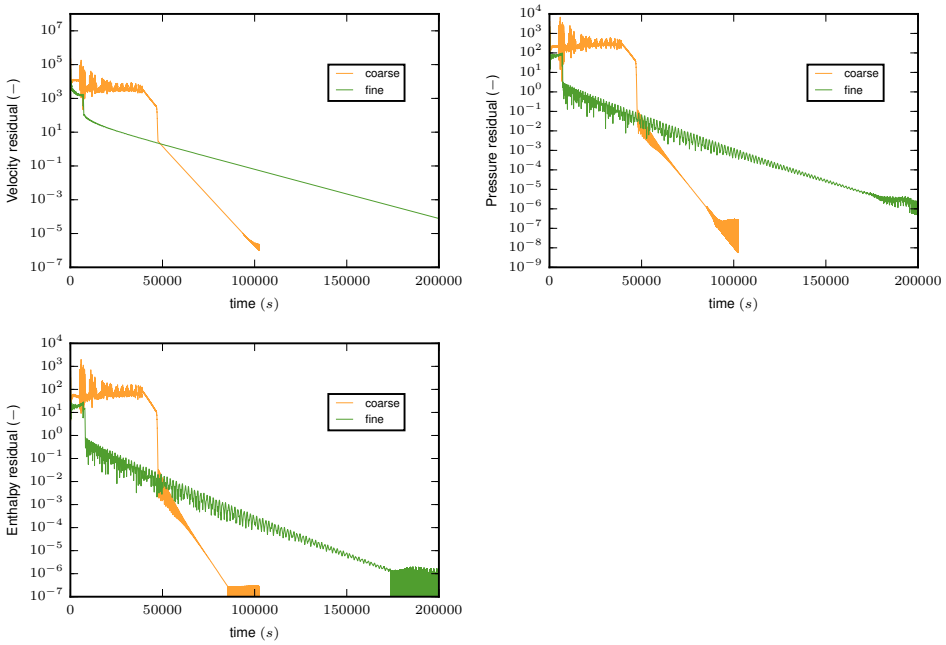

FIGURE A.8 – *Case 2: L^2 residuals.*

obtained on the two meshes for the low subsonic case 2 respectively and compare them to the 1D theoretical solution (cf. 1). FIGURE A.12 shows the 2D-Mach number field on the coarse mesh.

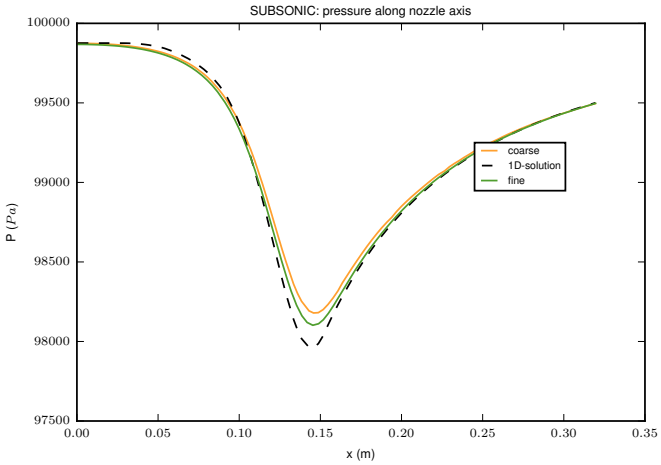

FIGURE A.9 – *Case 2: 1D pressure profile.*

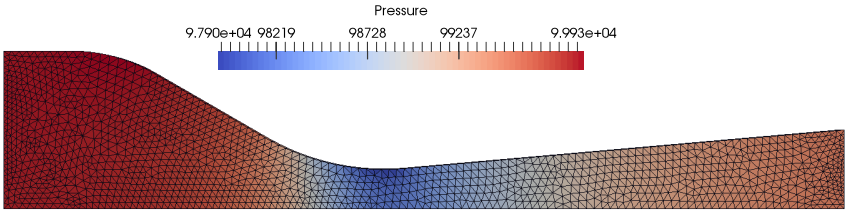

FIGURE A.10 – *Case 2: 2D pressure field.*

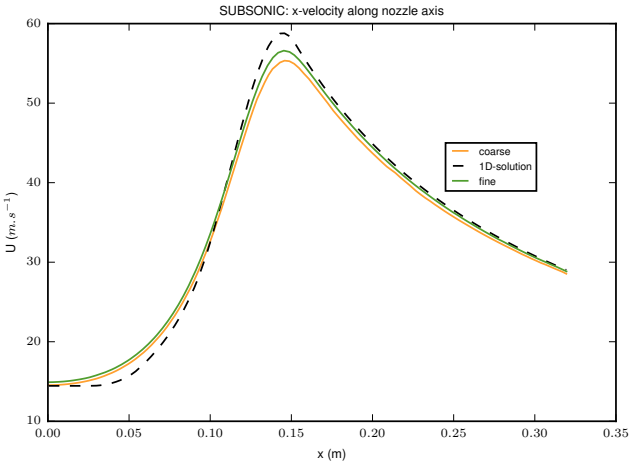

FIGURE A.11 – *Case 2: 1D x-velocity profile.*

Reference

[90] A. LALLEMAND. *Écoulements monodimensionnels des fluides compressibles*. B 8 165. Techniques de l'ingénieur, traité Génie énergétique (cit. on pp. 167, 170).

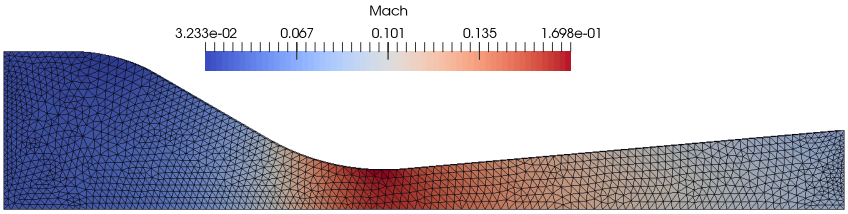

FIGURE A.12 – *Case 2: 2D Mach field.*

Appendix B

An incremental pressure-correction cell-centred finite volume scheme for compressible fluid flows

1 Introduction

In this appendix, a semi-implicit collocated finite volume scheme is proposed for the discretization of the compressible Euler equations. The time scheme is based on a fractional-step method using an incremental pressure-correction technique. This technique is relevant for steady-state flows. The numerical scheme is verified on several one-dimensional Riemann problems.

2 Set of governing equations: Euler equations

The Euler equations for compressible fluid flows are considered on a finite time interval $(0,T)$, $T \in \mathbb{R}_+^*$ and in an open connected bounded domain $\Omega \subset \mathbb{R}^d$ ($d = 1, 2$ or 3):

$$\left\{ \begin{array}{l} \partial_t \rho + \operatorname{div}(\rho \boldsymbol{u}) = 0, \\ \partial_t(\rho \boldsymbol{u}) + \mathbf{div}(\boldsymbol{u} \otimes \rho \boldsymbol{u}) + \boldsymbol{\nabla} P = 0 \ \text{ in } \Omega \times (0,T), \\ \partial_t(\rho e) + \operatorname{div}(\boldsymbol{u}(\rho e + P)) = 0. \end{array} \right. \tag{B.1}$$

where $\rho \geq 0$, $\boldsymbol{u}$, P and e denote the velocity, the pressure and the specific total energy of the fluid. We note $\boldsymbol{Q} = \rho \boldsymbol{u}$, the momentum per unit volume.

$\mathcal{P}$ is the equation of state (EOS) such that:

$$P = \mathcal{P}(\rho, \epsilon),$$

where $\epsilon = e - \frac{1}{2}|\boldsymbol{u}|^2$ is the specific internal energy.

We also define the speed of sound:

$$c^2 = \left(\frac{P}{\rho^2} - \frac{\partial \epsilon(P,\rho)}{\partial \rho} \right) / \left(\frac{\partial \epsilon(P,\rho)}{\partial P} \right).$$

This system (B.1) is complemented by initial conditions and boundary conditions on $\partial\Omega$.

Equations (B.1) can be written as follows:

$$\partial_t \boldsymbol{W} + \mathbf{div}(\boldsymbol{F}(\boldsymbol{W})) = 0, \tag{B.2}$$

where:

$\boldsymbol{W} = (\rho, \rho\boldsymbol{u}, \rho e)^{\mathsf{T}}$ is the conservative state vector,

and:

$$\boldsymbol{F}(\boldsymbol{W}) = (\rho\boldsymbol{u}, \boldsymbol{u}\otimes\rho\boldsymbol{u} + P\,\mathbf{Id}, \boldsymbol{u}(\rho e + P))^{\mathsf{T}} \text{ is the convective flux.}$$

3 Integral formulation

The integral formulation, described in chapter 1 [46] and in [40], is still applied to the compressible Euler equations. Set of equations (B.1) is integrated over fixed control volumes Ω_i, $i \in \{1, ..., N\}$, of the mesh of Ω, which may potentially contain many disjoint solid obstacles. We recall that the whole volume occupied by the fluid within Ω_i is denoted by Ω_i^ϕ, while the fluid surface (respectively the wall surface) is denoted by Γ_i^ϕ (respectively Γ_i^w) (see FIGURE B.1).

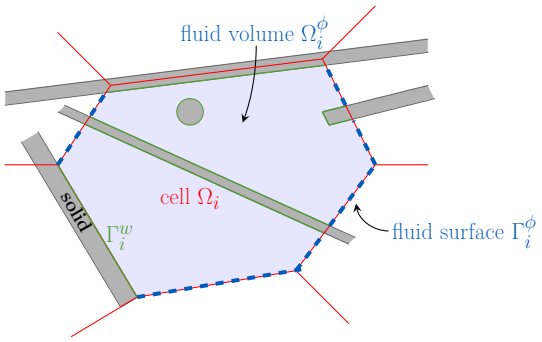

FIGURE B.1 – *Sketch of a cell including fluid and solid.*

The mean value of the fluid state $\boldsymbol{W}(\mathbf{x}, t)$, with $\mathbf{x} \in \Omega$ and $t \in (0, T)$, over each fluid control volume Ω_i^ϕ reads:

$$\boldsymbol{W}_i(t) = \frac{1}{\left|\Omega_i^\phi\right|}\int_{\Omega_i^\phi} \boldsymbol{W}(\boldsymbol{x}, t)\mathrm{d}\boldsymbol{x}.$$

The integral form of equations (B.1) over a bounded time interval $[t_0, t_1] \subset (0, T)$ and space with respect to the fluid part of the cell Ω_i, for all $i \in \{1, ..., N\}$ gives:

$$\left|\Omega_i^\phi\right|(\boldsymbol{W}_i(t_1) - \boldsymbol{W}_i(t_0)) + \int_{t_0}^{t_1}\int_{\Gamma_i^\phi} \boldsymbol{F}(\boldsymbol{W})\boldsymbol{n}\mathrm{d}\gamma dt + \int_{t_0}^{t_1}\int_{\Gamma_i^w} (0, P\boldsymbol{n}, 0)^{\mathsf{T}}\mathrm{d}\gamma dt = 0, \tag{B.3}$$

where $\Gamma_i = \partial\Omega_i^\phi$ denotes the whole boundary of the fluid cell Ω_i^ϕ and $\boldsymbol{n}(\boldsymbol{x})$ its unit outward normal vector. The pressure integral on the wall boundary is the unique contribution.

Set of equations (B.3) is rewritten by summing up on the interfaces of Ω_i:

$$\left|\Omega_i^\phi\right|(\boldsymbol{W}_i(t_1) - \boldsymbol{W}_i(t_0)) + \int_{t_0}^{t_1}\left(\sum_{j\in N(i)}\int_{\Gamma_{ij}^\phi} \boldsymbol{F}(\boldsymbol{W})\boldsymbol{n}\mathrm{d}\gamma\right)dt + \int_{t_0}^{t_1}\int_{\Gamma_i^w} (0, P\boldsymbol{n}, 0)^{\mathsf{T}}\mathrm{d}\gamma dt = 0. \tag{B.4}$$

We recall that the subscript ij refers to the interfaces between the neighbouring control volumes Ω_i and Ω_j, with $j \in N(i)$ and $N(i)$ defines the set of neighbouring cells of Ω_i.

4 Discretization

The proposed algorithm uses a fractional-step method and falls within the class of pressure-correction algorithm, introduced for incompressible flows in [25, 26, 27] and extended to compressible flows in [61, 62] and more recently in [52, 53, 54, 55]. This algorithm is integrated in the open-source *Code_Saturne* software [9].

The multi-dimensional compressible Euler equations are numerically solved with a first order semi-implicit collocated finite volume method, using the same control volumes for both the scalar and the vector unknowns [16]. The time discretization uses a prediction and a correction of the velocity allowing to satisfy the mass conservation.

We note that when the density is constant, the compressible algorithm recovers the standard incompressible algorithm, corresponding to SIMPLEC (Semi-Implicit Method for Pressure Linked Equations-Consistent) algorithm [63].

In the sequel, we consider one discrete value $\mathbf{W}_i^n$ per cell Ω_i at each discrete time t^n; $\mathbf{W}_i^n$ is an approximation of the mean value $\boldsymbol{W}_i(t^n)$.

4.1 Time scheme

The time discretization of equation (B.1) is based on a fractional-step method using an implicit first order Euler integration for each step.

$\Delta t = t^{n+1} - t^n$ denotes the time step, between two successive times t^n and t^{n+1} of the time interval $(0, T)$.

Starting with the initial condition ρ^{n-1} and $(\rho^n, \mathbf{u}^n, P^n)$, the algorithm is decomposed in three steps:

1. a predicted velocity $\tilde{\mathbf{u}}$ is computed from the momentum balance:
$$\frac{\rho^n \tilde{\mathbf{u}} - \rho^{n-1}\mathbf{u}^n}{\Delta t} + \mathbf{div}\ (\tilde{\boldsymbol{u}} \otimes \boldsymbol{Q}^n) + \boldsymbol{\nabla} P^n = 0, \tag{B.5}$$
2. an incremental pressure correction is found such that the mass balance is satisfied. The density $\rho^{n+1} = \rho^n + \frac{P^\star - P^n}{(c^2)^n}$ and the velocity $\mathbf{u}^{n+1}$ are updated:
$$\begin{cases} \dfrac{\rho^{n+1} - \rho^n}{\Delta t} + \operatorname{div}\left(\boldsymbol{Q}^{n+1}\right) = 0, \\ \dfrac{\boldsymbol{Q}^{n+1} - \rho^n \tilde{\boldsymbol{u}}}{\Delta t} + \boldsymbol{\nabla}\left(P^\star - P^n\right) = 0, \end{cases} \tag{B.6}$$
3. a total energy e^{n+1} is computed from the total energy balance, allowing to update the pressure P^{n+1} with the EOS.
$$\frac{\rho^{n+1} e^{n+1} - \rho^n e^n}{\Delta t} + \operatorname{div}\left(e^{n+1}\boldsymbol{Q}^{n+1}\right) + \operatorname{div}\left(P^\star \frac{\boldsymbol{Q}^{n+1}}{\rho^{n+1}}\right) = 0, \tag{B.7}$$
$$P^{n+1} = \mathcal{P}(\rho^{n+1}, \epsilon^{n+1}) \text{ with } \epsilon^{n+1} = e^{n+1} - \frac{1}{2}\frac{\rho^n}{\rho^{n+1}}\left|\boldsymbol{u}^{n+1}\right|^2. \tag{B.8}$$

Remark 4.1. *We note that the kinetic energy per unit volume, deduced from the discrete momentum balance over the time interval $[t^n, t^{n+1}]$, is $\frac{1}{2}\rho^n \left|\boldsymbol{u}^{n+1}\right|^2$.*

The time discretization is detailed below for the integral form (B.3) and a collocated space discretization.

4.1.1 Prediction step: momentum balance

A predicted velocity field $\tilde{\mathbf{u}}_i$, for all Ω_i, is obtained by solving the momentum balance equation (B.5) with a semi-implicit scheme; the velocity is implicit, while the pressure are explicit. The time scheme of the integral formulation of the momentum equation reads for any cell Ω_i:
$$\left|\Omega_i^\phi\right|\left(\rho^n \tilde{\mathbf{u}}_i - \rho^{n-1}\mathbf{u}_i^n\right) + \Delta t \int_{\Gamma_i^\phi} \tilde{\boldsymbol{u}}(\boldsymbol{Q}^n \cdot \boldsymbol{n})\mathrm{d}\gamma = -\Delta t \int_{\Gamma_i^\phi \cup \Gamma_i^w} P^n \boldsymbol{n}\mathrm{d}\gamma. \tag{B.9}$$

This first step provides the discrete unknown $\tilde{\mathbf{u}}_i$, by solving an invertible linear system for $\rho_i^n > 0$.

4.1.2 Correction step: mass balance

The second step, equation (B.6), corrects the mass flux to satisfy the discrete mass balance over the time interval Δt, for all Ω_i:

$$\left|\Omega_i^\phi\right| \left(\rho_i^{n+1} - \rho_i^n\right) + \Delta t \int_{\Gamma_i^\phi} \boldsymbol{Q}^{n+1} \cdot \boldsymbol{n} \mathrm{d}\gamma = 0. \tag{B.10}$$

The implicit mass flux $\boldsymbol{Q}^{n+1} \cdot \boldsymbol{n}$ is computed from semi-discrete simplified momentum equation (B.11) at the fluid interfaces, with the pressure temporal increment $\delta P^\star = P^\star - P^n$:

$$\boldsymbol{Q}^{n+1} \cdot \boldsymbol{n} = \rho^n \tilde{\boldsymbol{u}} \cdot \boldsymbol{n} - \Delta t \boldsymbol{\nabla}(\delta P^\star) \cdot \boldsymbol{n}. \tag{B.11}$$

Thus the integral form of equation (B.11) gives the following semi-discrete equation:

$$\left|\Omega_i^\phi\right| \left(\rho_i^{n+1} - \rho_i^n\right) - \Delta t \int_{\Gamma_i^\phi} \Delta t \boldsymbol{\nabla}(\delta P^\star) \cdot \boldsymbol{n} \mathrm{d}\gamma = - \int_{\Gamma_i^\phi} \rho^n \tilde{\boldsymbol{u}} \cdot \boldsymbol{n} \mathrm{d}\gamma. \tag{B.12}$$

The density time variation is linearly approximated with the acoustic relation:

$$\rho_i^{n+1} - \rho_i^n = \frac{\delta P_i^\star}{(c_i^2)^n}, \text{ with } (c_i^2)^n = c^2(\rho_i^n, P_i^n).$$

Equation (B.12) thus yields with the pressure increment:

$$\left|\Omega_i^\phi\right| \frac{\delta P_i^\star}{(c_i^2)^n} - \Delta t \int_{\Gamma_i^\phi} \Delta t \boldsymbol{\nabla}(\delta P^\star) \cdot \boldsymbol{n} \mathrm{d}\gamma = - \int_{\Gamma_i^\phi} \rho^n \tilde{\boldsymbol{u}} \cdot \boldsymbol{n} \mathrm{d}\gamma. \tag{B.13}$$

This second step provides, for all cells Ω_i, the pressure increment $\delta P^\star$ by solving an invertible linear system.

Thus, the density is updated such that:

$$\rho_i^{n+1} = \rho_i^n + \frac{\delta P_i^\star}{(c_i^2)^n}.$$

4.1.3 Velocity update

Finally, the discrete velocity is corrected with (B.11) rewritten at cells:

$$\mathbf{u}_i^{n+1} = \tilde{\mathbf{u}}_i - \frac{\Delta t}{\left|\Omega_i^\phi\right| \rho_i^n} \int_{\Gamma_i^\phi \cup \Gamma_i^w} \delta P^\star \boldsymbol{n} \mathrm{d}\gamma. \tag{B.14}$$

Remark 4.2. *The pressure increment is used in the correction step of the velocity to recover an implicit scheme of the momentum equation on the pressure by summing Equation (B.9) and (B.14):*

$$\left|\Omega_i^\phi\right| \left(\rho_i^n \mathbf{u}_i^{n+1} - \rho_i^{n-1} \mathbf{u}_i^n\right) + \Delta t \int_{\Gamma_i^\phi} \tilde{\boldsymbol{u}} (\boldsymbol{Q}^n \cdot \boldsymbol{n}) \mathrm{d}\gamma = -\Delta t \int_{\Gamma_i^\phi \cup \Gamma_i^w} P^\star \boldsymbol{n} \mathrm{d}\gamma. \tag{B.15}$$

4.1.4 Total energy balance

The total energy is updated with the following semi-implicit scheme: the total energy is implicit while the pressure, the density and the velocity are explicit from the previous steps.

$$\left|\Omega_i^\phi\right| \left(\rho_i^{n+1} e_i^{n+1} - \rho_i^n e_i^n\right) + \Delta t \int_{\Gamma_i^\phi} e^{n+1} (\boldsymbol{Q}^{n+1} \cdot \boldsymbol{n}) \mathrm{d}\gamma = -\Delta t \int_{\Gamma_i^\phi} \frac{P^\star}{\rho^{n+1}} (\boldsymbol{Q}^{n+1} \cdot \boldsymbol{n}) \mathrm{d}\gamma. \tag{B.16}$$

4.2 Space scheme

The space scheme uses a first order cell-centred finite volume method. Numerical fluxes are evaluated by considering one discrete value $\mathbf{W}_i^n$ per cell Ω_i: they are computed by using upwind or centred schemes.

The space scheme is similar to the one described in chapter 1 (see [46]). In particular, for congested media, the wall pressure in the wall boundary integrals is approximated with the same formula as in chapter 1 (section 4).

We can also cite works in [55], which propose a space discretization on collocated mesh of a pressure-correction method.

4.2.1 Prediction step: momentum balance

First, the convective numerical flux is summed on all the fluid interfaces Γ_{ij}^{ϕ} of the cell Ω_i and approximated here by an upwind scheme.

$$\left|\Omega_i^{\phi}\right| \mathbf{div}_i(\tilde{\boldsymbol{u}} \otimes \boldsymbol{Q}^n) = \int_{\Gamma_i^{\phi}} \tilde{\boldsymbol{u}}(\boldsymbol{Q}^n \cdot \boldsymbol{n}) \mathrm{d}\gamma = \sum_{j \in N(i)} \int_{\Gamma_{ij}^{\phi}} \tilde{\boldsymbol{u}}(\boldsymbol{Q}^n \cdot \boldsymbol{n}) \mathrm{d}\gamma = \sum_{j \in N(i)} \tilde{\boldsymbol{u}}_{ij}^{upw} \left(\boldsymbol{Q}^n \cdot \boldsymbol{n}\right)_{ij} S_{ij}^{\phi}. \tag{B.17}$$

The mass flux is known from the previous time step such that:

$$\left|\Omega_i^{\phi}\right| \frac{\rho_i^n - \rho_i^{n-1}}{\Delta t} + \sum_{j \in N(i)} \left(\boldsymbol{Q}^n \cdot \boldsymbol{n}\right)_{ij} S_{ij}^{\phi} = 0,$$

and the implicit advected velocity at the fluid interfaces is:

$$\tilde{\mathbf{u}}_{ij}^{upw} = \lambda_{ij}^n \tilde{\mathbf{u}}_i + (1 - \lambda_{ij}^n) \tilde{\mathbf{u}}_j, \tag{B.18}$$

with:

$$\lambda_{ij}^n = \begin{cases} 1 & \text{if } \left(\boldsymbol{Q}^n \cdot \boldsymbol{n}\right)_{ij} \geq 0, \\ 0 & \text{otherwise.} \end{cases}$$

Second, the approximation of the pressure gradient uses a centred scheme. The boundary integral is decomposed on the fluid interfaces and the walls for all cells Ω_i:

$$\left|\Omega_i^{\phi}\right| \boldsymbol{\nabla}_i P^n = \int_{\Gamma_i} P^n \boldsymbol{n} \mathrm{d}\gamma = \int_{\Gamma_i^w} P_w^n \boldsymbol{n} \mathrm{d}\gamma + \sum_{j \in N(i)} P_{ij}^n S_{ij}^{\phi}.$$

The fluid interface pressure is computed by a linear interpolation of the neighbouring cell pressures:

$$P_{ij}^n = \frac{h_{ij/i} P_i^n + h_{ij/j} P_j^n}{h_{ij/i} + h_{ij/j}} = (1 - \alpha_{ij}) P_i^n + \alpha_{ij} P_j^n. \tag{B.19}$$

with:

$$\alpha_{ij} = \frac{h_{ij/j}}{h_{ij/i} + h_{ij/j}},$$

and $h_{ij/i}$ (respectively $h_{ij/j}$) stands for the distance from the mass centre of the cell Ω_i (respectively Ω_j) to the interface Γ_{ij}^{ϕ}.

For the interior walls, we refer to chapter 1 (section 4.2) for details, a simple estimation is to take $P_w^n = P_i^n$, giving finally the following discrete gradient:

$$\left|\Omega_i^{\phi}\right| \boldsymbol{\nabla}_i P^n = \int_{\Gamma_i} P^n \boldsymbol{n} \mathrm{d}\gamma = \sum_{j \in N(i)} \left(P_{ij}^n - P_i^n\right) \boldsymbol{n}_{ij} S_{ij}^{\phi}. \tag{B.20}$$

4.2.2 Correction step: mass balance

Equation (B.13) is discretised in space by a centred scheme.

- Explicit mass flux approximation:

$$\left|\Omega_i^\phi\right| \operatorname{div}\left(\rho^n \tilde{\boldsymbol{u}}\right) = \int_{\Gamma_i^\phi} \rho^n \tilde{\boldsymbol{u}} \cdot \boldsymbol{n} \mathrm{d}\gamma = \sum_{j \in N(i)} \int_{\Gamma_{ij}^\phi} \rho^n \tilde{\boldsymbol{u}} \cdot \boldsymbol{n} \mathrm{d}\gamma = \sum_{j \in N(i)} \left(\rho^n \tilde{\boldsymbol{u}}\right)_{ij}^{cent} \cdot \boldsymbol{n}_{ij} S_{ij}^\phi, \tag{B.21}$$

The mass flux at the fluid interfaces is linearly interpolated between the two neighbouring cell values:

$$\left(\rho^n \tilde{\boldsymbol{u}}\right)_{ij}^{cent} \cdot \boldsymbol{n}_{ij} = \left(\alpha_{ij} \rho_i^n \tilde{\mathbf{u}}_i + (1 - \alpha_{ij}) \rho_j^n \tilde{\mathbf{u}}_j\right) \cdot \boldsymbol{n}_{ij}. \tag{B.22}$$

Remark 4.3. *This choice of approximation allows to recover the scheme of the incompressible algorithm presented in chapter 2. Nevertheless, for more numerical stability, we can prefer to use an upwind scheme on the advected density with respect to the normal interpolated velocity to the interface as described in chapter 1 (section 4.1).*

- Pressure gradient increment approximation at the interface:

The pressure gradient increment at the fluid interface is approximated with a "two-point flux approximation" scheme, which is consistent for admissible meshes, see [57]:

$$\boldsymbol{\nabla} \delta P^\star \cdot \boldsymbol{n}_{ij} = \left.\frac{\partial \delta P^\star}{\partial \boldsymbol{n}}\right|_{\Gamma_{ij}^\phi} = \frac{\delta P_j^\star - \delta P_i^\star}{h_{ij/i} + h_{ij/j}}. \tag{B.23}$$

Thus, the scheme yields for the Laplacian operator:

$$\begin{aligned} -\left|\Omega_i^\phi\right| \operatorname{div}_i(\Delta t \boldsymbol{\nabla} \delta P^\star) = -\int_{\Gamma_i^\phi} \Delta t \boldsymbol{\nabla} \delta P^\star \cdot \boldsymbol{n} \mathrm{d}\gamma &= -\sum_{j \in N(i)} \int_{\Gamma_{ij}^\phi} \Delta t \boldsymbol{\nabla} \delta P^\star \cdot \boldsymbol{n} \mathrm{d}\gamma \\ &= -\sum_{j \in N(i)} \frac{\Delta t}{h_{ij/i} + h_{ij/j}} \left(\delta P_j^\star - \delta P_i^\star\right) S_{ij}^\phi. \end{aligned}$$

The following discrete equation are solved with the pressure increment:

$$\frac{\left|\Omega_i^\phi\right|}{\Delta t} \frac{\delta P_i^\star}{(c_i^2)^n} - \sum_{j \in N(i)} \frac{\Delta t}{h_{ij/i} + h_{ij/j}} \left(\delta P_j^\star - \delta P_i^\star\right) S_{ij}^\phi = -\sum_{j \in N(i)} \left(\rho^n \tilde{\boldsymbol{u}}\right)_{ij}^{cent} \cdot \boldsymbol{n}_{ij} S_{ij}^\phi. \tag{B.24}$$

We deduce the updated mass flux at each fluid interface, satisfying the mass balance over $[t^n, t^{n+1}]$ at the discrete level:

$$\sum_{j \in N(i)} \left(\boldsymbol{Q}^{n+1} \cdot \boldsymbol{n}\right)_{ij} S_{ij}^\phi = \sum_{j \in N(i)} \left(\rho^n \tilde{\boldsymbol{u}}\right)_{ij}^{cent} \cdot \boldsymbol{n}_{ij} S_{ij}^\phi - \sum_{j \in N(i)} \frac{\Delta t}{h_{ij/i} + h_{ij/j}} \left(\delta P_j^\star - \delta P_i^\star\right) S_{ij}^\phi. \tag{B.25}$$

4.2.3 Velocity update

Using the discrete gradient (B.20), the discrete velocity update writes:

$$\mathbf{u}_i^{n+1} = \tilde{\mathbf{u}}_i - \frac{\Delta t}{\left|\Omega_i^\phi\right| \rho_i^n} \sum_{j \in N(i)} \left(\delta (P_{ij}^\star)^{cent} - \delta P_i^\star\right) \boldsymbol{n}_{ij} S_{ij}^\phi. \tag{B.26}$$

4.2.4 Total energy balance

Equation (B.16) of the total energy conservation is discretized by an upwind scheme:

$$\begin{aligned}\int_{\Gamma_i^\phi}\left(e^{n+1}+\frac{P^\star}{\rho^{n+1}}\right)(\boldsymbol{Q}^{n+1}\cdot\boldsymbol{n})\mathrm{d}\gamma &= \sum_{j\in V(i)}\int_{\Gamma_{ij}^\phi}\left(e^{n+1}+\frac{P^\star}{\rho^{n+1}}\right)(\boldsymbol{Q}^{n+1}\cdot\boldsymbol{n})\mathrm{d}\gamma \\ &= \sum_{j\in V(i)}\left(\left(e_{ij}^{n+1}\right)^{upw}+\left(\frac{P_{ij}^*}{\rho_{ij}^{n+1}}\right)^{upw}\right)\left(\boldsymbol{Q}^{n+1}\cdot\boldsymbol{n}\right)_{ij}S_{ij}^\phi.\end{aligned} \tag{B.27}$$

The upwind scheme is described by equation (B.18).

5 Summing up: discrete compressible Euler equations

The discrete compressible Euler equations are summed up for any cell Ω_i, $i\in\{1,...,N\}$:

$$\frac{\rho_i^n\tilde{\mathbf{u}}_i-\rho_i^{n-1}\mathbf{u}_i^n}{\Delta t}+\mathbf{div}_i(\tilde{\boldsymbol{u}}\otimes\boldsymbol{Q}^n)=-\boldsymbol{\nabla}_iP^n, \tag{B.28}$$

$$\begin{cases}\dfrac{1}{(c_i^2)^n}\dfrac{\delta P_i^\star}{\Delta t}-\mathrm{div}_i(\Delta t\boldsymbol{\nabla}\delta P^\star)=-\mathrm{div}_i(\rho^n\tilde{\boldsymbol{u}}),\\ \left(\boldsymbol{Q}^{n+1}\cdot\boldsymbol{n}\right)_{ij}S_{ij}^\phi=(\rho_{ij}^n\tilde{\boldsymbol{u}}_{ij})^{cent}\cdot\boldsymbol{n}_{ij}S_{ij}^\phi-\Delta t\boldsymbol{\nabla}\delta P^\star\cdot\boldsymbol{n}_{ij}S_{ij}^\phi,\ \forall\, j\in N(i),\end{cases} \tag{B.29}$$

$$P_i^\star=P_i^n+\delta P_i^\star\quad\text{and}\quad\rho_i^{n+1}=\rho_i^n+\frac{\delta P_i^\star}{(c_i^2)^n},$$

$$\mathbf{u}_i^{n+1}=\tilde{\mathbf{u}}_i-\frac{\Delta t}{\rho_i^n}\boldsymbol{\nabla}_i(\delta P^\star),$$

$$\begin{aligned}&\frac{\rho_i^{n+1}e_i^{n+1}-\rho_i^ne_i^n}{\Delta t}+\mathrm{div}_i(e^{n+1}\boldsymbol{Q}^{n+1})=-\mathrm{div}_i\left(\frac{P^\star}{\rho^{n+1}}\boldsymbol{Q}^{n+1}\right),\\ &P_i^{n+1}=\mathcal{P}(\rho_i^{n+1},\epsilon_i^{n+1})\text{ with }\epsilon_i^{n+1}=e_i^{n+1}-\frac{1}{2}\frac{\rho_i^n}{\rho_i^{n+1}}\left(\boldsymbol{u}_i^{n+1}\right)^2.\end{aligned} \tag{B.30}$$

Remark 5.1. *The Rhie and Chow filter [65] can be added to equation (B.29) to remove spatial oscillations on the variables see appendix 2.A in chapter 2.*

6 Numerical verification test cases: one-dimensional Riemann problems

This section is dedicated to the verification case of the compressible algorithm in a free medium (without obstacle).

One-dimensional Riemann problems are considered.

The computational domain is $\Omega=(-200,200)$ and consists of a one-dimensional tube with a membrane in the middle which separates two different constant fluid states. At the time $t=0$, the membrane bursts.

An ideal gas EOS (diatomic gas with $\gamma=\frac{7}{5}$) and a stiffened gas EOS are considered. The numerical solutions are compared with the exact solutions. Those solutions are derived in [20, 19].

All meshes used to solve this Riemann problem are uniform. The meshes contain N cells with $N=800,1600,3200,6400,12800,25600$ or 51200 cells.

The convergence order is measured with the L^1-norm of the relative error[1].

In the sequel, the space step dx is defined in m, the density ρ in $kg.m^{-3}$, the velocity u in $m.s^{-1}$ and the pressure P in Pa.

6.1 Sod shock tube

Initial conditions are given by, for the left and right states:

$$\begin{cases} (\rho_L, u_L, P_L) = \left(1, 0, 10^5\right), \\ (\rho_R, u_R, P_R) = \left(0.125, 0, 10^4\right). \end{cases} \tag{B.31}$$

The CFL_u number, based on the material velocity u, is equal to 0.1 *i.e.* $CFL_{u+c} \approx 1$. The exact solution is composed of a 1-rarefaction wave followed by a 2-contact discontinuity and a 3-shock wave. The profiles are given in FIGURE B.2 and the convergence curves in FIGURE B.3. The numerical rates of convergence are about 0.6 for the density, and slightly greater than 0.8 for the velocity and the pressure as shown in TABLE B.1. The results are similar to the ones obtained with the pressure-correction scheme described in chapter 1 or with the VFRoe-ncv scheme [58, 81]. A slight difference between this scheme and the two other schemes is visible on the shock wave: a spike appears on the front of the discontinuity. An upwind scheme instead of the centred scheme for the density could be improve the quality of the profiles. We note that the incremental pressure-correction scheme gives a slightly better accuracy than the pressure-correction scheme of chapter 1.

dx (m)	N	ρ cnv. order	u cnv. order	P cnv. order
5e-1	800			
2.5e-1	1600	0.6310	0.8812	0.8327
1.25e-1	3200	0.6223	0.8785	0.8595
6.25e-2	6400	0.6072	0.8772	0.8576
3.125e-2	12800	0.6010	0.9285	0.9144
1.5625e-2	25600	0.5804	0.9030	0.8960
7.8125e-3	51200	0.5632	0.8954	0.8782

TABLE B.1 – *Sod shock tube: L^1 convergence orders.*

6.2 Unsteady discontinuity contact for an ideal gas

Initial conditions are given by, for the left and right states:

$$\begin{cases} (\rho_L, u_L, P_L) = \left(1, 200, 10^5\right), \\ (\rho_R, u_R, P_R) = \left(0.125, 200, 10^5\right). \end{cases} \tag{B.32}$$

The CFL_u number is equal to 0.1 *i.e.* $CFL_{u+c} \approx 1$. The exact solution is only composed of a 2-contact discontinuity. The density discontinuity is recovered with numerical diffusion, see FIGURE B.4. The numerical convergence order is 0.5 for the density corresponding to the contact discontinuity wave, and approximately 1 for the velocity and the pressure (see FIGURE B.5 and TABLE B.2). Contrary to the VFRoe-ncv scheme, the Riemann invariants u and P of this wave are not preserved at the discrete level. We note that the other pressure-correction scheme in chapter 1 does not preserve anymore the Riemann invariants.

[1]The discrete relative L^1 error is defined as: $e_{L^1(\Omega)}(\varphi) = \frac{\sum_{i=1}^{N_{cell}} \left|\varphi_i^{exact} - \varphi_i^{computed}\right| |\Omega_i|}{\sum_{i=1}^{N_{cell}} \left|\varphi_i^{exact}\right| |\Omega_i|}$.

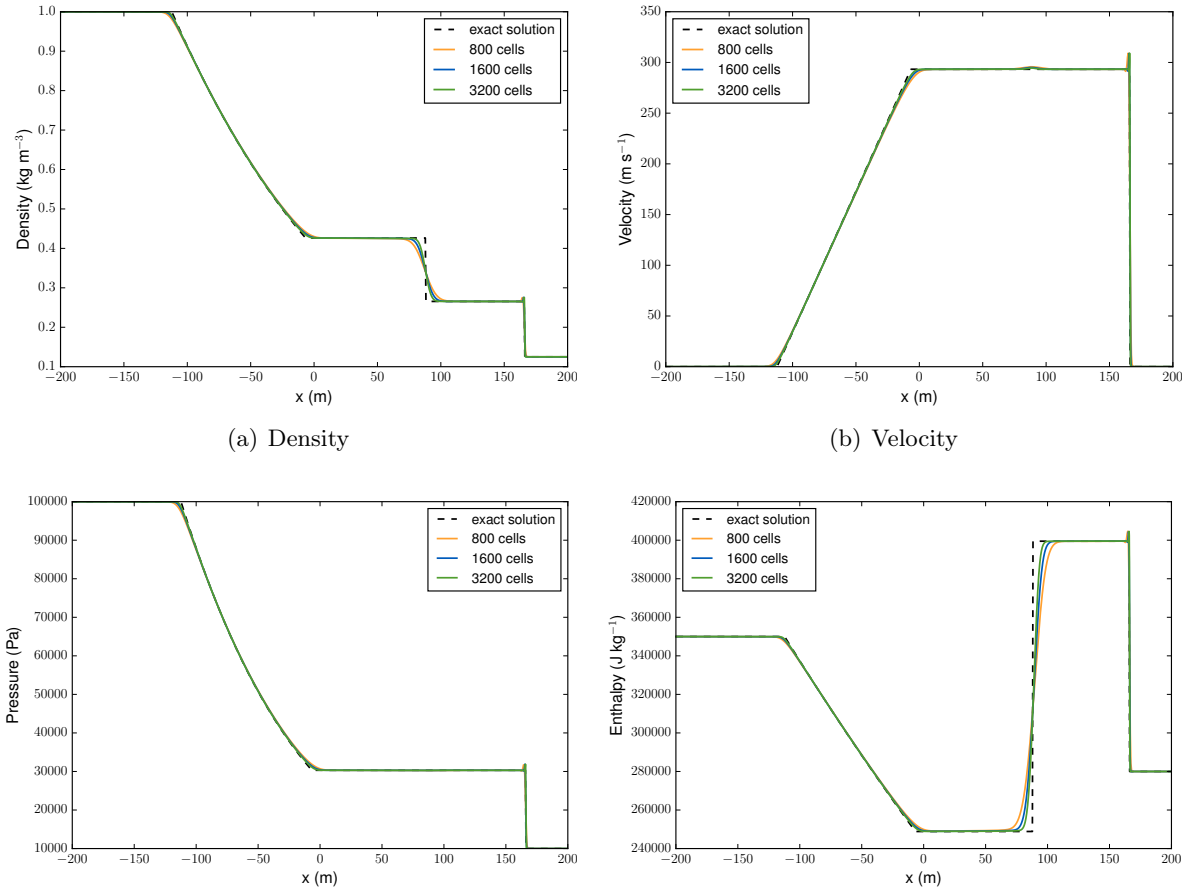

(a) Density (b) Velocity

(c) Pressure (d) Enthalpy

FIGURE B.2 – *Sod shock tube: comparison of the numerical solutions for 800, 1600 and 3200 cells with the exact solution.*

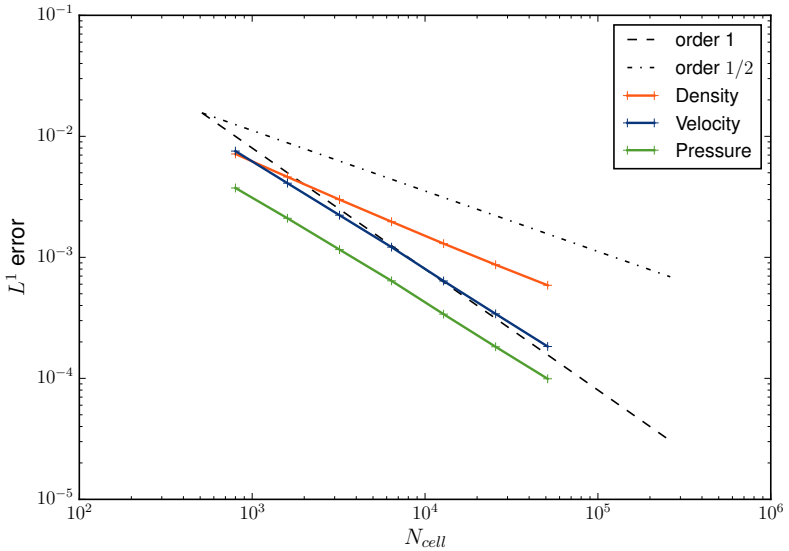

FIGURE B.3 – *Sod shock tube: L^1 convergence curves.*

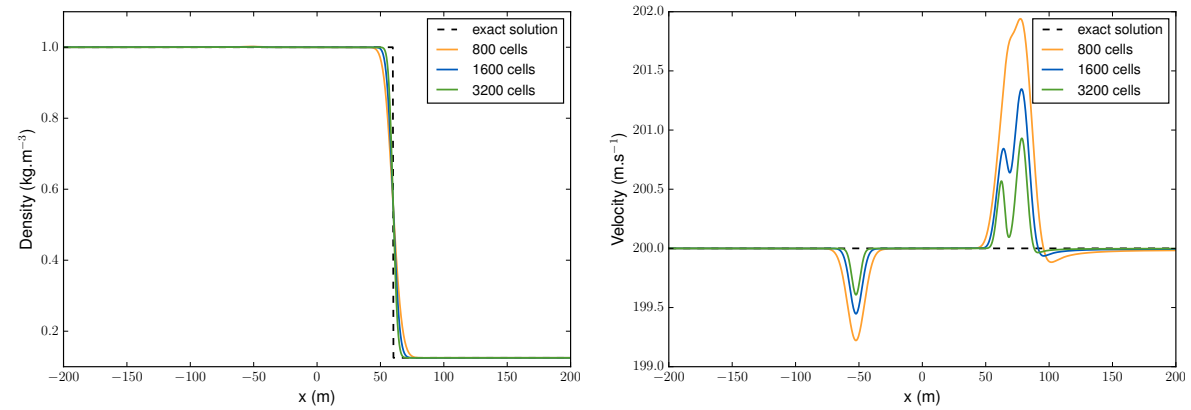

(a) Density

(b) Velocity

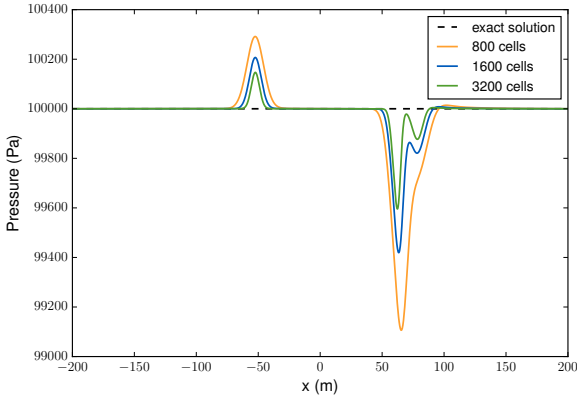

(c) Pressure

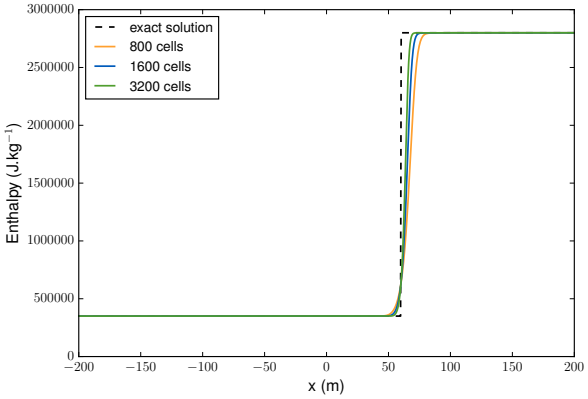

(d) Enthalpy

FIGURE B.4 – *Unsteady contact discontinuity for ideal gas: comparison of the numerical solutions for 800, 1600 and 3200 cells with the exact solution.*

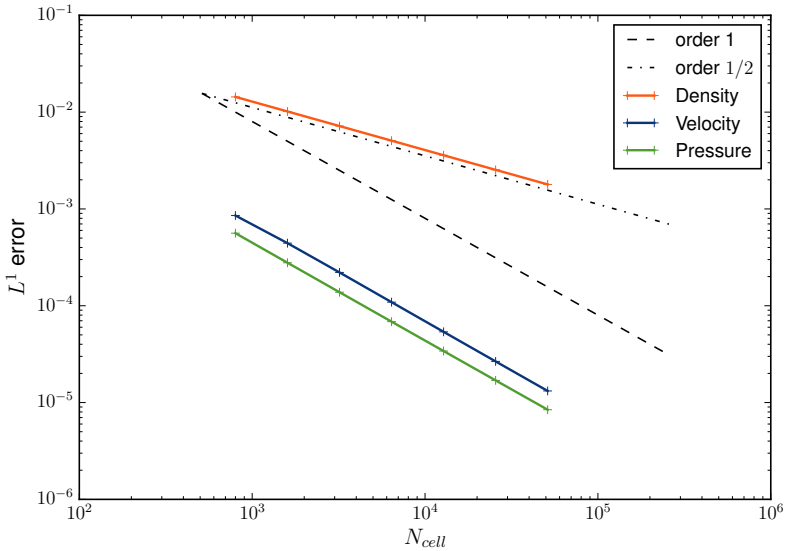

FIGURE B.5 – *Unsteady contact discontinuity for ideal gas: L^1 convergence curves.*

dx (m)	N	ρ cnv. order	u cnv. order	P cnv. order
5e-1	800			
2.5e-1	1600	0.5003	0.9478	1.0138
1.25e-1	3200	0.5007	1.0046	1.012
6.25e-2	6400	0.5010	1.0201	1.010
3.125e-2	12800	0.5008	1.0181	1.0084
1.5625e-2	25600	0.5006	1.0155	1.0070
7.8125e-3	51200	0.5004	1.0132	1.0058

TABLE B.2 – *Unsteady contact discontinuity for ideal gas: L^1 convergence orders.*

6.3 Riemann problem with a stiffened gas EOS

This verification test case is a one-dimensional Riemann problem with a stiffened gas EOS. The stiffened gas parameters are computed for a liquid water at a 165 *bar* pressure and a 583.15 K temperature: $\gamma_{SG} = 1.85768$ and $\Pi_\infty = 4.243468 \times 10^8$ Pa. Initial conditions are, for the left and right states:

$$\begin{cases} (\rho_L, u_L, P_L) = \left(800, 0, 1.65 \times 10^7\right), \\ (\rho_R, u_R, P_R) = \left(797, 6.827, 5.0 \times 10^6\right). \end{cases} \tag{B.33}$$

The CFL_u number is equal to 0.01 *i.e.* $CFL_{u+c} \approx 1$. This test case corresponds to a low Mach number flow. The Mach number is such that: $M = \frac{|u|}{c} \in \left[0, 10^{-2}\right]$. The exact solution is composed of a 1-rarefaction wave, a 2-contact discontinuity and a 3-shock wave. The scheme enables to capture the shock wave and to reproduce the stiff rarefaction wave profiles (see FIGURE B.6). The numerical convergence order is slightly greater than 0.5 (see FIGURE B.7 and TABLE B.3). The scheme is numerically stable with a numerical diffusion depending on the CFL_u number value.

dx (m)	N	ρ cnv. order	u cnv. order	P cnv. order
5e-1	800			
2.5e-1	1600	0.5134	0.5182	0.5178
1.25e-1	3200	0.5172	0.5211	0.5211
6.25e-2	6400	0.5247	0.5276	0.5277
3.125e-2	12800	0.5351	0.5389	0.5389
1.5625e-2	25600	0.5486	0.5536	0.5537
7.8125e-3	51200	0.5666	0.5733	0.5734

TABLE B.3 – *Stiffened gas Riemann problem: L^1 convergence orders.*

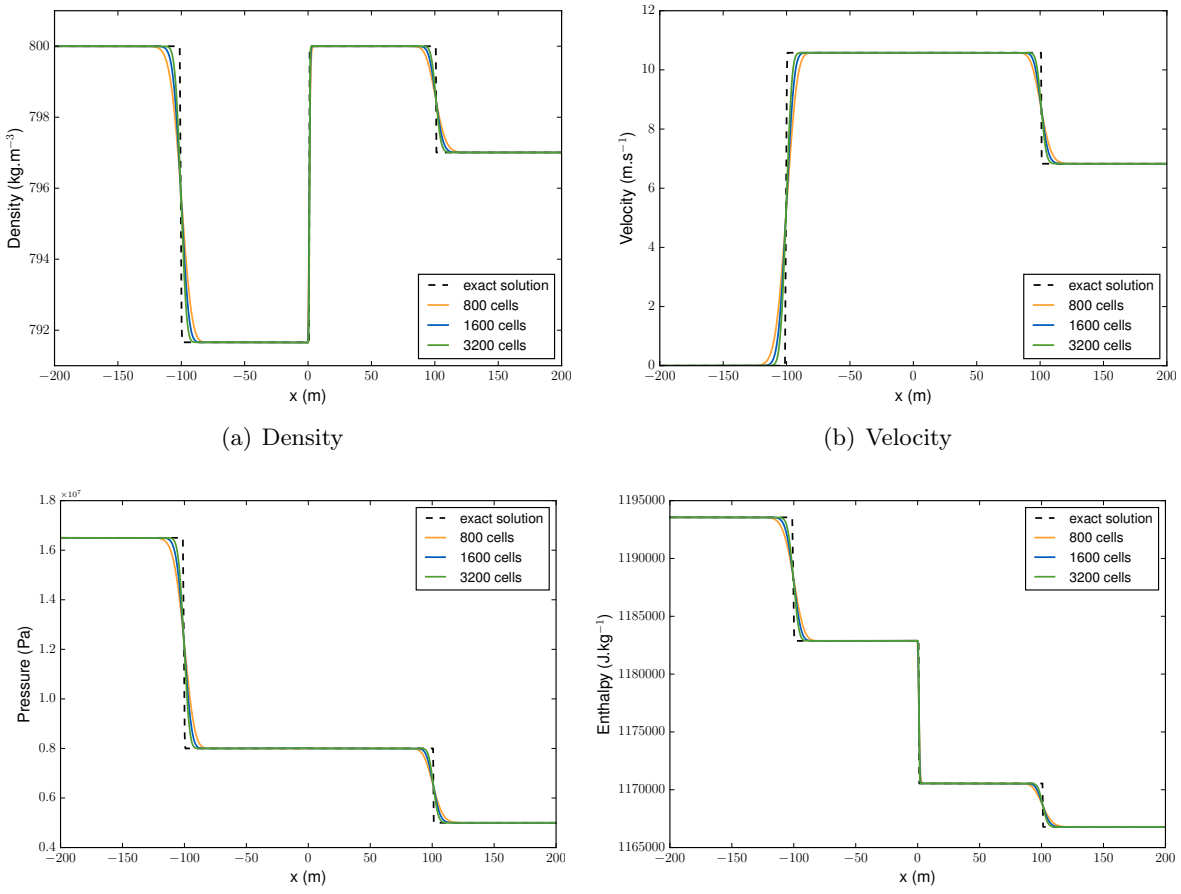

(a) Density (b) Velocity

(c) Pressure (d) Enthalpy

FIGURE B.6 – *Stiffened gas Riemann problem: comparison of the numerical solutions for 800, 1600 and 3200 cells with the exact solution.*

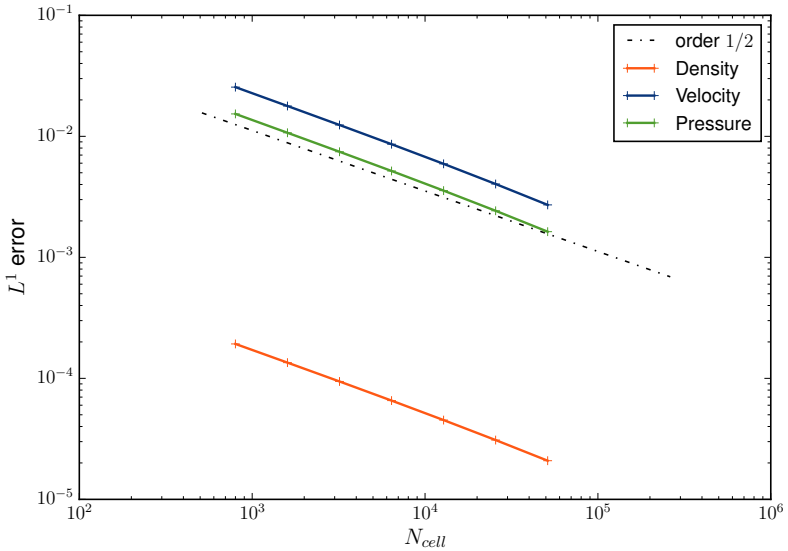

FIGURE B.7 – *Stiffened gas Riemann problem: L^1 convergence curves.*

7 Conclusion

A new first order collocated finite volume scheme using an incremental pressure-correction method is proposed.

This semi-implicit technique is typically suitable for steady-state or quasi steady-state flows and can use the new space scheme developed in chapter 2 to deal with fluid section jumps by preserving the analytic steady state.

It is interesting to note that this scheme enables to recover the standard scheme for incompressible flows described in chapter 2 by construction, when the density is constant.

The convergence of the scheme towards the exact solution is numerically verified by one-dimensional Riemann problems. Two analytical equations of state are tested: an ideal gas and a stiffened gas.

References

[9] *Code_Saturne 5.2.0 Theory Guide*. EDF R&D. 2018. URL: https://code-saturne.org/cms/sites/default/files/docs/5.2/theory.pdf (cit. on pp. 10, 28, 92, 93, 176).

[16] R. Eymard, T. Gallouët, and R. Herbin. "Finite Volume Methods". In: *Handbook for Numerical Analysis, P.G. Ciarlet, J.L. Lions eds, North Holland* 7 (2006), pp. 713–1020 (cit. on pp. 10, 29, 33, 92, 94, 120, 177).

[19] E. Godlewski and P.-A. Raviart. *Numerical approximation of hyperbolic systems of conservation laws*. Vol. 118. Applied Mathematical Sciences. New York: Springer-Verlag, 1996 (cit. on pp. 11, 12, 119, 120, 127, 181).

[20] J. Smoller. *Shock Waves and Reaction-Diffusion Equations*. Vol. 258. A Series of Comprehensive Studies in Mathematics. New York: Springer-Verlag, 1994 (cit. on pp. 11, 12, 47, 82, 119, 127, 181).

[25] A.-J. Chorin. "Numerical solution of the Navier-Stokes equations". In: *Mathematics of Computation* 22(104):745–762 (1968) (cit. on pp. 15, 29, 90, 92, 176).

[26] R. Temam. "Sur l'approximation de la solution des équations de Navier-Stokes par la méthode des pas fractionnaires (I)". In: *Archive for Rational Mechanics and Analysis* 32.5 (1969), pp. 135–153 (cit. on pp. 15, 90, 92, 176).

[27] R. Temam. "Sur l'approximation de la solution des équations de Navier-Stokes par la méthode des pas fractionnaires (II)". In: *Archive for Rational Mechanics and Analysis* 33.5 (1969), pp. 377–385 (cit. on pp. 15, 29, 90, 92, 176).

[40] X. Martin. "Modélisation d'écoulements fluides en milieu encombré d'obstacles". PhD thesis. Aix-Marseille Université, 2015. URL: https://tel.archives-ouvertes.fr/tel-01235089 (cit. on pp. 17, 90, 91, 176).

[46] C. Colas, M. Ferrand, J.-M. Hérard, J.-C. Latché, and E. Le Coupanec. "An Implicit Integral Formulation to Model Inviscid Fluid Flows in Obstructed Media". In: *Computers & Fluids* 188 (2019), pp. 136–163. URL: https://hal.archives-ouvertes.fr/hal-01969129 (cit. on pp. 20, 22, 90, 91, 113, 121, 176, 179).

[52] D.-R. Van Der Heul, C. Vuik, and P. Wesseling. "A conservative pressure-correction method for flow at all speeds". In: *Computers & Fluids* 32 (2003), pp. 1113–1132 (cit. on pp. 29, 176).

[53] T. Gallouët, L. Gastaldo, J.-C. Latché, and R. Herbin. "An unconditionnally stable pressure correction scheme for compressible barotropic Navier-Stokes equations". In: *ESAIM: Mathematical Modelling and Numerical Analysis* 44.2 (2010), pp. 251–287. URL: https://hal.archives-ouvertes.fr/hal-00179610 (cit. on pp. 29, 176).

[54] W. Kheriji, R. Herbin, and J.-C. Latché. "Pressure correction staggered schemes for barotropic one-phase and two-phase flows". In: *Computers & Fluids* 88 (2013), pp. 524–542. URL: https://hal.archives-ouvertes.fr/hal-00875348 (cit. on pp. 29, 176).

[55] C. Zaza. "Contribution to numerical methods for all Mach flow regimes and to fluid-porous coupling for the simulation of homogeneous two-phase flows in nuclear reactors". PhD thesis. Aix-Marseille Université, 2015. URL: \https://tel.archives-ouvertes.fr/tel-01135355 (cit. on pp. 29, 33, 38, 176, 179).

[57] R. Eymard, T. Gallouët, C. Guichard, R. Herbin, and R. Masson. "TP or not TP, that is the question". In: *Computational Geosciences* 18 (Aug. 2014), pp. 285–296. URL: https://hal.archives-ouvertes.fr/hal-00801648 (cit. on pp. 36, 94, 96, 111, 180, 192).

[58] T. Buffard, T. Gallouët, and J.-M. Hérard. "A sequel to a rough Godunov scheme: application to real gases". In: *Computers & Fluids* 29.7 (2000), pp. 813–847 (cit. on pp. 38–40, 76, 121, 127–129, 182).

[61] F. H. Harlow and A. A. Amsden. "Numerical calculation of almost incompressible flow". In: *Journal of Computational Physics* 3.1 (1968), pp. 80 –93 (cit. on pp. 90, 176).

[62] F. H. Harlow and A. A. Amsden. "A numerical fluid dynamics calculation method for all flow speeds". In: *Journal of Computational Physics* 8 (1971), pp. 197–213 (cit. on pp. 90, 176).

[63] K. C. Karki and S. V. Patankar. "Pressure based calculation procedure for viscous flows at all speeds in arbitrary configurations". In: *AIAA Journal* 27 (Sept. 1989), pp. 1167–1174 (cit. on pp. 92, 177).

[65] C. M. Rhie and W. L. Chow. "Numerical study of the turbulent flow past an airfoil with trailing edge separation". In: *AIAA Journal* 21.11 (1983), pp. 1525–1532 (cit. on pp. 111, 181).

[81] T. Gallouët, J.-M. Hérard, and N. Seguin. "Some recent Finite Volume schemes to compute Euler equations using real gas EOS". In: *International Journal for Numerical Methods in Fluids* 39 (2002), pp. 1073–1138. URL: https://hal.archives-ouvertes.fr/hal-01290885 (cit. on pp. 127, 133, 137, 147, 182).

Annexe C

Prise en compte des frottements visqueux dans la formulation intégrale

Dans cette annexe, on propose une technique numérique pour prendre en compte le frottement visqueux à la paroi des obstacles dans la formulation intégrale. Une discrétisation en espace utilisant une loi de paroi est construite. Elle permet de retrouver la chute de pression analytique du problème de l'écoulement laminaire en canal plan suivant la loi de Poiseuille sur des maillages grossiers encombrés. On note que la loi de paroi s'annule asymptotiquement lorsque le maillage est raffiné à la paroi, permettant ainsi de passer continûment de l'échelle composant à l'échelle locale CFD.

1 Formulation intégrale pour un écoulement de fluide visqueux incompressible

1.1 Équations de Navier-Stokes

L'écoulement de fluide est régi par le système d'équations aux dérivées partielles de Navier-Stokes, composé des équations de continuité et de quantité de mouvement :

$$\begin{cases} \operatorname{div} \boldsymbol{Q} = 0, \\ \partial_t \boldsymbol{Q} + \mathbf{div}\ (\boldsymbol{u} \otimes \boldsymbol{Q}) + \boldsymbol{\nabla} P = \mathbf{div}\, \boldsymbol{\tau}, \end{cases} \tag{C.1}$$

où :

- ρ, $\boldsymbol{u}$ et P sont respectivement la masse volumique, la vitesse et la pression du fluide. On note $\boldsymbol{Q} = \rho \boldsymbol{u}$, la quantité de mouvement volumique.
- $\boldsymbol{\tau}(\boldsymbol{u})$ représente le tenseur des contraintes visqueuses et s'écrit dans le cadre des équations de Navier-Stokes en régime incompressible :

$$\boldsymbol{\tau}(\boldsymbol{u}) = \mu \left(\boldsymbol{\nabla}\, \boldsymbol{u} + \boldsymbol{\nabla}\, \boldsymbol{u}^{\mathsf{T}} \right).$$

La contrainte d'incompressibilité, $\operatorname{div} \boldsymbol{u} = 0$, donne ainsi :

$$\mathbf{div}\, (\boldsymbol{\tau}(\boldsymbol{u})) = \mathbf{div}\, (\mu\, (\boldsymbol{\nabla}\, \boldsymbol{u})).$$

Dans la suite, la masse volumique ρ et la viscosité μ sont supposées être constantes.

1.2 Discrétisation de l'intégrale des contraintes visqueuses

La méthode numérique pour discrétiser les équations de Navier-Stokes est rappelée rapidement. Elle repose sur celle présentée dans le chapitre 2 pour les équations d'Euler en régime incompressible.

Elle utilise une méthode d'intégration temporelle à pas fractionnaires : tout d'abord, une prédiction de la vitesse $\tilde{\boldsymbol{u}}$ est obtenue en résolvant l'équation de quantité de mouvement avec un schéma semi-implicite. Puis l'équation continuité est vérifiée au moyen d'une technique de correction de pression. Finalement la vitesse est mise à jour avec une partie de l'équation de quantité de mouvement. Le tenseur des contraintes visqueuses est pris en compte de manière implicite en temps dans l'étape de prédiction.

En partant du temps initiale $t = t^n$, l'étape de prédiction s'écrit en intégrant en espace sur le volume fluide de la maille Ω_i^ϕ de bord fluide Γ_i^ϕ et solide Γ_i^w :

$$\left|\Omega_i^\phi\right| \rho \left(\tilde{\boldsymbol{u}}_i - \boldsymbol{u}_i^n\right) + \Delta t \int_{\Gamma_i^\phi} \tilde{\boldsymbol{u}}(\boldsymbol{Q}^n \cdot \boldsymbol{n})\boldsymbol{n} \mathrm{d}\gamma - \Delta t \int_{\Gamma_i^\phi \cup \Gamma_i^w} \boldsymbol{\tau}(\tilde{\boldsymbol{u}})\boldsymbol{n} \mathrm{d}\gamma = -\Delta t \int_{\Gamma_i^\phi \cup \Gamma_i^w} P^n \boldsymbol{n} \mathrm{d}\gamma. \quad \text{(C.2)}$$

L'intégrale de bord $\partial\Omega_i^\phi$ de la maille Ω_i est alors décomposée en une partie sur le bord fluide Γ_i^ϕ et une autre sur le bord solide Γ_i^w.

$$\begin{aligned}\int_{\Gamma_i^\phi \cup \Gamma_i^w} \boldsymbol{\tau}(\tilde{\boldsymbol{u}})\boldsymbol{n} \mathrm{d}\gamma = \int_{\Gamma_i^\phi} \boldsymbol{\tau}(\tilde{\boldsymbol{u}})\boldsymbol{n} \mathrm{d}\gamma + \int_{\Gamma_i^w} \boldsymbol{\tau}(\tilde{\boldsymbol{u}})\boldsymbol{n} \mathrm{d}\gamma &= \sum_{j \in N(i)} \int_{\Gamma_{ij}^\phi} \boldsymbol{\tau}(\tilde{\boldsymbol{u}})\boldsymbol{n} \mathrm{d}\gamma + \int_{\Gamma_i^w} \boldsymbol{\tau}(\tilde{\boldsymbol{u}})\boldsymbol{n} \mathrm{d}\gamma \\ &= \sum_{j \in N(i)} (\boldsymbol{\tau}(\tilde{\boldsymbol{u}}))_{ij} \boldsymbol{n}_{ij} S_{ij}^\phi + \int_{\Gamma_i^w} \boldsymbol{\tau}(\tilde{\boldsymbol{u}})\boldsymbol{n} \mathrm{d}\gamma.\end{aligned}$$

Le flux visqueux de gradient de vitesse aux faces est approximé au moyen d'un flux à deux points d'ordre 1 en espace. On suppose, dans un premier temps, que le maillage est admissible (structuré orthogonal) cf. [57], ce qui permet d'avoir un schéma consistant.

Sur le bord fluide, il vient :

$$(\boldsymbol{\tau}(\tilde{\boldsymbol{u}}))_{ij} \boldsymbol{n}_{ij} S_{ij}^\phi = \mu \boldsymbol{\nabla} \tilde{\boldsymbol{u}} \cdot \boldsymbol{n}_{ij} S_{ij}^\phi = \mu \frac{\tilde{\boldsymbol{u}}_j - \tilde{\boldsymbol{u}}_i}{h_{ij/i} + h_{ij/j}} S_{ij}^\phi, \quad \text{(C.3)}$$

avec $h_{ij/i} + h_{ij/j} = d_{i/j}$ la distance du centre de masse de la partie fluide Ω_i^ϕ de la maille i au centre de masse de la partie fluide Ω_j^ϕ de la maille voisine j.

Sur le bord solide, sous l'hypothèse d'une condition d'adhérence à la paroi immobile, $\boldsymbol{u}|_w = 0$, le schéma donne :

$$(\boldsymbol{\tau}(\tilde{\boldsymbol{u}}))_w \boldsymbol{S}_i^w = -\mu \frac{\tilde{\boldsymbol{u}}_i}{d_i^w} S_i^w, \quad \text{(C.4)}$$

où S_i^w est la surface de la paroi w dans la maille i et d_i^w est la distance du centre de masse de la partie fluide Ω_i^ϕ à la paroi solide w.

On note que si la cellule est encombrée (cf. FIGURE C.1), les distances $d_i^w = I'F_b$ et $h_{ij/i} = I'J'$ doivent être redéfinies.

Le calcul de ces grandeurs géométriques est réalisé qu'une fois, dans une étape de prétraitement, au début de la simulation numérique et peut être parallélisé en espace.

Le schéma en espace des contraintes visqueuses donne finalement pour une maille i quelconque :

$$\int_{\Gamma_i^\phi \cup \Gamma_i^w} \boldsymbol{\tau}(\tilde{\boldsymbol{u}})\boldsymbol{n} \mathrm{d}\gamma = \sum_{j \in N(i)} \mu \frac{\tilde{\boldsymbol{u}}_j - \tilde{\boldsymbol{u}}_i}{h_{ij/i} + h_{ij/j}} S_{ij}^\phi - \tilde{\boldsymbol{u}}_i \sum_w \mu \frac{S_i^w}{d_i^w}. \quad \text{(C.5)}$$

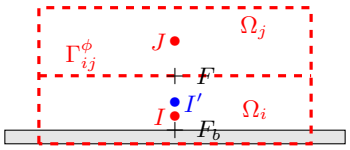

FIGURE C.1 – *Maille Ω_i encombré avec un solide (zone grise).*

2 Application à un écoulement de Poiseuille entre deux plaques parallèles

Afin de valider la prise en compte des termes de frottement visqueux dans l'approche intégrale décrite dans les parties précédentes, l'écoulement de Poiseuille [91] entre deux plaques parallèles infiniment fines, dont on connaît la solution analytique [18, 92], est simulé au moyen du code de CFD *Code_Saturne*.

2.1 Solution analytique

Le but de cette partie est d'établir le profil de vitesse et de pression du fluide analytique pour l'écoulement de Poiseuille et d'en déduire la contrainte visqueuse de frottement à la paroi. Ce problème correspond à un écoulement monodirectionnel simplement cisaillé à faible vitesse dans un canal.

Soit un écoulement stationnaire, laminaire et incompressible d'un fluide newtonien visqueux entre deux plaques planes immobiles et parallèles, de taille $L \times l$ distantes de $2e$ (cf. FIGURE C.2). Ces plaques définissent le domaine d'étude Ω de bord :

$$\partial\Omega = \partial\Omega^{w} \cup \partial\Omega^{in} \cup \partial\Omega^{out} = \{y = 0\} \cup \{y = 2e\} \cup \{x = 0\} \cup \{x = L\}.$$

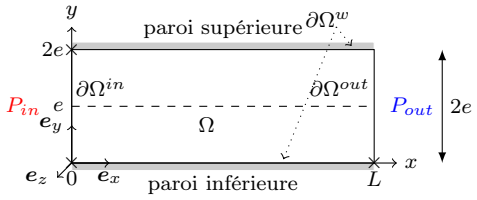

FIGURE C.2 – *Géométrie du canal entre deux plaques planes parallèles.*

L'écoulement étant incompressible, il est régi par les équations de Navier-Stokes incompressible (C.6), c'est-à-dire l'équation de continuité et l'équation de quantité de mouvement pour le champ de vitesse $\boldsymbol{u} = u\boldsymbol{e}_x + v\boldsymbol{e}_y + w\boldsymbol{e}_z$:

$$\begin{cases} \operatorname{div} \boldsymbol{u} = 0 \quad \text{dans } \Omega, \\ \partial_t \boldsymbol{u} + (\boldsymbol{u} \cdot \boldsymbol{\nabla})\, \boldsymbol{u} + \boldsymbol{\nabla} P = \mathbf{div}\, \boldsymbol{\tau} \quad \text{dans } \Omega, \\ \boldsymbol{u} = 0 \text{ sur } \partial\Omega^{w}, \\ P = P_{in} \text{ sur } \partial\Omega^{in} \text{ et } P = P_{out} \text{ sur } \partial\Omega^{out}, \end{cases} \tag{C.6}$$

avec le tenseur des contraintes visqueuses vérifiant : $\operatorname{div} \boldsymbol{\tau} = \operatorname{div} (\mu \boldsymbol{\nabla} \boldsymbol{u})$ et P la pression.

Le profil parabolique de vitesse est égale à :

$$u(y) = \frac{\tau_p}{2\mu}\frac{y}{e}(2e - y)\,. \tag{C.7}$$

Le profil de pression est en fonction de la condition limite d'entrée en pression P_{in} :

$$P(x) = -\frac{\tau_p}{e}x + P_{in}. \tag{C.8}$$

Par symétrie du problème par rapport au plan $x = e$, le maximum de vitesse U_{max} est atteint en $x = e$, centre du canal et sommet de la parabole, c'est-à-dire en $\left.\frac{\mathrm{d}u}{\mathrm{d}y}\right|_{y=e} = 0$:

$$U_{max} = u(e) = \frac{\tau_p e}{2\mu}. \tag{C.9}$$

On peut ainsi réécrire le champ de vitesse et de pression en fonction de U_{max} :

$$u(y) = U_{max}\frac{y}{e}\left(2 - \frac{y}{e}\right) \text{ et } P(x) = -\frac{2\mu U_{max}}{e^2}x + P_{in}. \tag{C.10}$$

La pression décroît linéairement avec x dans le canal. Cette chute de pression est due au frottement à la paroi, induit par la viscosité du fluide. Elle s'appelle perte de charge linéaire.

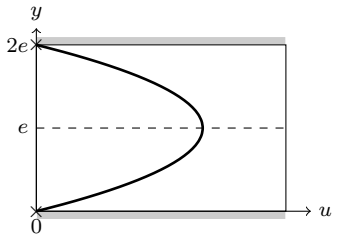

FIGURE C.3 – *Profil parabolique de vitesse* $u(y)$.

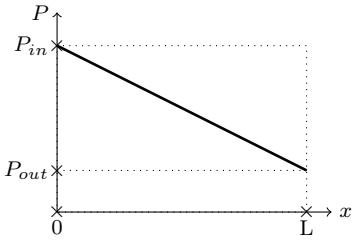

FIGURE C.4 – *Profil affine de pression* $P(x)$.

2.2 Erreur de discrétisation sur le frottement visqueux

Dans cette partie, on cherche à déterminer l'erreur commise sur la valeur analytique du frottement visqueux (cf. équation (C.9)) en fonction de la discrétisation du canal considérée.

2.2.1 Écoulement de Poiseuille multi-canal

Un écoulement, à l'équilibre, est considéré entre n plaques de surface $L.l$ et distantes de $2e$ en parallèle (cf. FIGURE C.5) ; on a ainsi $n-1$ écoulements de Poiseuille avec une baisse de pression égale à $-\Delta P = P_{in} - P_{out}$ dans chaque inter-canal. Cette perte de charge s'exprime en fonction de la vitesse débitante de manière exacte :

$$\Delta H = -\Delta P = \frac{3\mu\overline{u}L}{e^2}.$$

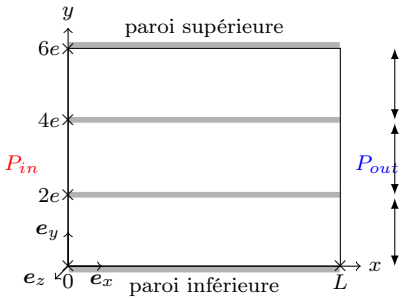

FIGURE C.5 – *Géométrie du multi-canal entre $n = 4$ plaques planes parallèles.*

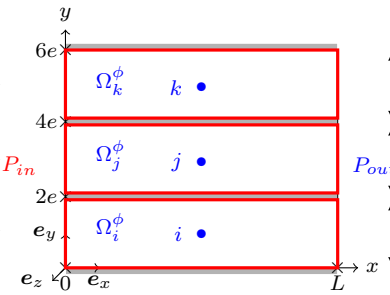

FIGURE C.6 – *une cellule par inter-canal avec $n = 4$.*

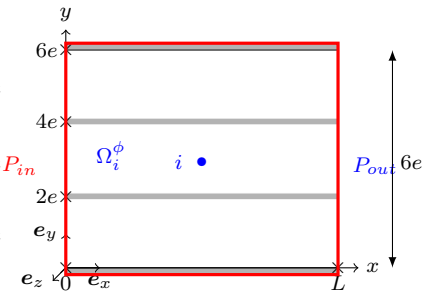

FIGURE C.7 – *une cellule d'ensemble avec $n = 4$.*

2.2.2 Discrétisation avec une cellule par inter-canal

Le multi-canal est maillé avec $n-1$ cellules adaptées, c'est-à-dire une cellule par inter-canal comme illustrée sur la FIGURE C.6.

L'équation de bilan de quantité de mouvement à l'équilibre (C.6) est discrétisée selon le schéma (C.2).

Pour toute cellule Ω_i^ϕ, avec $i \in [\![1, n-1]\!]$, on a l'égalité :

$$\sum_{j\in N(i)} (P_{ij} - P_i)\, \boldsymbol{n}_{ij} S_{ij}^\phi + \sum_{j\in N(i)} \mu \frac{u_i - u_j}{d_{i/j}} S_{ij}^\phi + \sum_{f_b} \mu \frac{u_i}{d_i^w} S_{f_b}^w = 0.$$

Ce qui donne, sachant que $u_i = u_j$:

$$(P_{out} - P_i)\, 2.e.l\ \boldsymbol{e}_x - (P_{in} - P_i)\, 2.e.l\ \boldsymbol{e}_x + \mu \frac{2.L.l}{e} u_i \boldsymbol{e}_x = 0$$
$$\Rightarrow \Delta H = -\Delta P = P_{in} - P_{out} = \frac{\mu L}{e^2} u_i = \frac{\mu L}{e^2} \overline{u}.$$

Ainsi, à vitesse débitante $\overline{u}$ fixée, la perte de charge est sous-estimée d'un facteur 3 avec une seule cellule maillant l'inter-canal.

2.2.3 Discrétisation avec une cellule pour le multi-canal

Le multi-canal est maillé avec une seule cellule pour $n-1$ inter-canaux (cf. FIGURE C.7). Les parois sont alors implicites, elles ne sont pas maillées. De la même manière, on applique le schéma (C.2) de l'équation de bilan de quantité de mouvement dans la cellule Ω_i^ϕ. Il en découle l'égalité suivante :

$$(P_{out} - P_i)\, 6.e.l\ \boldsymbol{e}_x - (P_{in} - P_i)\, 6.e.l\ \boldsymbol{e}_x + \mu \frac{6.L.l}{e} u_i \boldsymbol{e}_x = 0.$$

La même approximation de perte de charge, sous-estimée d'un facteur 3, est calculée :

$$\Delta H = -\Delta P = P_{in} - P_{out} = \frac{\mu L}{e^2} u_i = \frac{\mu L}{e^2} \overline{u}. \tag{C.11}$$

Finalement, dans les deux cas de maillage, le frottement est sous-estimé d'un facteur 3 par rapport à la référence, qui est la valeur analytique, à pression ou à vitesse débitante fixée.

2.2.4 Écoulement de Poiseuille dans un sous-canal maillé régulièrement

Maillage régulier

Le canal, entre deux plaques, est maillé avec $N = n_x.n_y$ cellules :

- n_x cellules selon l'horizontale x.
- n_y cellules selon la hauteur y.

L'axe $y = e$ est un axe de symétrie du maillage. Le pas d'espace constant est selon y : $\Delta y = \frac{2e}{n_y} = \frac{2R_H}{n_y}$, et selon x : $\Delta x = \frac{L}{n_x}$.

Un exemple de la grille cartésienne est tracé sur la FIGURE C.8 (pour $n_x = 8$ et $n_y = 4$).

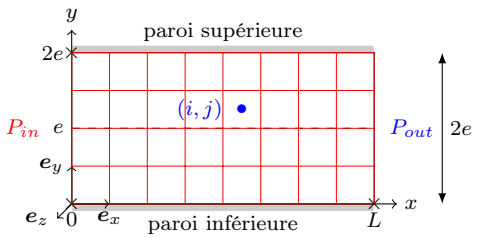

FIGURE C.8 – *Maillage du canal avec $n_x \times n_y$ cellules.*

Bilan de quantité de mouvement sur une cellule

L'équilibre de quantité de mouvement (C.6) est écrit pour une cellule quelconque $\Omega^{\phi}_{(i,j)}$ de l'intérieur du maillage de centre $(i,j) \in [\![1, n_x]\!] \times [\![1, n_y]\!]$.

$$\mu \frac{u_{(i,j-1)} - u_{(i,j)}}{\Delta y} \Delta x.l + \mu \frac{u_{(i,j+1)} - u_{(i,j)}}{\Delta y} \Delta x.l = \Delta y.l \left(P_{(i+1,j)} - P_{(i-1,j)} \right). \tag{C.12}$$

L'équilibre est également écrit pour une cellule de bord $\partial\Omega^w$ du maillage de centre (i, n_y) ou $(i, 1)$ notée $\Omega^{\phi}_{c_b}$, pour tout $i \in [\![1, n_x]\!]$.

$$\mu \frac{u_{(i,n_y-1)} - u_{(i,n_y)}}{\Delta y} \Delta x.l - \mu \frac{u_{(i,n_y)}}{\Delta y} \Delta x.l = \Delta y.l \left(P_{(i+1,n_y)} - P_{(i-1,n_y)} \right). \tag{C.13}$$

$$- \mu \frac{u_{(i,1)}}{\Delta y} \Delta x.l - \mu \frac{u_{(i,2)} - u_{(i,1)}}{\Delta y} \Delta x.l = \Delta y.l \left(P_{(i+1,n_y)} - P_{(i-1,n_y)} \right). \tag{C.14}$$

Notons que la vitesse $u_{(i,j)} = u_j$ ne dépend pas de son indice i. De plus, par symétrie du problème et du maillage, $u_j = u_{n_y-j+1}$ pour tout $j \in [\![1, n_y]\!]$.

En sommant sur les n_x cellules suivant x les équations précédentes (C.12) (C.13) et (C.14), et en posant $\Delta P = P_{in} - P_{out}$, on obtient donc le système linéaire ci-dessous pour n_y cellules suivant y :

$$\begin{cases} \mu\dfrac{u_2-u_1}{\Delta y}L.l-\mu\dfrac{u_1}{\frac{\Delta y}{2}}L.l & =-\Delta y.l.\Delta P \\ \mu\dfrac{u_1-u_2}{\Delta y}L.l+\mu\dfrac{u_3-u_2}{\Delta y}L.l & =-\Delta y.l.\Delta P \\ \vdots & \vdots \\ \mu\dfrac{u_{n_y-2}-u_{n_y-1}}{\Delta y}L.l+\mu\dfrac{u_{n_y}-u_{n_y-1}}{\Delta y}L.l & =-\Delta y.l.\Delta P \\ \mu\dfrac{u_{n_y-1}-u_{n_y}}{\Delta y}L.l-\mu\dfrac{u_{n_y}}{\frac{\Delta y}{2}}L.l & =-\Delta y.l.\Delta P. \end{cases} \tag{C.15}$$

Ce système se simplifie :

$$\begin{cases} -3u_1+u_2 & =-\dfrac{\Delta y^2}{\mu.L}\Delta P \\ u_1-2u_2+u_3 & =-\dfrac{\Delta y^2}{\mu.L}\Delta P \\ \vdots & \vdots \\ u_{n_y-2}-2u_{n_y-1}+u_{n_y} & =-\dfrac{\Delta y^2}{\mu.L}\Delta P \\ u_{n_y-1}-3u_{n_y} & =-\dfrac{\Delta y^2}{\mu.L}\Delta P. \end{cases} \tag{C.16}$$

Le système (C.16) peut se mettre sous forme matricielle :

$$\begin{pmatrix} -3 & 1 & 0 & \cdots & \cdots & \cdots & 0 \\ 1 & -2 & 1 & 0 & \cdots & \cdots & 0 \\ 0 & 1 & -2 & 1 & 0 & \cdots & 0 \\ \vdots & \ddots & \ddots & \ddots & \ddots & \ddots & \vdots \\ 0 & \cdots & 0 & 1 & -2 & 1 & 0 \\ 0 & \cdots & \cdots & 0 & 1 & -2 & 1 \\ 0 & \cdots & \cdots & \cdots & 0 & 1 & -3 \end{pmatrix} \begin{pmatrix} u_1 \\ \vdots \\ \vdots \\ \vdots \\ \vdots \\ \vdots \\ u_{n_y} \end{pmatrix} = -\frac{\Delta y^2}{\mu.L}\Delta P \begin{pmatrix} 1 \\ \vdots \\ \vdots \\ \vdots \\ \vdots \\ \vdots \\ 1. \end{pmatrix} \tag{C.17}$$

Calcul de la vitesse centre cellule

Pour déterminer l'expression de de la vitesse u_j, le système matriciel tridiagonal symétrique est inversé. En sommant sur les n_y lignes de (C.16), on obtient :

$$u_{n_y}=u_1=u_{c_b}=n_y\frac{\Delta y^2\Delta P}{4\mu L}=\frac{e^2\Delta P}{\mu n_y L}. \tag{C.18}$$

Ainsi, en réalisant un pivot de Gauss sur le système linéaire, on calcule pour tout $j\in[\![1,n_y]\!]$:

$$\begin{aligned} u_j=u_{n_y-j+1} &= \frac{\Delta Pe^2}{n_y^2L\mu}\left(n_y+2n_y-4+2n_y-8+\cdots+2n_y-4(j-1)\right) \\ &= \frac{\Delta Pe^2}{L\mu}\frac{n_y+2(j-1)n_y-\sum_{k=1}^{j-1}4k}{n_y^2} \\ &= \frac{\Delta Pe^2}{L\mu}\frac{(2j-1)n_y-2j(j-1)}{n_y^2}. \end{aligned} \tag{C.19}$$

2.3 Loi de paroi pour pondérer le frottement visqueux

Le but est de calculer une loi de paroi pour retrouver le frottement analytique. Cette loi est fonction de grandeurs géométriques du maillage. Cherchons le frottement pariétal à une cellule de bord sous la forme :

$$F_p = \tau_p S_{f_b}^w = \beta \cdot \mu \frac{u_{c_b}}{d_i^w} S_{f_b}^w, \tag{C.20}$$

avec β : la loi de paroi, coefficient de pondération du frottement fonction du paramètre $\frac{\Delta y}{R_H}$, tel que : $\beta \longrightarrow 1$ lorsque $\frac{\Delta y}{R_H} \longrightarrow 0$.

Posons $\beta = 1 + \tilde{\beta}$.

Le bilan de quantité de mouvement (C.6) est réécrit avec ce frottement pariétal pour un maillage régulier $d_i^w = \frac{\Delta y}{2}$:

$$\begin{cases} \mu \dfrac{u_2 - u_1}{\Delta y} L.l - \mu \dfrac{u_1}{\frac{\Delta y}{2}} L.l \left(1 + \tilde{\beta}\right) & = -\Delta y.l.\Delta P \\ \mu \dfrac{u_1 - u_2}{\Delta y} L.l + \mu \dfrac{u_3 - u_2}{\Delta y} L.l & = -\Delta y.l.\Delta P \\ \vdots & \vdots \\ \mu \dfrac{u_{n_y-2} - u_{n_y-1}}{\Delta y} L.l + \mu \dfrac{u_{n_y} - u_{n_y-1}}{\Delta y} L.l & = -\Delta y.l.\Delta P \\ \mu \dfrac{u_{n_y-1} - u_{n_y}}{\Delta y} L.l - \mu \dfrac{u_{n_y}}{\frac{\Delta y}{2}} L.l \left(1 + \tilde{\beta}\right) & = -\Delta y.l.\Delta P. \end{cases} \tag{C.21}$$

En sommant sur les n_y lignes, la vitesse de cellules de bord est déterminée :

$$u_{c_b}\left(\tilde{\beta}\right) = \frac{n_y \Delta y^2 \Delta P}{4\mu L\left(1 + \tilde{\beta}\right)} = \frac{e^2 \Delta P}{\mu n_y L\left(1 + \tilde{\beta}\right)}. \tag{C.22}$$

De la même manière que précédemment pour obtenir la vitesse u_j sans loi de paroi, la vitesse $u_j(\tilde{\beta})$ est calculée pour tout $j \in [\![1, n_y]\!]$:

$$\begin{aligned} u_j(\tilde{\beta}) = u_{n-j+1}(\tilde{\beta}) &= \frac{\Delta P e^2}{L\mu}\left(\frac{1}{n_y(1+\tilde{\beta})} + \frac{2n_y - 4 + 2n_y - 8 + \cdots + 2n_y - 4(j-1)}{n_y^2}\right) \\ &= \frac{\Delta P e^2}{L\mu}\left(\frac{1}{n_y(1+\tilde{\beta})} + \frac{2(j-1)n_y - 2j(j-1)}{n_y^2}\right). \end{aligned} \tag{C.23}$$

On en déduit la vitesse débitante définie par :

$$\overline{u} = \frac{1}{S}\int_S \boldsymbol{u} \cdot \boldsymbol{dS} = \frac{1}{2e}\int_0^{2e} u(y)dy \simeq \frac{1}{n_y}\sum_{j=1}^{n_y} u_j.$$

$$\begin{aligned}
\overline{u} = \frac{1}{n_y}\sum_{j=1}^{n_y} u_j(\tilde{\beta}) &= \frac{1}{n_y}\sum_{j=1}^{n_y} \frac{\Delta P e^2}{L\mu}\left(\frac{1}{n_y(1+\tilde{\beta})} + \frac{2(j-1)n_y - 2j(j-1)}{n_y^2}\right) \\
&= \frac{\Delta P e^2}{L\mu}\left(\frac{1}{1+\tilde{\beta}} + \frac{2}{n_y}\sum_{j=1}^{n_y}(j-1) - \frac{2}{n_y^2}\sum_{j=1}^{n_y} j(j-1)\right) \\
&= \frac{\Delta P e^2}{L\mu}\left(\frac{1}{1+\tilde{\beta}}\frac{2}{n_y}\frac{n_y(n_y-1)}{2} - \frac{2}{n_y^2}\frac{n_y(n_y^2-1)}{3}\right) \\
&= \frac{\Delta P e^2}{L\mu}\left(\frac{1}{1+\tilde{\beta}} + n_y - 1 - \frac{2(n_y^2-1)}{3n_y}\right) \\
&= \frac{\Delta P e^2}{L\mu}\left(\frac{1}{1+\tilde{\beta}} + \frac{n_y^2 - 3n_y + 2}{3n_y}\right).
\end{aligned} \tag{C.24}$$

Pour $\tilde{\beta} = 0$, on trouve l'expression de la vitesse débitante discrète sans loi de paroi :

$$\overline{u}(\tilde{\beta} = 0) = \frac{\Delta P e^2}{3\mu L n_y^2}(2 + n_y^2). \tag{C.25}$$

Le ratio entre la vitesse débitante discrète $\overline{u}(\tilde{\beta} = 0)$ et la vitesse débitante analytique donne :

$$\alpha = \frac{\overline{u}(\tilde{\beta} = 0)}{\overline{u}^{th}} = \frac{2}{n_y^2} + 1. \tag{C.26}$$

Remarque 1. *Pour $n_y = 1$, on retrouve que la vitesse débitante discrète est sous-estimée d'un facteur 3 par rapport à la vitesse débitante analytique :* $\overline{u}(\tilde{\beta} = 0) = \dfrac{\Delta P e^2}{\mu L}$.

Pour déterminer la loi de paroi β, on identifie la vitesse débitante analytique $\overline{u}^{th}$ et la vitesse débitante discrète $\overline{u}(\tilde{\beta})$ à ΔP fixée.

$$\overline{u}(\tilde{\beta}) = \frac{\Delta P e^2}{L\mu}\left(\frac{1}{1+\tilde{\beta}} + \frac{n_y^2 - 3n_y + 2}{3n_y}\right) = \overline{u}^{th} = \frac{e^2 \Delta P}{3\mu L}. \tag{C.27}$$

Il en résulte :

$$\tilde{\beta} = \frac{1}{\frac{3}{2}n_y - 1} \quad \text{et} \quad \beta = \frac{1}{1 - \frac{2}{3n_y}}. \tag{C.28}$$

La loi de paroi s'écrit alors en fonction de grandeurs géométriques :

$$\tilde{\beta} = \frac{1}{\frac{3R_H}{\Delta y} - 1} \quad \text{et} \quad \beta = \frac{1}{1 - \frac{\Delta y}{3R_H}}. \tag{C.29}$$

Dans le Tableau C.1 sont récapitulées les valeurs des coefficients pour $n_y \in \{1, 2, 3, 4, 5\}$: Sur la Figure C.9 est tracés la loi de paroi β et $\tilde{\beta}$ (branche d'hyperbole en fonction du nombre de cellules n_y) et le ratio α :

n_y	$\tilde{\beta}$	β	α
1	2	3	3
2	$1/2 = 0{,}5$	$3/2 = 1{,}5$	$3/2 = 1{,}5$
3	$2/7 \approx 0{,}286$	$9/7 \approx 1{,}286$	$11/9 \approx 1{,}222$
4	$1/5 = 0{,}2$	$6/5 = 1{,}2$	$9/8 = 1{,}125$
5	$2/13 \approx 0{,}154$	$15/13 \approx 1{,}154$	$27/25 = 1{,}08$

TABLEAU C.1 – *Valeurs coefficients de pondération pour* $n_y \in \{1, 2, 3, 4, 5\}$.

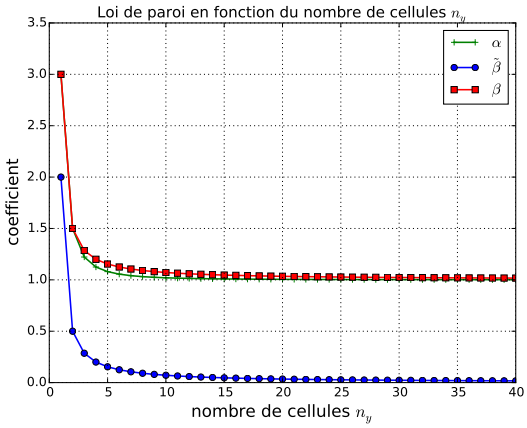

FIGURE C.9 – β, $\tilde{\beta}$ *et* α *en fonction de* n_y.

3 Simulations numériques d'un canal plan sur maillages grossiers

Le but est de simuler avec *Code_Saturne* l'écoulement de Poiseuille 2D dans le plan (x, y) entre deux plaques planes parallèles supposées infinies afin de retrouver le profil de pression analytique et ainsi les pertes de charge exactes en sortie du canal. La simulation est réalisée en 3D, mais la direction z est une invariante du problème. Le nombre de mailles selon x et y est un paramètre de calcul qui modifie la modélisation des frottements à la paroi comme cela a été vu précédemment.

3.1 Paramètres du calcul

Paramètres physiques

Le canal est représenté par un parallélépipède rectangle d'un volume de 20 m^3, 20 m de longueur dans la direction x pour 1 m de hauteur et de profondeur dans les directions y et z.

Paramètres	Valeurs
Longueur L	20 m
Largeur $2e$	1 m
Hauteur l	1 m

TABLEAU C.2 – *Paramètres géométriques du canal.*

Le domaine Ω, représentant l'intérieur du canal, est discrétisé avec un maillage cartésien régulier en $n_x \times n_y \times n_z = N$ cellules. Dans l'étude, le nombre de cellules selon x, n_x, et selon

y, n_y, sont variables, alors que le nombre de cellule selon z est fixé : $n_z = 1$. Chaque cellule est identique, d'un volume $\frac{20}{n_x} \times \frac{1}{n_y}\ m^3$.

Les caractéristiques et paramètres physiques de l'écoulement étudié sont récapitulés dans le Tableau C.3 :

Paramètres	symboles	valeurs
Masse volumique	ρ	1000 $kg.m^{-3}$
Viscosité dynamique	μ	10^{-3} $kg.m^{-1}.s^{-1}$
Pression entrée	P_{in}	0,24 ou 0,08 Pa
Pression sortie	P_{out}	0 Pa

Tableau C.3 – *Paramètres physiques de l'écoulement.*

Les conditions aux limites $C.L.$ du problème sur le bord $\partial\Omega$ sont :

- En entrée, sur le bord $x = 0$, une $C.L.$ de Neumann homogène est appliquée sur la vitesse, pour garantir une vitesse libre. La condition sur la pression est de deux types au choix :
  1. $C.L.$ de Dirichlet : la pression est fixée, $P_{in} = \dfrac{3\mu\overline{u}}{e^2}L$.
  2. $C.L.$ de Neumann : $\dfrac{\partial P_{in}}{\partial \boldsymbol{n}} = \dfrac{3\mu\overline{u}}{e^2}$ (pente du profil de pression analytique).
- Sur les parois supérieures ($y = 1$) et inférieures ($y = 0$), une $C.L.$ de Dirichlet homogène est imposée : la vitesse y est imposée nulle. Une condition de Neumann homogène est appliquée sur la pression.
- En sortie, sur le bord $x = 20$, une $C.L.$ de Dirichlet homogène est également imposée : la pression P_{out} est nulle. Comme pour l'entrée, une $C.L.$ de Neumann homogène est appliquée sur la vitesse.
- Une symétrie orthogonale par rapport au plan $z = 0{,}5$ est imposée pour avoir invariance par translation suivant l'axe z des grandeurs physiques et se ramener ainsi à un problème plan. La symétrie est réalisée par une condition de Neumann homogène sur les champs scalaires tel que la pression P, et par une condition de Dirichlet homogène sur la composante normale des champs vectoriels au plan de symétrie telle que la composante de vitesse w et par une condition de Neumann homogène sur les composantes tangentielles telles que u et v.

Remarque 2. *En entrée et sortie, la vitesse n'est pas fixée, seule la pression est fixée.*

Traitement numérique des conditions aux limites

La condition aux limites de Dirichlet est appliquée aux faces de bord des cellules. Pour une variable quelconque, ψ, à une face de bord, f_b, où la valeur A^D est imposée, on a :

$$\psi_{f_b} = A^D$$

La condition aux limites de Neumann est imposée par l'intermédiaire de la valeur centre cellule $\psi_{I'}$ et la valeur A^N donnée. En utilisant une approximation du 1^{er} ordre, on a :

$$\frac{\partial \psi}{\partial \boldsymbol{n}} = \frac{\psi_{f_b} - \psi_{I'}}{\overline{I'F}} = \frac{A^N}{\overline{I'F}}, \text{ on en déduit : } \quad \psi_{f_b} = A^N + \psi_{I'}$$

où $\overline{I'F}$ est la mesure algébrique du centre cellule à la face de bord f_b.

Paramètres numériques

Les équations de Navier-Stokes sont résolues de manière instationnaire, avec l'algorithme SIMPLEC vitesse-pression c'est-à-dire avec prédiction de la vitesse puis correction. Chaque cellule est initialisée avec une vitesse de 1 $m.s^{-1}$.

Paramètres	valeurs
nombre d'itération maximum	400 ou 100000
pas de temps variable Δt	[0,1 ;20]
précision solver vitesse/pression	10^{-14}
critère de convergence sur le résidu en temps	$\varepsilon = 10^{-9}$

TABLEAU C.4 – *Paramètres numériques.*

3.2 Simulations sans raffinement du maillage dans la direction transverse au canal

Les cas test ont pour but de retrouver par la simulation numérique le profil linéaire de pression avec une pente sous-estimée d'un facteur 3 par rapport à celle analytique et donc la perte de charge exacte également divisée par 3, avec une seule cellule maillant l'inter-canal ($n_y = 1$). Des simulations numériques sont réalisées avec un nombre de cellules n_x variables suivant la longueur du canal x. Huit valeurs de n_x ont été testées : $N = n_x \in \{2, 3, 10, 25, 50, 100, 200, 400\}$.

Remark 3.1. *De premiers cas test ont été effectués avec une condition aux limites sur la vitesse différente de celle décrite précédemment : en entrée du canal, sur $\partial\Omega^{in}$, la composante de la vitesse selon le sens de l'écoulement, u, est fixée égale à la vitesse débitante $\overline{u} = 1$ $m.s^{-1}$. Mais ces cas test ne donnaient pas le profil analytique linéaire du champ de pression, la pente de la droite n'est pas constante. Ceci est due aux conditions limites choisies, qui sont sur-contraignantes pour le problème posé (C.6). La pente de la pression et la valeur de la vitesse sont imposées en entrée. La C.L. de Dirichlet sur la vitesse et celle de Neumann sur la pression sont incompatibles avec le filtre de Rhie&Chow, qui permet de supprimer les modes de pression parasites apparaissant lors de la résolution de l'équation de Poisson. De même pour $n_y = 2$ cellules, le profil analytique n'est pas retrouvé.*

Dans ces cas test, les calculs sont réalisées avec les conditions aux limites du TABLEAU C.5. Comme décrites précédemment dans la partie 3.1, une condition de Dirichlet sur la pression en entrée et sortie ainsi qu'une condition de Neumann homogène sur la vitesse, afin d'avoir une vitesse libre en entrée, sont appliquées. La valeur de la pression à l'entrée imposée est divisée par 3 par rapport à la valeur théorique dans le but de prédire la vitesse débitante analytique, non sur-estimée d'un facteur 3. Les résultats numériques donnent le profil de pression et la

Bord	*C.L.*
$\partial\Omega^{in}$	$P_{f_b}^{in} = \dfrac{\mu\overline{u}}{e^2} L$ et $\dfrac{\partial u}{\partial \boldsymbol{n}}^{in} = 0$
$\partial\Omega^{w}$	$\boldsymbol{u}\|^{w} = 0$
$\partial\Omega^{out}$	$P_{f_b}^{out} = 0$

TABLEAU C.5 – *C.L. de Dirichlet cas test.*

vitesse débitante théoriques avec une grande précision. La vitesse calculée est égale à 1 $m.s^{-1}$ à 10^{-6} près pour $n_x \in \{10, 25, 50, 100, 200, 400\}$. L'erreur relative sur la pression est très faible (cf. erreur L^2 et L^1 dans le Tableau C.7). Ces erreurs relatives discrètes, L^2 et L^1, sont définies par (P^{th}, la pression théorique) :

$$\frac{\|P - P^{th}\|_{L^2}}{\|P^{th}\|_{L^2}} = \sqrt{\frac{\sum_{i=1}^{N} \left(P^{th}(x_i) - P_i\right)^2 |\Omega_i|}{\sum_{i=1}^{N} P^{th}(x_i)^2 \left|\Omega_i^{\phi}\right|}} \text{ et } \frac{\|P - P^{th}\|_{L^1}}{\|P^{th}\|_{L^1}} = \frac{\sum_{i=1}^{N} \left|P_i - P^{th}(x_i)\right| \left|\Omega_i^{\phi}\right|}{\sum_{i=1}^{N} |P^{th}(x_i)| \left|\Omega_i^{\phi}\right|}$$

Du fait que le profil de pression est affine en fonction de l'abscisse x, les résultats de la simulation dépendent très peu du nombre de cellules n_x. Il suffit de deux valeurs pour tracer le profil linéaire. Ainsi la perte de charge calculée ne dépend pas du nombre de cellules selon x (cf. Tableau C.6).

n_x	Δt	itération	P_I^{in}	P_I^{out}	$P_{f_b}^{in}$	$P_{f_b}^{out}$	$\Delta H^{th}/3$
3	10	143	0,0667	0,013	0,08	0	0,08
10	1	135	0,076	0,004	0,08	0	0,08
25	0,8	97	0,0784	0,0016	0,08	0	0,08
50	0,6	102	0,0792	0,0008	0,08	0	0,08
100	0,4	103	0,0796	0,0004	0,08	0	0,08
200	0,2	105	0,0798	0,0002	0,08	0	0,08
400	0,1	108	0,0799	0,0001	0,08	0	0,08

Tableau C.6 – *Valeurs de pression entrée-sortie pour différentes tailles de mailles.*

n_x	3	10	25	50	100	200	400
Δx	6,66667	2	0,8	0,4	0,2	0,1	0,05
erreur L^1	$6{,}85.10^{-8}$	$3{,}99.10^{-9}$	$6{,}57.10^{-9}$	$1{,}55.10^{-9}$	$1{,}69.10^{-9}$	$1{,}39.10^{-9}$	$1{,}23.\ 10^{-9}$
erreur L^2	$6{,}54.10^{-8}$	$4{,}90.10^{-9}$	$6{,}71.10^{-9}$	$1{,}58.10^{-9}$	$1{,}70.10^{-9}$	$1{,}40.10^{-9}$	$1{,}23.\ 10^{-9}$

Tableau C.7 – *Erreur L^1 et L^2 sur la pression $P(x)$.*

Le calcul pour $n_x = 3$ cellules est comparé avec celui obtenu avec une condition aux limites de Neumann sur la pression en entrée et toujours une vitesse libre en entrée : $\dfrac{\partial P^{in}}{\partial \boldsymbol{n}} = \dfrac{\mu \overline{u}}{e^2}$. On trouve le même ordre d'erreur 10^{-8} (cf. Tableau C.8).

$C.L.$ sur P^{in}	P_I^{in}	$P_{f_b}^{in}$	P_I^{out}	$P_{f_b}^{out}$	erreur L^2 P	erreur L^2 $\overline{u}$
Dirichlet	0,06667	0,08	0,01333	0	$6{,}54.10^{-8}$	$3{,}6.10^{-5}$
Neumann	0,06667	0,08	0,01333	0	$6{,}41.10^{-8}$	$9{,}7.10^{-5}$

Tableau C.8 – *Erreur L^2 sur la pression $P(x)$ et sur la vitesse débitante $\overline{u}$ pour $n_x = 3$.*

En conclusion, conformément à la théorie, la simulation numérique du champ de vitesse de l'écoulement de Poiseuille dans un canal plan ne dépend pas du raffinement du maillage selon l'horizontale (vitesse constante suivant l'axe Ox). Seul le champ de pression dépend de x, mais de manière linéaire, donc une cellule devrait suffire en théorie au calcul de ce champ de manière exacte. En effet, une fonction linéaire est dans l'espace de discrétisation spatiale en Volumes Finis (espace des fonctions affines par cellule). En pratique, il faut au moins trois cellules selon x

($n_x = 3$) pour avoir un résultat très proche de la solution analytique de référence (erreur L^2 de l'ordre de 10^{-8}). Ce problème est du à l'implémentation du calcul dans *Code_Saturne*. A partir de $n_x = 10$, l'erreur ne diminue plus et est de l'ordre de 10^{-9}.

3.3 Simulations avec raffinement du maillage dans la direction transverse au canal

On choisit par la suite de fixer $n_x = 10$ (erreur L^2 sur la pression est de l'ordre de 10^{-9} pour $n_y = 1$) et de faire varier le nombre de cellule n_y pour améliorer la discrétisation du profil parabolique de vitesse. Le maillage est toujours adapté au canal.

3.3.1 Cas test : $n_y = 2$

Une simulation numérique est réalisée avec un maillage avec raffinement 2D : le nombre de cellule suivant y est $n_y = 2$. La condition aux limites de Dirichlet sur la pression est appliquée. La vitesse centre cellule est initialisée avec une vitesse de 1 $m.s^{-1}$.

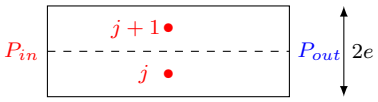

FIGURE C.10 – $n_y = 2$ *cellules par canal.*

Le calcul donne une vitesse débitante $\overline{u} = \frac{u_j + u_{j+1}}{2} = u_j = u_{j+1}$ (canal symétrique), égale à la valeur centre cellule, d'environ 1,5 $m.s^{-1}$. La vitesse débitante est sur-estimée d'un facteur $\alpha = \frac{3}{2} = 1{,}5$ ($\overline{u} = 1{,}5\ \overline{u}^{th}$) à une erreur relative de $1{,}25.10^{-4}$. Ce facteur est prédit par la formule (C.28) (cf. TABLEAU C.1).

$C.L.$	n_x	n_y	Δt	iter	$\overline{u}$	P_I^{in}	$P_{f_b}^{in}$	P_I^{out}	$P_{f_b}^{out}$	erreur L^2 P
Dirichlet	10	2	20	49367	1,4998	0,228	0,240	0,012	0	$2{,}43.10^{-12}$

TABLEAU C.9 – *Pression de bord et vitesse débitante pour* $n_y = 2$.

3.3.2 Cas test : $n_y = 3$

L'écoulement est simulé avec $n_y = 3$ cellules suivant la hauteur y. Les mêmes conditions aux limites que le cas précédent sont appliquées aux bords.

Le profil de pression est calculé avec une erreur L^2 de $2{,}83.10^{-8}$, tandis que la vitesse débitante est sur-estimé d'un facteur 1,2217. L'erreur relative sur le facteur $\alpha = 1{,}222$ (cf. TABLEAU C.1) est de $1{,}4.10^{-3}$.

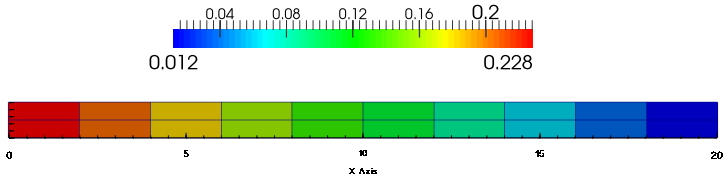

FIGURE C.11 – *Champ de pression pour* $n_y = 2$.

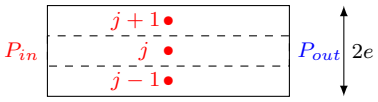

FIGURE C.12 – $n_y = 3$ *cellules par canal.*

$C.L.$	n_x	n_y	Δt	iter	$\overline{u}$	P_I^{in}	$P_{f_b}^{in}$	P_I^{out}	$P_{f_b}^{out}$	erreur L^2 P
Dirichlet	10	3	20	80263	1,2217	0,228	0,240	0,012	0	$2{,}83.10^{-8}$

TABLEAU C.10 – *Pression de bord et vitesse débitante pour* $n_y = 3$.

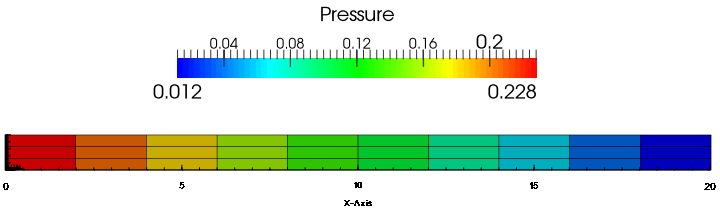

FIGURE C.13 – *Champ de pression.*

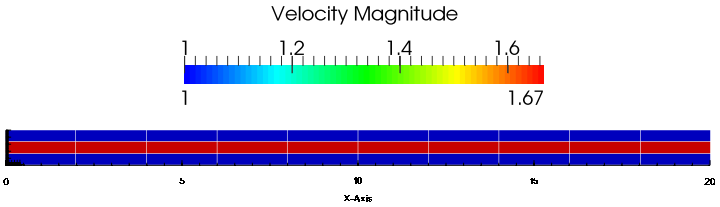

FIGURE C.14 – *Champ de vitesse.*

3.3.3 Cas test : $n_y = 4$

Le calcul est réalisé avec $n_y = 4$ cellules. On retrouve le coefficient théorique $\alpha = 1.125$ à une erreur de 3.10^{-4} (cf. TABLEAU C.11). La vitesse débitante $\overline{u}$ n'est surestimée que de 12,5%.

$C.L.$	n_x	n_y	Δt	iter	$\overline{u}$	P_I^{in}	$P_{f_b}^{in}$	P_I^{out}	$P_{f_b}^{out}$	erreur L^2 P
Dirichlet	10	4	20	63274	1,1247	0,228	0,240	0,012	0	$2{,}36.10^{-8}$

TABLEAU C.11 – *Pression de bord et vitesse débitante pour* $n_y = 4$.

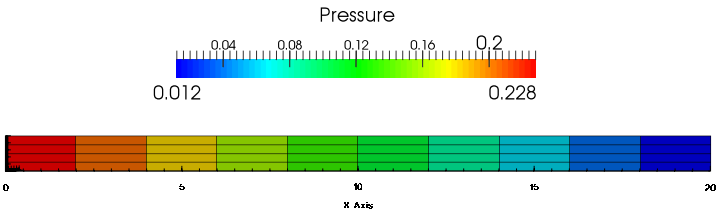

FIGURE C.15 – *Champ de pression.*

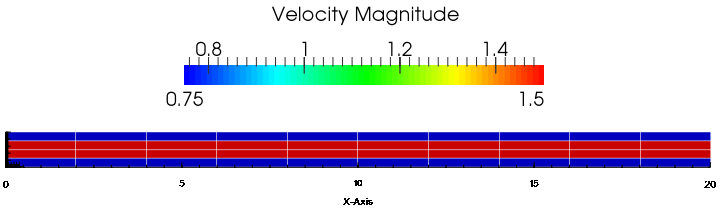

FIGURE C.16 – *Champ de vitesse.*

3.3.4 Cas test : $n_y = 5$

La simulation est refaite avec $n_y = 5$ cellules selon y. L'erreur sur la vitesse débitante n'est plus que de 8%. L'erreur sur le coefficient $\alpha = 1{,}08$ est de 1.10^{-4}.

$C.L.$	n_x	n_y	Δt	iter	$\overline{u}$	P_I^{in}	$P_{f_b}^{in}$	P_I^{out}	$P_{f_b}^{out}$	erreur L^2 P
Dirichlet	10	5	10	80924	1,0799	0,228	0,240	0,012	0	$5{,}62.10^{-10}$

TABLEAU C.12 – *Pression de bord et vitesse débitante pour $n_y = 5$.*

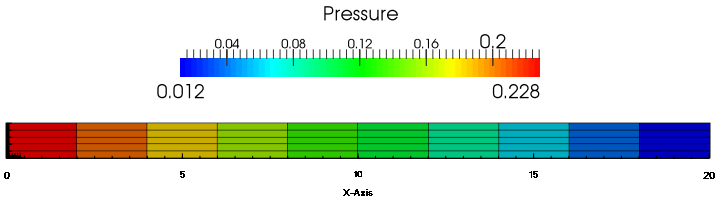

FIGURE C.17 – *Champ de pression.*

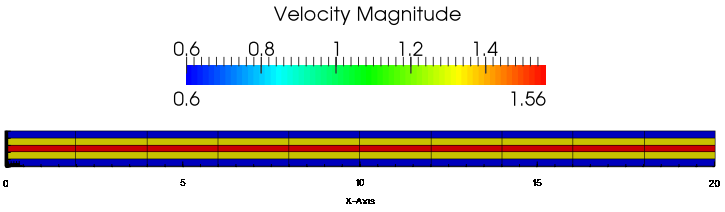

FIGURE C.18 – *Champ de vitesse.*

Les valeurs numériques calculées en fonction du nombre de cellules suivant la hauteur du canal, $n_y \in \{1, 2, 3, 4, 5\}$, sont récapitulées dans le TABLEAU C.13 ($n_x = 10$). Ces calculs sont effectués sans loi de paroi pour corriger le frottement à la paroi.

n_y	α	$\overline{u}$	erreur $\overline{u}$	ΔP	erreur L^2 P
1	3	2,9993	200%	0,24	2,94e-12
2	1,5	1,4998	50%	0,24	2,43e-12
3	$11/9 \approx 1{,}222$	1,2217	22%	0,24	2,83e-8
4	1,125	1,1247	12,5%	0,24	2,36e-8
5	1,08	1,0799	8%	0,24	5,62e-10

TABLEAU C.13 – *Vitesse débitante pour $n_y \in \{1, 2, 3, 4, 5\}$ sans loi de paroi.*

Les mêmes simulations numériques sont refaites avec cette fois-ci la loi de paroi β pour pondérer le frottement (cf. la formule (C.28)). La vitesse débitante et la perte de charge le long du canal sont bien prédites (cf. Tableau C.14).

n_y	β	$\overline{u}$	erreur $\overline{u}$	ΔP	erreur L^2 P
1	3	1	1,8e-4	0,24	2,91e-12
2	1,5	1	9,3e-5	0,24	5,33e-13
3	$9/7 \approx 1{,}286$	1	4,2e-4	0,24	2,67e-8
4	1,2	1	1,0e-4	0,24	1,25e-9
5	$15/13 \approx 1{,}154$	1	2,1e-3	0,24	2,71e-11

Tableau C.14 – *Vitesse débitante pour $n_y \in \{1, 2, 3, 4, 5\}$ avec loi de paroi.*

4 Simulations numériques d'un canal plan sur maillages grossiers encombrés

4.1 Présentation du calcul en milieu encombré

Le but de l'approche sur maillage encombré est de simuler l'écoulement de Poiseuille entre deux plaques avec les parois de bord prisent non plus en explicite (maillage adapté aux parois) comme dans les chapitres précédents mais, en implicite, c'est-à-dire que les arêtes ou faces du maillage ne sont pas nécessairement placées sur les parois. Les parois sont définies dans une étape de pré-traitement, dans laquelle sont calculées les surfaces fluides S^{ϕ} et solides S^{w}, les volumes fluides $\left|\Omega_i^{\phi}\right|$ et les taux de porosité. Les grandeurs géométriques : distance à la paroi et distance inter-cellule $I'J'$ pour chaque cellule doivent aussi être mises à jour pour obtenir le bon frottement à la paroi solide et entre couche de fluide.

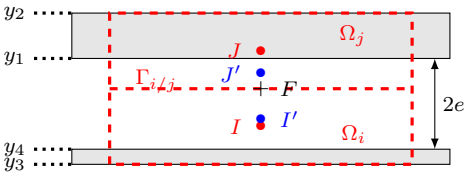

FIGURE C.19 – *Paroi implicite avec 2 cellules.*

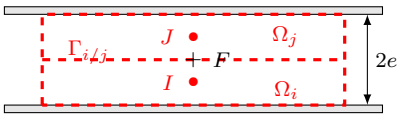

FIGURE C.20 – *Paroi explicite avec 2 cellules.*

Un obstacle, plaque dans le cas de l'écoulement de Poiseuille, est repéré grâce à ses ordonnées basse et haute. Il traverse tout le maillage, et est donc de longueur L. Pour deux obstacles, l'obstacle du haut est repéré par y_1 et y_2 et celui du bas par y_3 et y_4.
L'ensemble des cas test est réalisé avec une condition aux limites de Dirichlet sur la pression et de Neumann homogène sur la vitesse en entrée et sortie.
Les calculs sont effectués avec un nombre de cellules n_x suivant l'horizontale x égale à 10 et les cellules sont initialisées avec une vitesse de 1 $m.s^{-1}$.

4.2 Traitement numérique du frottement à la paroi de l'obstacle

Le frottement pariétal F_p est calculé comme un terme source volumique et est donc implicité dans l'équation de Navier-Stokes. Il est calculé en sommant sur toutes les cellules de bord de l'obstacle.

Soit Ω_i une cellule intersectant (cf. FIGURE C.19) ou en contact (cf. FIGURE C.20) avec l'obstacle, le frottement (contribution d'une face de bord) s'approxime par :

$$F_{p_i} = \frac{1}{\left|\Omega_i^{\phi}\right|}\tau_{p_i}S_i^w = \frac{1}{\left|\Omega_i^{\phi}\right|}\beta\left(\frac{R_H}{\Delta y}\right)\mu\frac{u_i}{d_i^w}S_i^w = \frac{1}{\left|\Omega_i^{\phi}\right|}\beta\left(\frac{R_H}{\Delta y}\right)\mu\frac{u_i}{I'F_b}S_i^w,$$

avec

- u_i : vitesse centre cellule de bord,
- $I'F_b$: distance du centre de gravité de la cellule modifiée I' à la face de bord de la paroi de l'obstacle. La modification faite porte directement sur cette distance et non sur la position du centre de la cellule fluide,
- S_i^w : norme de la surface de bord solide.

4.3 Simulations avec raffinement du maillage dans la direction transverse au canal

4.3.1 Cas test avec obstacles aux bords : $n_y = 1$

La géométrie 3D du canal est maillée comme précédemment par 10 parallélépipèdes ($\Delta z = l = 1\ m$ et $\Delta x = \frac{L}{10} = \frac{20}{10} = 2\ m$), mais leur hauteur est changée : $\Delta y = 1,2\ m$.
Deux obstacles sont placés sur les bords $\partial\Omega^w$ du canal comme représentés sur les schémas ci-dessous :

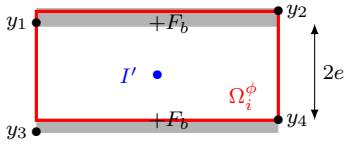

FIGURE C.21 – *(1) : parois semi-implicites.*

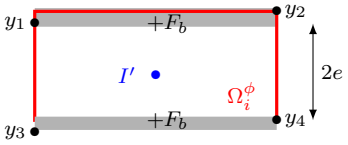

FIGURE C.22 – *(2) : parois implicites.*

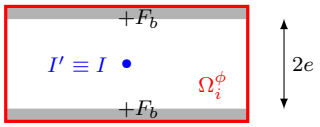

FIGURE C.23 – *(3) : parois implicites avec obstacles symétriques (centre cellule non modifié).*

Dans la configuration (1), la paroi est implicite en haut du canal et explicite en bas. La configuration (2) a deux parois implicites dont l'une, celle du bas, adaptée au maillage. Dans la configuration (3), les deux parois implicites sont à l'intérieur de la cellule.
Les quantités géométriques liées aux maillages, *i.e.* les distances aux faces de bord solide haute et basse $d_i^w = I'F_b$, sont recalculées afin de prendre en compte le centre de gravité modifié I' de la cellule fluide Ω_i^ϕ.
Le calcul est effectué avec la loi de paroi $\beta = 3$ pour pondérer le frottement dans le cas $n_y = 1$ et le pas de temps Δt est pris égale à 20.
Les résultats des simulations numériques, effectuées pour différentes positions d'obstacles, sont présentés dans le TABLEAU C.15. Dans la configuration (1), la vitesse débitante $\overline{u}$ est d'environ 1,5 $m.s^{-1}$ (surestimée de 50% par rapport à $\overline{u}^{th}$) car la loi de paroi n'est pas appliquée sur la paroi explicite (paroi inférieure).

config	itérations	porosité	y_1	y_2	y_3	y_4	$\overline{u}$ $(m.s^{-1})$	erreur L^2 P
(2)	16651	0,833	1	1,2	0	0	0,99992	2,91e-12
(1)	49367	0,833	1	1,2	-0,01	-0,02	1,4998	1,47e-11
(3)	16651	0,833	1,1	1,2	0	0,1	0,9992	3,41e-12

TABLEAU C.15 – *Résultats pour différentes configurations, $\Delta y = 1,2$ et $n_y = 1$.*

D'autres tests sont réalisés avec un autre maillage, ayant comme pas d'espace $\Delta y = 1$, pour vérifier la continuité de la formulation avec bord implicite. On obtient une vitesse débitante sensiblement égale. Les profils de pression et de vitesse sont tracés sur les FIGURES C.24 et C.25 pour la position des obstacles suivantes : $y_1 = 1$ / $y_2 = 1,2$ et $y_3 = 0$ / $y_4 = 0$ correspondant à la configuration (2) : parois implicites. On retrouve les profils analytiques et une vitesse débitante de 1 $m.s^{-1}$ à une erreur relative de 8.10^{-5}.

config	itérations	porosité	y_1	y_2	y_3	y_4	$\overline{u}$ $(m.s^{-1})$	erreur L^2 P
(1)	49367	1	1	1	-0,01	-0,02	1,4998	1,58e-12
(1)bis	49256	0,999	0,999	1	-0,01	-0,02	1,4968	2,71e-12
(1)ter	49367	1-1e-8	1-1e-8	1	-0,01	-0,02	1,4998	1,78e-12

TABLEAU C.16 – *Résultats pour différentes configurations,* $\Delta y = 1$ *et* $n_y = 1$.

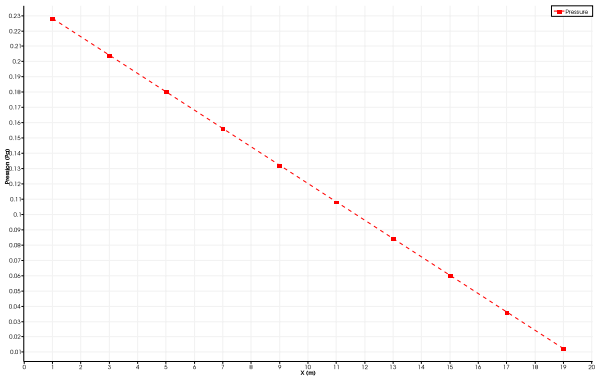

FIGURE C.24 – *Profil de pression* $P(x)$.

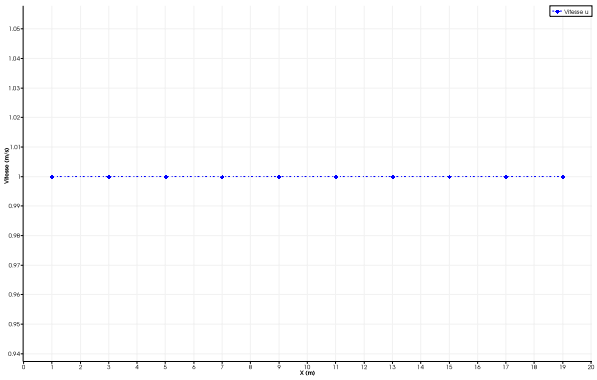

FIGURE C.25 – *Profil de vitesse* $u(x)$.

4.3.2 Cas test avec obstacles aux bords : $n_y = 2$

Les simulations numériques sont réalisées avec $n_y = 2$ cellules dans l'inter-canal suivant la direction y et $n_x = 10$ cellules dans le sens de l'écoulement x. La hauteur de deux parallélépipèdes est changée et vaut 1,6 m. Ainsi le pas d'espace Δy devient 0,8 m.
De la même manière, deux obstacles sont placés sur les bords $\partial\Omega^w$ pour former un canal de hauteur $2e = 1$ m. Deux configurations sont testées : une asymétrique et l'autre symétrique (cf. FIGURE C.26).

FIGURE C.26 – *(4) et (5) : parois implicites avec 2 cellules.*

La troisième configuration, FIGURE C.27, correspond à un obstacle qui recouvre plus d'une cellule entièrement sur deux cellules. La porosité de la cellule Ω_j est nulle. La hauteur du maillage est 2,4 m et le pas d'espace Δy est 1,2 m.

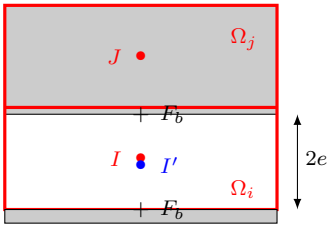

FIGURE C.27 – *(6) : parois implicites avec 2 cellules dont une totalement obstruée.*

Comme les cellules fluides ne sont pas de même taille, le calcul est effectué sans loi de paroi, $\beta = 1$. Le maximum d'itération est fixé à 100000.
Les résultats numériques obtenus pour les trois configurations décrites sont regroupés dans le TABLEAU C.17. La configuration (4) correspond à un cas où les deux cellules fluides Ω_i^ϕ et Ω_j^ϕ n'ont pas la même taille. La valeur sur-estimée de vitesse débitante, donnée par le calcul (**??**), est de 2,04 $m.s^{-1}$. On retrouve approximativement cette valeur : $\overline{u} = 2,033\ m.s^{-1}$, sachant que le calcul n'a pas totalement convergé. Le fait que le volume fluide de la cellule Ω_j est non nulle, *i.e.*qu'on ait deux cellules dans le canal, améliore l'approximation du frottement pariétal et donc la vitesse comparativement à un cas une cellule où $\overline{u} = 3\ m.s^{-1}$. Dans la configuration (5), le domaine fluide est symétrique, on est équivalent à un maillage adapté régulier à 2 cellules. La valeur attendue est : $\alpha = 1,5$. Alors que dans la configuration (6), on se retrouve dans le cas d'un canal maillé avec 1 cellule, où la vitesse est surestimée d'un facteur 3.

Config	Δy	Δt	Iter	y_1	y_2	y_3	y_4	u_i	u_j	$\overline{u}$ (m/s)	erreur L^2 P
(4)	0,8	10	100000	1	1,6	0	0	2,392	0,598	2,033	1,91e-7
(5)	0,8	20	49367	1,3	1,6	0	0,3	1,4998	1,4998	1,4998	3,08e-12
(6)	1,2	10	100000	1	2,4	0	0	2,9634	0/1	2,9634	6,23e-11
(4)bis	0,5	20	49819	0,9	1	0	0	1,349	1,0802	1,2295	2,16e-8
(4)ter	0,5	20	49367	1	1	0	0	1,4998	1,4998	1,4998	5,65e-12

TABLEAU C.17 – *Résultats pour différentes configurations, $n_y = 2$.*

Le dernier cas, configuration (4)ter, ne modifie en rien les centres de gravité des cellules, on vérifie bien que l'on a une vitesse débitante proche de 1,5 $m.s^{-1}$ à 2.10^{-4}.
Les champs de pression et de vitesse en approche poreuse sont représentés sur les FIGURES suivantes :

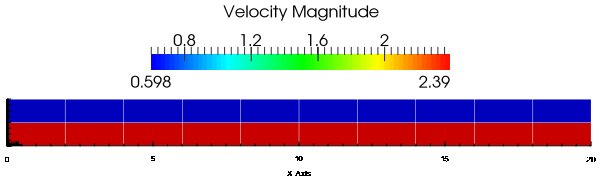

FIGURE C.28 – *Champ de vitesse pour la configuration (4).*

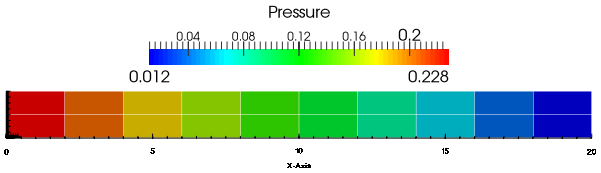

FIGURE C.29 – *Champ de pression pour la configuration (4).*

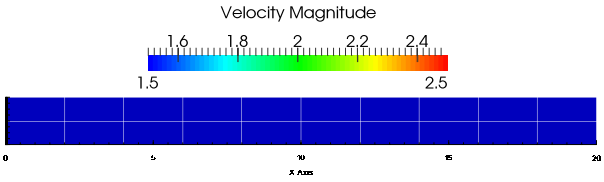

FIGURE C.30 – *Champ de vitesse pour la configuration (5).*

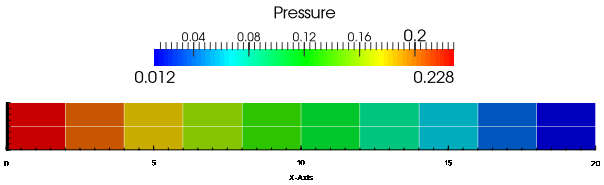

FIGURE C.31 – *Champ de pression pour la configuration (5).*

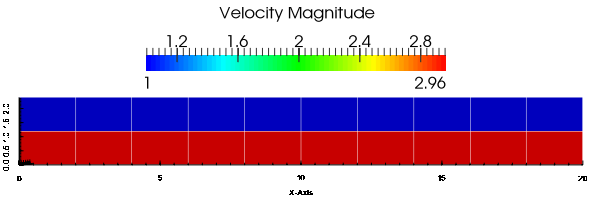

FIGURE C.32 – *Champ de vitesse pour la configuration (6).*

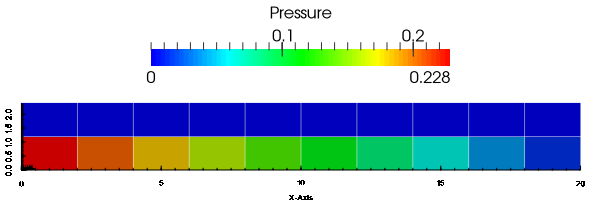

FIGURE C.33 – *Champ de pression pour la configuration (6).*

4.3.3 Cas test avec obstacle central : $n_y = 3$

La simulation numérique est réalisée avec $n_y = 3$ cellules dans l'inter-canal suivant la direction y et toujours $n_x = 10$ cellules dans le sens de l'écoulement x. La hauteur totale des trois parallélépipèdes vaut 3,3 m et le pas d'espace Δy est 1,1 m.

Contrairement aux deux cas test précédents, un obstacle est placé au centre du maillage entre $y = 1$ et 2,3 et l'autre obstacle est quant à lui placé au bord inférieur de $\partial\Omega^w$, $y = 0$. Les deux obstacles forment un multi-canal de hauteur $2e = 1$ m chacun avec paroi implicite en bas et paroi explicite en haut du maillage.

Les résultats de la simulation sont obtenus sans loi de paroi $\beta = 1$ au bout de 100000 itérations et donnés dans le TABLEAU C.18. La vitesse débitante est d'environ 3 $m.s^{-1}$.

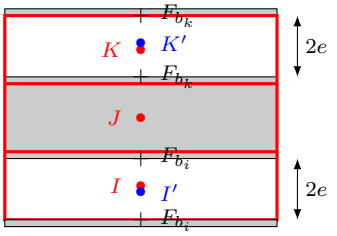

FIGURE C.34 – *(7) : parois implicites avec 3 cellules et barreau central.*

Δy	Δt	Iter	y_1	y_2	y_3	y_4	u_i	u_j	u_k $(m.s^{-1})$
1,1	10	100000	1	2,3	0	0	2,9634	0	2,959

TABLEAU C.18 – *Résultats avec un barreau central et $\Delta y = 1{,}1$ et $n_y = 3$.*

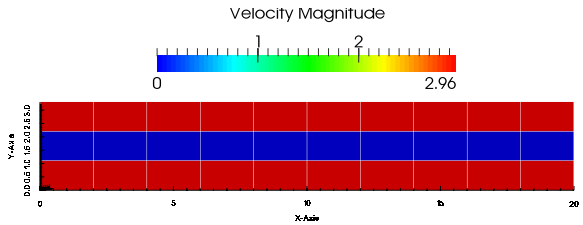

FIGURE C.35 – *Champ de vitesse pour la configuration (7).*

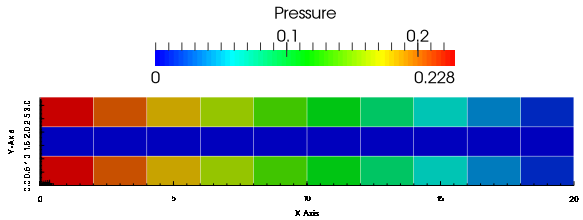

FIGURE C.36 – *Champ de pression pour la configuration (7).*

4.3.4 Cas test avec obstacle central : $n_y = 2$

Ce cas test correspond à un maillage de hauteur 2,4 m avec deux cellules suivant y et 10 suivant x. Le pas d'espace d'une cellule est $\Delta y = 1{,}2$ m.

Comme dans la section précédente, le premier obstacle est placé au bord inférieur de $\partial\Omega^w$, $y = 0$, et rend la paroi inférieure implicite. Le deuxième obstacle est placé quant à lui au centre du domaine maillé, entre $y = 1$ et 1,4. La paroi supérieure du domaine est explicite. Les obstacles forment un multi-canal (cf. FIGURE C.37).

Les résultats numériques, sans loi de paroi ($\beta = 1$), donnent une vitesse débitante à 100000 itérations d'environ 3 $m.s^{-1}$, correspondant au cas une cellule maillant l'inter-canal. L'erreur L^2 sur la pression est très faible : $5{,}16.10^{-11}$. La porosité cellule est de 0,8333.

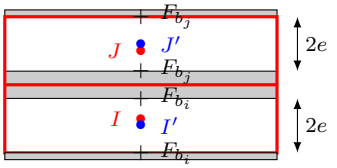

FIGURE C.37 – *(8) : parois implicites avec 2 cellules et barreau central.*

Δy	Δt	Iter	y_1	y_2	y_3	y_4	u_i	u_j $(m.s^{-1})$
1,2	10	100000	1	1,4	0	0	2,9634	2,9634

TABLEAU C.19 – *Résultats avec un barreau central, $\Delta y = 1{,}2$ et $n_y = 2$.*

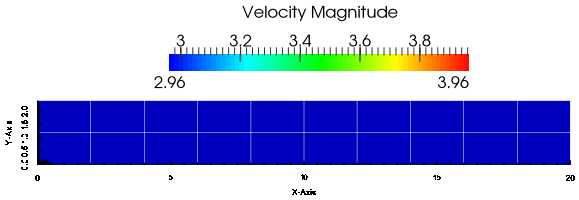

FIGURE C.38 – *Champ de vitesse pour la configuration (8).*

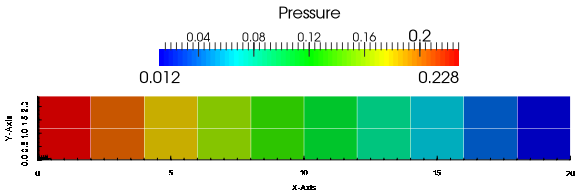

FIGURE C.39 – *Champ de pression pour la configuration (8).*

4.3.5 Cas test avec obstacle central : $n_y = 4$

Un autre calcul est réalisé avec 4 cellules suivant y pour mailler un domaine de hauteur 2,4 m ($n_x = 10$). Un obstacle central entre $y = 1$ et 1,4 est positionné, ainsi que qu'un autre sur la paroi inférieure ($y = 0$). Cela correspond à la configuration (8), mais avec deux cellules de taille différente pour mailler l'inter-canal.

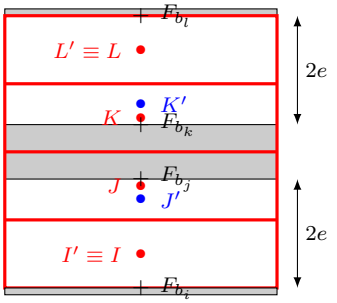

FIGURE C.40 – *(9) : parois implicites avec 4 cellules et barreau central.*

Les résultats du calcul donnent une vitesse débitante de 1,56 $m.s^{-1}$, dans le cas de deux cellules de taille différente maillant le canal. L'erreur L^2 sur la pression est de 5.10^{-9}. La porosité est de 0,8333 dans les mailles encombrées.

Δy	Δt	Iter	y_1	y_2	y_3	y_4	u_i	u_j	$\overline{u}$ $(m.s^{-1})$
0,8	10	100000	1	1,4	0	0	1,7991	1.1997	1,56

TABLEAU C.20 – *Résultats avec un barreau central, $\Delta y = 0{,}8$ et $n_y = 4$.*

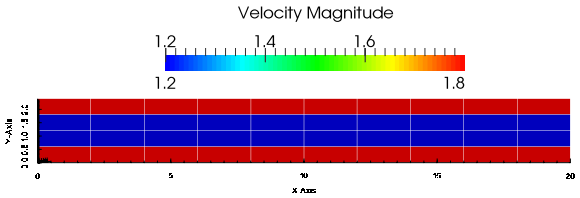

FIGURE C.41 – *Champ de vitesse pour la configuration (9).*

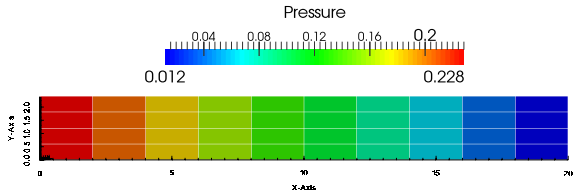

FIGURE C.42 – *Champ de pression pour la configuration (9).*

5 Conclusion

Une méthodologie a été proposée pour prendre en compte les effets visqueux dans la formulation intégrale. Elle permet de passer continûment grâce à une loi de paroi de l'échelle composant utilisant des corrélations (avec moins d'une maille par sous-canal) à l'échelle locale CFD où ces effets sont discrétisés directement sans corrélation.

La formulation intégrale est vérifiée sur un cas analytique : le canal plan avec une loi de Poiseuille régissant un écoulement laminaire. La loi de paroi permet de corriger le calcul du frottement visqueux à la paroi et ainsi de retrouver la chute de pression (perte de charge régulière) analytique. Les tests numériques sont réalisés avec plusieurs configurations de maillages grossiers, qui sont soit libres (obstacles au bord du maillage) soit encombrés (obstacles dans le maillage).

Une perspective d'amélioration pour la suite est d'étudier un cas d'application avec variations discontinues de la section du canal pour un écoulement visqueux en conduite. Une autre voie d'amélioration serait de simuler avec maillage grossier un écoulement turbulent dans un canal pour se rapprocher de configurations réelles dans le cœur de réacteur. L'objectif serait alors de se comparer à des cas de validation du code THYC [4] utilisant une approche poreuse. Pour cela, on devra établir des lois de frottement à la paroi en fonction d'autres corrélations de pertes de charge.

Références

[4] S. Aubry, C. Caremoli, J. Olive et P. Rascle. "The THYC three-dimensional thermal-hydraulic code for rod bundles : recent developments and validation tests". In : *Nuclear technology* 112.3 (1995), p. 331–345 (cf. p. 10, 14, 28, 110, 215).

[18] P. Chassaing. *Mécanique des fluides, éléments d'un premier parcours*. 3e édition. Cépaduès, 2010 (cf. p. 11, 13, 193).

[57] R. Eymard, T. Gallouët, C. Guichard, R. Herbin et R. Masson. "TP or not TP, that is the question". In : *Computational Geosciences* 18 (août 2014), p. 285–296. URL : https://hal.archives-ouvertes.fr/hal-00801648 (cf. p. 36, 94, 96, 111, 180, 192).

[91] J.L.M. Poiseuille. *Le mouvement des liquides dans les tubes de petits diamètres*. 1844 (cf. p. 193).

[92] R. Comolet. *Mécanique expérimentale des fluides, Dynamique des fluides réels, turbomachines*. T. 2. 4e édition. Masson, 1994 (cf. p. 193).